Processus contrôlant la dispersion et la spéciation redox du fer dissous d'origine hydrothermale (dorsale médio-atlantique)

David González Santana

DOCTORAT SCIENCES BRETAGNE DE LA MER LOIRE ET DU LITTORAL

UBO Université de Bretagne Occidentale

THESE DE DOCTORAT DE

L'UNIVERSITE
DE BRETAGNE OCCIDENTALE
COMUE UNIVERSITE BRETAGNE LOIRE

ECOLE DOCTORALE N° 598
Sciences de la Mer et du littoral
Spécialité : Chimie Marine

Par

David GONZÁLEZ SANTANA

Processus contrôlant la dispersion et la spéciation redox du fer dissous d'origine hydrothermale (dorsale médio-atlantique)

Processes driving the dispersion and redox speciation of hydrothermally sourced dissolved iron (Mid-Atlantic Ridge)

Thèse présentée et soutenue à Plouzané, le 11/12/2020
Unité de recherche : LEMAR

Rapporteurs avant soutenance :

Peter CROOT Professor, National University of Ireland Galway, Irlande
Rob MIDDAG Senior scientist, Royal Netherlands Institute for Sea Research (NIOZ), Pays-Bas

Composition du Jury :

Président :	Guillaume ROULLET	Directeur de recherche, Université de Bretagne Occidentale, France
Examinateurs :	Peter CROOT	Professor, National University of Ireland Galway, Irlande
	Rob MIDDAG	Senior scientist, Royal Netherlands Institute for Sea Research, Pays-Bas
	Valérie CHAVAGNAC	Directrice de recherche, Université Toulouse-III-Paul-Sabatier, France
	Jessica FITZSIMMONS	Assistant professor, Texas A&M University, Etats-Unis
Dir. de thèse :	Géraldine SARTHOU	Directrice de recherche, Université de Bretagne Occidentale, France
Co-Dir. de thèse :	Hélène PLANQUETTE	Chargée de recherche, Université de Bretagne Occidentale, France

Acknowledgements

I would like to thank **Université de Bretagne Occidentale** for funding these three years of my PhD. Similarly, I would like to thank **ISblue** for the funding which allowed me to participate in international conferences and research mobilities. I also thank **Luis Tito de Morais**, director of the Laboratoire des Sciences de l'environnement marin for hosting me in his laboratory.

I would like to extend my gratitude to i) my Internal Monitoring Committee: **Karine Salin** and **Solène Connan**, ii) my External Monitoring Committee: **Maeve C. Lohan** and **Cécile Guieu**, and iii) my PhD Thesis jury members: **Peter Croot** and **Rob Middag**, **Valérie Chavagnac**, **Jessica Fitzsimmons** and **Guillaume Roullet** for accepting to evaluate my PhD Thesis.

I thank both my supervisors **Géraldine Sarthou** and **Hélène Planquette** for this great opportunity. They have constantly supported me both in the academic (training me on how to use the SF-ICP-MS, preparing me for oral presentations at conferences, and reading and commenting all my written work, *(and lending me your car (and your son's scooter) to get to IFREMER faster)* and in the daily personal related topics (including French bureaucracy). Thanks to them I have also been able to participate in two research cruises, two international conferences and a mobility to analyse Fe(II) oxidation kinetics samples.

I thank Maeve C. Lohan for allowing me to participate in the GA13 cruise and for personally collecting the oxidation kinetics samples. Similarly, **Lise Artigue** who collected the pH samples, the rest of the trace metal sampling (**Dakota Gibbs**, **Wenhao Wang** and **Arthur Gourain**), the PI (**Alessandro Tagliabue**) and all the scientific and crew members of the FRidge cruise.

In the same manner, I thank **Géraldine Sarthou**, **Verónica Arnone** and **Matthieu Bressac** for being a great trace metal sampling team during the GPpr14 cruise, with two great PIs (**Cécile Guieu** and **Sophie Bonnet**), the crew (*l'équipage*) and most of the scientific crew.

I thank **Hannah Whitby**, **Arthur Gourain** and **Thomas Holmes** for collecting and neatly labelling the dissolved trace metal samples during the GApr07 cruise.

I also must acknowledge and thank **Géraldine Sarthou**, **Hélène Planquette, Eva Bucciarelli**, **Floriane Desprez de Gesincourt**, **Morgane Gallinari**, **Hannah Whitby** and **Wen-Hsuan Liao** for helping me clean every Monday thousands of bottles for trace metal sampling.

I would also like to mention my office mates (**Natalia, Natasha, Hannah, Marie, Maria, Wen Hsuan** and **Manu**) and other PhD students (**Marc**, **José**, **Jordan**, **Nicolas**, …). It was great to have such a happy and helpful group of people around; if I needed help, I could turn around and quickly obtain help from any of them. I will always remember baking hundreds of small baked goods for Hannah's wedding using two small electric ovens, cycling around Brittany trying to complete as many STRAVA challenges as possible and doing picnics in the sunny (although rare) Brittany days. I have to especially thank **Natalia** and **Marc**, who *willingly* (that's what friends are for?) brought me fresh vegetables during the COVID-19 confinement *and became my taxi drivers during the PhD (★★★★☆; clean taxi, although they normally took me to barns instead of bars*).

Finally, I would like to thank my **family** who were always there helping me through the tough and lonely COVID-19 confinement moments and understanding why I spent so much time at sea (including a Christmas).

Table of Contents

Table of figures

List of tables

Preamble

In recent years, Research Journals have started to implement the use of graphical abstracts, a summary figure which is available in the online versions of the manuscripts. Elsevier (https://www.elsevier.com/authors/journal-authors/graphical-abstract, last accessed 12/10/2020) defines a graphical abstract as "*a single, concise, pictorial and visual summary of the main findings of the article. This could either be the concluding figure from the article or a figure that is specially designed for the purpose, which captures the content of the article for readers at a single glance.*" Using this definition, I decided to create a graphical abstract for each section of the Thesis. Moreover, I opted for creating a common template based on the central theme of the Thesis. As such the cover page of the introduction presents a "hydrothermal template" which will be used and modified for each specific chapter of the Thesis.

1. Introduction

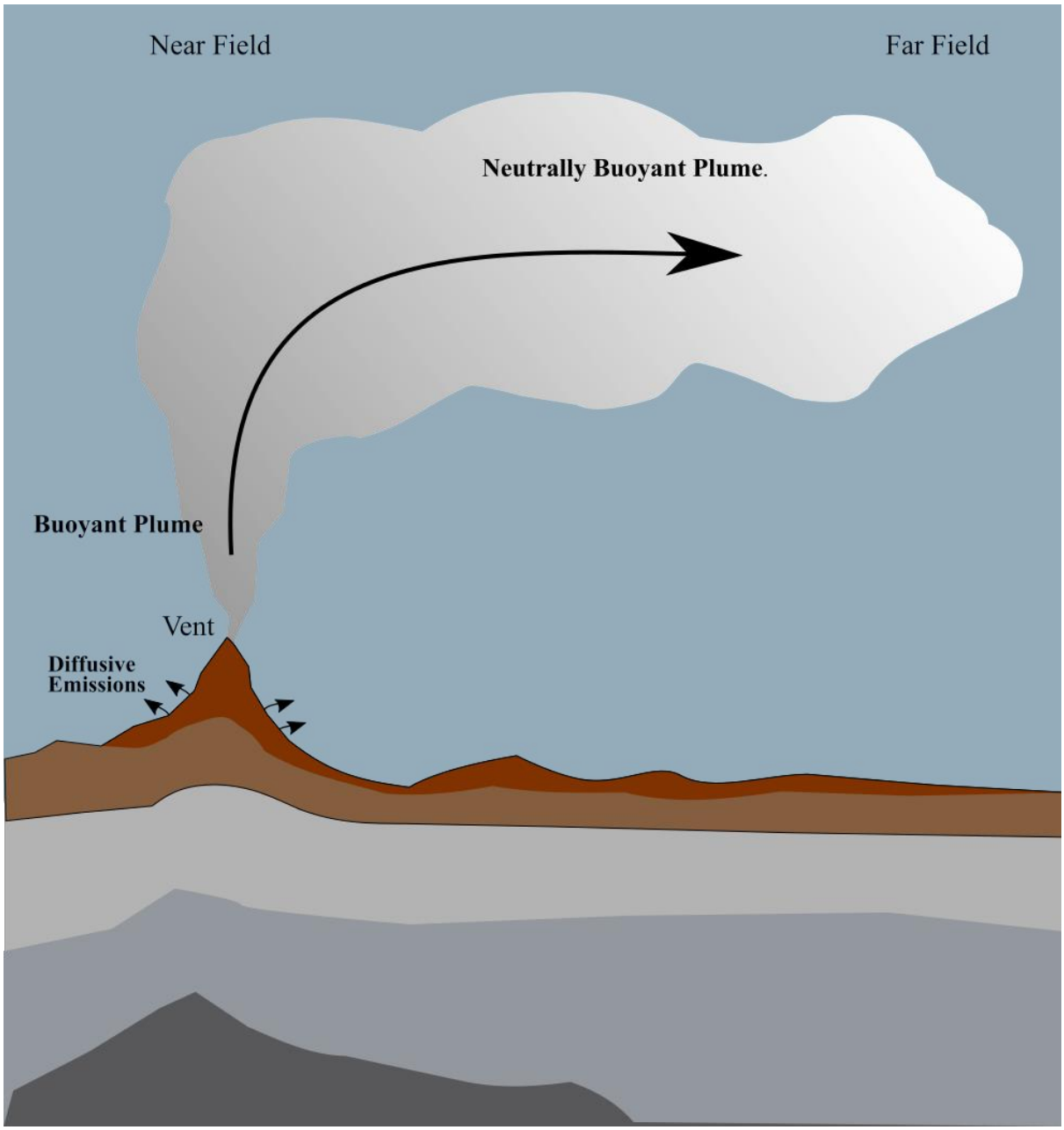

Graphical abstract of the Introduction. It shows a hydrothermal system with a vent producing the buoyant plume. This plume ascends (the arrow within the plume facilitates this perception) until it reaches neutral buoyancy becoming the neutrally buoyant plume. The plume is transported by the ocean currents far from its original location.

1.1. Iron influence on natural systems

Aquatic iron (Fe) biogeochemistry has received wide spread interest over the past decades with numerous studies linking Fe to carbon cycling and global climate (e.g. Martin, 1990; de Baar et al., 2005; Mahowald et al., 2005). Over 45% of global photosynthesis occurs in aquatic environments (Falkowski et al., 1998) and photosynthetic systems are heavily dependent on iron (Raven, 1990; Raven et al., 1999). As planktonic species have specific Fe requirements, available Fe concentrations can influence the structure and abundances of phytoplanktonic communities present in the seawater (Boyd et al., 2000; Timmermans et al., 2001).

1.2. Iron: an essential nutrient

Prior to the Great Oxygenation Event, ~2.4 billion years (Gyr) ago, oceanic Fe was found in its reduced form ferrous iron (Fe(II)) (Thibon et al., 2019). Life on Earth developed 3.8-4.5 Gyr ago (Betts et al., 2018; Baumgartner et al., 2019) most probably in hydrothermal systems (Dodd et al., 2017). Therefore, it is thought that Fe requirement in biology is most likely a result of the ubiquitous presence of Fe when early life developed (Saito et al., 2003). From the ferruginous conditions that prevailed during most of the Archean, the ancient ocean evolved toward euxinic (anoxic and sulphide rich) conditions and after the development of oxygenic photosynthesis, to a predominantly oxic environment (Camacho et al., 2017). Nowadays, due to its low solubility (Liu and Millero, 2002) in oxygenated waters, Fe is present in very low concentrations in the oceans (0.05-2 nmol L^{-1}) (Landing and Bruland, 1987; Martin et al., 1990; de Baar and De Jong, 2001) despite its high abundance in the Earth's crust (5.6%; fourth most abundant element) (Taylor, 1964).

As a result, Fe often limits productivity where subsurface nutrient are not depleted, including the main oceanic upwelling regions (Hutchins et al., 1998, 2002), the Pacific Ocean (de Baar et al., 2005; Boyd et al., 2007), the subpolar North Atlantic Ocean (Moore et al., 2006) and the polar Southern Ocean (Boyd et al., 2000). It is important to note that macronutrients and micronutrients other than Fe, such as cobalt (Co) and zinc (Zn) may also co-limit marine phytoplankton (Figure 1-1). Variability in the stoichiometries of nutrient supply and biological demand are key determinants of oceanic nutrient limitation (Moore et al., 2013).

Laboratory phytoplankton cultures have been used to study the elemental composition of plankton. Averaging trace-metal composition of eukaryotic marine phytoplankton (Ho et al.,

2003) provides an extension of essential trace metals to Redfield formula ($C_{106}N_{16}P_1$) of $(C_{106}N_{16}P_1)_{1000}Fe_8Mn_4Zn_{0.8}Cu_{0.4}Co_{0.2}Cd_{0.2}$. However, the applicability of laboratory cultures to natural waters is uncertain because the experimental conditions and the composition of the culture media used may not match those of natural waters (e.g. $(C_{72}P_1S_{0.7})_{1000}Zn_{5.4}Fe_{1.8}Ni_{0.61}Mn_{0.26}$; Twining et al., 2004).

To date, the spatial patterns and importance of co-limitation therefore remain unclear.

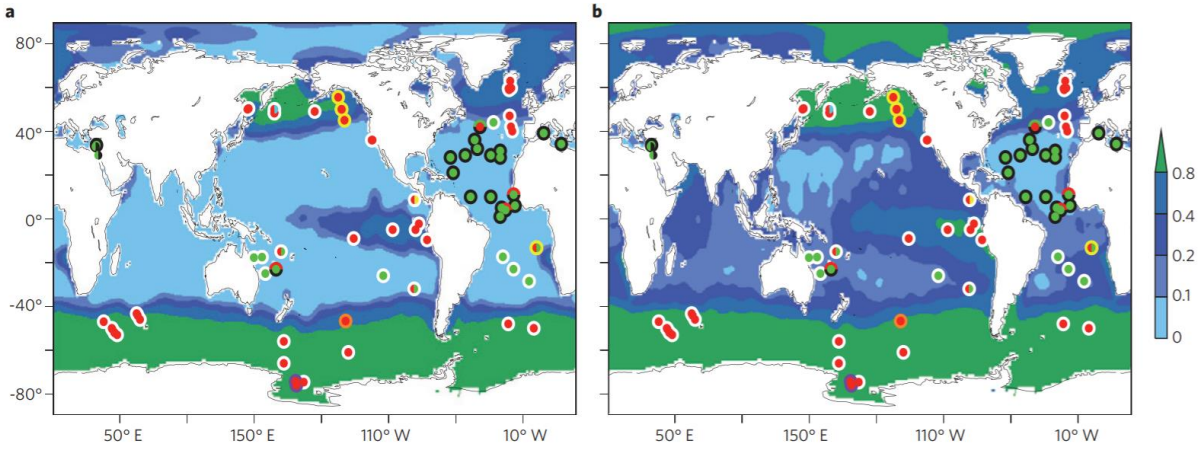

Figure 1-1. Nutrient limitation patterns. Backgrounds indicate annual average surface concentrations of nitrate (a) and phosphate (b) in µmol kg^{-1}. To assist comparison, nitrate is scaled by the mean N:P ratio of organic matter (divided by 16). Symbols indicate the primary (central circles) and secondary (outer circles) limiting nutrients as inferred from chlorophyll and/or primary productivity increases following artificial amendment of: N (green), P (black), Fe (red), Si (orange), Co (yellow), Zn (cyan) and vitamin B12 (purple). Divided circles indicate potentially co-limiting elements. White outer circles indicate that no secondary limiting nutrient was identified, which in many cases will be because of the lack of a test. Figure from Moore et al. (2013).

1.2.1. "The iron hypothesis"

The development of trace-metal clean sampling and analytical methods during the late 1970s (Bruland et al., 1979) allowed for the first reliable ocean Fe measurements (Gordon et al., 1982; Landing and Bruland, 1987). Moreover, shipboard Fe-enrichment experiments resurfaced the hypothesis that Fe limitation affected primary production of certain oceanic regions such as the Southern Ocean (Martin and Fitzwater, 1988; Martin et al., 1990). These experiments led to the formulation of the "iron hypothesis" (Martin, 1990), which proposed that high Fe-rich dust inputs during glacial periods augmented the utilisation of major nutrients and produced a net sink in the atmospheric carbon dioxide concentration. Based on this hypothesis, it was proposed that Fe fertilization of HNLC areas would increase primary production in the ocean. Two approaches were used for the *in situ* fertilization experiments. Artificial fertilization experiments were initiated in 1993 in the Galapagos region and since then several Fe-

enrichment experiments have been designed in different regions worldwide (Yoon et al., 2018), confirming Fe limitation in the Pacific Ocean (de Baar et al., 2005; Boyd et al., 2007), subpolar North Atlantic Ocean (Moore et al., 2006) and upwelling regions (Hutchins et al., 1998, 2002).

A second approach was to investigate naturally fertilized areas with a reference region where Fe supply is low. For example, the CROZEX (Planquette et al., 2007; Pollard et al., 2007) and the KEOPS projects carried out above the Crozet and Kerguelen Plateau (Blain et al., 2008; Chever et al., 2010) in the Southern Ocean.

1.3. Physico-chemical speciation of iron in the ocean

Depending on the conditions of the environment, iron in the ocean can take various forms, which define its speciation. The transport and distribution of Fe strongly depends on hydrodynamic conditions and the physico-chemical properties of the seawater. The Fe speciation is controlled by pH, Eh (redox potential) and the presence or absence of dissolved components in seawater that react with Fe (both ferrous (Fe(II)) and ferric (Fe(III)) species) to form dissolved complexes, colloids or poorly soluble mineral phases.

Knowing the Fe speciation is thus necessary to be able to understand the interactions that are established and the mechanisms that control Fe reactions, distribution and concentrations in the marine environment. The determination of the physico-chemical speciation of Fe follow two different pathways, the physical or the chemical approaches.

1.3.1. Physical speciation

Iron in seawater can be operationally defined according to filtration pore size (Figure 1-2), with the following mass balance:

$$Fe_{total} = pFe + cFe + sFe \quad (1\text{-}1)$$

Where Fe_{total} is the total Fe concentration and is formed by particulate Fe (pFe, particles greater than 0.45 µm) and dissolved Fe (dFe = cFe + sFe). Dissolved Fe is formed by colloidal sized particles (cFe; between 0.02 and 0.45 µm) and the soluble Fe fraction (sFe; smaller than 0.02 µm).

At sea, particulate Fe (pFe) can be collected on 0.45, 0.4, or 0.2 µm pore size filters. The filtrate is defined as the dissolved phase (dFe). Currently, the GEOTRACES protocol

(www.geotraces.org) recommends the use of cartridge filters with a final pore size of 0.2 µm if the particulate fraction is not going to be collected, so some concentration variations do still exist depending on the filter which is used. Dissolved samples can further be filtered through a 0.02 µm pore-size filter (cross-flow filtration can also be used (Schlosser and Croot, 2008)) to obtain the soluble Fe (sFe). The colloidal sized fraction (cFe; 0.02 to 0.2 µm) can be computed from the concentration subtraction (cFe = dFe – sFe). The proportion of sFe/dFe varies across ocean basin from anywhere between 0.04 and 1.00 (Hawkes et al., 2013; Nishioka et al., 2013; Fitzsimmons et al., 2014, 2015).

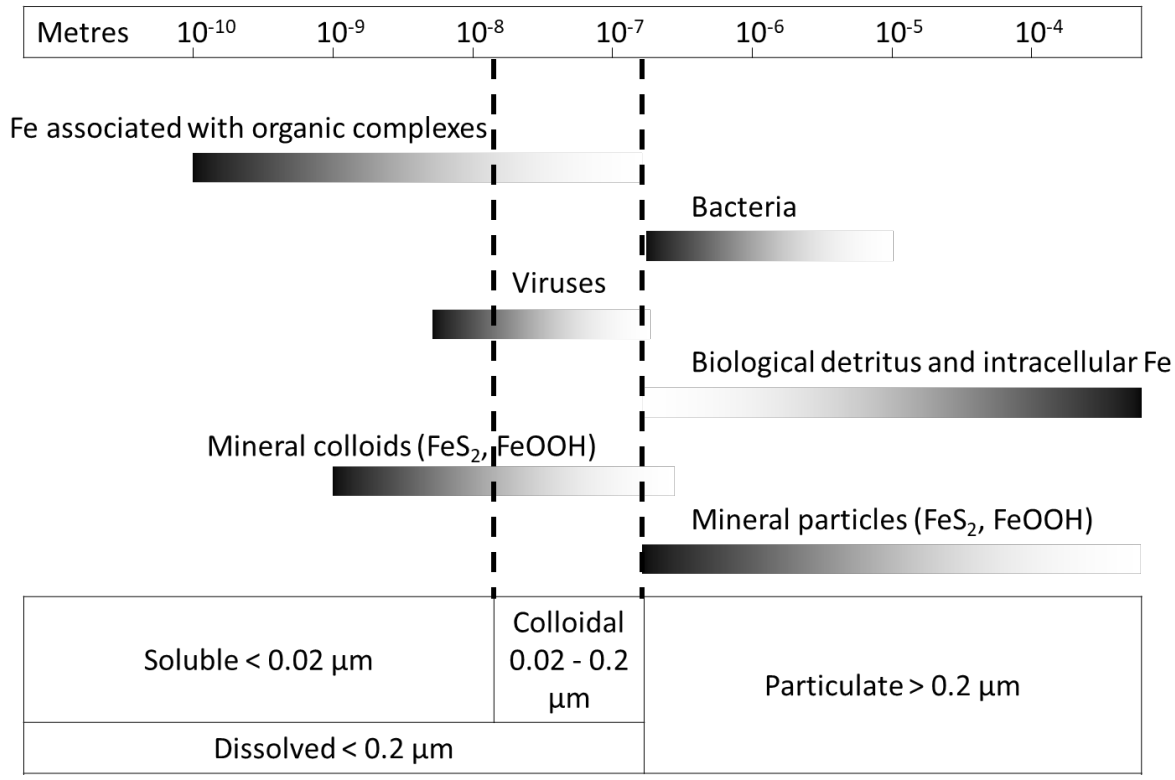

Figure 1-2. Operationally defined size fractionation of Fe. Figure from Lough et al. (2019b). Size fractionation determination is operationally defined, and the recommended filter and pore sizes are stated in the GEOTRACES cookbook (www.geotraces.org).

1.3.2. Chemical speciation

The second approach to classify the Fe components in seawater is based on their chemical properties. This approach also divides the Fe into three fractions:

$$Fe_{total} = Fe' + FeL + Fe_{inert} \quad (1\text{-}2)$$

Where Fe' denotes labile inorganic Fe complexes (the free Fe and inorganic complexes), FeL represents Fe organic ligand complexes exchangeable within a time scale of <1 day and Fe_{inert}

stands for the Fe fraction bound up in matrices that are essentially non-labile (Figure 1-3, Gledhill and Buck, 2012).

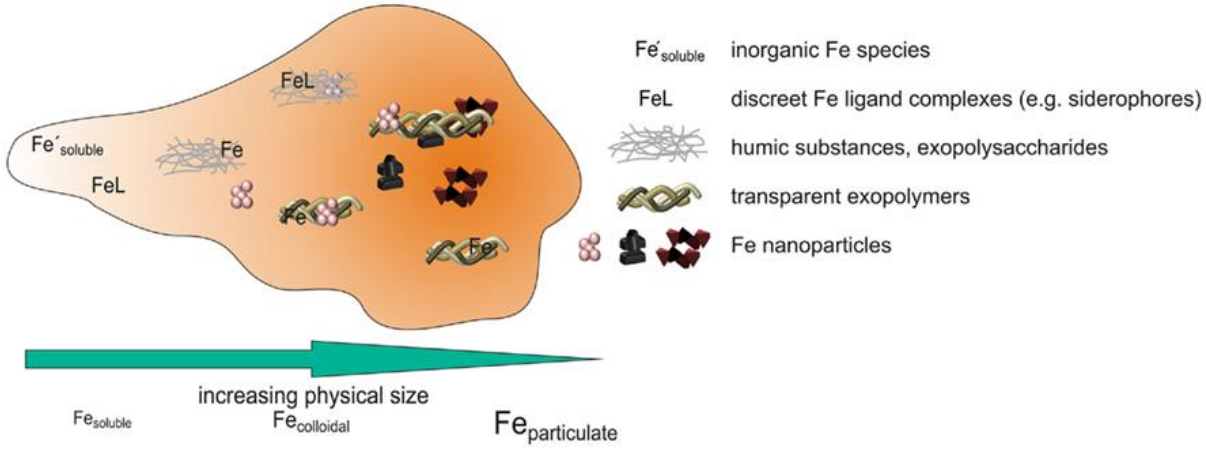

Figure 1-3. Schematic figure illustrating potential component of the iron pool identified in seawater. Decreasing kinetic lability of iron within the components is represented by deeper orange background shading. Figure from Gledhill and Buck, (2012).

Iron exists in two redox states, ferrous (Fe(II)) and ferric (Fe(III)). Each species exhibits different chemical characteristics. Iron (II) is very soluble, but is rapidly oxidized in the presence of oxygen and hydrogen peroxide (Millero et al., 1987; King et al., 1995; Santana-Casiano et al., 2005). Iron(III) is the thermodynamically stable species in natural waters, but it can be reduced to Fe(II) under certain processes: (i) Photo-reduction of Fe(III)-L complexes, Fe-oxides and hydroxides (Waite and Morel, 1984; Miller et al., 1995; Voelker and Sedlak, 1995; Laglera and Van den Berg, 2007), (ii) bio-reduction in superficial cells (Maldonado and Price, 1999, 2001), (iii) abiotically due to the presence of certain organic compounds and exudates (Santana-Casiano et al., 2010, 2014), and (iv) microbial reduction (Sunda, 2001).

1.3.2.1. Inorganic speciation

Iron (II) and Fe(III) interactions with inorganic anions in natural waters can be computed using the specific interactions and ion pairing models (Millero et al., 1995; Santana-Casiano et al., 2004). These models calculate the interactions of Fe(II) and Fe(III) with major and minor ligands (Cl^-, SO_4^{2-}, OH^-, HCO_3^-, CO_3^{2-}, and HS^-) which allow to estimate the activity coefficients and speciation of Fe(II) and Fe(III) in natural waters over a wide range of pH, seawater composition and ionic strength. In the ocean pH range, the predominant Fe(III) species is $Fe(OH)_3$ (Figure 1-4), while $Fe(OH)_2^+$ and $Fe(OH)_4^-$ are found in much lower concentrations.

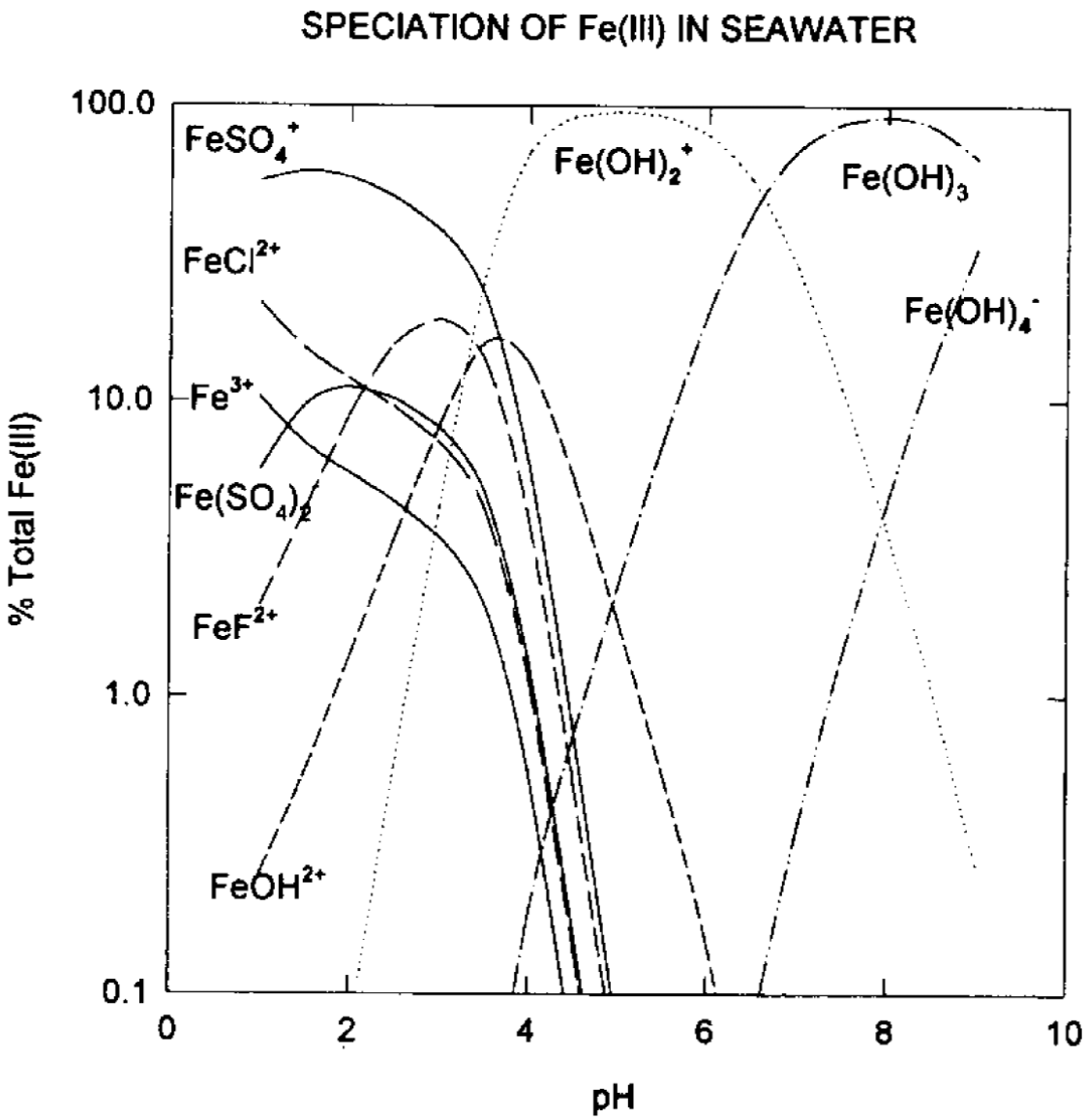

Figure 1-4. The speciation of Fe(III) in seawater (S=35) as a function of pH_F. Figure from Millero et al. (1995).

The inorganic speciation of Fe(II) in the range of pH 6.5 to 8.2 (Figure 1-5) is controlled by the species Fe^{2+}, $FeCl^+$ and $FeSO_4$. At pH 8.2, the $FeCO_3$ species begin to acquire importance, becoming the dominant species at pH above 8.2. Furthermore, the concentrations of the species $FeOH^+$, $Fe(OH)_2$ and $Fe(CO_3)_2^{2-}$ increase slightly with pH. Although the concentrations of these four species are very low, they cannot be neglected because their rate constants are high (Santana-Casiano et al., 2006) and their contribution to the Fe(II) oxidation process is important.

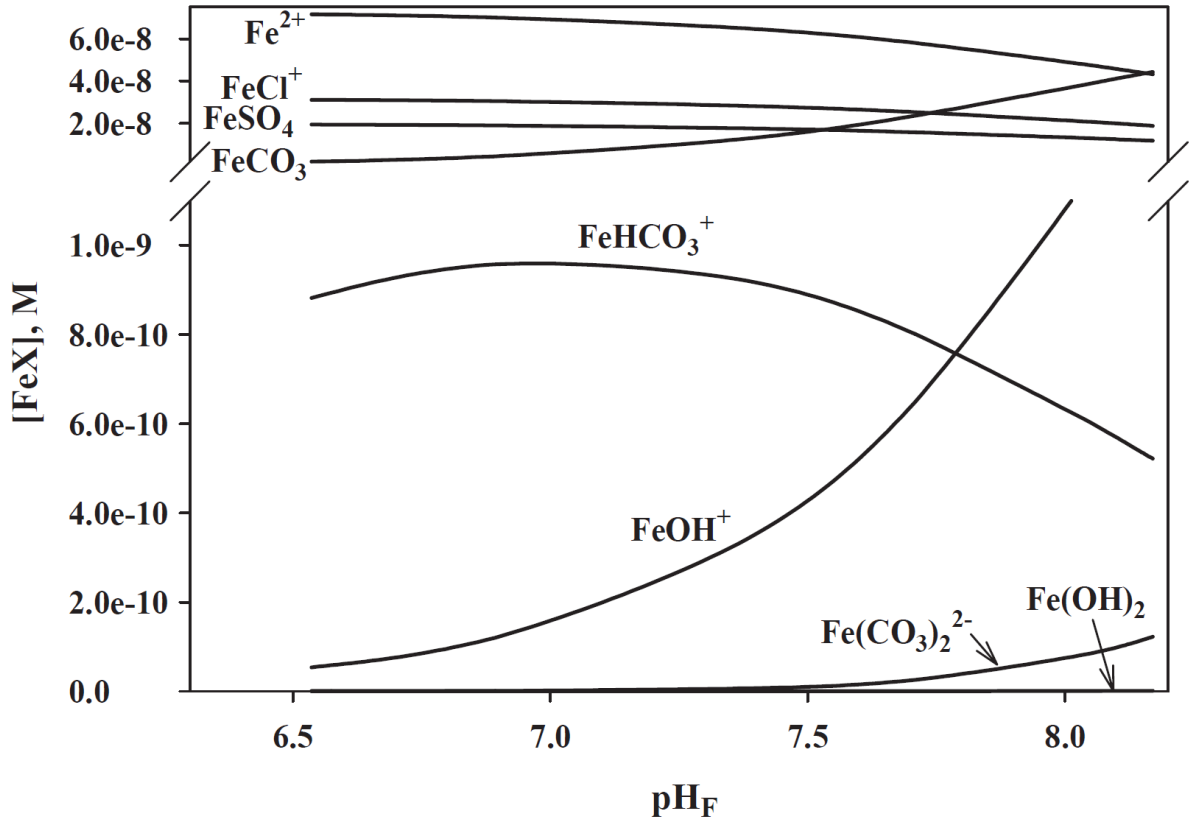

Figure 1-5. The speciation of Fe(II) in seawater (S=35) as a function of pH_F. Figure from Santana-Casiano et al. (2006).

The proportion of dFe expected to be present in the forms of Fe(II) and Fe(III), according to thermodynamics, is influenced by the prevailing redox conditions in the marine environment as well as by the complexation process of the two Fe forms.

The reduction half-reaction from Fe(III) to Fe(II) is defined by this equation:

$$Fe^{3+} + e^- \rightarrow Fe^{2+} \quad p\varepsilon^\circ = 13.0 \tag{1-3}$$

From the previous equation, the Nernst expression is deduced, which gives us the relationship of activities between ferrous and ferric iron:

$$log\frac{[Fe^{2+}]}{[Fe^{3+}]} = 13.0 - p\varepsilon \tag{1-4}$$

Where pε is the redox intensity ($p\varepsilon = -nFE / RT$, where n is the number of transferred electrons in the reaction, F is the Faraday's constant, E is the redox potential, R is the gas constant, and T is the absolute temperature).

Under oxic conditions, the oxygen/water pair controls the redox process:

$$\frac{1}{4}O_2(g) + H^+ + e^- = \frac{1}{2}H_2O \quad p\varepsilon^\circ = 20.75 \tag{1-5}$$

for a pH = 8 and $pO_2 = 10^{-0.7}$ atm.

$$p\varepsilon = p\varepsilon^{\circ} - log\frac{1}{P_{O_2}^{1/4}[H^+]} = 12.58 \quad (1\text{-}6)$$

Under these conditions, $[Fe^{2+}]/[Fe^{3+}] = 10^{0.42} = 2.63$

Because free ions only represent a fraction of the total ferrous (75.84 %) and ferric ($2.9x10^{-9}$ %) iron present in the marine environment (Millero et al., 1995), the Fe(II)/Fe(III) expected ratio is of the order of 10^{-10} in oxic seawater.

Under anoxic conditions, the sulfate/hydrogen sulfide pair controls the pε of the system

$$\frac{1}{8}SO_4^{2-} + \frac{9}{8}H^+ + e^- = \frac{1}{8}HS^- + \frac{1}{2}H_2O \;\; p\varepsilon^{\circ} = 4.25 \quad (1\text{-}7)$$

for a pH = 8, $[HS^-] = 10^{-5}$ mol L^{-1}, and $[SO_4^{2-}] = 10^{-2}$ mol L^{-1}

$$p\varepsilon = p\varepsilon^{\circ} - log\frac{[HS^-]^{1/8}}{[SO_4^{2-}]^{1/8}[H^+]^{9/8}} = -4.38 \quad (1\text{-}8)$$

Under these conditions $[Fe^{2+}]/[Fe^{3+}] = 10^{17.38}$, with Fe(II)/Fe(III) of the order of 10^7.

However, these theoretical proportions, calculated in accordance with thermodynamics and the concept of chemical equilibrium, are modified in the ocean due to the fact that the system is in a dynamic state of non-equilibrium in which the reactions occur simultaneously and they are affected by the biogeochemistry. In particular, the presence of marine organisms can remove dissolved inorganic compounds from seawater or contribute, among others, to the increase of dissolved organic compounds.

1.3.2.2. Organic speciation

The presence of dFe at concentrations above the theoretical inorganic solubility of Fe is thought to be facilitated by organic complexation of Fe with stabilizing organic ligands (Boyd and Ellwood, 2010). In the ocean, over 99% of the dFe is formed by Fe(III) bound to natural organic ligands (Rue and Bruland, 1997; Hutchins et al., 1999; Bruland et al., 2001; Croot et al., 2001; Gledhill and Buck, 2012). Iron-binding organic ligands have been classified into four classes based on their absolute ligand strength ($\log k_{FeL,Fe'}^{cond}$) (Bundy et al., 2015). The strongest ligands are classified as L_1 ($\log k_{FeL,Fe'}^{cond} \geq 12$), followed by L_2 ($12 > \log k_{FeL,Fe'}^{cond} \geq 11$), L_3 ($11 > \log k_{FeL,Fe'}^{cond} \geq 10$), and L_4 ($\log k_{FeL,Fe'}^{cond} < 10$). In the North Atlantic Ocean, the four classes of ligands can be found ubiquitously through the whole water column (Buck et al.,

2015). However, within hydrothermal vent plumes dFe concentrations can exceed ligand concentrations (Bennett et al., 2008; Hawkes et al., 2013; Buck et al., 2015), oversaturating the organic stabilization effect.

1.3.3. Iron (II) oxidation kinetics

Reduced forms of Fe can be naturally produced in pore waters of sediments, in anoxic basin waters, in hydrothermal environments and by photochemical processes (Croot et al., 2001). In the current oxic ocean, Fe(II) is thermodynamically unstable and is rapidly oxidised to Fe(III).

The oxidation kinetics of Fe(II) has been studied in different aqueous media and conditions to understand the behaviour of Fe(II) in natural waters (Stumm and Lee, 1961; Tamura et al., 1974; Kester et al., 1975; Millero et al., 1987; King et al., 1995; Emmenegger et al., 1998; Santana-Casiano et al., 2000, 2004, 2005; Rose and Waite, 2002; González-Dávila et al., 2006). According to these studies, the rate of oxidation of Fe(II) with O_2 can be expressed as an apparent rate constant (k_{app}), regardless of the mechanism that describes the process.

$$\frac{d[Fe(II)]}{dt} = -k_{app}[Fe(II)][O_2] \quad (1\text{-}9)$$

Where $k_{app} = k[OH^-]^2$

The brackets indicate the total molar concentration. When the reaction is studied in excess of O_2, the reaction can be considered pseudo-first order as expressed in equation 1-10:

$$\frac{d[Fe(II)]}{dt} = -k'[Fe(II)] \quad (1\text{-}10)$$

where $k' = k_{app}\,[O_2]$ and is given in s^{-1}, k_{app} is expressed in $M^{-1}\ s^{-1}$.

In the presence of more than one oxidant (González-Dávila et al., 2006), as in the case of O_2, $O_2^{\bullet -}$ and H_2O_2, equation is extended to:

$$\frac{d[Fe(II)]}{dt} = -\sum_j k_{app,i}[Oxidant]_j[Fe(II)] = \left(k_{app,O_2}[O_2] + k_{app,O_2^{\cdot -}}[O_2^{\cdot -}] + k_{app,H_2O_2}[H_2O_2]\right)[Fe(II)] \quad (1\text{-}11)$$

being $k_{app,j} = \sum_i k_{i,j}\,\alpha_i$

The most accepted mechanism to describe the oxidation of Fe(II) with O_2 in natural waters is the Haber-Weiss mechanism in which:

$$Fe(II) + O_2 \rightarrow Fe(III) + O_2^{\bullet -} \quad (1\text{-}12)$$

$$Fe(II) + O_2^{\bullet -} \xrightarrow{2H^+} Fe(III) + H_2O_2 \quad (1\text{-}13)$$

$$Fe(II) + H_2O_2 \rightarrow Fe(III) + OH^{\bullet} + OH^- \quad (1\text{-}14)$$

$$Fe(II) + OH^{\bullet} \rightarrow Fe(III) + OH^- \quad (1\text{-}15)$$

At micromolar concentrations of Fe(II), a 4:1 stoichiometry has been described for the oxidation of Fe(II) with oxygen (Millero et al., 1987; King, 1998), and a 2:1 stoichiometric ratio for the oxidation with H_2O_2 (Millero and Sotolongo, 1989).

At nanomolar concentrations of Fe(II), it has been shown that the reactions (Eqs. 1-12 to 1-15) need to be considered (Santana-Casiano et al., 2005). The reactive intermediates of oxygen, the superoxide anion ($O_2^{\bullet -}$) and the $OH^{\bullet}$ radicals produced in the Fe(II) oxidation process can in turn act as oxidants and even react with other reduced compounds (Br^-, Cl^-, HCO_3^- and dissolved organic matter) (Emmenegger et al., 1998). The new radicals generated can enhance the role of the intermediate radicals $OH^{\bullet}$ in the reaction (15). These radical derivatives are extremely reactive (King et al., 1995; Emmenegger et al., 1998). In addition, it is also necessary to take into account the reaction of Fe(III) with $O_2^{\bullet -}$ (King et al., 1995; Rose and Waite, 2002), the reaction of $O_2^{\bullet -}$ with the inorganic Cu(II) present in the solution and hydrolysis of Fe(III) to form insoluble iron $Fe(OH)_3$ (Rose and Waite, 2002, 2003a).

$$Fe(III) + O_2^{\bullet -} \rightarrow Fe(II) + O_2 \quad (1\text{-}16)$$

$$Fe(III) + 3OH^- \rightarrow Fe(OH)_{3(s)} \quad (1\text{-}17)$$

$$Cu(II) + O_2^{\bullet -} \rightarrow Cu(I) + O_2 \quad (1\text{-}18)$$

$$Cu(I) + O_2^{\bullet -} + 2H^+ \rightarrow Cu(II) + H_2O_2 \quad (1\text{-}19)$$

In the presence of organic compounds, Fe will also interact with ligands according to the equations:

$$Fe(II) + L \Leftrightarrow Fe(II)L \quad (1\text{-}20)$$

$$Fe(II)L + O_2 \rightarrow Fe(III)L + O_2^{\bullet -} \quad (1\text{-}21)$$

$$Fe(III) + L \Leftrightarrow Fe(III)L \quad (1\text{-}22)$$

$$Fe(III)L \Leftrightarrow Fe(II) + L' \quad (1\text{-}23)$$

The organic complexation of Fe influences the kinetics in a similar way as the inorganic complexation (Santana-Casiano et al., 2000, 2004) and the apparent rate constant must include the contribution of the inorganic and organic species of Fe(II) (Eqs. 1-24 and 1-25):

$$K_{app} = \sum_i k_i \alpha_i + \sum_L k_L \alpha_L \quad (1\text{-}24)$$

α_i = [FeX_i]/[Fe(II)], is the inorganic fraction of Fe(II) complexes and α_L is the fraction of Fe(II)-L complexes

$$k_{app} = k_{Fe^{2+}}\alpha_{Fe^{2+}} + k_{FeOH^+}\alpha_{FeOH^+} + k_{Fe(OH)_2}\alpha_{Fe(OH)_2} + k_{FeHCO_3^+}\alpha_{FeHCO_3^+} + k_{Fe(CO_3)}\alpha_{Fe(CO_3)} + k_{Fe(CO_3)_2^{2-}}\alpha_{Fe(CO_3)_2^{2-}} + k_{Fe(CO_3)OH^-}\alpha_{Fe(CO_3)OH^-} + k_{FeCl^+}\alpha_{FeCl^+} + k_{FeSO_4}\alpha_{FeSO_4} + \sum_L k_{FeL}\alpha_L \quad (1\text{-}25)$$

The first empirical equation describing the Fe(II) oxidation rates (k') in seawater at different temperature, pH and salinity was reported by Millero et al. (1987), which was latter updated by Santana-Casiano et al. (2005) for nanomolar concentrations.

$$\log(k') = 35.407 - 6.7109 \times pH + 0.5342 \times pH^2 - \frac{5362.6}{T} - 0.04406 \times \sqrt{S} - 0.002847 \times S \quad (1\text{-}26)$$

$$k' = \frac{10^{log(k')}}{60} \quad (1\text{-}27)$$

Where k' (s^{-1}, converted to min^{-1} using Eq. 1-27) is dependent on pH, temperature (T, K) and salinity (S).

Temperature (T), pH, and oxygen (O_2) are the primary variables that directly affect the Fe(II) oxidation rates (Stumm and Lee, 1961; Millero et al., 1987; Millero and Sotolongo, 1989; Santana-Casiano et al., 2005). However, other factors such as the inorganic complexation of Fe(II), due to the specific ionic composition, or organic complexation can influence these oxidation rates (Millero, 1985; Rose and Waite, 2003a; Statham et al., 2005).

Equation 1-26 was developed to study Fe(II) oxidation kinetics constants in seawater ranging from 10 to 25 °C. However, deep ocean waters present colder *in situ* temperatures. There is a scientific requirement to expand the applicability of the Fe(II) oxidation kinetics equation.

1.4. Iron marine biogeochemical cycle

Understanding the sources and mechanisms by which Fe are incorporated and cycle through the global oceans is a key goal of earth system science. The marine biogeochemistry of Fe is influenced by low solubility, redox speciation, and biological activity. Furthermore, its seawater concentration is also dependent on its sources and sinks (Figure 1-6).

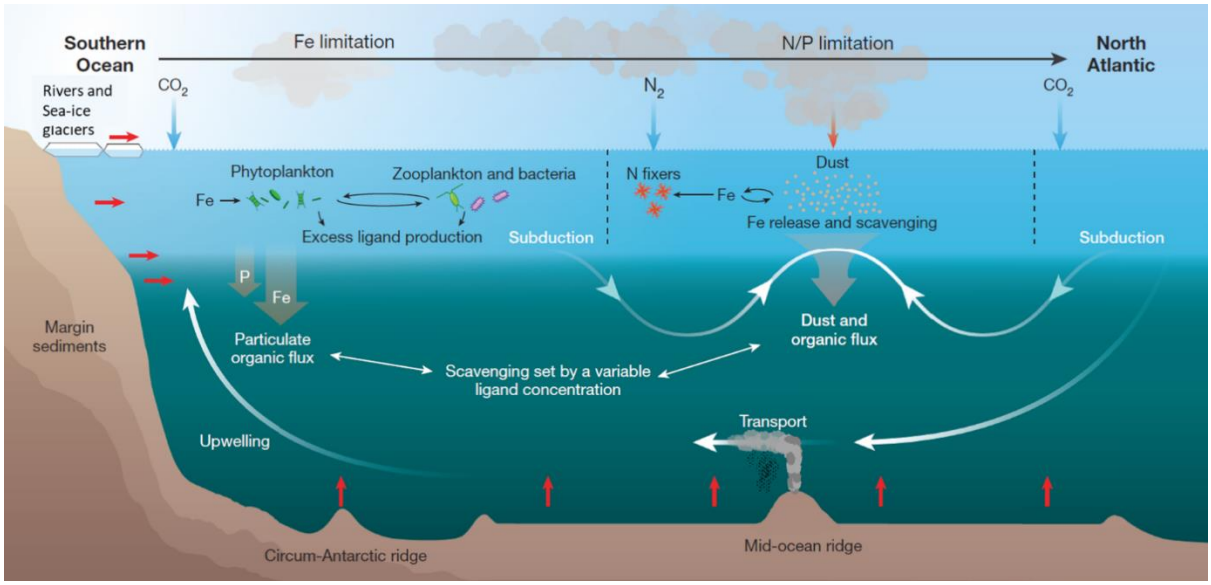

Figure 1-6. Schematic of the major processes in the ocean iron cycle. Figure modified from Tagliabue et al. (2017).

1.4.1. Iron sinks and sources

The main removal pathways of Fe are the active biological uptake, scavenging, precipitation, and sedimentation (Worsfold et al., 2014). Biological uptake is an active process mediated by living organisms, which have specific Fe requirements depending on the species. Iron requirements of oceanic eukaryotic species are lower than those required by coastal eukaryotic species and cyanobacteria (Brand, 1991). Scavenging is a passive process where trace metals, including Fe, are adsorbed to organic (both living and dead) and inorganic particulate material and settle in the water column (Goldberg, 1954; Turekian, 1977). Precipitation is a physical process which occurs when seawater cations neutralize the negatively charged Fe-bearing colloids allowing for flocculation and coagulation of smaller sized particles. Precipitation is the primary riverine Fe removal pathway, reducing dissolved Fe concentrations by about 90% (Boyle et al., 1977). Finally, sedimentation is the process by which the sinking particles arrive to the ocean bed, settle, and accumulate.

The major inputs of Fe to the oceans are from the atmosphere, continental shelf sediments, hydrothermal vents, rivers and glacial melt in polar regions (Worsfold et al., 2014).

It was first considered that the atmosphere was the main source of Fe to the ocean, but in the early 2000s, studies revealed that Fe supply from aerosols was not the only important source of Fe to the water column (Mahowald et al., 2005). Studies described the input from shelf sediments to be as significant as dust input which can support high productivity in shallow

coastal regions (Hutchins and Bruland, 1998; Elrod et al., 2004; Birchill et al., 2019). In glacial regions, the flux of bioavailable Fe supplied by melting glaciers and icebergs can be similar to the aeolian flux (Lannuzel et al., 2008). Similarly, during the 90's, it was assumed that the input of Fe to the marine environment from hydrothermal vents was negligible (German et al., 1991a) as it was assumed that Fe oxidised and precipitated in its insoluble form close to the vents. Recent studies have shown that Fe can be transported up to 4000 km away from hydrothermal vents (Saito et al., 2013; Fitzsimmons et al., 2014; Resing et al., 2015) and can account for up to 25% of primary production in the Southern Ocean (Tagliabue et al., 2010, 2014), and could trigger phytoplankton blooms (Ardyna et al., 2019). It is therefore crucial to investigate this hydrothermal source with a new perspective.

1.5. Hydrothermal systems

Hydrothermal circulation is a phenomenon taking place over the entire planet and refers to the circulation of fluids within the Earth's crust and mantle. External manifestations of hydrothermal activity are both observed on land (geysers and hot springs) and at the seafloor (black and white smokers).

1.5.1. Mid Ocean Ridge hydrothermal systems

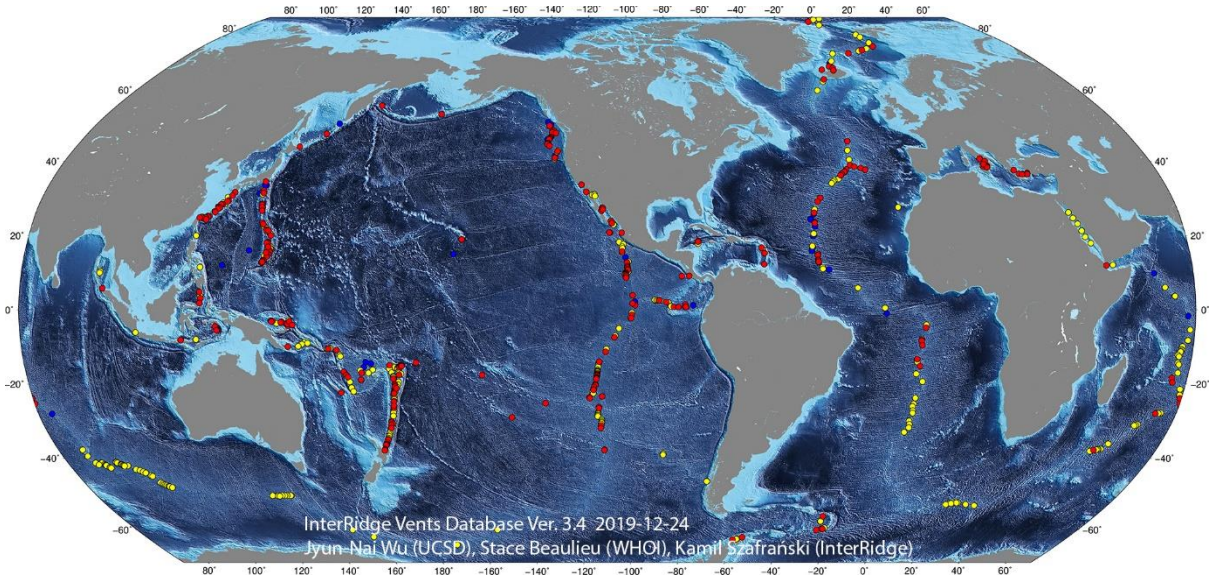

Figure 1-7. Global distribution of hydrothermal vent systems. Confirmed vent sites are shown in red, and unconfirmed vent sites in yellow. Figure from InterRidge Vents Database Version 3.4 (Beaulieu and Szafrański, 2020), last accessed 06/08/2020.

The first deep sea hydrothermal systems were discovered in the late 1970s in the Pacific Ocean on the Galapagos rift (Corliss et al., 1978). Since then, deep-sea hydrothermal systems have been intensively studied geologically, physically, biologically, and chemically. The interaction between the research fields has allowed for a deeper understanding of these extreme environments.

Submarine vent sites are globally distributed along four tectonic settings; mid-ocean ridges (MOR), back-arc basin spreading centres, volcanic arcs, and intra-plate volcanoes (Figure 1-7). The full list of discovered vent sites, characteristics and year of discovery can be found on the InterRidge vents database (http://vents-data.interridge.org, last accessed 04/08/2020).

Most of the discovered hydrothermal vent systems are related to different deep ocean (up to 4000 m deep) spreading centres along MOR, such as the Mid-Atlantic Ridge (MAR) or the East Pacific Rise (EPR). Other shallower systems (between 200 and 2000 m deep), referred to as intermediate hydrothermal vents, have been found within back-arc basins, such as the Mariana Arc (Resing et al., 2009), Tonga Arc (Massoth et al., 2007) and the Lau back-arc basin (Fouquet et al., 1991). Aside from these deeper vents, shallower-marine hydrothermal vents exist and are related to volcanic (oceanic island) arcs (e.g. Butterfield et al., 2011; Hawkes et al., 2014; Guieu et al., 2018).

In order for deep-sea hydrothermal venting to occur, cold and oxic seawater found in the ocean needs to seep through cracks and fissures that exist in the oceanic crust and get exposed to a heat source (magma chamber, Figure 1-8). The heat sources can heat the pressurised seawater to temperatures above 450 °C. These regions are defined as “recharge zones”. Under these conditions, different minerals are produced, such as anhydrite which reduces fluid sulphate (SO_4^{2-}), smectite (e.g. saponite, $(Ca_{0.5},Na)_{0.3}(Mg,Fe^{2+})_3(Si, Al)_4O_{10}(OH)_2•(H_2O)$), chlorite ($ClO_2^-$) and caminite ($Mg_7(SO_4)_5(OH)_4•(H_2O)$) which decrease fluid concentrations of magnesium and in some cases deplete magnesium (Gartman and Findlay, 2020). The loss of alkalinity due to water-rock interactions leads to a fluid enrichment in protons and the consequent acidification of the fluid to pH values as low as 3 (Seyfried and Ding, 1993). As the fluid keeps moving down closer to the Earth’s core, it reaches the “reaction zone”, where most of the metal leaching from the host rock takes place. Due to the high temperatures and low pH (down to pH 2), metals such as Fe, Cu, Mn and Zn get enriched within the fluid (German and Von Damm, 2004). As the vent site depth decreases (decrease in pressure), the seawater boiling point also decreases (Bischoff and Rosenbauer, 1984); as such metal

enrichment is reduced in shallower vent sites (e.g. Smith and Cronan, 1983). The resulting vent fluids from hydrothermal systems are often highly enriched in reducing inorganic chemical species (electron donors, e.g. H^+, Cl^-, Mn^{2+}, Fe^{2+} and S^{2-}).

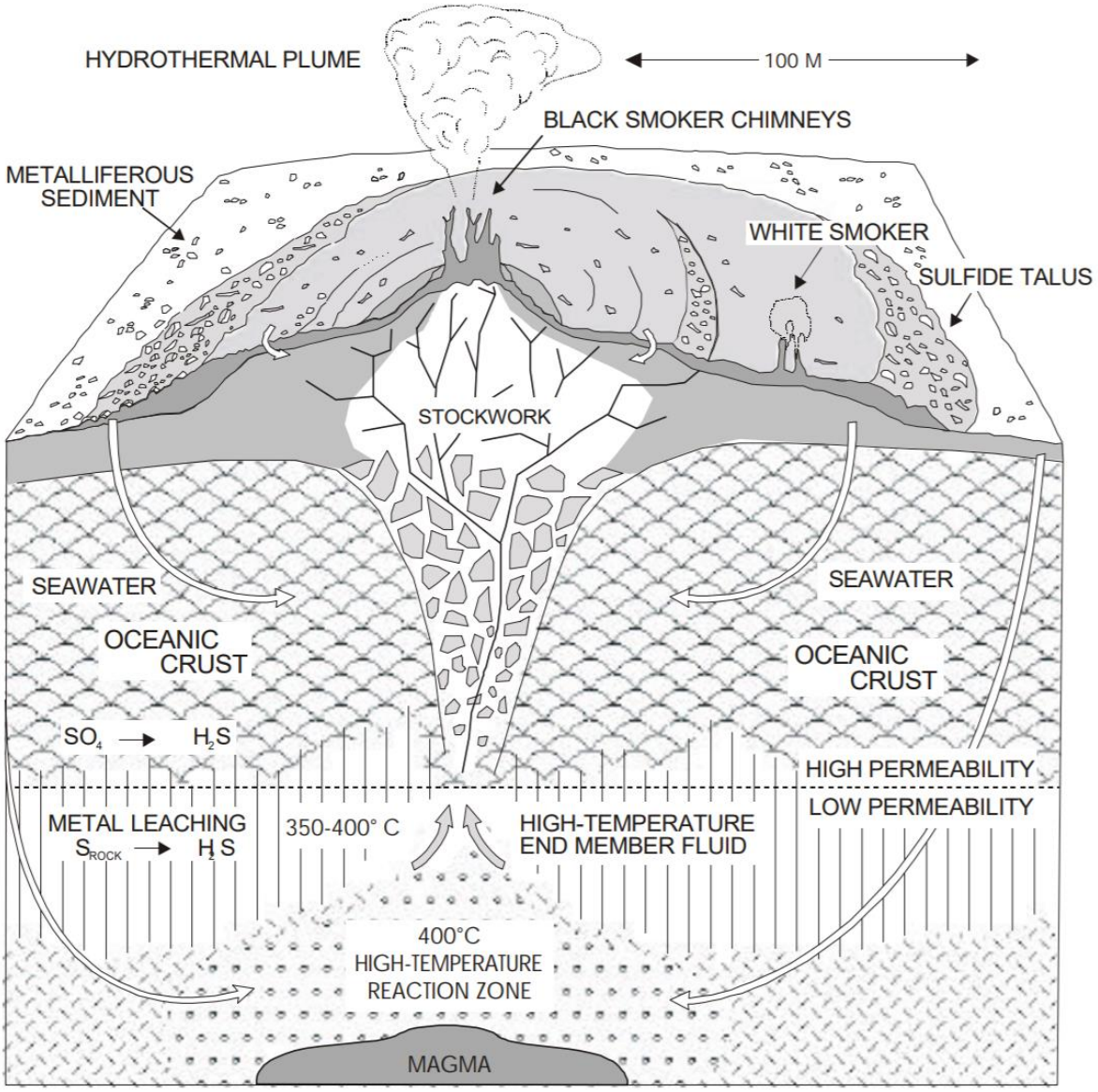

Figure 1-8. Cross-section showing the principal components of a seafloor hydrothermal system. Figure from Herzig et al. (2002).

The hot and acidic fluid slowly becomes less dense and reaches a buoyancy in which it starts to ascend the Earth crust towards the seafloor. As it ascends, it can mix with entrained seawater forming polymetallic sulphides (Herzig et al., 2002). Once it reaches the seafloor the hot fluid mixes with the surrounding cold and oxygenated overlying seawater, which immediately produces the oxidation and precipitation of dissolved metals (e.g. Fe, Zn, Cu) and forming sulphide minerals (e.g. pyrite (FeS_2), sphalerite ((Zn,Fe)S) and chalcopyrite ($CuFeS_2$),

respectively) or oxyhydroxides. The precipitation of these minerals can build up in the vent source forming several meter-high chimneys, known as “black smokers”, where the precipitation of large concentrations of metals act as the smoke. Vent fluids also include high concentrations of gasses, such as He, H_2, H_2S, CO_2 and CH_4.

An important process within hydrothermal plumes is the oxidation of Fe(II) because the scavenging of elements from solution by freshly formed Fe(III) (German et al., 1991a), leads to co-precipitation of many other vent-sourced metals. This thus modifies the gross hydrothermal fluxes to the deep ocean and acts as a net sink in the chemical budget of certain key tracers (Statham et al., 2005; Wang et al., 2012). All metals which are not precipitated around the vent outlet, are discharged within the buoyant plume. This plume keeps ascending in the water column entraining surrounding seawater while reducing its particle load until it reaches a similar buoyancy. At this point, it is referred to as the neutrally buoyant plume (also found as the non-buoyant plume; NBP). The NBP then drifts horizontally and is transported by oceanic currents. Recent studies have shown that the NBP plumes transport can reach basin scale distances of up to 4500 km (Resing et al., 2015; Fitzsimmons et al., 2017).

Almost immediately after the discovery of the first hydrothermal system, submarine hydrothermal venting was recognized as a potentially important source and sink of key elements (Edmond et al., 1979). However, with the discovery of the first high-temperature black smokers (Spiess et al., 1980), a further appreciation arose that the gross fluxes emitted from high-temperature venting were modified significantly in hydrothermal plumes. For the vast majority of chemical tracers enriched in vent fluids, net fluxes to the oceans are modified as these tracers are incorporated into Fe-rich polymetallic sulphide and oxyhydroxide particles that sink to the seafloor at and close to mid ocean ridges (Mottl and McConachy, 1990; German et al., 1991a; Kadko, 1993). This view of the restricted role that hydrothermal systems might play in the global-scale budgets persisted for more than a decade. However, for those trace elements and isotopes that are readily scavenged by Fe, it was recognised that the net effect of submarine venting could remove dissolved trace elements and isotopes (TEIs) from the deep ocean into underlying sediments (Elderfield and Schultz, 1996). However, the last decade has resurfaced the interest in hydrothermalism as a significant trace metal source. Many projects within the GEOTRACES program (www.geotraces.org) have studied the influence of hydrothermalism not only in a regional scale but have also confirmed that hydrothermalism can have a basin scale impact in all ocean basins (Wu et al., 2011; Klunder et al., 2011, 2012;

Noble et al., 2012; Saito et al., 2013; Nishioka et al., 2013; Fitzsimmons et al., 2014, 2015, 2017; Hawkes et al., 2014; Horner et al., 2015; Resing et al., 2015).

The dynamics of Fe precipitation in the buoyant plume (its specific location, the mechanism of precipitation, and the rate at which it occurs) are of key interest in defining the impact of hydrothermal systems on the oceanic chemistry of trace elements (Rudnicki and Elderfield, 1993).

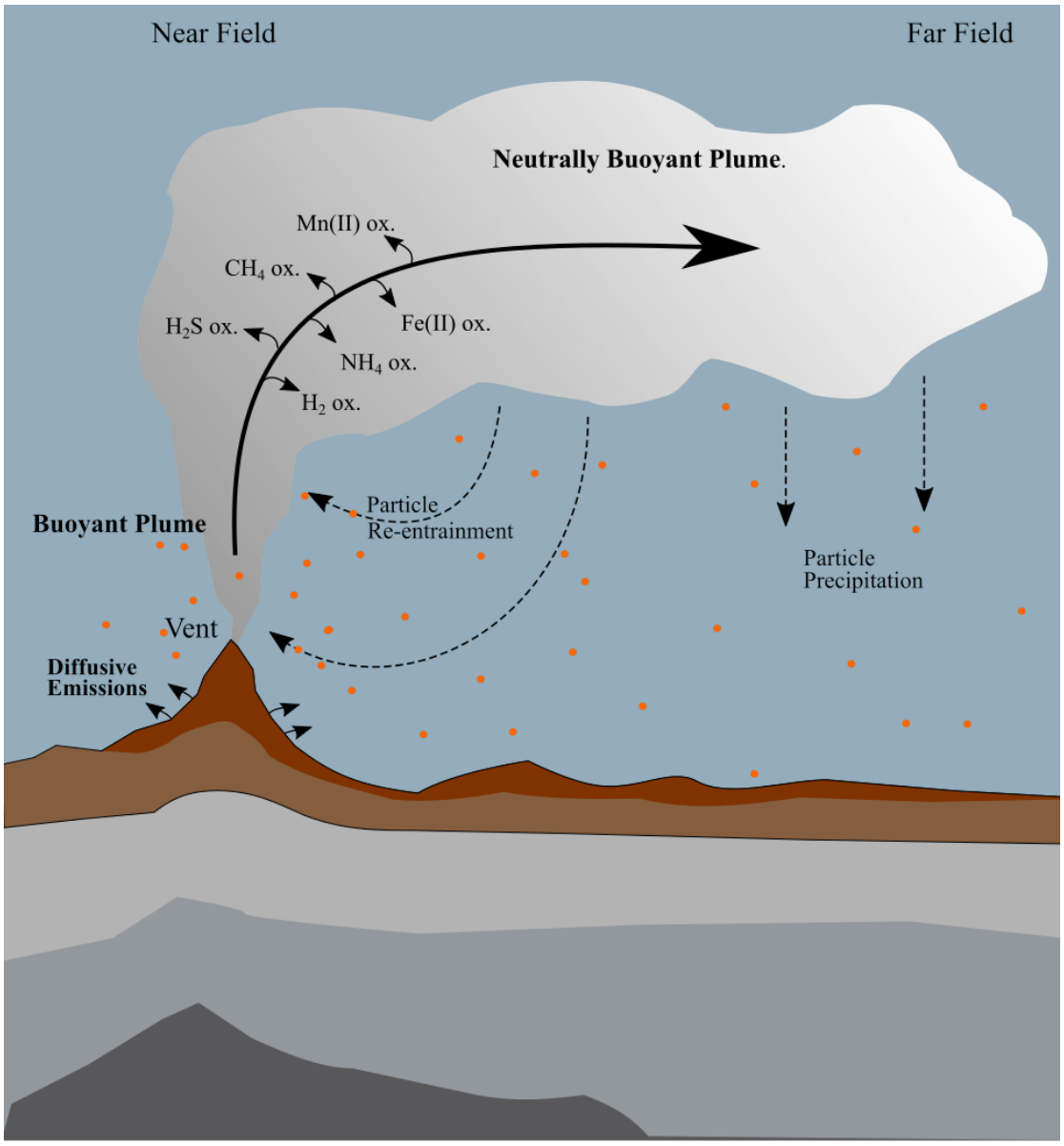

Figure 1-9. Schematic representation of a hydrothermal plume. The buoyant plume (rising plume) is warmer and less dense than the surrounding seawater. Oxidation increases up plume as plume fallout and re-entrainment and dilution occurs. There is rapid particle formation, especially in the first meters. In the near field, reduced species are present within the plume and oxidation plays a relevant role. Far field, species mainly remain in their oxidised forms.

The precipitation of minerals from hydrothermal fluids is influenced both by cooling, which reduces the saturation state of many minerals, and mixing with ambient seawater, which results in a decrease in pH (due to metal-sulphide precipitation) followed by an increase in pH as ambient seawater and oxidised species interact with the hydrothermal fluid (Figure 1-9) (Ding and Seyfried, 2007; Gartman et al., 2014). Oxidised species form particles with a wide range of sizes. The smallest particles are defined as nanoparticles, which have one or more dimensions less than 100 nm in size. Nanoparticles are a main component of vent chimneys, such as the high prevalence of pyrite nanoparticles observed in the chimneys of TAG (Gartman et al., 2014). Nevertheless, insoluble sulphides and oxides may achieve oceanic transport as nanoparticles due to their low settling speeds. Both oxyhydroxide (Fe(III)) colloids and pyrite nanoparticles (Fe(II)) have been detected in hydrothermal vent systems (Yücel et al., 2011; Sands et al., 2012).

Furthermore, nanoparticle formation could play a more important role other than having slower settling speed than larger plume particles. The presence of these nanoparticles could act as a stabilization mechanism allowing for a more persistent dFe hydrothermal source (Bennett et al., 2008; Sander and Koschinsky, 2011; Hawkes et al., 2013; Fitzsimmons et al., 2017). Furthermore, pyrite nanoparticles are more resistant to oxidation than dFe(II) and iron sulphide (FeS). Therefore, it has been suggested that the discharge of Fe in the form of pyrite nanoparticles increases the probability that vent-derived Fe will be transported over long distances in the deep ocean (Yücel et al., 2011; Gartman and Luther, 2014). However, the resulting nanoparticle effect on Fe(II) oxidation kinetics still remains unquantified.

Recent models do not only consider hydrothermal vents as trace metal sources, but also remark the importance of diffusive emissions (German et al., 2015; Lough et al., 2019a). Even though diffusive fluxes are smaller than vent fluxes, the coverage area is significantly greater, therefore, diffusive venting could potentially dominate the supply of dissolved Fe from hydrothermal systems to the deep ocean.

1.6. Scope and Thesis outline

1.6.1. Scientific aims

The aim of this Thesis was to improve the knowledge on the fate of hydrothermally sourced Fe considering both the chemical and physical speciation of Fe. To accomplish this, several goals were targeted.

i) **The first goal was to better constrain the Fe(II) oxidation rate constants in the deep ocean and hydrothermal environments.** The most up-to-date pre-existing Fe(II) oxidation kinetics equations temperature range was limited to temperatures above 10 °C. Although this temperature range is useful for a wide range of oceanic regions such as mid ocean and surface depths and laboratory experiments, the viability of this equation had not been verified for deep ocean waters reaching 2 °C (temperature range of the surrounding seawater where the MAR hydrothermal vents sites are located). Furthermore, it is important to increase the number of hydrothermal sites where Fe(II) oxidation kinetics experiments have been performed. Moreover, such studies should present the Fe(II) oxidation constant variability within the hydrothermal plumes.

ii) **The second goal was to examine Fe(II) concentration in the deep ocean and in hydrothermal environments along the MAR**. Iron (II) was measured at six hydrothermal sites on the MAR at multiple depths within the neutrally buoyant plumes. However, this goal has an underlying unknown. Due to the fast Fe(II) oxidation rates in oxic seawater, sampling times are in most cases longer than Fe(II) half-life, more than one hour for deep samples compared to an oxidation rate ranging from minutes to hours (Millero et al., 1987). Consequently, measured deep ocean Fe(II) concentrations are skewed by Fe(II) oxidation. Therefore, goal 2 required goal 1 to theoretically constrain Fe(II) oxidation rates, and these oxidation rates could then be used to calculate the original Fe(II) concentration (ie. when the sample was in the deep ocean).

iii) **The third goal was to constrain Fe transport and underlying processes within the first kilometres of the TAG hydrothermal vent site**. Samples (dissolved and particulate) had to be collected within one neutrally buoyant plume at multiple distances and changes in Fe concentration could then be computed and processes be identified.

1.6.1.1. A Thesis congruent with the GEOTRACES programme

My PhD work was within the framework of the GETOTRACES programme. GEOTRACES, which started in 2010 (Schrope, 2010), is an international program which aims to improve the understanding of biogeochemical cycles and large-scale distribution of trace elements and their isotopes in the marine environment (https://www.geotraces.org/geotraces-science-plan/). The program goals are to identify processes and quantify fluxes that control the distribution of key trace elements and isotopes in the ocean, and to establish the sensitivity of these distributions to changing environmental conditions. Research is organized in three complementary themes: (i) Fluxes and processes at ocean interfaces, (ii) Internal cycling, and (iii) Development of proxies for past changes.

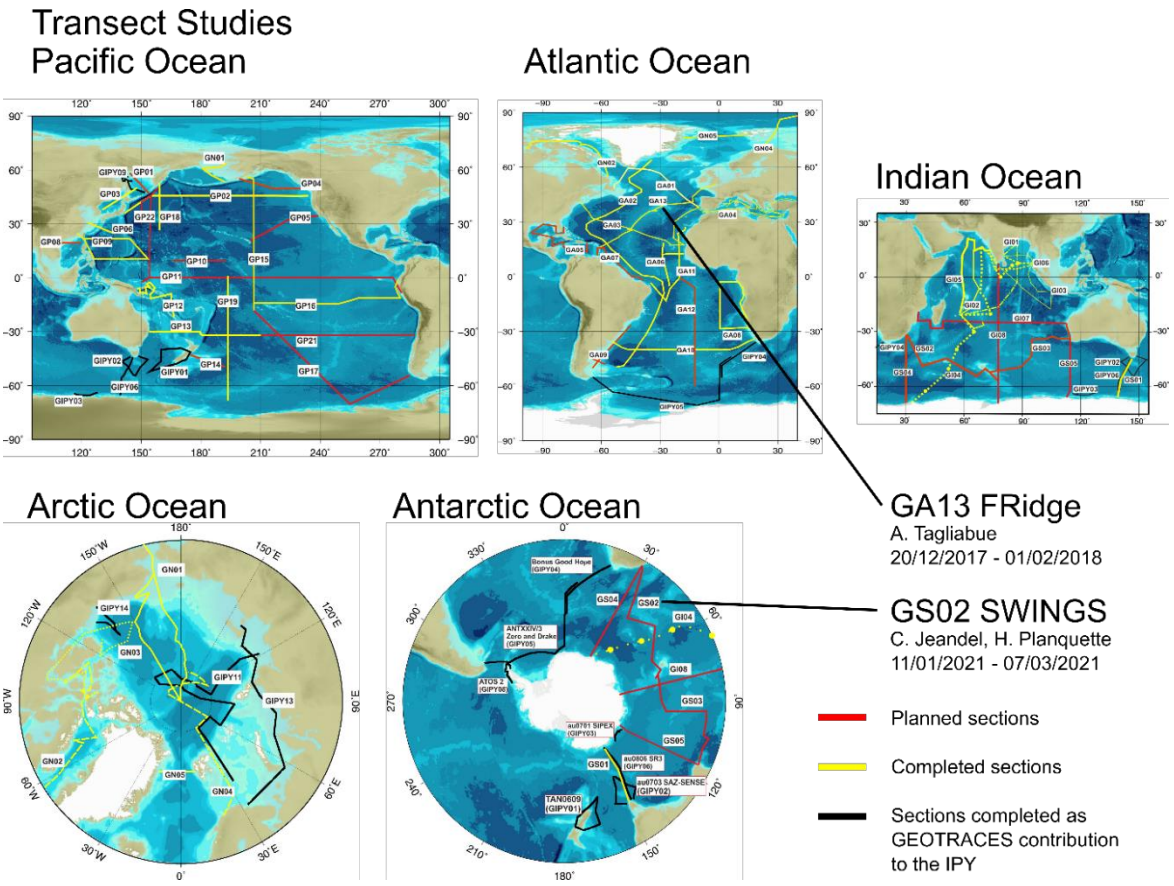

Figure 1-10. GEOTRACES programme transect studies. Figure modified from ww.geotraces.org (last accessed 01/09/2020). During this PhD, I participated on the GA13 (FRidge) cruise. Next year, I will participate in the GS02 (SWINGS) cruise implementing ideas developed during the PhD.

Trace metal and isotope samples are collected in research cruises that have been divided into three types:

- Section cruises (Figure 1-10):
    - Cruises which measure the key parameters listed in the Science Plan over the full depth of the water column.

    - The sections are discussed and approved by the International GEOTRACES Scientific Steering Committee.
- Process Studies (Figure 1-11):
    - Cruises focusing a particular process relevant to the cycling of trace metals and isotopes.
    - They must be approved by the International GEOTRACES Scientific Steering Committee.
- Compliant data cruises:
    - Cruises that collect some trace element or isotope data.

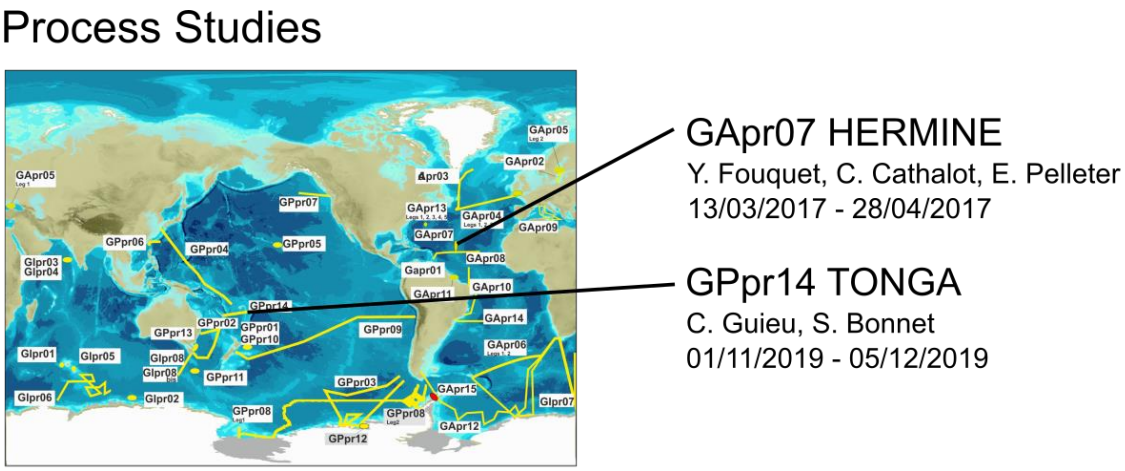

Figure 1-11. GEOTRACES programme process studies. Figure modified from www.geotraces.org (last accessed 01/09/2020). During this PhD I obtained dissolved trace metal samples from the GApr07 (HERMINE) cruise. I also participated on the GPpr14 (TONGA) cruise, where I analysed dissolved ferrous iron (dFe(II)) and collected samples for future Fe(II) oxidation kinetics experiments.

In this Thesis, I participated in the GA13 (FRidge) transect cruise to achieve my PhD goals i) and ii). I also analysed the dissolved trace metal samples collected during the GApr07 (HERMINE) process study to accomplish goal iii). Moreover, I participated on a second process study GPpr14 (TONGA) where I analysed dFe(II) concentrations and collected Fe(II) oxidation kinetics samples to perform future inter-basin comparisons. The TONGA results are not included in my PhD manuscript. Finally, I have also prepared for a fourth transect study, GS02 (SWINGS), where I will apply some the perspectives and knowledge achieved during this Thesis.

1.6.2. Outline

This Thesis is structured into six chapters. The current chapter provides a general introduction. The second describes the materials and methods used during the Thesis for trace metal analyses (i.e. flow injection analysis by chemiluminescence and Sector Field Inductively Coupled

Plasma Mass Spectrometer (SF-ICP-MS) coupled to a SeaFAST system). This chapter also presents the main characteristics of the research cruises and a brief description of each studied hydrothermal vent site where the samples were collected from.

Chapters three to five consist of three manuscripts.

In chapter 3, employing a lab-based approach, an improved Fe(II) oxidation kinetics equation was obtained in order to better estimate oxidation rates for seawater temperatures ranging from 2 to 25 °C. This manuscript also investigated Fe(II) oxidation rates in the deep North Atlantic Ocean along the Mid Atlantic Ridge. I also studied the Fe(II) oxidation rate in six hydrothermal vent sites, doubling the number of hydrothermal vent sites were Fe(II) oxidation kinetics studies have been performed. Furthermore, I present, for the first time, the Fe(II) oxidation kinetics variabilities within individual hydrothermal plumes. This manuscript is currently under review for Geochimica et Cosmochimica Acta.

The fourth chapter is written in a manuscript format. It is comprised of the ferrous Fe data analysed during the FRidge cruise. This data was combined with the Fe(II) oxidation kinetics equation presented in chapter 3 to obtain a theoretical original Fe(II) concentration so as to account for the fast Fe(II) half-life. In this chapter, I analysed the Fe(II) samples and the soluble and dissolved Fe (sFe and dFe, respectively) samples were analysed by Dr A.J.M. Lough (NOCS/University of Leeds ongoing collaboration). The sFe and dFe concentrations are not presented in the chapter, and are only used to describe the ratio between Fe(II) and these size fractions. This manuscript will be submitted after the PhD defence.

The fifth chapter is a peer-reviewed and published manuscript as open access in July 2020 in Frontiers in Marine Science journal. This manuscript presents high depth resolution dFe and dissolved manganese concentrations at six sites following the TAG hydrothermal plume. The dissolved trace metal data that I analysed were combined with particulate Fe data that were analysed by Dr M. Cheize and Dr H. Planquette to develop a box model. This model could quantify the different processes that affected the Fe concentrations and size fractionation.

Chapter six includes a general conclusion with a synthesis of the work and draws some perspectives, outlining future research goals.

This Thesis also includes three appendices. Appendix A presents the MATLAB® script used for the ICP-MS raw data compiler that should be useful for future SF-ICP-MS users. Section

B gives an overview of related scientific work, conferences and research cruises I have joined during my PhD studies. Appendix C displays the published manuscript presented in Chapter 5.

1. Introduction (Français)

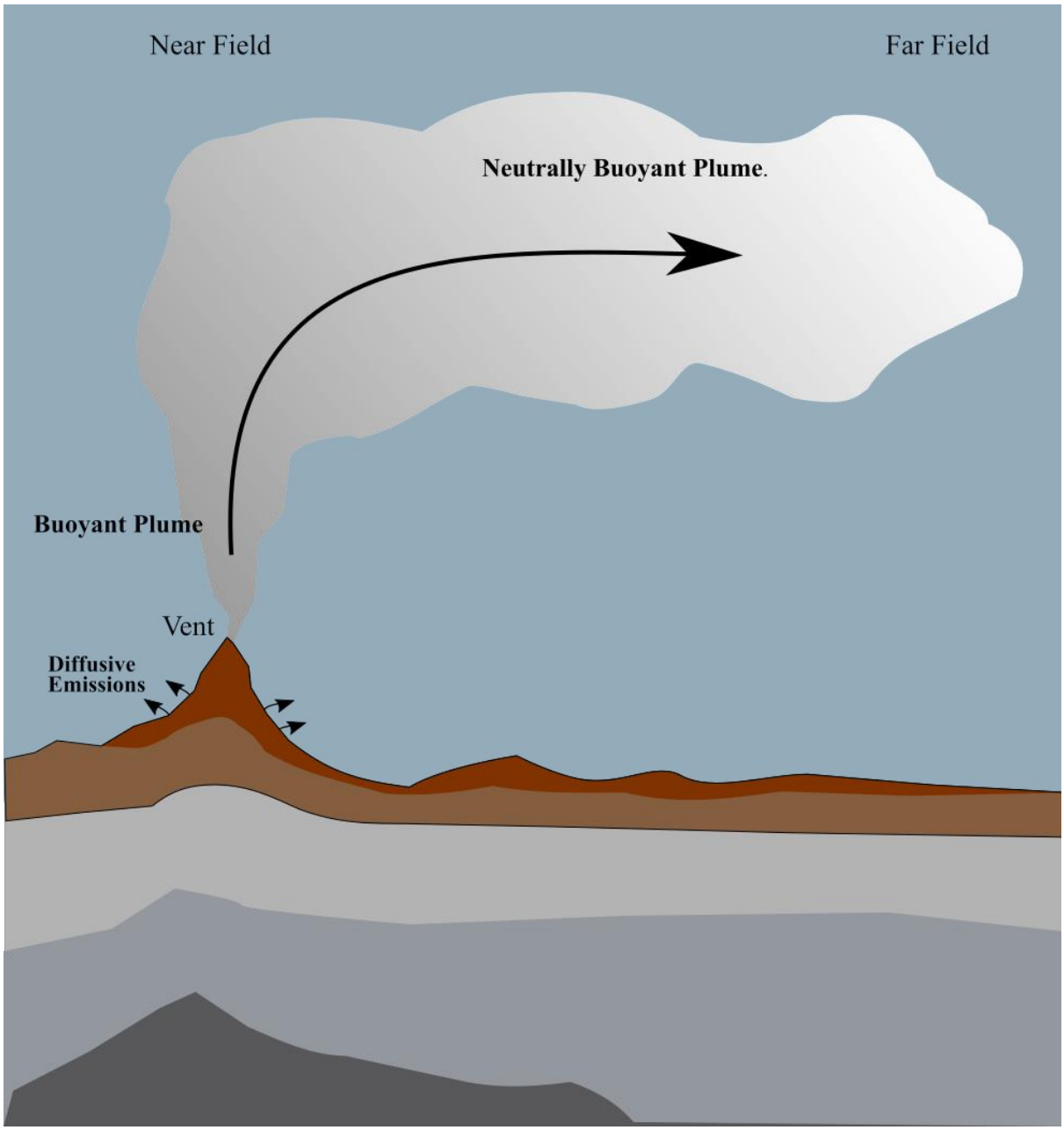

The main sections of the introduction have been translated to French in accordance with the mandatory minimum requirements of l'Ecole Doctorale des Sciences de la Mer et du Littoral and the Université de Bretagne Occidentale.

Ces dernières années, les revues scientifiques, dans les versions en ligne, ont de plus en plus recours aux résumés graphiques, sorte de figure de synthèse des principaux résultats développés dans l'article. J'ai décidé de créer un résumé graphique pour chaque chapitre de ma thèse. J'ai opté pour la création d'un schéma symbolisant l'objet central de ma thèse : ainsi, la page de couverture de l'introduction présente un système hydrothermal. Un évent produit le panache flottant. Ce panache monte (la flèche à l'intérieur du panache facilite cette perception) jusqu'à ce qu'il atteigne une flottabilité neutre, ce qu'on appelle le panache à flottabilité neutre. Ce panache est transporté par les courants océaniques loin de son emplacement d'origine.

1.1.(Français) Influence du fer sur les systèmes naturels

La biogéochimie du fer aquatique (Fe) a suscité un grand intérêt au cours des dernières décennies. De nombreuses études ont établi un lien entre le Fe, le cycle du carbone et le climat mondial (par ex. Martin, 1990 ; de Baar et al., 2005 ; Mahowald et al., 2005). Etant donné que plus de 45 % de la photosynthèse mondiale a lieu dans les milieux aquatiques (Falkowski et al., 1998) et que les systèmes photosynthétiques dépendent fortement du fer (Raven, 1990 ; Raven et al., 1999), la relation entre la disponibilité du Fe et le phytoplancton a attiré l'attention de la communauté scientifique. Les concentrations de fer disponibles peuvent influencer la structure et l'abondance des communautés phytoplanctoniques présentes dans les océans (Boyd et al., 2000 ; Timmermans et al., 2001).

1.2.(Français) Nutriments essentiels

Il y a environ 2,4 milliards d'années (Gyr), avant la Grande Oxygénation, le Fe océanique était présent sous sa forme réduite (Thibon et al., 2019). La vie sur Terre s'est développée il y a 3,8 à 4,5 Gyr (Betts et al., 2018 ; Baumgartner et al., 2019), très probablement dans des systèmes hydrothermaux (Dodd et al., 2017). Par conséquent, le besoin en Fe de l'activité biologique pourrait être le résultat des concentrations élevées de Fe au début de la vie (Saito et al., 2003). Des conditions ferrugineuses qui prévalaient pendant la plus grande partie de l'Archéen, l'océan ancien a évolué vers des conditions euxiniques (anoxiques et riches en sulfures) et après le développement de la photosynthèse, vers un environnement à prédominance oxique (Camacho et al., 2017). Aujourd'hui, le Fe est présent en très faibles concentrations dans les océans (0,05-2 nmol L^{-1}) (Landing et Bruland, 1987 ; Martin et al., 1990 ; de Baar et De Jong, 2001), malgré sa forte abondance dans la croûte terrestre (5,6 % ; quatrième élément le plus abondant) (Taylor, 1964).

Le fer, en raison de sa faible solubilité (Liu et Millero, 2002), limite souvent la productivité là où les nutriments de subsurface ne sont pas épuisés (Figure 1-1), notamment dans les principales régions avec des remontées d'eau profonde (Hutchins et al., 1998, 2002), l'océan Pacifique (de Baar et al., 2005 ; Boyd et al., 2007), l'océan Atlantique Nord subpolaire (Moore et al., 2006) et l'océan Austral polaire (Boyd et al., 2000). Le phosphore, les vitamines et les micronutriments autres que le Fe, comme le cobalt (Co) et le zinc (Zn), peuvent également être limitants pour le phytoplancton marin. Les tendances spatiales et l'importance de la co-limitation restent cependant peu connues. La variabilité des rapports stoechiométriques des

nutriments et de la demande biologique sont les principaux déterminants de la limitation des nutriments dans l'océan.

Des cultures de phytoplancton en laboratoire ont été utilisées pour étudier la composition élémentaire du plancton. La composition moyenne en métaux traces du phytoplancton marin eucaryote (Ho et al., 2003) fournit une extension à la formule de Redfield ($C_{106}N_{16}P_1$) comprenant les métaux traces essentiels $(C_{106}N_{16}P_1)_{1000}Fe_8Mn_4Zn_{0.8}Cu_{0.4}Co_{0.2}Cd_{0.2}$. Cependant, l'applicabilité des données expérimentales (e.g., cultures de laboratoire) aux eaux naturelles est incertaine car les conditions expérimentales et la composition des milieux de culture utilisés peuvent ne pas correspondre à celles des eaux naturelles (Twining et al., 2004).

1.4.(Français) Le cycle du fer

La biogéochimie marine du Fe est influencée par sa faible solubilité, sa spéciation redox et organique et le rôle qu'il joue dans les cycles biologiques. En outre, sa concentration dans l'eau de mer dépend de ses sources et de ses puits (Figure 1-6). La compréhension des sources et des mécanismes par lesquels le fer et d'autres métaux traces sont assimilés et circulent dans les océans du monde entier est un objectif clé pour mieux comprendre les grands cycles biogéochimiques.

1.4.1.(Français) Sources et puits de fer

Les principales sources de Fe dans les océans proviennent de l'atmosphère, des sédiments, des sources hydrothermales, des rivières et de la fonte des glaciers dans les régions polaires (Worsfold et al., 2014). Au début des années 2000, des études ont révélé que l'apport de Fe par les aérosols n'était pas la seule source importante de Fe dans la colonne d'eau (Mahowald et al., 2005). Des études ont décrit l'apport des sédiments comme étant aussi important que l'apport de poussière. Cet apport peut engendrer une productivité élevée dans les régions côtières peu profondes (Hutchins et Bruland, 1998 ; Elrod et al., 2004 ; Birchill et al., 2019). Dans les régions polaires, le flux de Fe biodisponible fourni par la fonte des glaciers et des icebergs peut être similaire au flux éolien (Lannuzel et al., 2008). Au cours des années 90, German et al. (1991) ont supposé que l'apport de Fe dans le milieu marin par les sources hydrothermales était négligeable, car le Fe s'oxydait et précipitait à proximité des cheminées. Des études récentes ont montré que le Fe pouvait être transporté jusqu'à 4000 km de distance

des sources hydrothermales (Saito et al., 2013 ; Fitzsimmons et al., 2014 ; Resing et al., 2015) et soutenir jusqu'à 25% de la production primaire dans l'océan Austral (Tagliabue et al., 2010, 2014) et entraîner des efflorescences de phytoplancton (Ardyna et al., 2019). L'une des principales conclusions du programme GEOTRACES (www.geotraces.org) est qu'il existe de nombreuses sources externes de Fe dans l'océan qui sont importantes tant à l'échelle régionale que mondiale. Leur importance relative par rapport à la concentration de Fe observée varie selon les régions et les saisons.

Les modèles biogéochimiques océaniques mondiaux (Groupe de travail 15 du SCOR ; Projet d'intercomparaison des modèles de fer (FeMIP) ; https://scor-int.org/group/151/) comprennent actuellement des données provenant des quatre interfaces océaniques (atmosphère, dorsales, continents et sédiments marins) afin de comprendre le cycle biogéochimique du Fe et de paramétrer les modèles globaux représentant le cycle biogéochimique du carbone (Pitchford et Brindley, 1999 ; Moore et al., 2002 ; Homoky et al., 2016).

Les puits principaux du Fe sont l'absorption biologique active, le scavenging, la précipitation et la sédimentation (Worsfold et al., 2014). L'absorption biologique est un processus actif réalisé par les organismes vivants, qui ont des besoins spécifiques en Fe selon les espèces. Les besoins en Fe des espèces eucaryotes océaniques sont inférieurs à ceux des espèces eucaryotes côtières et des cyanobactéries (Brand, 1991). Le scavenging est un processus passif au cours duquel les métaux traces, y compris le Fe, sont adsorbés sur des particules organiques (vivantes et mortes) et inorganiques, qui sédimentent dans la colonne d'eau (Goldberg, 1954 ; Turekian, 1977). La précipitation est un processus physique qui se produit lorsque les cations de l'eau de mer neutralisent les colloïdes chargés négativement contenant du Fe, permettant la floculation et la coagulation de particules de plus petite taille. La précipitation est le puits principal du Fe, réduisant les concentrations de Fe dissous d'environ 90 % (Boyle et al., 1977). Enfin, la sédimentation est le processus par lequel les particules chutent dans la colonne d'eau, se déposent au fond de l'océan, et s'y accumulent.

1.5.(Français) Systèmes hydrothermaux

La circulation hydrothermale est un phénomène qui se produit sur l'ensemble de la planète et fait référence à la circulation des fluides dans la croûte terrestre et le manteau. Les manifestations externes de l'activité hydrothermale sont observées à la fois sur terre (geysers et sources chaudes) et au fond des océans (fumeurs noirs et blancs).

1.5.1.(Français) Systèmes hydrothermaux de la dorsale médio-océanique

Les premiers systèmes hydrothermaux en eaux profondes ont été découverts à la fin des années 1970 dans l'océan Pacifique, sur la faille des Galápagos (Corliss et al., 1978). Depuis, les systèmes hydrothermaux profonds ont fait l'objet d'études intensives au niveau géologique, physique, biologique et chimique. Les interactions entre les différents domaines de recherche ont permis une meilleure compréhension de ces environnements extrêmes.

Les sites d'évents sous-marins sont répartis dans le monde entier selon quatre configurations tectoniques : les dorsales médio-océaniques (MOR), les centres d'expansion des bassins d'arrière-arc, les arcs volcaniques et les volcans intra-plaques (Figure 1-7). La liste complète des sites d'évent découverts, leurs caractéristiques et l'année de leur découverte sont disponibles sur la base de données InterRidge (http://vents-data.interridge.org, dernièrement consulté le 04/08/2020).

La plupart des systèmes d'évents hydrothermaux sont liés à différents centres d'expansion des océans profonds (jusqu'à 4000 m de profondeur) le long des MOR, comme la dorsale médio-atlantique (MAR) ou l'East Pacific Rise (EPR). D'autres systèmes moins profonds (entre 200 et 2000 m de profondeur), appelés évents hydrothermaux intermédiaires, ont été découverts dans des bassins d'arrière-arc, tels que l'Arc des Mariannes (Resing et al., 2009), l'Arc des Tonga (Massoth et al., 2007) et le bassin d'arrière-arc de Lau (Fouquet et al., 1991). Outre ces cheminées plus profondes, des cheminées hydrothermales marines moins profondes existent et sont liées aux arcs volcaniques (îles océaniques) (par exemple Butterfield et al., 2011 ; Hawkes et al., 2014 ; Guieu et al., 2018).

Pour qu'il y ait des cheminées hydrothermales profondes, les eaux de mer froides et oxygénées présentes dans l'océan doivent s'infiltrer à travers les fissures de la croûte océanique et être exposées à une source de chaleur (chambre magmatique, Figure 1-8). Les sources de chaleur peuvent chauffer l'eau de mer pressurisée à des températures supérieures à 450 °C. Ces régions sont définies comme des "zones de recharge". Dans ces conditions, différents minéraux sont produits, tels que l'anhydrite qui réduit le sulfate fluide (SO42-), la smectite (par exemple la saponite, (Ca0,5,Na)0,3(Mg,Fe2+)3(Si,Al)4O10(OH)2•(H2O)), le chlorite (ClO2-) et la caminite (Mg7(SO4)5(OH)4•(H2O)) qui réduisent le magnésium fluide et dans certains cas épuisent le stock de magnésium (Gartman et Findlay, 2020). La perte d'alcalinité due aux interactions eau-roche, conduit à un enrichissement du fluide en protons et à l'acidification du

fluide à des valeurs de pH aussi faibles que 3 (Seyfried et Ding, 1993). À mesure que le fluide se rapproche du noyau terrestre, il atteint la "zone de réaction", où se produit la majeure partie de la lixiviation des métaux de la roche d'accueil. En raison des températures élevées et du faible pH (jusqu'à pH 2), les métaux tels que le Fe, le Cu, le Mn et le Zn s'enrichissent dans le fluide (German et Von Damm, 2004). À mesure que la profondeur du site de l'évent diminue (baisse de pression), le point d'ébullition de l'eau de mer diminue (Bischoff et Rosenbauer, 1984) ainsi que l'enrichissement en métaux (par exemple Smith et Cronan, 1983).

Le fluide chaud et acide devient moins dense et atteint une flottabilité dans laquelle il commence à remonter depuis la croûte terrestre vers le fond de l'océan. Au cours de son ascension, il peut se mélanger à l'eau de mer et former des sulfures polymétalliques (Herzig et al., 2002). Une fois qu'il atteint le fond de l'océan, le fluide chaud se mélange à l'eau de mer froide et oxygénée environnante, produisant immédiatement l'oxydation et la précipitation des métaux dissous (par exemple Fe, Zn, Cu) et la formation de minéraux sulfurés (par exemple la pyrite (FeS2), la sphalérite ((Zn,Fe)S) et la chalcopyrite (CuFeS2), respectivement) ou d'oxyhydroxydes. Les précipitations de ces minéraux peuvent s'accumuler au niveau des évents en formant des cheminées de plusieurs mètres de haut, appelées "fumeurs noirs", où la précipitation de grandes concentrations de métaux produit la fumée. Les fluides comprennent également des concentrations élevées de gaz, tels que He, H2, H2S, CO2 et CH4.

Un processus important au sein des panaches hydrothermaux est l'oxydation du Fe(II). Le piégeage des éléments de la solution par le Fe(III) fraîchement formé (German et al., 1991) conduit à la co-précipitation de nombreux autres métaux provenant de l'évent. Cela modifie les flux hydrothermaux bruts vers les profondeurs de l'océan et agit comme un puits net dans le budget chimique de certains traceurs clés (Statham et al., 2005 ; Wang et al., 2012). Les métaux qui ne sont pas précipités autour de la sortie de l'évent sont rejetés dans le panache flottant. Ce panache continue à monter dans la colonne d'eau en entraînant l'eau de mer environnante et en réduisant sa charge de particules jusqu'à ce qu'il atteigne une densité similaire. À ce stade, il est appelé panache flottant neutre (également appelé panache non flottant, NBP). Le NBP dérive alors horizontalement et est transporté par les courants océaniques. Des études récentes ont montré que le transport des NBP peut atteindre des distances à l'échelle du bassin allant jusqu'à 4500 km (Resing et al., 2015 ; Fitzsimmons et al., 2017).

Presque immédiatement après la découverte du premier système hydrothermal, les cheminées hydrothermales sous-marines ont été reconnues à la fois comme une source et un puits

potentiellement importants d'éléments clés dans les bilans géochimiques globaux des océans (Edmond et al., 1979). Avec la découverte des premiers fumeurs noirs à haute température (Spiess et al., 1980), il a été mis en évidence que les flux bruts émis par les évents à haute température étaient modifiés de manière significative dans les panaches hydrothermaux. Pour la grande majorité des traceurs chimiques enrichis en fluides de ventilation, les flux nets vers les océans sont modifiés car ces traceurs sont incorporés dans des particules de sulfure et d'oxyhydroxydes polymétalliques riches en Fe qui coulent au fond de l'océan au niveau ou près des dorsales océaniques (Mottl et McConachy, 1990 ; German et al., 1991 ; Kadko, 1993). Cette vision du rôle limité des systèmes hydrothermaux dans les budgets à l'échelle mondiale a persisté pendant plus d'une décennie. Cependant, pour les éléments traces et les isotopes qui sont facilement piégés par les oxyhydroxydes de Fe, il était estimé que l'effet net de la ventilation sous-marine était un puits pour les éléments traces et les isotopes dissous (ITE) depuis l'océan profond vers les sédiments (Elderfield et Schultz, 1996). Cependant, la dernière décennie a vu resurgir l'intérêt pour l'hydrothermalisme en tant que source importante de métaux traces. Dans le cadre du programme GEOTRACES (www.geotraces.org) plusieurs projets ont montré l'importance de l'hydrothermalisme à l'échelle régionale mais ont également confirmé que l'hydrothermalisme pouvait avoir un impact à l'échelle du bassin dans l'ensemble des bassins océaniques (Wu et al, 2011 ; Klunder et al., 2011, 2012 ; Noble et al., 2012 ; Saito et al., 2013; Nishioka et al., 2013 ; Fitzsimmons et al., 2014, 2015, 2017 ; Hawkes et al., 2014 ; Horner et al., 2015 ; Resing et al., 2015).

La dynamique de précipitation du Fe dans le panache hydrothermal (ie. sa localisation spécifique, le mécanisme des précipitations et la vitesse à laquelle elles se produisent) a un intérêt majeur pour définir l'impact des systèmes hydrothermaux sur la chimie océanique des éléments traces (Rudnicki et Elderfield, 1993).

La précipitation des minéraux des fluides hydrothermaux est influencée par le refroidissement, qui réduit l'état de saturation de nombreux minéraux. En outre, elle est influencée par le mélange avec l'eau de mer environnante, qui entraîne une diminution du pH (due à la précipitation des sulfures métalliques) suivie d'une augmentation du pH lorsque l'eau de mer ambiante et les espèces oxydées interagissent avec le fluide hydrothermal (Ding et Seyfried, 2007 ; Gartman et al., 2014). Les espèces oxydées forment des particules de tailles très diverses. Les plus petites sont définies comme des nanoparticules, qui sont de dimensions inférieures à 100 nm. Les nanoparticules sont un composant principal des cheminées de ventilation : par exemple la prévalence des nanoparticules de pyrite est observée dans les cheminées de TAG

(Gartman et al., 2014). Les sulfures et les oxydes insolubles peuvent être transportées sur de longues distances en raison de leur faible vitesse de sédimentation.

La formation de nanoparticules pourrait jouer un rôle plus important que le simple fait d'avoir une vitesse de sédimentation plus faible que les particules de panache de plus grandes tailles. En effet, la présence de ces nanoparticules pourrait agir comme mécanisme de stabilisation, permettant ainsi de maintenir de manière plus persistante une source hydrothermale de dFe (Bennett et al., 2008 ; Sander et Koschinsky, 2011 ; Hawkes et al., 2013 ; Fitzsimmons et al., 2017). De plus, les nanoparticules de pyrite sont plus résistantes à l'oxydation que le dFe(II) et le sulfure de fer (FeS). Par conséquent, il a été suggéré que la décharge de Fe sous forme de nanoparticules de pyrite augmente la probabilité que le Fe dérivé des évents soit transporté sur de longues distances dans l'océan profond (Yücel et al., 2011 ; Gartman et Luther, 2014). Cependant, l'effet des nanoparticules sur la cinétique d'oxydation du Fe(II) reste encore à quantifier.

Les modèles récents ne considèrent pas seulement les évents hydrothermaux comme des sources de métaux à l'état de traces, mais montrent également l'importance des émissions diffusives (German et al., 2015 ; Lough et al., 2019a). Même si les flux diffusifs sont plus petits que les flux des évents, la zone de couverture est sensiblement plus grande. Les évents diffusifs pourraient donc potentiellement dominer l'apport en Fe dissous des systèmes hydrothermaux vers l'océan profond.

1.6.(Français) Objectifs de la Thèse

Le but de cette thèse était d'améliorer les connaissances sur le devenir du fer d'origine hydrothermale en considérant à la fois sa spéciation chimique et physique. Pour y parvenir, plusieurs objectifs ont été visés :

i) Le premier objectif était de mieux comprendre le taux d'oxydation du Fe(II) dans l'océan profond et les environnements hydrothermaux. La gamme de température des équations de cinétique d'oxydation du Fe(II) préexistantes était limitée à des températures supérieures à 10 °C. Bien que cette gamme de température soit utile pour un large éventail de régions océaniques telles que les profondeurs intermédiaires et de surface et les expériences en laboratoire, l'applicabilitéde cette équation n'avait jamais encore été vérifiée pour les eaux profondes

atteignant 2 °C (gamme de température de l'eau de mer environnante où se trouvent les sites des évents hydrothermaux de MAR).

ii) Le second objectif était d'examiner les concentrations de Fe(II) dans l'océan profond et dans les environnements hydrothermaux le long de la dorsale médio-atlantique (MAR). Le fer (II) a été mesuré sur six sites hydrothermaux de la MAR à de multiples profondeurs dans les panaches à flottabilité neutre. Cependant, en raison des taux d'oxydation rapides du Fe(II) dans l'eau de mer oxygénée, les temps d'échantillonnage sont dans la plupart des cas plus longs que les temps de demi-vie du Fe(II). Ils sont en effet de plus d'une heure pour les échantillons profonds alors que les taux d'oxydation vont de quelques minutes à quelques heures (Millero et al., 1987). Par conséquent, les concentrations de Fe(II) mesurées en profondeur sont biaisées par l'oxydation du Fe(II). L'objectif 2 nécessitait donc que l'objectif 1 soit atteint afin de contraindre théoriquement les taux d'oxydation du Fe(II). Ces taux d'oxydation pouvaient alors être utilisés pour estimer la concentration initiale de Fe(II), c'est-à-dire lorsque l'échantillon se trouvait dans l'océan profond.

iii) Le troisième objectif consistait à étudier le transport du fer et les processus sous-jacents dans les premiers kilomètres du site de l'évent hydrothermal TAG. Les échantillons (dissous et particulaires) ont été collectés dans le panache à flottabilité neutre à des différentes distances du site TAG (de 500 m à 75 km). Les changements de concentrations de Fe pouvaient alors être étudiés et les processus identifiés.

2. Materials and Methods

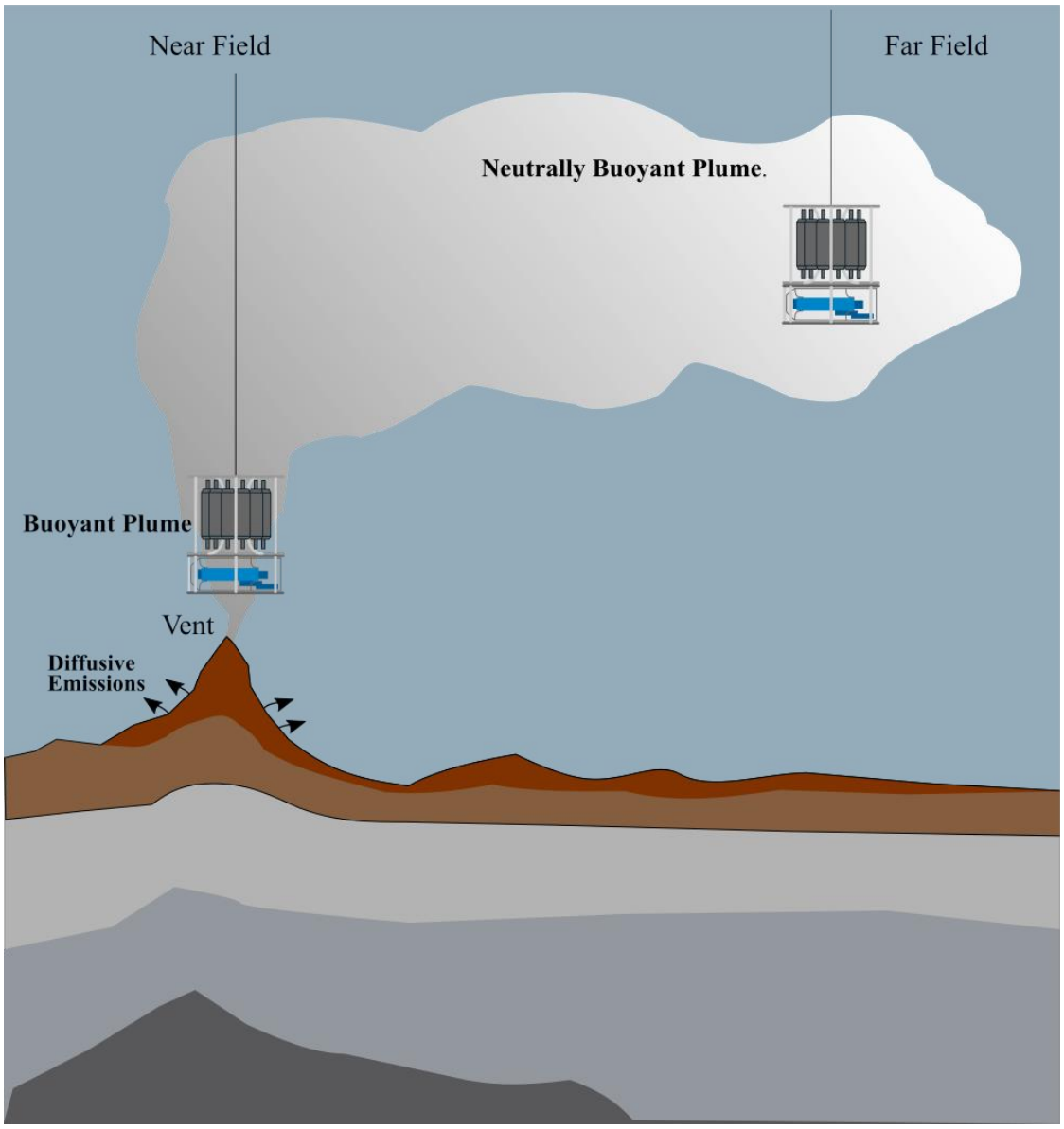

Graphical abstract of the Materials and Methods section. The graphical abstract presents two rosette samplers. The one on the left represents sampling close to the vent site in a near field station. The sampler on the right represents a second cast deployed in a station far field. In both cases, the sampling is taking place within the hydrothermal plume, first in the buoyant plume and in the latter within the neutrally buoyant plume.

The rosette sampler image used in the schematic was downloaded from Wikipedia.com (https://en.wikipedia.org/wiki/Rosette_sampler, last accessed 14/10/2020); however, the original source was not found. It presents a rosette sampler with sampling bottles. Below the sampler, the blue shape represents the CTD logger.

2.1. Sampling sites and characteristics

This Thesis was based on a suite of samples collected from two cruises: the U.K. GEOTRACES cruise FRidge (JC156) and the French GEOTRACES process study cruise HERMINE (GApr07; DOI 10.17600/17000200).

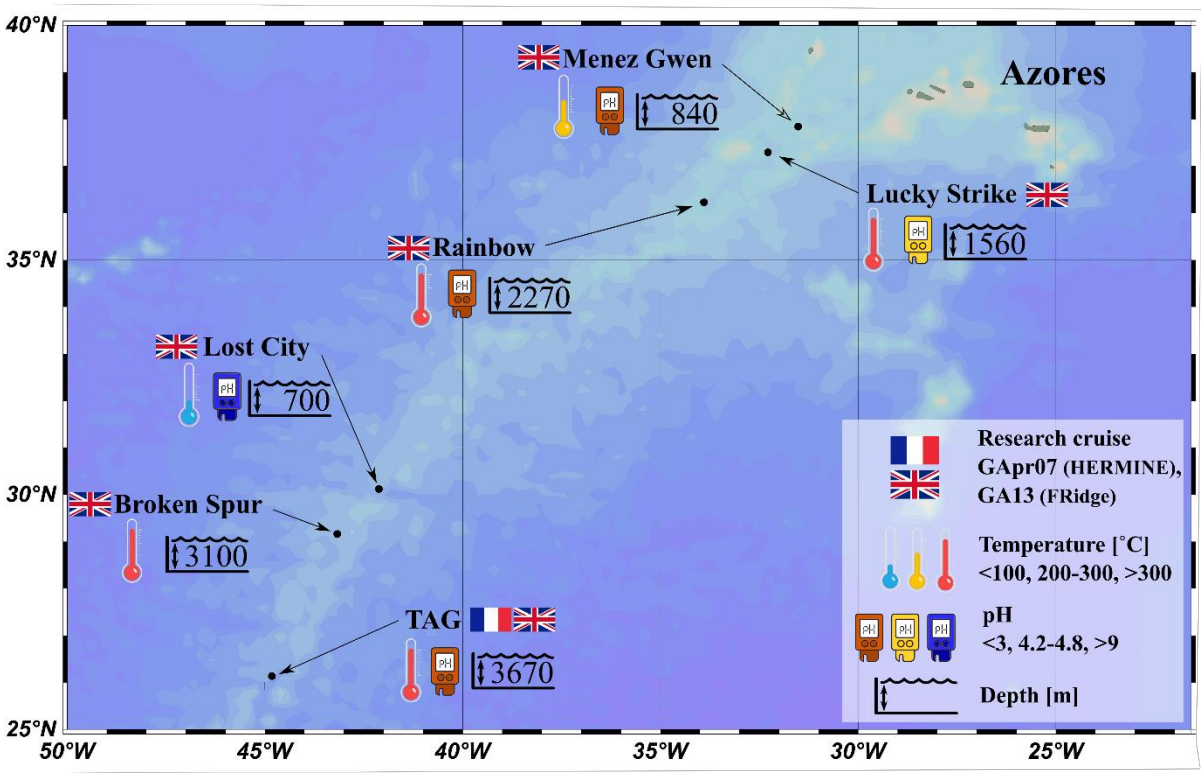

Figure 2-1. Hydrothermal vent sites studied in this Thesis (modified from Gonzalez-Santana et al., under review for GCA).

The FRidge transect cruise travelled following the GA13 section along the Mid Atlantic Ridge (MAR) on board the *RRS James Cook* (PI: A. Tagliabue). This cruise departed from Southampton, UK on December 20th, 2017 and arrived into Guadeloupe, France on February 1st, 2018. Sampling was focused on six hydrothermal vent sites along the MAR (Figure 2-1). During this cruise I analysed dissolved Fe(II) and pH. Iron (II) oxidation kinetic samples were collected by Dr M. Lohan and the FRidge sampling team (Lise Artigue, Dakota Gibbs, Wenhao Wang and Arthur Gourain) for further analyses that I performed at the QUIMA group at the Universidad de Las Palmas de Gran Canaria, Spain, during a 3+1-month PhD mobility.

The HERMINE cruise was a process study cruise focusing on the TAG hydrothermal vent site (Figure 2-1). The cruise took place during spring 2017 (13th March to 28th April) on board the French Research Vessel N/O *Pourquoi Pas?* (PIs: Y. Fouquet, C. Cathalot and E. Pelleter).

Dissolved and particulate trace metal samples were collected by the HERMINE sampling team (Hannah Whitby, Arthur Gourain and Thomas Holmes).

Name	*Latitude*	*Longitude*	*Depth (m)*	*Basement Rocks*	*Geological Control*	*Distance from Axis*
Menez Gwen	37°50′N	31°31′W	820	E-MORB	Top central volcano, axial graben, volcaniclastic	0
Lucky Strike	37°17′N	32°16′W	1650	E-MORB	Top central volcano, lava lake (300 m), caldera	0
Rainbow	36°14′N	33°54′W	2400	Harzburgite	Center of nontransform offset, ultramafic dome	6
Lost City	30°10′N	42°10′W	700	Harzburgite	Top of an intersection massif, detachment fault	15
Broken Spur	29°10′N	43°10′W	3050	MORB	Top of neovolcanic ridge, axial summit fissure	0
TAG	26°08′N	44°49′W	3670	MORB	Rift wall, central part of segment, volcanic centres	7

Table 2-1. Location and main characteristics of the six hydrothermal vent sites investigated in this Thesis. Table modified from Fouquet et al. (2013b).

A common goal of these two cruises was to study the impact of hydrothermal sources in the Fe biogeochemical cycle, yet different approaches were undertaken. The FRidge cruise investigated six hydrothermal vent sites and its surrounding environments, to observe differences between sites. Indeed, the selected hydrothermal vent sites represent a wide range of possible hydrothermal conditions due to different underlying geological conditions (Table 2-1) resulting in different end-member chemical composition (Table 2-2). The HERMINE cruised only focused on one hydrothermal vent site, the TAG hydrothermal site, and followed its hydrothermal plume dispersion towards the south-southwest at a scale of few tens of kilometres along the ridge valley, while focusing on the processes that were occurring within the hydrothermal plume.

The following subsections provide a brief summary of each hydrothermal site characteristic, from north to south along the MAR.

		E-MORB			N-MORB				Ultramafic Rocks		
	Seawater	Menez Gwen[b]	Lucky Strike[c]	Lucky Strike[c]	Broken Spur[d]	TAG[e] Black Smoker	TAG[e] White Smoker	Snake Pit[f]	Rainbow[g]	Logatchev[h]	Lost City[i]
Depth (m)		850	1,700	1,700	3,200	3,670	3,670	3,460	2,300	3,000	800
T° (°C)	2	284	185	324	360	363	301	301	365	353	91
Cl (mM)	546	380	413	554	469	650	-	550	750	515	549
pH	7.8	4.4	3.4	5	-	3.1	-	3	2.8	3.3	11
Mg (mM)	53	0	0	0	0	0	-	0	0	0	19
SO_4 (mM)	28.2	0	0	0	0	0	-	0	0	0	-
Br (µM)	838	666	735	924	749	1,045	-	847	1,178	818	-
Si (mM)	0.178	8.2	8.2	16.3	-	20	19.1	20	6.9	8.2	-
Li (µM)	26	270	265	365	1,030	430	-	835	340	245	
Na (mM)	464	313	344	444	420	550	-	515	553	438	485
K (mM)	10.2	23	21	31	19	18	17.1	23	20	22	
Ca (mM)	10.2	32	31	42	12	28	27	11	67	28	23.3
Rb (µM)	1.3	30	23	48	13	9.5	9.4	12	37	28	-
Sr (µM)	87	110	80	130	45	103	91	54	200	138	-
Ag (nM)	0.023	4.3	4.7	25	-	51	-	31	47	11	-
Al (µM)	<0.1	-	4	11	-	10	-	12	2	4	-
As (nM)	23	247	-	199	-	<11	-	115	-	49.5	-
Ba (µM)	0.14	>12	>6	>80	>21	>19	-	>4.3	>67	>4.5	-
Cd (nM)	0.7	<9	18	79	-	66	-	440	130	63	-
Co (µM)	0.03	<2	<2	<2	-	<2	-	<2	13	<2	-
Cs (nM)	2	330	200	330	144	110	113	170	333	385	-
Cu (µM)	0.0033	<2	<2	30	43	130	3	35	140	27	-
Fe (µM)	<0.001	<2	70	920	1,970	5,170	3,830	2,400	24,000	2,500	-
In (nM)	0.0009	<1	<1	<1	-	2.2	-	<1	3.2	<1	-
Mn (µM)	<0.001	59	77	450	254	710	750	400	2,250	330	-
Mo (nM)	104	11	2.7	84	-	5	-	3	2	1	-
Ni (µM)	<2	<2	<2	<2	-	<2	-	<2	3	<2	-
Pb (nM)	0.013	21	35	130	-	110	-	265	148	86	-
Sb (nM)	1.2	3	<3	6.3	-	3.9	-	11	3.1	<3	-
Tl (nM)	0.069	12	7.1	16	-	13	-	25	9	7	-
Zn (µM)	0.028	<2	<2	40	72	83	350	53	160	29	-
Y (pM)	146	300	320	3,300	-	6,800	-	3,400	19,100	5,600	-
REE (pM)	10	160	190	2,550	900	1,800	-	4,300	16,800	3,600	-
H_2S (mM)	0	<1.5	0.6	3.4	11	6.7	0.5	5.9	1.2	0.8	0.064
CO_2 (mM)	2.3	17	13	28	7.1	3.4	-	6.7	16	10.1	-
CH_4 (mM)	0.0003	1.35	0.5	0.97	0.13	0.147	-	0.062	2.5	2.1	0.28
H_2 (mM)	0.0004	0.024	0.02	0.73	1.03	0.37	-	0.48	16	12	0.43–15

Table 2-2. Composition of the End-Member hydrothermal fluids along the Mid Atlantic Ridge. From Fouquet et al. (2013b).

2.1.1. Menez Gwen

Menez Gwen was discovered in 1994 (Fouquet et al., 1994). It is formed by a circular volcano 700 m high and 17 km in diameter. At the top of the volcano, an axial graben 6 km long, 2 km wide and 300 m deep is open to the north and south (a graben is a valley with a distinct escarpment on each side). A geological characteristic from this site is the presence of a 1400 m long, 400 m wide and up to 8 m deep lava lake with lavas as fresh as those observed on super-fast spreading ridges (Charlou et al., 2000). The Menez Gwen active site is near the top of the young volcano at the bottom of the graben (Figure 2-2). The active site is 200 m^2 and at depths ranging 847 to 871 m deep. Young and small (<5 m) chimneys are mainly anhydrite (white chimneys) formed from the heating of surrounding seawater with the hot (T = 281°C)

and clear hydrothermal fluids. Around the chimneys, diffusive emissions can be observed discharging from mounds enriched in barite (a mineral composed of barium sulphate ($BaSO_4$)). The Menez Gwen end-member fluid is affected by its shallow depth (low pressure) and its uniform exit temperatures (~284°C), with low chlorinities, silica and metal concentration. The end-member pH is 4.2-4.4.

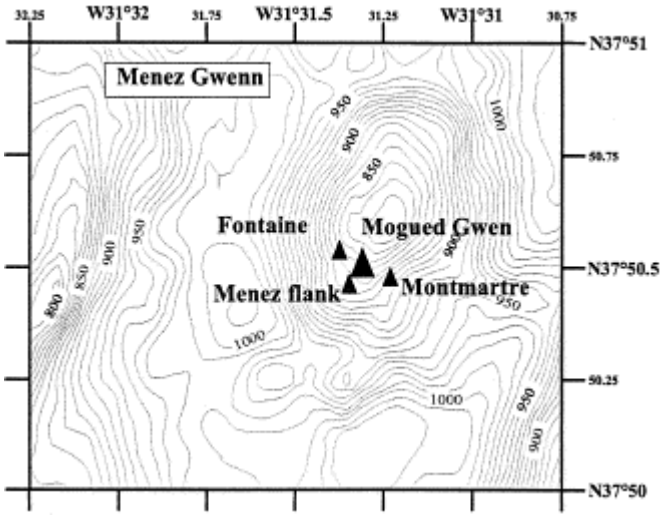

Figure 2-2. Menez Gwen hydrothermal field at 37°50′N. Figure from Charlou et al. (2000).

2.1.2. Lucky Strike

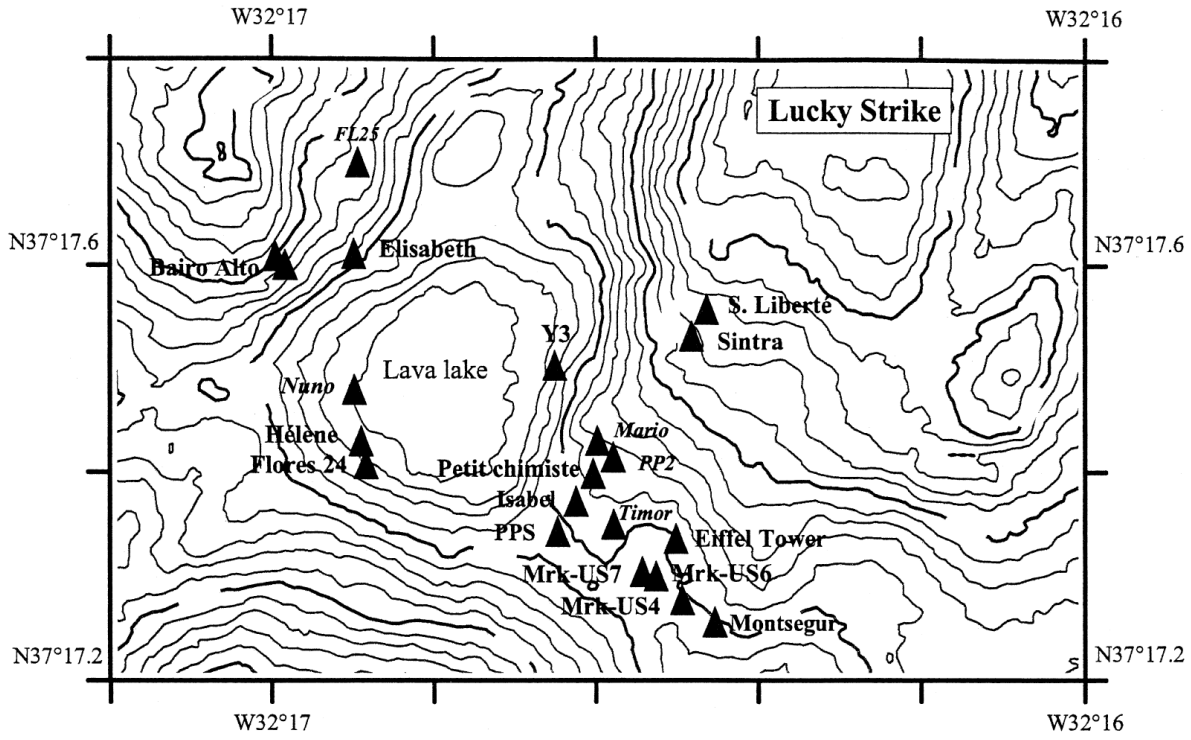

Figure 2-3. Lucky Strike hydrothermal field at 37°17′N. Figure from Charlou et al. (2000).

The Lucky Strike hydrothermal field was discovered in 1992 (Langmuir et al., 1997), when eight active vent sites and a large area of relict sulphides were discovered (Figure 2-3). These active venting sites were dispersed over an area about 700 m long and 300 m wide at depths ranging from 1630 to 1730 m. The discovered black smoker chimneys had end-member fluid temperatures reaching 333 °C, although the flanges (shelf-like overhanging ledges) and certain chimneys (rich in barite) present end-member temperatures ranging 200 to 212 °C. Chimney end-member temperatures vary from north to south, with northern vents presenting cooler fluids with higher chlorinities and lower gas volumes, while southern vent fluids are warmer and present larger gas volumes (Langmuir et al., 1997). In 1994 a 200 m diameter lava lake surrounded by active vent sites and areas of diffusive hydrothermal flow was discovered (Charlou et al., 2000). Researchers using the relationship between the active vent sites and the surrounding substrate suggest that the Lucky Strike hydrothermal system has a long history, which may have been rejuvenated recently (Charlou et al., 2000).

2.1.3. Rainbow

The Rainbow vent field was discovered in 1997 (Fouquet, 1997; Fouquet et al., 1998). Rainbow vent site is found at 2270-2320 m (Bogdanov et al., 2002), within the average range (2000 to 3000 m) of oceanic ridge depth (Searle, 2013).

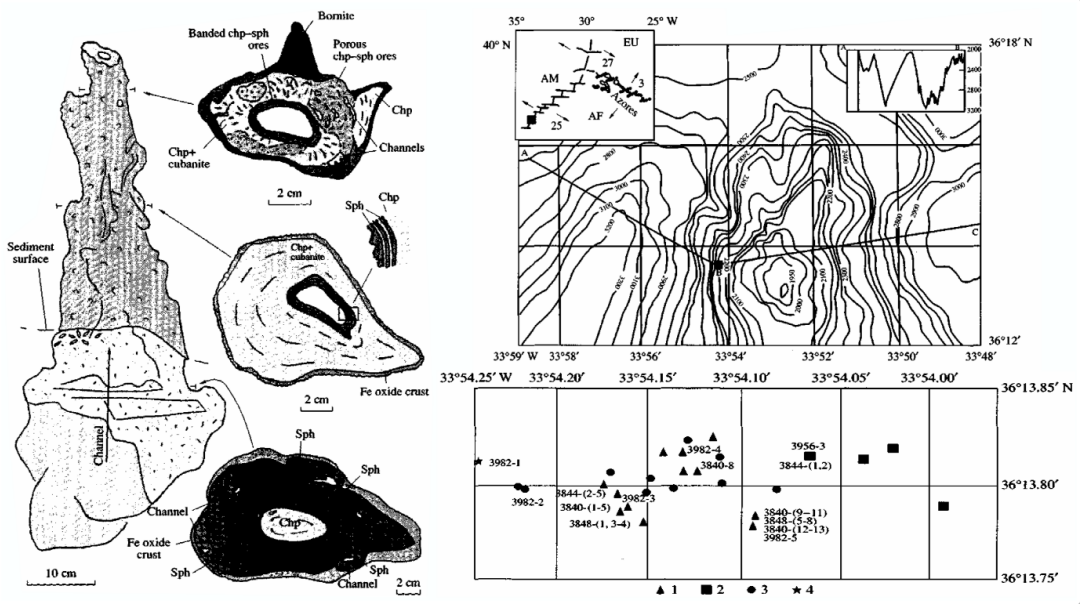

Figure 2-4. Sketch showing the structure of a tubular inactive black smoker collected from Rainbow site 3848-6 (made of chalcopyrite (chp, copper iron sulphide) and sphalerite (sph, zinc sulphide that also contains iron)). Bathymetric map of the Rainbow hydrothermal field showing the location of (1 triangle) large active hydrothermal mounds, (2 squares) small active black smokers, (3 circles) relict mounds and (4 stars) sites with serpentinite. Figure modified from Bogdanov et al. (2002).

The hydrothermal field is formed by twelve active discrete high-temperature (~365 °C) vents and multiple relict hydrothermal indicators. Active chimneys vary in height from small 5 cm tall edifices to 3 m high black smokers (Figure 2-4). The most abundant edifices are active and relict mounds that can be up to 30 m high and 10 m wide with numerous sulphide chimneys varying from 12 cm in the base of the mound to 4 m high in the summit (Bogdanov et al., 2002). The Rainbow hydrothermal fluids present the lowest end-member pH (between 2.9 and 3.1), highest chloride concentrations, and highest temperature of any MAR hydrothermal vent fluid (Fouquet et al., 1998; Douville et al., 2002). Rainbow vent fluids have transition metal (Fe, Mn), Y, and REE concentrations that are amongst the highest ever measured along the MAR (Douville et al., 2002; Fouquet et al., 2013b).

2.1.4. Lost City

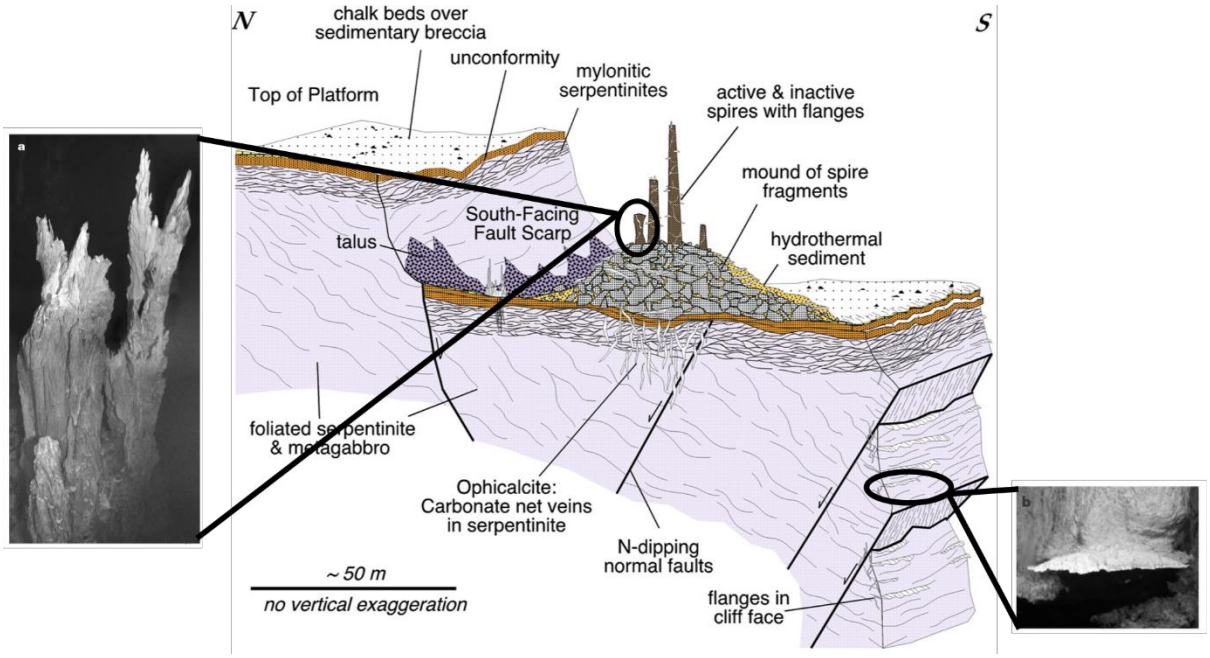

Figure 2-5. Diagrammatic sketch showing geologic and tectonic relationships at Lost City combined with a photo of an inactive 8-m-tall carbonate chimney in the eastern portion of the Lost City field and a photo of an aragonite and brucite 1 m wide flange venting 40 °C fluids. The figure combines the photos from Kelley et al. (2001) and the sketch from Kelley et al. (2005).

The Lost City hydrothermal filed was discovered in 2000 (Kelley et al., 2001, 2005). It is located south of the seafloor mountain Atlantis Massif at depths between 700 and 800 m. Lost City hydrothermal field presents thirty active and inactive venting structures made of carbonate and magnesium hydroxide minerals, reaching up to 60 m in height (Figure 2-5). Furthermore, south of the 400 m terrace, hydrothermally produced flanges can reach a length of up to 2 m (Figure 2-5). Chemically, Lost City is different to the other studied vent sites. It is an alkaline

hydrothermal vent, with average pH ranging from 9.0 to 9.8 (Kelley et al., 2005). The vent fluid is relatively cold (40-75 °C) with trace metal concentrations lower than the other studied hydrothermal vent sites (Ludwig et al., 2006). However, hydrothermal fluid trace metal concentrations can reach concentration 10^4 times higher than background seawater concentrations (Demina et al., 2015).

2.1.5. Broken Spur

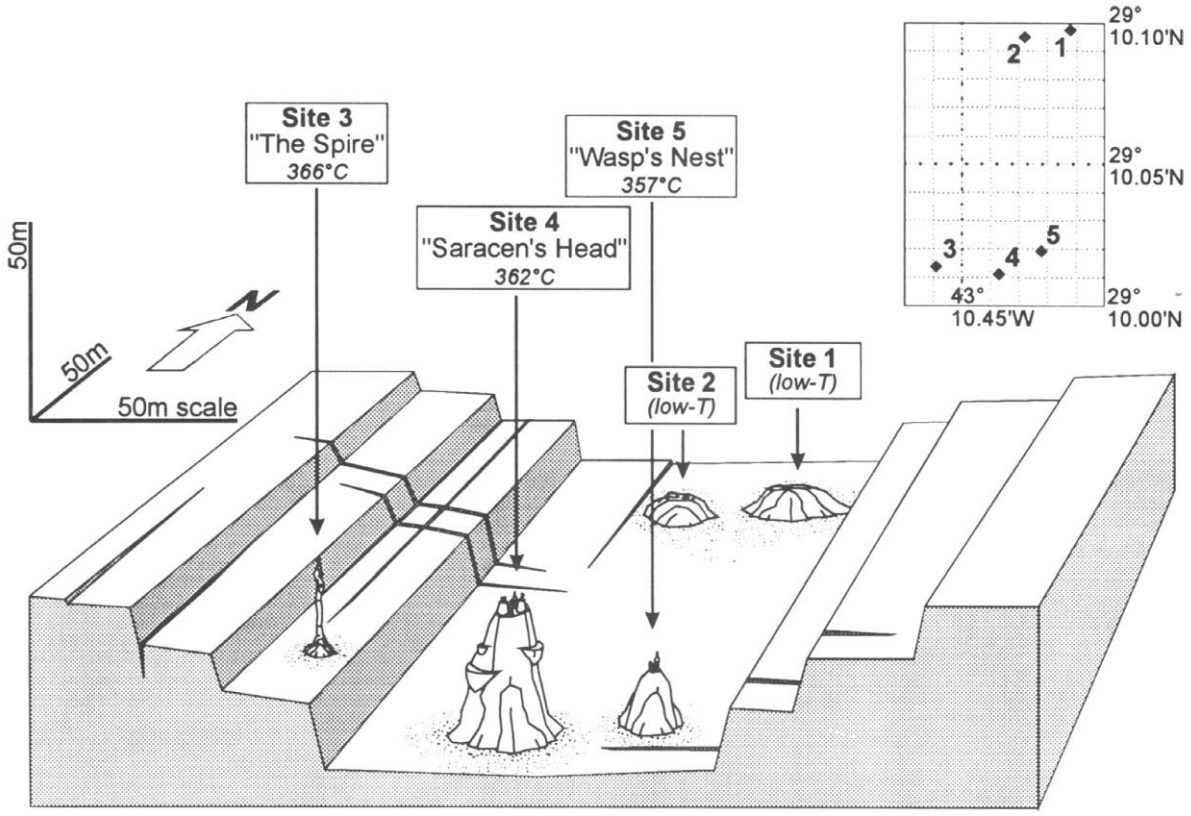

Figure 2-6. Schematic drawing of the setting and morphology of the hydrothermal deposits found at the Broken Spur hydrothermal vent site during the Alvin dives 2624 and 2625. Figure from Duckworth et al. (1995).

Broken Spur was discovered in 1993 at a depth between 3050 and 3091 m (Murton and Van Dover, 1993). It extends over an area of 150 m by 60 m, with active vent sites positioned along as east to west transect (Duckworth et al., 1995). The largest mound is named “Saracen’s Head”, a 37 m high and 20 m in diameter sulphide mound (Site 4 in Figure 2-6). Hydrothermal vents at Broken Spur were subdivided into three types by Duckworth et al. (1995). Type I are hydrothermally immature, anhydrite-rich, 'beehive' diffusers and delicate chimney tips (organ-pipes). Type II are hydrothermally mature, chalcopyrite-rich ($CuFeS_2$) chimney samples. Type III samples are dominated by iron disulphides and are from the base of chimneys or from the outer crust of sulphide mounds.

2.1.6. TAG

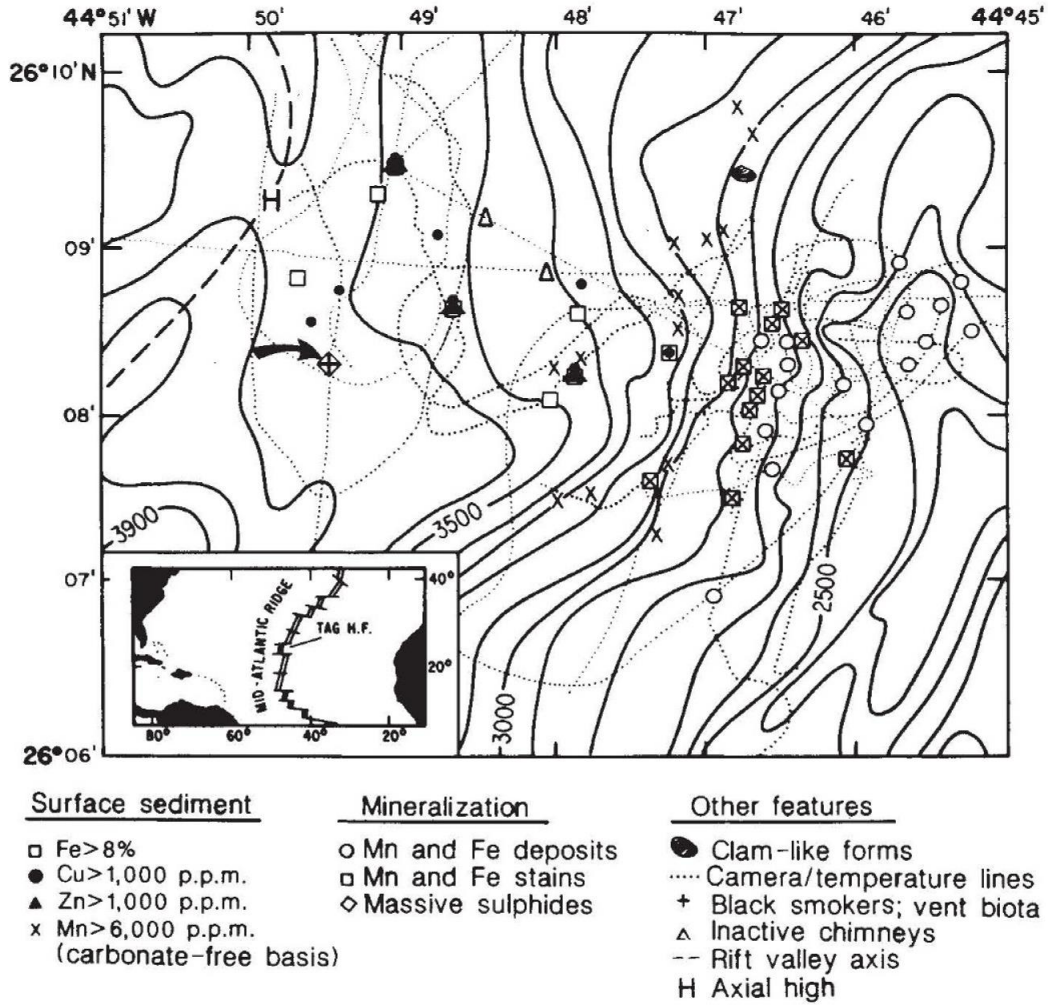

Figure 2-7. Bathymetric map of the TAG hydrothermal field. The arrow points to the location where the first black smokers were found. Figure from Rona et al. (1986).

The Trans-Atlantic Geotraverse hydrothermal (TAG) site played a pivotal role in hydrothermal understanding. Before its discovery in 1984, it was thought that the heat flow on slow spreading ridges was insufficient to produce high temperature venting (Macdonald, 1983). This idea persisted until the discovery of a deep source of Mn (Klinkhammer et al., 1985) and surveys showed the existence of a hydrothermal vent site (Figure 2-7) (Rona et al., 1986). It was with this discovery where the interest in worldwide hydrothermal activity started, since it was then known that hydrothermal activity was not limited to fast-spreading ridges, but also in slow-spreading ridges which account for over half the length of the spreading centres (Rona et al., 1986). Since then, TAG has become one of the most comprehensively studied seafloor hydrothermal fields and is well characterized in terms of activity (e.g. Lalou et al., 1995), fluid composition (e.g. Von Damm, 1995), and deposits (e.g. Mills et al., 2001).

The TAG active mound is situated at a depth of around 3620 m and corresponds to a seafloor massive sulphide mound measuring 250 m in diameter and 50 m in height.

2.2. Sample collection

Seawater samples were collected according to the GEOTRACES guidelines (http://www.geotraces.org/images/Cookbook.pdf). Briefly, a titanium rosette fitted with 24 x 10 L trace metal-clean Teflon-coated OTE (Ocean Test Equipment) bottles (GA13) or GO-FLO bottles (General Oceanics) (GApr07), and a CTD profiler (Sea-bird Scientific), were deployed on a conducting Kevlar wire to collect samples from the water column. Sampling depths were determined while the rosette was being deployed and the bottles were closed at a lowered retrieval speed while the rosette was going up. In both cruises, the bottles were transported into an ISO Class 6 clean air van and inverted three times to avoid settling of particles and pressurized to < 8 psi with 0.2 μm filtered nitrogen (N_2, Air Liquide; GApr07) or filtered pressurized air (GA13).

As Fe(II) is a fast oxidising Fe fraction, sampling for this metal requires high sampling priority, right after gas samples in unpressurized samples. During the FRidge cruise, I collected unfiltered samples for Fe(II) in thoroughly rinsed acid-cleaned 60 mL low-density polyethylene bottles (LDPE; Nalgene®) as soon as the rosette bottles were in the clean room and inserted the sample bottles in an ice-filled plastic cooler box. This kept the samples in the dark and chilled until they were analysed reducing the Fe(II) oxidation rate and any photo-production/consumption of Fe(II). pH samples were collected by a second sampler just after the Fe(II) samples (also from unpressurized sampler bottles) in 125 mL borosilicate bottles and kept in the dark until analysis.

During the FRidge cruise, unfiltered samples for oxidation kinetic experiments were also collected for the QUIMA-ULPGC group (Spain) by a third sampler (Dr Maeve Lohan). These samples were frozen just after the sample collection and remained frozen until the analysis in the QUIMA lab at the University of Las Palmas de Gran Canaria.

During both cruises, samples for dissolved trace metals, including Fe and Mn, were collected in TM-clean LDPE bottles (Nalgene®) after filtration through acid-cleaned 0.45 μm pore-size polyethersulfone filters (Supor®, 25 mm) mounted on Swinnex® filter holders, following Planquette and Sherrell (2012). Seawater samples were then acidified to ~ pH 1.7 with 2 ‰

(v/v; 0.024 M) hydrochloric acid (HCl, Ultrapure® Merck) under an ISO class 6 laminar flow hood, double bagged, and stored for over six months at ambient temperature in the dark before shore-based analysis (Lohan et al., 2006).

2.3. Analytical determination

2.3.1. Dissolved iron (II) determination

Dissolved Fe(II) was determined on board GA13 cruise by flow injection analysis (FIA-CL). This FIA method is characterised by its low cost and transportability, making it an ideal system to be used for on-board analyses. The main disadvantage of this method is it limitation of only analysing one metal size fraction at a time. The FIA included in-line sample filtration through a 0.2 µm syringe filters (Anotop, Whatman, changed daily or after each hydrothermal sample), preconcentration on resin-immobilized 8-hydroxyquinoline and chemiluminescence detection, modified after the method of Bowie, et al. (2002a). Luminol (Sigma-Aldrich) was cleaned using a Chelex 100 (Sigma-Aldrich) filled column. 200 µL of 0.1 M dimethylglyoxime (DMG, Sigma-Aldrich) was added to each litre of clean luminol to reduce cobalt (II) interferences (Bowie et al. 2002). The main changes with previous studies was a consequence of the expected high Fe(II) concentrations. The luminol concentration had to consider the type of sample that were going to be analysed so as to not overload the detector. The original luminol concentration was 10 µM. Above hydrothermal vent sites, the luminol reagent was diluted by 50 %. Similarly, loading times were reduced. Standards used for shipboard analyses included a primary stock solution of 0.02 mol L^{-1} dFe(II), weekly prepared by dissolving ferrous ammonium sulphate hexahydrate (Fisher) in ultrapure 0.1 N hydrochloric acid solution (ROMIL); this solution was stabilized by the addition of 100 mmol L^{-1} sodium sulphite (Sigma-Aldrich). Working standards with concentrations of 200 mmol L^{-1} and 200 nmol L^{-1} dFe(II) were prepared daily by serial dilution of the primary stock solution with ultrapure 0.01 N and 0.001 N hydrochloric acid solution, respectively. Aged, low-Fe(II) seawater (obtained over 24h before analysis from 2000 m depth and kept in the dark) adjusted to pH 5.5 with 2 mol L^{-1} ammonium acetate buffer was spiked with dFe(II) standard to obtain calibration standards generally in the range of 0-1 nmol L^{-1} dFe(II).

The analytical limit of detection was estimated daily as the dFe(II) concentration corresponding to a signal equal to three times the standard deviation of quadruplicate analyses of the blank (Bowie et al., 2004; Sarthou et al., 2011). For the blank solution, we used filtered, aged, low-

Fe(II) seawater that was stored in the dark for over 24h. The average limit of detection was 0.02 ± 0.02 nmol L^{-1} (n=42) for all of the daily shipboard analyses. Currently, there are no Fe(II) standards that can be used to ascertain the accuracy of Fe(II) concentrations. During the FRidge cruise, I tried to mitigate this by preparing the primary Fe(II) stock weekly instead of monthly. This allowed for the intercomparison of two 0.2 nmol L^{-1} dFe(II) standards prepared from different primary stocks (0.20 ± 0.04, n_{stocks} = 6, $n_{analysis}$ = 11).

2.3.2. Oxidation kinetics studies

Iron (II) oxidation kinetic rate constants were measured following the methodology described by King et al. (1995). Continuous Fe(II) concentrations were determined using the FeLume System (Waterville Analytical), with a data point acquisition every 1 s. This direct Flow Injection Analysis system uses luminol (5-amino-2,3-dihydro-1,4-phthalazinedione, Sigma-Aldrich) as the reagent (King et al., 1995) which reacts with Fe(II). The sample was continuously aerated with pure air (Carburos Metalicos S.A., Figure 2-8). A 0.8 nmol L^{-1} addition of Fe(II) (ammonium iron(II) sulfate hexahydrate, Sigma-Aldrich) was introduced into each sample and the Fe(II) concentration was continuously monitored until the signal had reduced by 70 %. This method produces apparent rate constants (k_{app}) because the oxidation rate constant is measured on a Fe(II) spike rather than on the ambient Fe(II). Although, the oxidation rate constant is not affected by the initial Fe(II) in solution (Millero et al., 1987; Roy et al., 2008; Roy and Wells, 2011; Santana-González et al., 2018), the equilibrium with the organic ligands and particle surfaces could be affected. Moreover, due to the effects of organic complexation and that the concentrations of the organic ligands in each sample are not constant, the apparent oxidation rate constants are consequently not true constants.

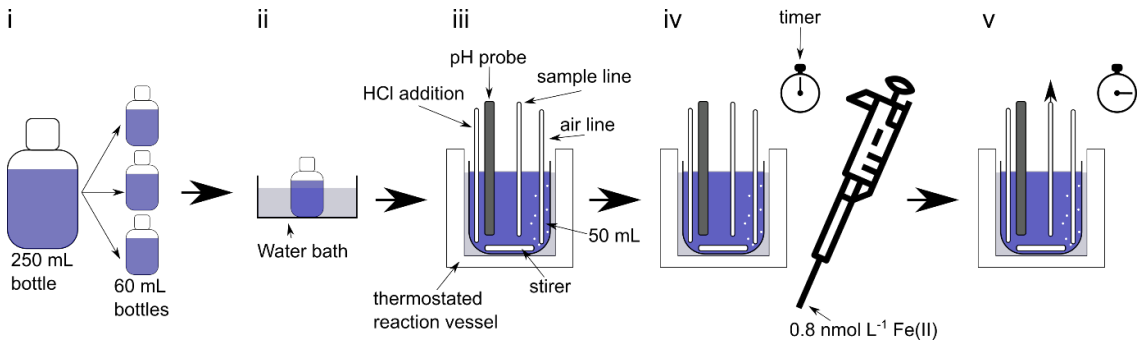

Figure 2-8. Sample preparation for oxidation kinetic experiments. i) 50 mL of the sample was poured into 60 mL LDPE bottles, ii) samples were left in a water bath set at the experiment temperature, iii) sample was poured into the reaction vessel, iv) Fe(II) was added to the sample and the timer started (initial [Fe(II)] = 0.8 nmol L^{-1}), v) the sample concentration was continuously monitored considering the reaction time.

Some previous oxidation kinetic studies have found a second-order dependency of the Fe(II) concentration against time (e.g. Statham et al., 2005). However, in oxygen saturated samples a pseudo-first order rate dependency was obtained, where the slope (ln([Fe(II)] against time) represents the pseudo-first order rate constant *k'* (Eq. 2-1). The linearity remained longer than the half-life time and was thus considered acceptable in all the analyses ($R^2 = 0.983 \pm 0.017$, n samples = 298). The observed linearity confirms that the equilibrium between the added Fe(II) with organic ligands and particles is achieved before 30 s (our first Fe(II) determination time limit). The *k'* error associated with these high R^2 values was 2% for *in situ* condition experiments, and 1% for experiments carried out at 25 °C. The half-life ($t_{1/2}$) of Fe(II) in seawater can be calculated from *k'* (Eqs. 2-1 and 2-2).

$$d[Fe(II)]/dt = -k_{app}[O2][Fe(II)] \quad (2\text{-}1)$$

In oxygen saturated concentrations, the corresponding pseudo-first order rate constant $k' = k_{app}[O_2]$.

$$t_{1/2} = \ln(2)/k' \quad (2\text{-}2)$$

Iron (II) blanks were obtained from a 2 h aerated, magnetically stirred sample which was kept in the dark to achieve the oxidation of Fe(II) (Santana-Casiano et al., 2005). Iron (II) blanks in the 2 h aerated sample were always below the detection limit. Calibration curves (0 to 1 nmol L^{-1}) were produced daily and confirmed linearity in the Fe(II) signal. The detection limit, defined as three times the standard deviation of the blank after being aerated for 10 minutes, was lower than 50 pmol L^{-1}. Reproducibility was checked by running the same sample three times throughout the day after an addition of 1 nmol L^{-1} of Fe(II) with an agreement in concentrations that was better than ± 0.1 nmol L^{-1}. Accuracy could not be determined since reference materials currently do not exist. Results are systematically given as $t_{1/2}$ (in min), followed by the measured *k'* (in min^{-1}).

This method has been recently used (Santana-González et al., 2017, 2018, 2019); however, a small development was performed to limit any seawater interaction with the reaction chamber. A thermostated reaction vessel (Afora) was used to regulate and maintain the sample temperature and a LDPE inner chamber was used to limit any contamination issues. The LDPE chamber was produced from a modified 60 mL LDPE sample bottle. These studies were undertaken at ULPGC (Figure 2-8).

2.3.3. Dissolved trace metals

Inductively coupled plasma mass spectrometry (ICP-MS) is now the most commonly used metal analysis method in shore-based laboratories due to its high precision and low detection limits (picomolar range) (Lagerström et al., 2013). Moreover, multi-elemental determinations can be performed on a single sample. However, the disadvantages of this method are its high costs, high space requirements, and therefore lack of transportability, so on-board analysis is not possible. Moreover, after installation, an initial cleaning (purging) of about two months is required to decrease blank levels. Furthermore, the reactivation of an ICP-MS requires at least one weak of cleaning and conditioning with alternating blanks and low-level seawater to regain the desired blank levels (Wuttig et al., 2019).

Trace metal measurements were carried out within 12 months after collection on a SF-HR-ICP-MS Element XR instrument (Thermo Fisher, Bremen, Germany), at Pôle Spectrométrie Océan (IFREMER, France). The spectrometer was coupled to an ESI seaFAST-pico™ introduction system and run with a method analytically similar to that of Lagerström et al. (2013). Sample preconcentration allows for subnanomolar trace metal concentration determination. It consists of flowing the sample through a NOBIAS Chelate-PA 1 resin which captures the desired seawater component, it then has to be liberated in a much lower volume (e.g. using an acid). Preconcentration factors generally range from 10 to 70 times. Lowest preconcentration factors are used in high trace metal environments such as rainwater, sea-ice and close to ocean-land interfaces. The preconcentration factor is increased to 40 for typical seawater samples; however, higher preconcentration factors are required in remote open ocean waters such as the Southern Ocean, where a factor close to 70 is required (Wuttig et al., 2019).

Calibrations were performed using low trace metal concentration internal seawater with known standard additions of a mixed solution containing Fe, Mn, Cu, Co, Ni, Pb and Zn. Nine-point calibrations were performed at the beginning, half-way (after 30 samples) and at the end (after the other 35 samples) of the SF-HR-ICP-MS run. The average slope of the first and second calibrations was used for the first half of the samples, while the second and third calibration were used for the second half of the samples. This standard addition technique effectively minimized the sensitivity differences caused by the matrix effect. We performed an internal standardization using 10 ppb In (indium) in order to correct the changes of sensitivity of our instrument. Four triplicate reference materials (SAFe S, SAFe D2, GSC and GSP, and two in-house seawaters) were analysed daily during each analytical run to ascertain accuracy and

precision. Each analytical session consisted of about 9 calibration points, 4 reference samples (2 intercomparison reference materials and 2 in-house seawaters, Table 2-3) and 60-65 samples. Analysed SAFe standards were validated with the consensus values, but we could not validate for the GSC and GSP standards. Precision was further assessed through duplicate samples (every 10th sample was a duplicate). The computed average dMn and dFe deviation from duplicate measurements of the same sample with concentrations < 1.5 nmol kg^{-1} was 64 and 66 pmol kg^{-1}, respectively (n = 44). The standard deviation of the reported concentrations was calculated from the duplicate analysis of samples combined with the concentration determination from the three daily calibration curves. The detection limit (defined as three times the standard deviation of the blank) was 0.018 nmol L^{-1} for both elements. No analytical improvements were developed during the PhD Thesis; however I made a Matlab® script to convert the raw data into indium corrected total counts (Appendix A).

		SAFE D2			SAFE S			GSP			GSC			In-house 1			In-house 2		
		avg.	SD	n	avg.	SD	n	avg.	SD	n	avg.	SD	n	avg.	SD	n	avg.	SD	n
dMn	This study	0.34	0.07	20	0.76	0.08	9	0.18	0.08	4	0.61	0.08	18	0.31	0.05	30	0.22	0.04	6
(nmol kg^{-1})	Consensus	0.35	0.05		0.79	0.03		0.78	0.08	9	2.18	0.08	8						
dFe	This study	0.96	0.08	20	0.16	0.01	9	0.26	0.01	4	1.09	0.11	18	1.35	0.11	24	0.35	0.06	6
(nmol kg^{-1})	Consensus	0.93	0.02		0.09	0.05		0.16	0.05	11	1.54	0.12	13						

Table 2-3. Average intercomparison reference material and in-house seawater concentrations obtained during the ICP-MS analysis.

2.3.4. Potentiometric pH

In situ pH was determined at 25 ˚C. This was achieved by adjusting the sample temperature using a water bath. Potentiometric pH was measured onboard GA13 and during laboratory-based kinetics experiments on the free scale using a Tris buffer solution (Millero, 1986) at ULPGC. A potentiometric pH sensor was used instead of the more accurate and reproducible spectrophotometric method (0.005-0.01 ±0.0003 and 0.001-0.002 ±0.0004, respectively) due to its ease of use, continuous pH determination without sample waste and that the accuracy required was 0.01. Laboratory-based kinetics experiments used a Titrino 719 (Metrohm™) which automatically added 0.01M hydrochloric acid (HCl, PANREAC Hiperpur-plus) in order to keep the pH constant. In this system, the same pH electrode was used.

2.4. Hardware development for FIA analysis

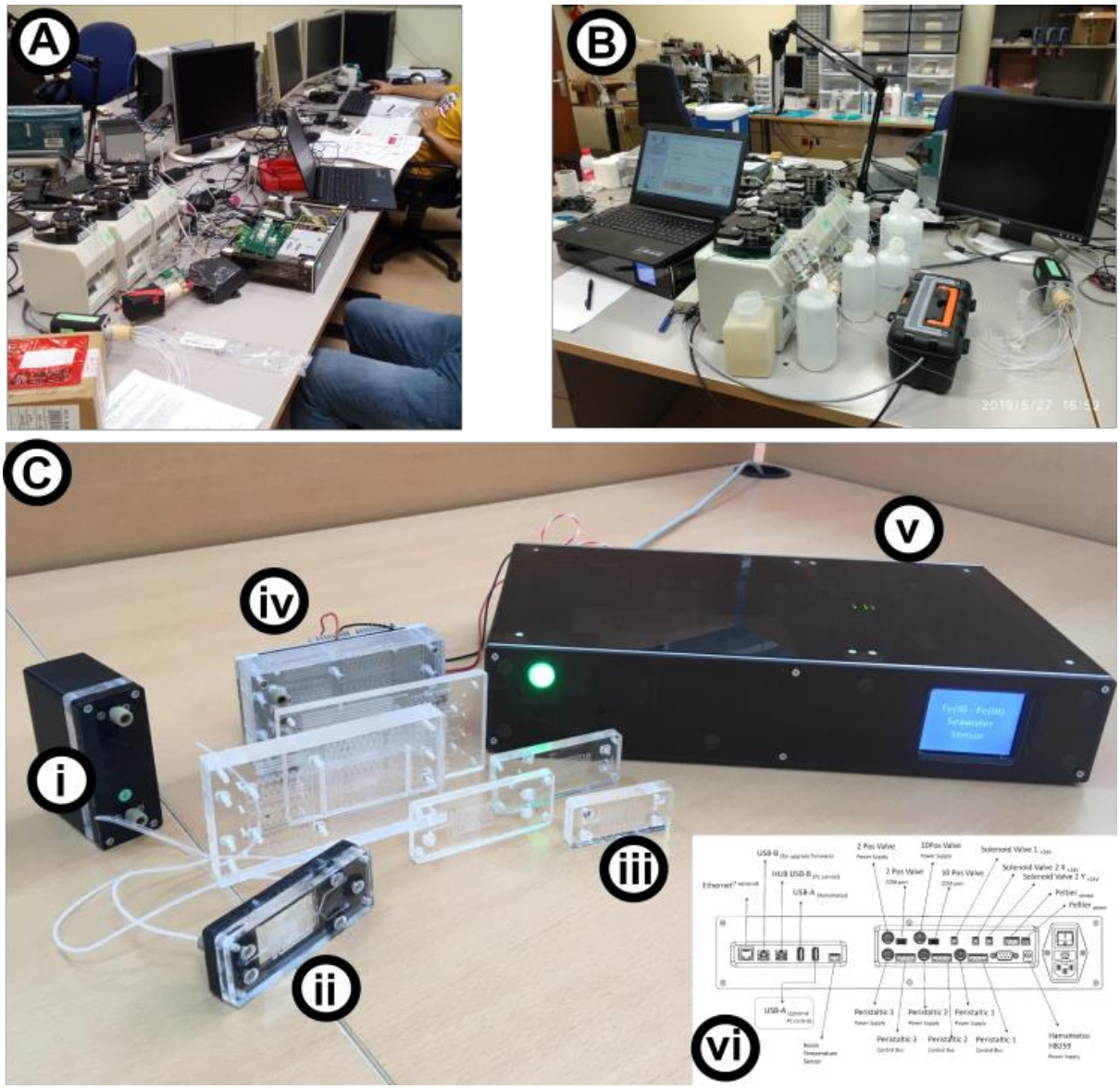

Figure 2-9. Flow injection system developed during this PhD. A) Photo from the setup while developing the software of the controller box. B) Photo from the first reagent test C) Final TEFIA system (v 0.1). i) Photon Multiplier Tube with the 1-1 detection chamber used for Fe(III) determination. ii) 2-1 detection chamber used to mix the luminol with the Fe(II), the two entry points forming a Y. After, it loops in front of a mirror occupying the area in front of the photon multiplier tube detection region. iii) Small mixing chambers that are used instead of mixing coils. iv) Reagent and sample mixing chamber. It includes a thermoelectric cooler (Peltier device) and temperature sensors to heat the solution to a user defined temperature (±0.001 ˚C). v) Controller box (v 0.1). vi) Diagram with connections of the TEFIA v0.1 system.

A basic FIA system is formed by one peristaltic pump, one solenoid valve, one two-way valve, one signal detector (photon multiplier tube), a controller box, a temperature controlled mixing loop and a laptop. This system can be improved by including an autosampler, so that multiple samples can be prepared in advanced, and the system does not have to be checked every three

to 8 minutes. The number of peristaltic pumps can be increased to reduce sample and reagent waste. The addition of peristaltic pumps also requires an increase in used two-way valves.

The most efficient FIA system (considering sample and reagent use) is a three-pump peristaltic system. Its initial costs are highest since it requires two pumps and one two-way valve and one autosampler more than the most basic system. This system can work autonomously and efficiently for the longest time. Even if the increase in cost may not be the limiting factor when buying a new equipment, space and electric supply may affect the usability of an FIA, especially considering that it is a system that will be used on board research ships with limited bench space.

With this in mind, I developed the TEFIA system (Figure 2-9; following the Standard Operating Procedure (SOP) for Fe(III) Luminol/Peroxide Flow Injection Analysis (FIA) System; Version: 14th November 2012 by Simon Ussher, Angela Milne, Matthew Fishwick, Robert Clough, Maeve Lohan, Antony Birchill) at the QUIMA laboratory with the help of the *Instituto Universitario de Microelectrónica Aplicada* (IUMA) at the Universidad de Las Palmas de Gran Canaria. All the peripheral devices are powered and controlled by the controller box (Figure 2-9-C-v), and managed by a user-friendly program which can be opened in any laptop.

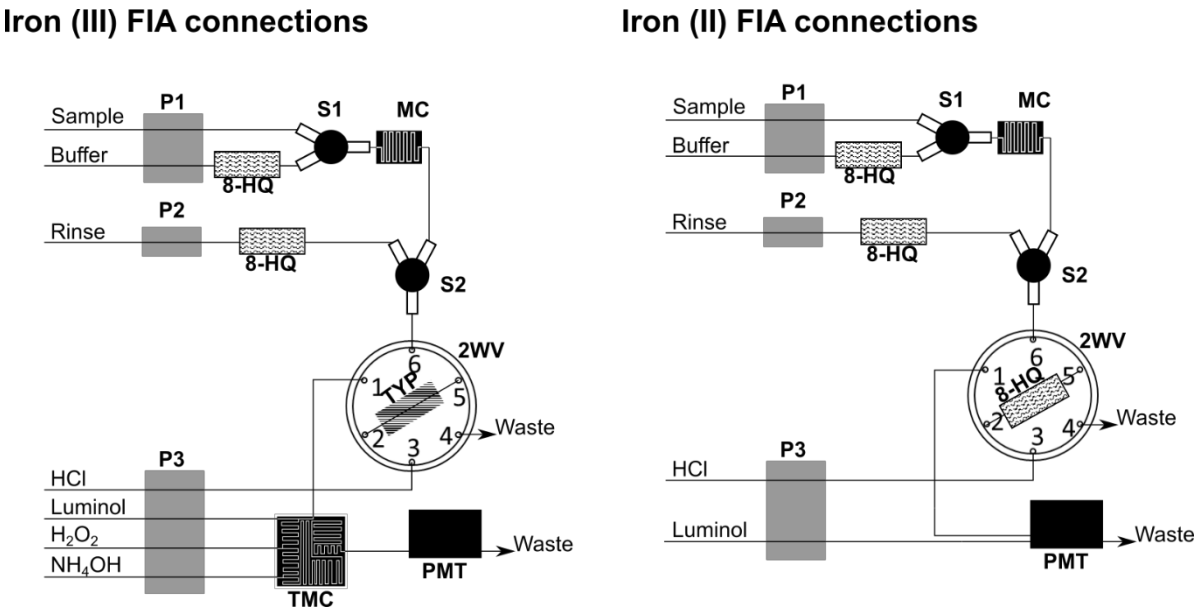

Figure 2-10. Iron (III) and iron (II) FIA-connection template. The system uses 3 peristaltic pumps (P1-P3), 2 solenoid valves (S1 and S2), 1 two-way valve (2WV), a photon multiplier tube (PMT), a sample and buffer mixing coil (MC) and 2 8-HQ cleaning columns. The iron (III) system also requires a Toyopearl preconcentration column (TYP), and a temperature-controlled mixing coil, where the iron reacts with the luminol, peroxide and ammonia solution (TMC). The iron (II) system requires an 8-HQ preconcentrating column instead of a TYP column. The PMT connection for both systems is different.

The requirements were:

- The system can be used for Fe(III) and Fe(II) determination (Figure 2-10).
- It has to be a 3-pump peristaltic system.
- High precision temperature control for the mixing loop without the use of a water bath.
- Efficient mixing between sample and reagents
- Reduce hardware cables. The controller box has to control all the peripheral devices and supply power to them, reducing required ship regulated power sockets.

2.4.1. PMT development

Photon multiplier tubes have a limited detection area window. Therefore, the emitting solution has to travel the longest possible distance in the small area. Before the TEFIA system, this was achieved using the thinnest walled transparent PVC tubing (e.g. AlteVin 01-94-1561) forming a spiral centered in the PMT detector. This system works, but is difficult to implement for Fe(II) systems that require the luminol and sample mixing to occur just before the detection. The TEFIA system uses a methacrylate cell (Figure 2-9-C-i and Figure 2-9-C-ii) which reduces light attenuation increasing the sensitivity of the system. The Fe(II) chamber also has the luminol and sample connection just in the start of the PMT detection window, so there is no signal loss.

2.4.2. MC development

Original mixing coils are made of braided PTFE tubing. The tubing is cut to size and the user braids it and assumes that mixing is carried out properly after multiple knots are made. The IUMA group has experience in modelling microfluidic systems, so the developed MC have been tested to obtain a good mixture without allowing for air/solution bubble retention (Figure 2-9-C-iii). The TEFIA includes a precise temperature controller with temperature varying by less than 0.001 ˚C. The TMC is also built using methacrylate (Figure 2-9-C-iv).

3. Variability in iron (II) oxidation kinetics across diverse hydrothermal sites on the northern Mid Atlantic Ridge

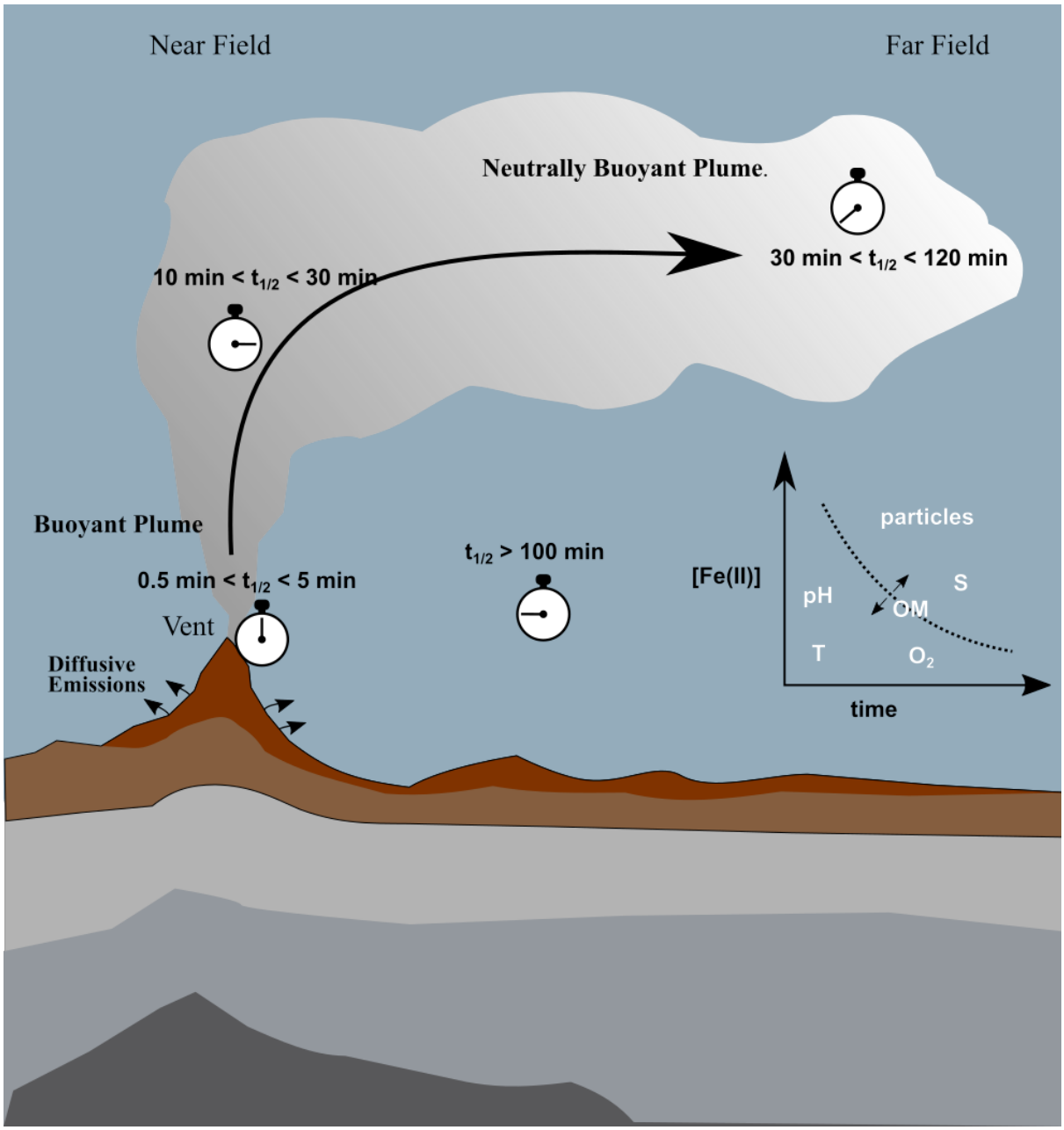

Graphical abstract of chapter 3. Cold deep ocean waters have Fe(II) half-life times ($t_{1/2}$) longer than 100 minutes; however, in hydrothermally affected waters, they are shorter. Close to the vent sites, they range from 0.5 to 5 minutes and increase to 10 - 30 minutes in the buoyant plume. In the NBP, the Fe(II) half-life times increase and range from 30 to 120 minutes. There are multiple factors that influence the Fe(II) half-life time. On the one hand, increases in pH, temperature (T), and oxygen (O_2) produce shorter values. On the other hand, increases in salinity (S) and particles produce a longer Fe(II) half-life. Although organic matter (OM) tends to increase the Fe(II) half-life times, some organic compounds may reduce them. It is therefore difficult to predict the absolute effect that organic matter will produce in the Fe(II) half-life

A version of this chapter is currently under review in *Geochimica et Chosmochimica Acta*.

David González-Santana[1], Melchor González-Dávila[2], Maeve C. Lohan[3], Lise Artigue[4], Hélène Planquette[1], Géraldine Sarthou[1], Alessandro Tagliabue[5], J. Magdalena Santana-Casiano[2]

[1]Univ Brest, CNRS, IRD, Ifremer, LEMAR, F-29280 Plouzane, France.

[2]Instituto de Oceanografía y Cambio Global, IOCAG, Universidad de Las Palmas de Gran Canaria, Las Palmas de Gran Canaria, Spain.

[3]Ocean and Earth Science, University of Southampton, National Oceanography Centre, Southampton, SO14 3ZH, United Kingdom.

[4]LEGOS, University of Toulouse, CNRS, CNES, IRD, UPS, 31400 Toulouse, France.

[5]School of Environmental Sciences, University of Liverpool, Liverpool, United Kingdom.

3.1. Abstract

One of the recently recognized main sources of iron to the deep ocean inventory is the hydrothermal activity associated with mid-ocean ridges. Little is known about the oxidation kinetics of iron(II) within these environments, especially the dependence on physico-chemical parameters such as temperature (T), pH, particle size-fractionation and the effect of organic matter.

Following sample collection during the GA13 section cruise, the iron(II) oxidation at six hydrothermal vent sites (Menez Gwen, Lucky Strike, Rainbow, Lost City, Broken Spur and TAG) along the Mid-Atlantic Ridge were investigated, revealing high variability. The Fe(II) oxidation rate constant analysis from multiple stations at two sites (Rainbow and TAG), revealed that factors other than T and pH controlled the oxidation rate. Experiments on the effect of particle size-fractionation and organic matter at different pH showed that the presence of organic ligands and colloidal size particles delayed the oxidation process, while not affecting the pH dependency.

Furthermore, investigating the Fe(II) oxidation rate constants dependence to a range of temperatures (between 2 and 25 ºC) and pH (between 7 and 8) on a set of selected hydrothermal samples allowed us to derive a multiparametric equation to model the iron(II) oxidation rate constants in the ocean. This equation covers a larger range of temperatures than previous published equations, improving its applicability for global biogeochemical models.

3.2. Introduction

It is now well-established that phytoplankton growth is limited by the concentration of dissolved iron (Fe) in up to 30% of the world oceans (Moore et al., 2013). Iron in the ocean, can be found as both ferric (Fe(III)) and ferrous (Fe(II)) iron, where 99% of the dissolved Fe(III) is complexed by organic ligands (Rue and Bruland, 1995). In oxic waters, Fe(II) tends to oxidize to the most thermodynamically stable form, Fe(III), in a period of minutes to hours (Santana-Casiano et al., 2005). Oxidation of Fe causes the solubility to decrease (Millero et al., 1995), therefore, reducing its bioavailability (Shaked et al., 2005; Morel et al., 2008).

Recently, in the context of the international GEOTRACES program (www.geotraces.org), several studies showed that Fe supplied by hydrothermal activity from mid-ocean ridges can have a substantial impact on Fe distributions at basin scales (Conway and John, 2014; Resing

et al., 2015; Fitzsimmons et al., 2017; Tagliabue et al., 2017). Hydrothermal venting contributions could represent up to 11-22 % of the dissolved iron (dFe, filtered by 0.2 μm) present in the global deep ocean (Bennett et al., 2008), and as such, accounts for a similar dFe flux as continental riverine runoff (Elderfield and Schultz, 1996). Therefore, hydrothermalism acts as an important Fe source in the deep ocean which could potentially affect the global biological carbon pump (Resing et al., 2015).

The concentration of dissolved Fe(II) (dFe(II)) in the open ocean is very low, between 0.02 and 2 nmol L^{-1}, due to its fast oxidation under oxic conditions following the Fenton reaction mechanism (González-Davila et al., 2005; Santana-Casiano et al., 2005). However, specific oceanic regions present dFe(II) concentrations which are orders of magnitude higher. In marine sediment interstitial waters, concentrations can reach around 300 μmol L^{-1} (de Baar and De Jong, 2001), upwelling systems can increase Fe(II) concentrations up to 50 nmol L^{-1} (Hong and Kester, 1986), while hydrothermal fluids can contain as much as 25 mmol L^{-1} of dFe(II) (German and Von Damm, 2004). Water emanating from hydrothermal systems contains high concentrations of Fe(II) amongst other elements (Mottl et al., 1979; Mandernack and Tebo, 1993). Studies conducted at hydrothermal vent sites in different ocean basins have revealed different Fe(II) oxidation rate constants, with Fe(II) half-life times varying from 0.5 to 220 min, which has important implications for the dispersion of produced Fe-oxide phases (Massoth et al., 1998; Field and Sherrell, 2000; Statham et al., 2005; Wang et al., 2012; Santana-González et al., 2017; Rouxel et al., 2018). Recently, Gartman and Findlay (2020) compiled all the available data for Fe(II) half-life in hydrothermal systems. However, only four hydrothermal vent sites had been sampled. One was the TAG vent site, while the other three were located in the Indian and Pacific Ocean. The values were computed with high Fe(II) spikes (500 nmol L^{-1}) which strongly affect the role played by the different reactive oxygen species (González-Dávila et al., 2006).

Temperature (T), pH, and oxygen concentration (O_2) are the primary variables that directly affect the Fe(II) oxidation (Stumm and Lee, 1961; Millero et al., 1987; Millero and Sotolongo, 1989; Santana-Casiano et al., 2005). Salinity also affects the Fe(II) oxidation, as reported in previous laboratory experiments (Millero et al., 1987; Santana-Casiano et al., 2005). However, other factors such as changes in the inorganic complexation of Fe(II) due to the specific ionic composition of the vent fluid, or organic complexation can influence these oxidation rate constants (Rose and Waite, 2003a; Statham et al., 2005). Therefore, the oxidation rate constants are not true constants and could be termed “apparent” due to the effect of organic complexation

(Voelker and Sulzberger, 1996), as the nature and concentrations of organic ligands vary between samples. Moreover, pyrite nanoparticles formed in hydrothermal vent sites, have been estimated to oxidize more slowly than dissolved Fe(II) (Yücel et al., 2011), showing that particle composition also influences the oxidation rate constants. The first empirical equation describing the Fe(II) oxidation rate constants in seawater was reported by Millero et al. (1987), and later updated by Santana-Casiano et al. (2005) for nanomolar concentrations. This equation has been included in coupled physical-biogeochemical models in the ocean (OGCBMs) to take into consideration the oxidation of Fe(II) (Tagliabue and Völker, 2011). However, this equation was established for water temperatures ranging from 10 to 25 ºC, which leads to discrepancies for the Fe(II) oxidation rate constants for cold, deep ocean water masses.

The aims of this study were to measure the oxidation kinetic constants (k') of Fe(II) from different hydrothermal vents and to investigate whether the variations of pH, T and S can explain the observed variability, or if other factors such as the presence of particles, colloids or dissolved organic matter (DOM) are significant contributors. This updated version of the equation incorporates a wider range of temperatures, which lowers the error associated with the theoretical Fe(II) oxidation rate constants. Thus, it becomes applicable to the calculation of theoretical Fe(II) oxidation for the deep waters in which hydrothermal systems are typically found.

3.3. Methods

3.3.1. Sampling sites and characteristics

Seawater samples were collected during the GA13 section cruise (JC156) along the Mid Atlantic Ridge (MAR) onboard the *RRS James Cook*. This cruise departed Southampton, UK on December 20th, 2017 and arrived into Guadeloupe, France on February 1st, 2018. Sampling focused on six hydrothermal vent sites along the MAR: Menez Gwen (37˚ 50'N 31˚ 31'W; Charlou et al., 2000), Lucky Strike (37˚ 17'N 32˚ 16'W; Charlou et al., 2000), Rainbow (36˚ 14'N 33˚ 54'W; Douville et al., 2002) , Lost City (30˚ 7'N 42˚ 7'W; Kelley et al., 2001), Broken Spur (29˚N; James et al., 1995), and TAG (26˚N; Gamo et al., 1996) (Figure 3-1). These six hydrothermal vent sites represent a wide range of possible hydrothermal conditions due to different underlying geological conditions. Lost City and Menez Gwen are the shallowest sites, with the vent site depths located at 700-720 m and 840-850 m, respectively. The Lucky Strike hydrothermal field is situated between 1560 and 1730 m depth. The Rainbow vent site is found

at 2270-2280 m, within the average range (2000-3000 m) of oceanic ridge depth (Searle, 2013), while Broken Spur and TAG are deeper hydrothermal systems located at 3100-3300 m and 3670-3700 m, respectively. Chemically, Lost City is an alkaline hydrothermal vent, with pH ranging from 9.0 to 9.8. The vent fluid is cold (40-75 °C compared to 185-365 °C at the other vent sites) with extremely low concentrations of most trace elements (eg. Fe below the detection limit compared to 2-24000 µmol L^{-1} at the other vent sites) (Ludwig et al., 2006; Fouquet et al., 2013a). All other hydrothermal vent sites are acidic with pH lower than 4, and act as important sources of trace metals (Charlou et al., 2000; Douville et al., 2002; Andreani et al., 2014). Geologically, Menez Gwen and Lucky Strike are similar, their basement rocks are mafic, enriched-Mid-Ocean Ridge Basalt (E-MORB, enriched with light rare earth elements, LREE), and present sulfide mounds. Rainbow also presents sulfide mounds, but its basement rock is ultramafic. Further south, the alkaline Lost City is also situated above an ultramafic base with carbonate chimneys. Finally, Broken Spur and TAG have sulfide mounds and basement rocks formed by normal-MORB (N-MORB, LREE depletion) (references within Fouquet et al., 2010).

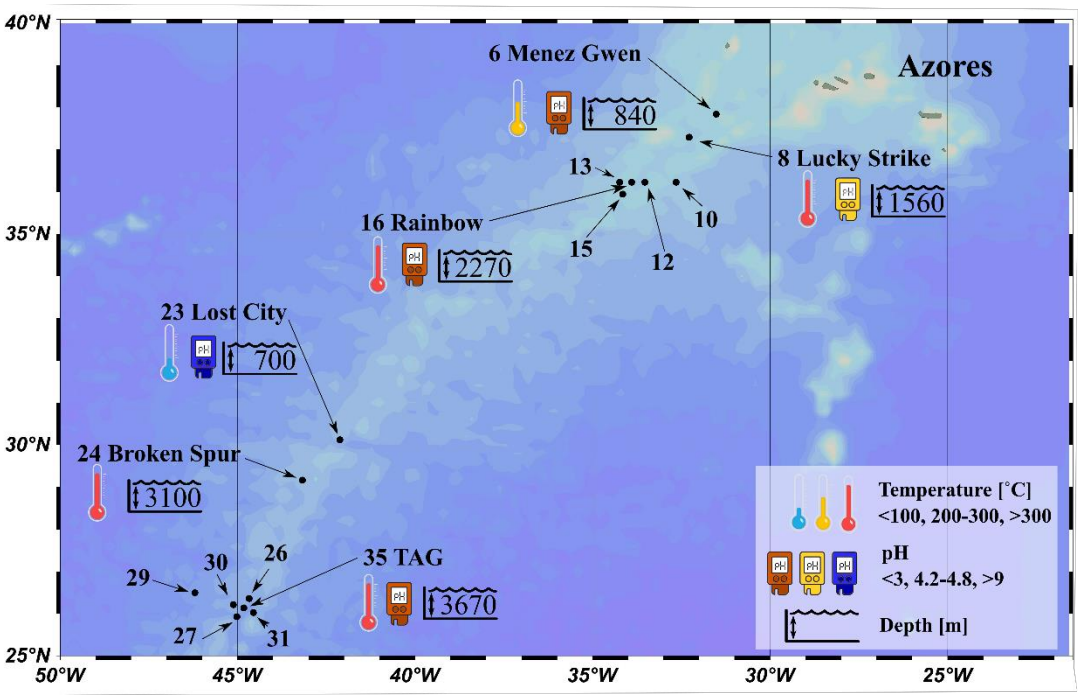

Figure 3-1. Map of the investigated hydrothermal vent sites along the MAR , showing the station numbers and hydrothermal vent site names for the sampling sites. Symbols represent endmember characteristics. The pH of the Broken Spur endmember was not available.

Seawater samples were collected according to the GEOTRACES guidelines (http://www.geotraces.org/images/Cookbook.pdf). Briefly, a titanium rosette fitted with 24 x 10 L trace metal-clean Teflon-coated OTE (Ocean Test Equipment) bottles, a CTD profiler

(Sea-bird Scientific), light scattering sensor (PMEL MAPR), and a redox potential sensor (PMEL MAPR), were deployed on a conducting Kevlar wire to collect samples from the water column. Sampling depths were actively chosen from the continuous T, salinity (S), light scattering sensor (https://data-search.nerc.ac.uk:443/geonetwork/srv/api/records/8ba648f2759d57fbb2246671f8065939) and redox potential readings.

Upon recovery, the OTE bottles were transported into an ISO class 6 clean air van. Unfiltered samples (UF) for Fe(II) oxidation kinetics were immediately transferred into thoroughly rinsed acid-cleaned 250 mL or 1 L low-density polyethylene bottles (LDPE; Nalgene) following the GEOTRACES Cookbook (http://www.geotraces.org/images/Cookbook.pdf) and frozen at -20 ˚C. Samples remained frozen in a -20 ˚C freezer for one year before their analysis. pH samples were collected in 125 mL borosilicate bottles and kept in the dark until the time of analysis.

3.3.2. pH determination

pH was measured onboard and during laboratory-based kinetic experiments in the free scale using a Tris buffer solution (Millero, 1986). Onboard pH samples were kept in the dark, inserted into a 25 ˚C water bath, and measured at 25 ˚C, within less than 1 hour after collection. Laboratory-based kinetic experiments used a Titrino 719 (Metrohm^{TM}) which automatically added 0.01M hydrochloric acid (HCl, PANREAC Hiperpur-plus) in order to keep the pH constant. The pH at *in situ* conditions were computed considering the total alkalinity for an average profile of the area (https://www.nodc.noaa.gov/ocads/oceans/GLODAPv2/, last accessed 18/05/2020). This average profile was obtained from plotting all the available alkalinity data from the studied region. The associated error of the estimate was ±6 µmol kg^{-1}. Gray et al. (2011) showed that computed pH values are relatively insensitive to errors in alkalinity, and that pH controls the magnitude and variability. A change in 400 µmol kg^{-1} in total alkalinity values (e.g. from 2325 to 2725 µmol kg^{-1}) will change the pH in +0.005, which lies within the error of determination for potentiometric pH. The set of constants from Lueker et al. (2000) were used.

All the pH data in the text and in the figures, including kinetics and profile data are expressed in the free scale.

3.3.3. Iron (II) measurements

In order to measure the Fe(II) oxidation rate constants, continuous Fe(II) concentrations were determined using the FeLume System (Waterville Analytical), with a data point acquisition every 1 s. This direct Flow Injection Analysis system uses luminol (5-amino-2,3-dihydro-1,4-phthalazinedione, Sigma-Aldrich) as the reagent (King et al., 1995) which reacts with a subproduct of oxidized Fe(II) (O_2^-). The sample was continuously aerated with pure air (Carburos Metalicos S.A.). A 0.8 nmol L^{-1} addition of Fe(II) (ammonium iron(II) sulfate hexahydrate, Sigma-Aldrich) was introduced into each sample and the Fe(II) concentration was continuously monitored until the signal had reduced by 70 %. This method produces apparent rate constants (k_{app}) because the oxidation rate constant is measured on a Fe(II) spike rather than on the ambient Fe(II). Although, the oxidation rate constant is not affected by the initial Fe(II) in solution (Millero et al., 1987; Roy et al., 2008; Roy and Wells, 2011; Santana-González et al., 2018), the equilibrium with the organic ligands and particle surfaces could be affected. Moreover, due to the effects of organic complexation and that the concentrations of the organic ligands in each sample are not constant, the apparent oxidation rate constants are consequently not true constants.

Some previous oxidation kinetic studies have found a second-order dependency of the Fe(II) concentration against time (e.g. Statham et al., 2005). However, in oxygen saturated samples a pseudo-first order rate dependency was obtained, where the slope (ln([Fe(II)] against time) represents the pseudo-first order rate constant *k'* (Eq. 3-1). The linearity remained longer than the half-life time and was thus considered acceptable in all the analyses ($R^2 = 0.983 \pm 0.017$, n samples = 298). The observed linearity confirms that the equilibrium between the added Fe(II) with organic ligands and particles is achieved before 30 s (our first Fe(II) determination time limit). The *k'* error associated with these high R^2 values was 2% for *in situ* condition experiments, and 1% for experiments carried out at 25 °C. The half-life ($t_{1/2}$) of Fe(II) in seawater can be calculated from *k'* (Eqs. 3-1 and 3-2).

$$d[Fe(II)]/dt = -k_{app}[O2][Fe(II)] \quad (3\text{-}1)$$

In oxygen saturated concentrations, the corresponding pseudo-first order rate constant $k' = k_{app}[O_2]$.

$$t_{1/2} = \ln(2)/k' \quad (3\text{-}2)$$

The minimum energy required to start the oxidation reaction (activation energy, E_a, J mol^{-1}) and the corresponding preexponential or frequency factor (A) were computed from the calculated *k'* using the empirical Arrhenius equation, where R is the universal gas constant (8.314 J mol^{-1} K^{-1}):

$$\log(k') = \log(A) - \frac{E_a}{R \cdot \ln(10) \cdot T} \quad (3\text{-}3)$$

Iron (II) blanks were obtained from a 2 h aerated, magnetically stirred sample which was kept in the dark to achieve the oxidation of Fe(II) (Santana-Casiano et al., 2005). Iron (II) in theses blanks always below the detection limit. Calibration curves (0 to 1 nmol L^{-1}) were produced daily and confirmed linearity in the Fe(II) signal. The detection limit, defined as three times the standard deviation of the blank after being aerated for 10 minutes, was lower than 50 pmol L^{-1}. Reproducibility was checked by running the same sample three times throughout the day after an addition of 1 nmol L^{-1} of Fe(II) with an agreement in concentrations that was better than ± 0.1 nmol L^{-1}. Accuracy could not be determined since reference materials currently do not exist. Results are systematically given as $t_{1/2}$ (in min), followed by the measured *k'* (in min^{-1}).

3.3.4. Experimental setup

Using natural seawater samples, kinetic experiments were carried out under different conditions, with pH and T set to *in situ* conditions (data shown in the supplementary Table S1), and with pH and T normalized to constant values, in unfiltered, filtered and filtered and UV-irradiated samples. These later experiments required a high sample volume, limiting the number of experiments.

3.3.4.1. Quantification of the temperature and pH effect on the iron (II) oxidation rate constant

In order to improve the temperature range of the existing Fe(II) oxidation kinetic equation, 1 L samples of deep ocean water were collected during the JC156 cruise, at stations 13 (2339 m), 16 (2051 m), 24 (2829 m), 30 (2700 m), 31 (2796 m), and 35 (1999, 3350 and 3601 m). The samples remained frozen at -20 °C during one year until analysis. Two days prior to the analysis, samples were thawed in a 4 °C fridge. This allowed a slow melting of the samples in the dark, thus limiting any photoproduction of Fe(II) and also removal of any superoxide and hydroxyl radicals in the sample (Voelker and Sedlak, 1995).

The samples were then transferred into 60 mL LDPE bottles (one for each condition). Temperature effect experiments were performed at constant pH, and those for pH effect at constant temperature. The temperature effect experiments were carried out at *in situ* temperature, 10, 20 and 25 °C at a fixed pH of 8. The pH effect experiments were carried out at *in situ* pH, and pH 7, 7.5 and 8 at a fixed temperature of 25 °C.

3.3.4.2. Oxidation rate constants through the water column at the six hydrothermal vent sites

To assess the expected Fe(II) oxidation rate constants at *in situ* conditions, the experiments were carried out at *in situ* potential temperature and pH ($T_{is}pH_{is}$). The temperature was then increased to 25 ˚C ($T_{25}pH_{is}$) to obtain the temperature effect on the oxidation rate constants. A third set of experiments were performed at 25 ˚C and pH 8 ($T_{25}pH_{8}$). The T and pH normalization of all the samples allowed for the interpretation of the effect of other variables, such as organic matter and particles, in the oxidation rate constants. This allows to investigate where seawater composition is influencing the oxidation rate, a process that cannot be isolated when comparing two samples with different temperatures and/or pH.

The day before the experiments, three to four frozen samples were taken out of the freezer and placed in a fridge set to 4 ˚C. The next morning, a temperature-controlled water bath was set to the coldest *in situ* potential temperature (supplementary Table S1). While the water bath was cooling down, each sample was subsampled into three 60 mL acid cleaned LDPE bottles and placed back into the fridge. One of the subsamples was inserted into the temperature-controlled water bath, which was set to the original *in situ* potential temperature of the sample. The sample was left in the water bath for acclimatization during 15 min and then transferred into the reaction vessel. In the reaction vessel, the sample was aerated prior to and during the study. After 10 minutes of aeration, the Fe(II) addition was made and the Fe(II) concentration and time were continuously monitored ($T_{is}pH_{is}$). After finishing with the *in situ* temperature subsamples, the temperature of the water bath was increased to 25 ˚C and the $T_{25}pH_{is}$ and $T_{25}pH_{8}$ experiments were carried out, following the respective 15 min acclimatization period for each sample.

3.3.4.3. Experimental setup to assess the effect of colloidal and organic matter

The unused unfiltered (UF) sample volumes remaining from the quantification of the temperature and pH effect experiments were used to assess the impact of particles, colloids and organic matter. Unfiltered samples underwent sequential filtration. Three aliquots were filtered through 0.2 µm (F0.2; Whatman® Anodisc), and one of them was then filtered through 0.02 µm (F0.02; Whatman® Anotop®), while the last aliquot was filtered through 0.02 µm followed by 4h of UV-irradiation (F0.02+UV). All samples were left in the dark for 6 days to limit the effect of any photochemically generated reactive oxygen species (ROS) produced during the UV-irradiation (Yuan and Shiller, 2001; Roy et al., 2008). All samples were analyzed following the same procedure as for the assessment of the pH effect (see section 2.4.2 above). In order to assess whether the generated ROS species could affect the Fe(II) oxidation rate constants determined after 0.02 µm filtration and UV-irradiation, the effect of the amount of hydrogen peroxide (H_2O_2) generated during this process was considered when analyzing the samples (Yuan and Shiller, 2001; O'Sullivan et al., 2005). Other short-lived ROS species such as hydroxyl radicals were not accounted for, since their nanosecond half-life times do not allow for their determination using our analytical method.

3.4. Results

3.4.1. Temperature and pH effects on the oxidation rate constants

Experiments for the temperature effect study were carried out at a pH of 8. When plotting log *k'* vs. 1/T (K^{-1}) (Figure 3-2, Eq. 3-3), results showed an average slope ($-\Delta E_a/R/\ln(10)$) of -4992 ± 232. Notably, the data obtained from samples collected west of TAG at 2700 m depth (Station 30) showed a slope of -3732 ± 216, which is more than three standard deviations away from the average value. This lower slope corresponds to a much lower activation energy for this sample, with a value of 71 ± 4 KJ mol^{-1}. This effect was probably caused by the interaction of organic compounds or particles with the Fe(II) species which affected the limiting Fe(II) oxidation step, and therefore a result of a different oxidation reaction mechanism. If this sample is removed, the average slope increases to -5434 ± 183, and the activation energy of all the samples considered was 104 ± 3 KJ mol^{-1}. These values are within the experimental error of previous determinations from Gulf Stream water (-5362 ± 162, and an activation energy of 103 ± 3 KJ mol^{-1} ; Santana-Casiano et al., 2005).

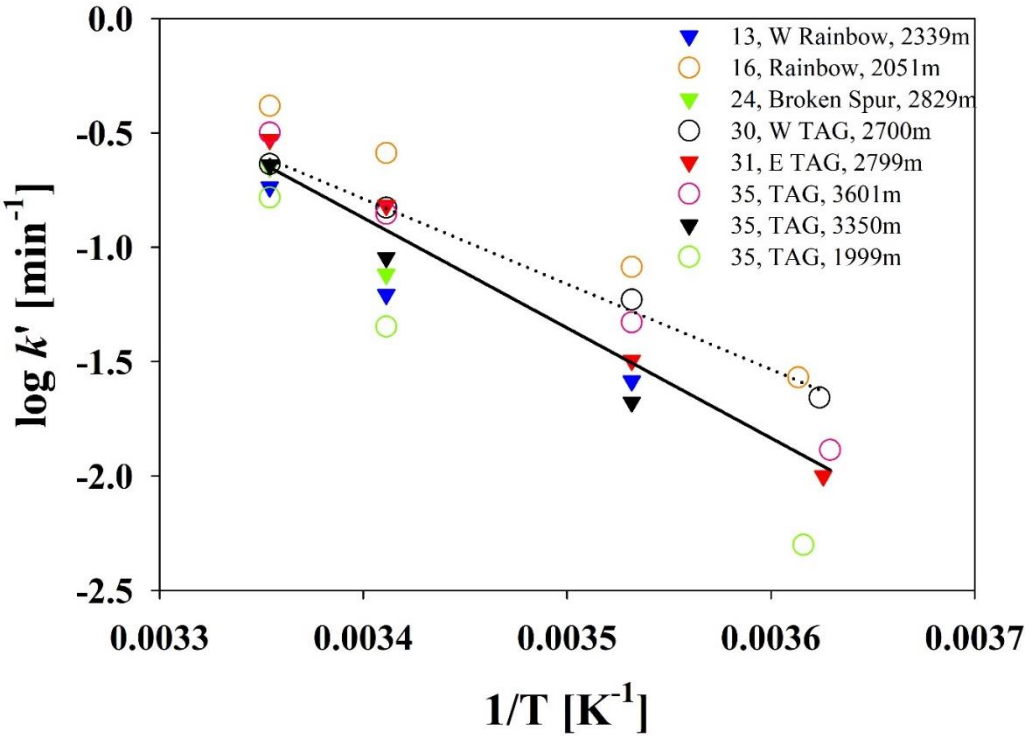

Figure 3-2. Arrhenius relationship between the oxidation rate constant (log k' (min^{-1})) and temperature (1/T (K^{-1})) in the range 2 to 25 ºC for eight selected samples. Note that the sample from station 30 (W TAG, 2700m, open squares, dotted line) shows a different behavior than samples from other stations.

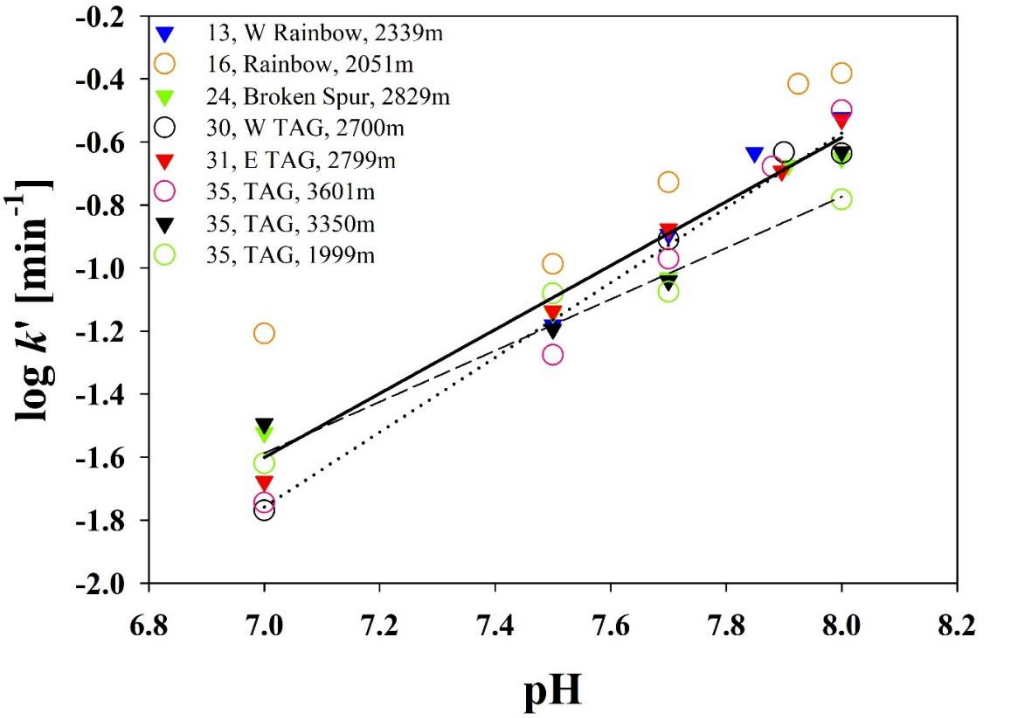

Figure 3-3. pH effect (from 7.0 to 8.0) on the Fe(II) oxidation rate constants (log k' (min^{-1})) for eight selected samples collected along the MAR . Note that the samples from 2700 m depth to the west of TAG (Stn 30, open squares) and from 1999 m depth at the TAG site (Stn 35, open diamonds) have different slopes than samples from other stations (data from these two stations are plotted with dotted lines).

When experiments were carried out at a constant T of 25 ºC and at 5 different pH values in the range from 7 to 8, log *k'* and pH were linearly related, with slopes of 1.00 ± 0.06 (Figure 3-3) and with no data points outside of 3 standard deviations. As with the temperature relationship, the sample from the station West of TAG at 2700 m presented a slope (1.19 ± 0.08) out of the 1:1 dependence. A second sample, (TAG at 1999 m depth, over 1600 m above the vent site) showed a lower slope (0.81 ± 0.12).

The use of colder samples in this study, allowed a better estimation of Fe(II) oxidation kinetic rate constants at temperatures lower than 10 ºC, increasing the range of applicability of the Fe(II) oxidation kinetics equation of Santana-Casiano et al. (2005). Using the equation and dataset from Santana-Casiano et al. (2005), which had a wider range in pH and salinity, together with the additional pH data and a wider range of temperature from the present study, a revised equation was obtained. The pH and salinity dependence did not change, while the T relationship was modified (Eq. 3-4). Thus, a more accurate calculation of theoretical Fe(II) oxidation for deep waters is presented:

$$\log k'(s^{-1}) = 35.627 - 6.7109 * pH + 0.5342 * pH^2 - 5434.02/T - 0.04406 * S^{1/2} - 0.002847 * S \quad (3\text{-}4)$$

	Millero et al. (1987)	**Santana-Casiano et al. (2005)**	**Santana-González et al. (2019)**	**González-Santana et al. (Eq. 3-4 of this chapter)**
RSS	0.019	0.003	0.006	0.002
RMSE	0.019	0.008	0.011	0.007
log(L)	24.2	33.6	32.5	36.7

Table 3-1. Statistical comparison of the available Fe(II) oxidation kinetics equations with the measured oxidation rate constants for deep ocean waters without including the hydrothermal neutrally buoyant plumes. Low residual sum of squares (RSS) and root mean square error (RMSE) indicate the best equation fit to observations. Greater than two points of difference in the difference in logarithms of the likelihood (Δlog(L)) presents a better fit.

The T factor has been modified from -5362.6/T to -5434.02/T obtained from the average slope of Figure 3-2. To assess the performance of the updated Fe(II) oxidation kinetic equation (Eq. 3-4), it was compared to three existing equations. The chosen equations were the first derived equation (Millero et al., 1987), the equation by Santana-Casiano et al. (2005), and a recent equation using Labrador Seawater (Santana-González et al., 2019). The four equations were

compared to the measured oxidation rate constants at *in situ* pH and T conditions. The residual sum of squares (RSS) and root mean square error (RMSE) between predicted and observed values were calculated. Smallest values of RSS and RMSE indicate the best equation fit to observations. Additionally, the difference in logarithms of the likelihood (Δlog(L)), based on a Gaussian error distribution with a constant variance of log-transformed data, was used to compare the equation performance (Armstrong et al., 2001 and references therein). The log(L) was calculated as in Moriceau et al. (2009), where a difference in log(L) of at least two points is considered as a criterion of a better fit to the observations. The three most recent equations present better RSS, RMSE and log(L), with the new equation presented here providing consistently better statistical results (Table 3-1).

3.4.2. Iron(II) oxidation rate constants throughout hydrothermal plumes along the MAR

Figures 3-4 and 3-5 present the half-life times of Fe(II) sampled at each hydrothermal site with Figure 3-5 summarizing the results using boxplots. The measured $t_{1/2}$ values presented a wider range than those determined using the physico-chemical parameters in the improved theoretical equation. The Lost City vent site, was the only station where all the measured $t_{1/2}$ at $T_{is}pH_{is}$ conditions presented measured oxidation rate constants higher (smaller $t_{1/2}$) than the theoretically calculated rates. At $T_{25}pH_8$ conditions, all the measured oxidation rate constants were higher than the theoretical ones for all stations except at TAG.

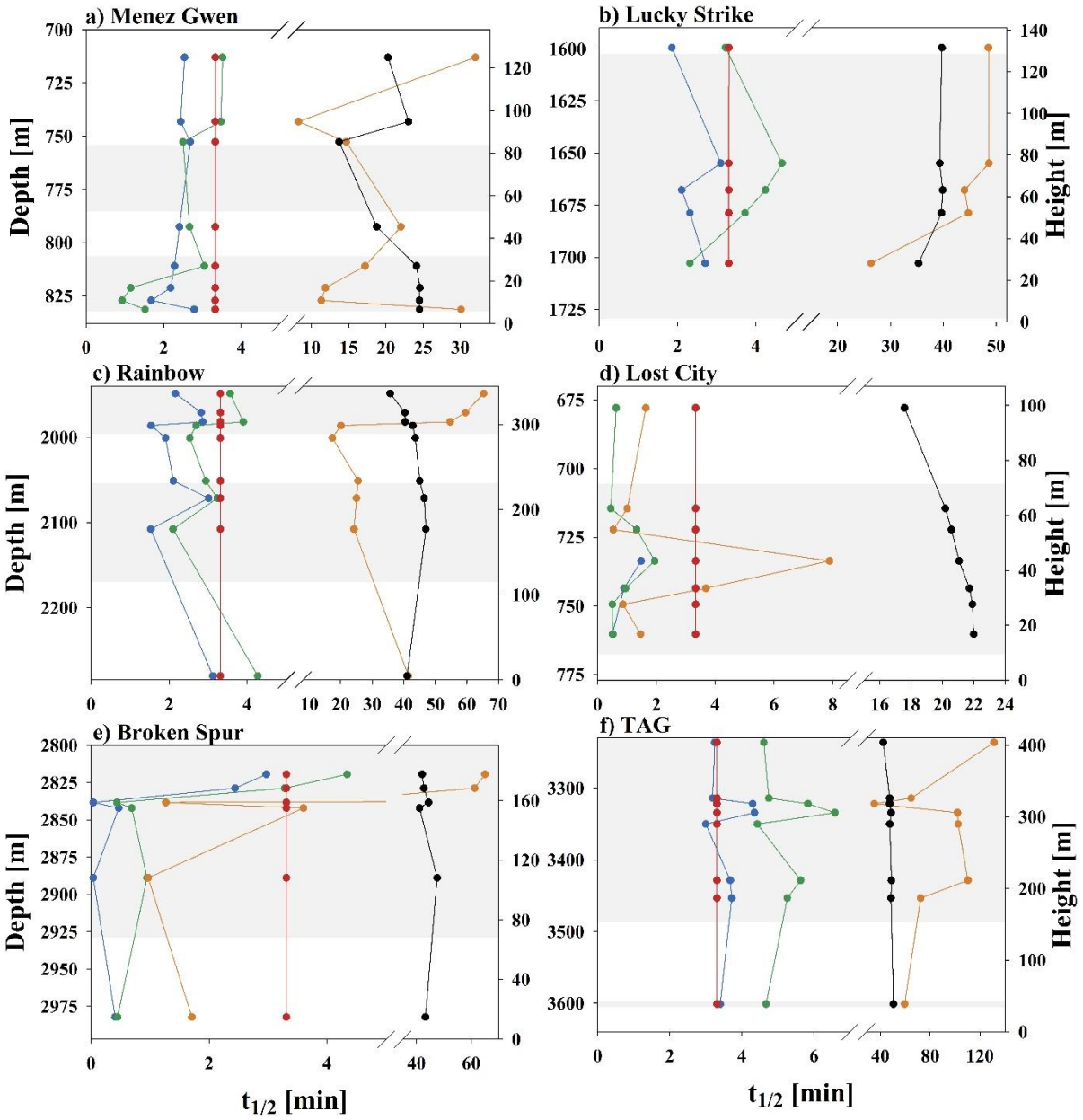

Figure 3-4. The measured Fe(II) half-life ($t_{1/2}$, min) at $T_{is}pH_{is}$ (orange), $T_{25}pH_{is}$ (green), and $T_{25}pH_{8}$ (blue), and the theoretical (Theo) values for $T_{is}pH_{is}$ (black), and $T_{25}pH_{8}$ (red), at the six vents . The shaded area shows the anomaly depths determined using light scattering data. Both, the depth (left y-axis) and the height above the seafloor (right y-axis) of the sampling are indicated.

The theoretical $t_{1/2}$ values presented in Figure 3-5a, show the expected high variability in the Fe(II) half-life times associated with T, pH and S. These discrepancies were further highlighted in the measured samples, where only Menez Gwen and Lucky Strike theoretical values are within the measured results (a paired t-test did not show a statistical difference between the theoretical and the measured $t_{1/2}$, with $P > 0.35$ for both).

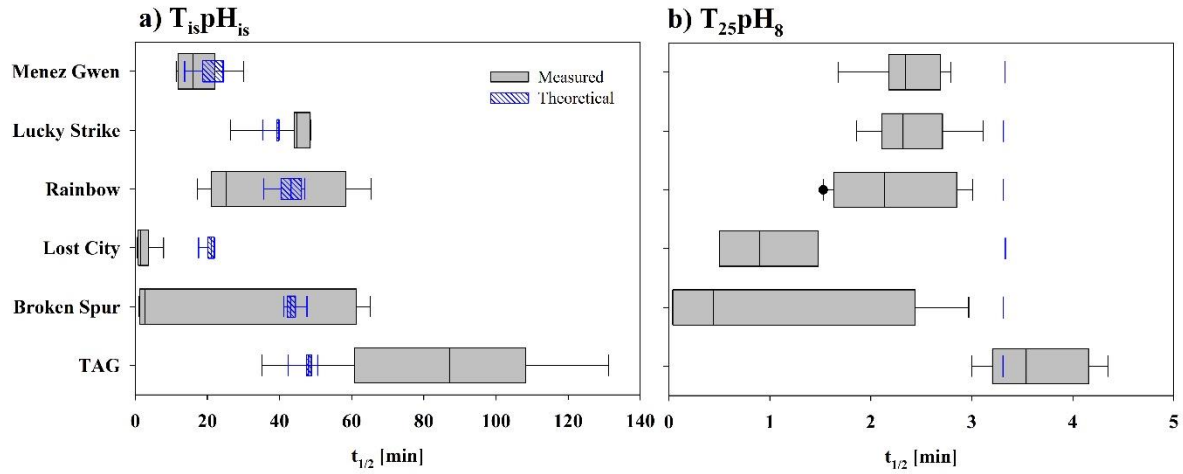

Figure 3-5. Boxplots of the Fe(II) half-life ($t_{1/2}$, min) within the six hydrothermal plumes . a) The measured $t_{1/2}$ at *in situ* conditions (grey) and the theoretical $t_{1/2}$ (blue; obtained using Eq. 3-4). b) The measured $t_{1/2}$ at constant temperature (25 ºC) and pH 8 (grey) and the corresponding theoretical $t_{1/2}$, the slight variances are caused by S changes (blue).

At Menez Gwen (Figure 3-4 a), measured *in situ* $t_{1/2}$ varied between 8.3 and 32.0 min (*k'* between 0.084 and 0.022 min^{-1}), with the fastest measured $t_{1/2}$ observed in the samples collected at 743, 821, and 827 m. When the temperature was increased and fixed to 25 ºC, while the pH was kept at *in situ* conditions (Supplementary Table S1), a significant T effect was observed in *k'*, with the measured $t_{1/2}$ decreasing to less than 4 min. When the pH was fixed to a constant value of 8 along the water column, the measured $t_{1/2}$ was slightly affected indicating a small effect, as the change in pH was always lower than 0.22. Overall, at T_{25}, samples presented measured $t_{1/2}$ in the same order of magnitude as the theoretical T_{25} pH_8. Samples collected within the lower part of the plume, at less than 30 m above the seafloor (hereafter *asf*) presented higher oxidation rate constants than theoretical ones ($t_{1/2}$ decreased).

Lucky Strike (Figure 3-5a) presented lower oxidation rate constants than Menez Gwen related to lower temperatures in deeper waters (from about 8.5 ºC to 4.5 ºC). From 1600 m to 1680 m, measured $t_{1/2}$ averaged 46.5 ± 2.5 min (*k'* of 0.015 ± 0.001 min^{-1}, n = 4) (Figure 3-4 b). This $t_{1/2}$ average is higher than the theoretical value of 39.7 min, while at 1703 m, the Fe(II) half-life decreased to 26.3 min (*k'* to 0.026 min^{-1}). Overall, at T_{25}, samples presented measured $t_{1/2}$ in the same order of magnitude as the theoretical T_{25} pH_8. *In situ* pH averaged 7.89, where the increase in acidity produced a lower oxidation rate constant than the measured $t_{1/2}$ at T_{25} pH_8.

At Rainbow, station 16, the $t_{1/2}$ measured at *in situ* conditions presented a wide range of variation, from 17.3 to 65.3 min (*k'* varied from 0.040 min^{-1} to 0.011 min^{-1}). The theoretically

expected values were within that range, with an average value of 39 ± 3 min (n=8, Figure 3-4 c). The shortest half-life times were observed between 1986 m and 2108 m (175 to 295 m *asf*) averaging 22.2 ± 3.6 min (*k'* = 0.032 ± 0.006 min^{-1}) while the slowest half-life times were found below the plume and above 300 m *asf* (Figure 3-4 c). The light scattering data shows that the Rainbow plume reached heights over 400 m *asf* (although samples were only collected within the first 330 m). Temperature was an important factor controlling the oxidation rate constant, with values at T_{25} conditions presenting rate constants similar to the theoretical value. When the pH was fixed to 8, small changes were observed, and most of the values were close to the theoretical value except for those around 1986 m and 2108 m which were lower (faster oxidation).

Lost City (Figure 3-4 d), the only alkaline hydrothermal vent, was drastically different from the other hydrothermal sites (Figure 3-4 d), with temperatures around 10 ºC and pH_{is} of 8.07 (Supplementary Table S1). The theoretical $t_{1/2}$ associated with these temperatures and pH ranged between 16 and 20 min. However, most of the measured $t_{1/2}$ were shorter than 3 min, reaching 0.5 min (*k'* = 1.299 min^{-1}) at 725 m with the shortest $t_{1/2}$ of 7.8 min (*k'* of 0.088 min^{-1}) at 750 m. At 750 m depth with $T_{25}pH_{is}$ conditions, the $t_{1/2}$ decreased to 1.9 min (*k'* of 0.357 min^{-1}) and further decreased to 1.5 min (*k'* of 0.468 min^{-1}) at $T_{25}pH_8$ conditions. All the measured $t_{1/2}$ were significantly shorter than the theoretical $t_{1/2}$ of 3.2 min (*k'* = 0.218 min^{-1}) at normalized conditions.

Broken Spur presented the widest range in measured $t_{1/2}$, with values under *in situ* conditions ranging from 1.0 to 65.1 min (*k'* ranging from 0.714 min^{-1} at 2929 m to 0.011 min^{-1} at 2858 m; Figure 3-4 e). Two different behaviors can be observed. The two shallowest samples (2820 and 2830 m) were collected in local light scattering minima, with $t_{1/2}$ averaging 63.2 ± 2.7 min (*k'* of 0.011 ± 0.001 min^{-1}) and values slightly higher than the theoretical ones. Deeper than 2830 m, the samples were collected in local light scattering maxima, where half-life times were shorter with an average $t_{1/2}$ of 1.9 ± 1.2 min (averaged *k'* of 0.464 ± 0.220 min^{-1}). Experiments at $T_{25}pH_8$ also showed that samples below 2830 m presented shorter $t_{1/2}$ (faster *k'*) than what was theoretically expected.

Half-life times measured at *in situ* conditions from the TAG vent site samples presented the widest range in $t_{1/2}$ (Figures. 3-4 and 3-5 a), varying from 35.1 to 131.2 min (k' between 0.019 min^{-1} and 0.005 min^{-1}). These samples were characterized by little variability of T_{is} (2.67 ± 0.01 ºC) and pH_{is} (8.17 ± 0.01), producing a stable theoretical $t_{1/2}$ of 43 ± 2 min. Furthermore,

the measured $t_{1/2}$ were the longest obtained in these experiments. When the experiments were repeated at both fixed T_{25} and pH_8 the measured values encompassed the theoretical value of 3.3 min, with values slightly higher at around 3325 m (4.3-4.4 min). Therefore, even when temperature and pH affected the observed oxidation rate constants, the high range of values at *in situ* conditions could not be explained by only these two physico-chemical variables.

3.4.3. Investigating the spatial variability of Fe(II) oxidation rate constants around Rainbow and TAG sites

To investigate the spatial variability in $t_{1/2}$ for Fe(II), samples were collected from four stations around the Rainbow site at 0.3º (30 km) S (Stn 15), E (Stn 12) and W (Stn 13) and 1º (120 km) E (Stn 10) (Figure 3-1) and from five stations around TAG at 0.3º N (Stn 26), S (Stn 27), W (Stn 30), and E (Stn 31) and 1º W (Stn 29) (Figure 3-1). At both vent sites, turbidity and light scattering anomalies matched and described the shape of the plume (gray shading in Figure 3-4). The Rainbow plume anomaly was observed between 1930-1995 m, 2060-2090 m, and most strongly between 2100 and 2210 m. At the TAG site, the signal was three times lower than that observed at Rainbow, indicating the presence of a lower amount of particles, which could also be due to a displacement of the sampling with respect to the vent site. The largest anomalies were measured between 3160-3390 m, with several minor anomalies above (e.g. 2980-3030 m) and below (e.g. 3430-3520 m and 3600-3625 m; Figure 3-4).

Turbidity and light scattering were useful for tracking the plume displacement even at 30 km from the vent site. The Rainbow plume was observed to the south and west (Stn. 13 and 15) at depths between 2000 and 2040 m, and 2270 and 2300 m. For TAG, only stations 27 (south of TAG, but inside the MAR valley) and 31 (east) showed deeper and thinner turbidity anomalies between 3400 and 3690 m and a smaller signal between 2920 and 3060 m.

For the Rainbow field, samples collected at the vent site in the 1980-2150 m range had shorter $t_{1/2}$ at *in situ* conditions (faster *k'*) than the theoretical $t_{1/2}$ (Figure 3-6 a). All the other samples (except for Stn 10 at 2430 m) had higher $t_{1/2}$ values than those calculated theoretically, and greater $t_{1/2}$ than what was observed at Rainbow at depths shallower than 1980 m, indicating very low oxidation rate constants. This allowed Fe(II) to stay in solution three times longer than under inorganic seawater conditions. However, when T and pH were fixed (Figure 3-6 b), the oxidation rate constants between stations were much closer to the theoretical value, indicating the T and pH control over the Fe(II) oxidation rate constant. Nevertheless, plume

samples at the 2100-2210 m range and around 2400 m indicated $t_{1/2}$ values that were still at least double the theoretical value.

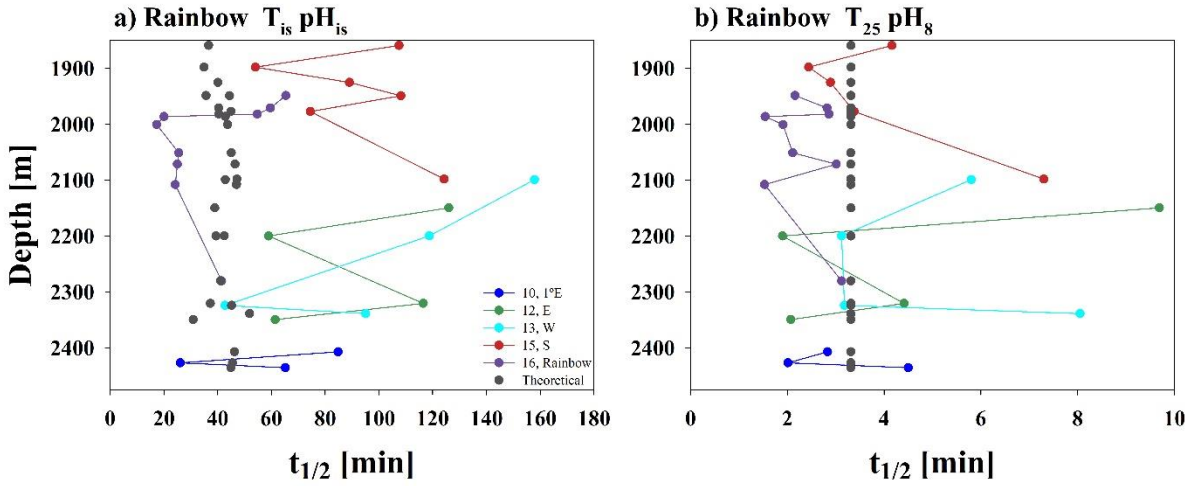

Figure 3-6. The Fe(II) half-life ($t_{1/2}$, min) at the Rainbow field a) under *in situ* conditions and b) normalized to constant T of 25 ºC and a pH of 8.

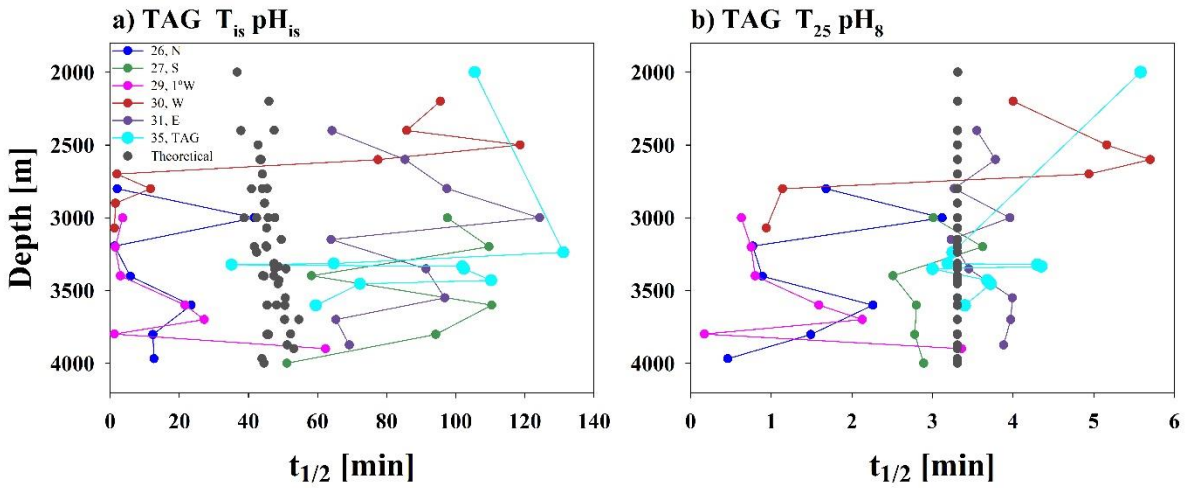

Figure 3-7. The Fe(II) half-life ($t_{1/2}$, min) at the TAG field a) under *in situ* conditions (see also Supplementary Table S1) and b) normalized to constant T of 25 ºC and a pH of 8.

At the TAG hydrothermal field, stations situated towards the N and W of TAG presented shorter $t_{1/2}$ (faster *k'*) than those at the vent site and towards the S and E (Figure 3-7 a). Station 30, situated 30 km W of TAG, exhibited both patterns, with long $t_{1/2}$ (slow rates) at depths shallower than 2600 m and short $t_{1/2}$ (fast rates) at depths below 2700 m. When all the TAG hydrothermal field station samples were normalized (i.e. $T_{25}pH_8$; Figure 3-7 b), most of the variability were removed, and $t_{1/2}$ averaged 3 ± 1.5 min. The same pattern as for *in situ* conditions were maintained, with stations situated towards the N and W having shorter $t_{1/2}$ than

the theoretical values. These three stations were characterized by their lower turbidity in the deep waters.

3.4.4. The effect of particles, colloids, and organic matter on the oxidation rate constant

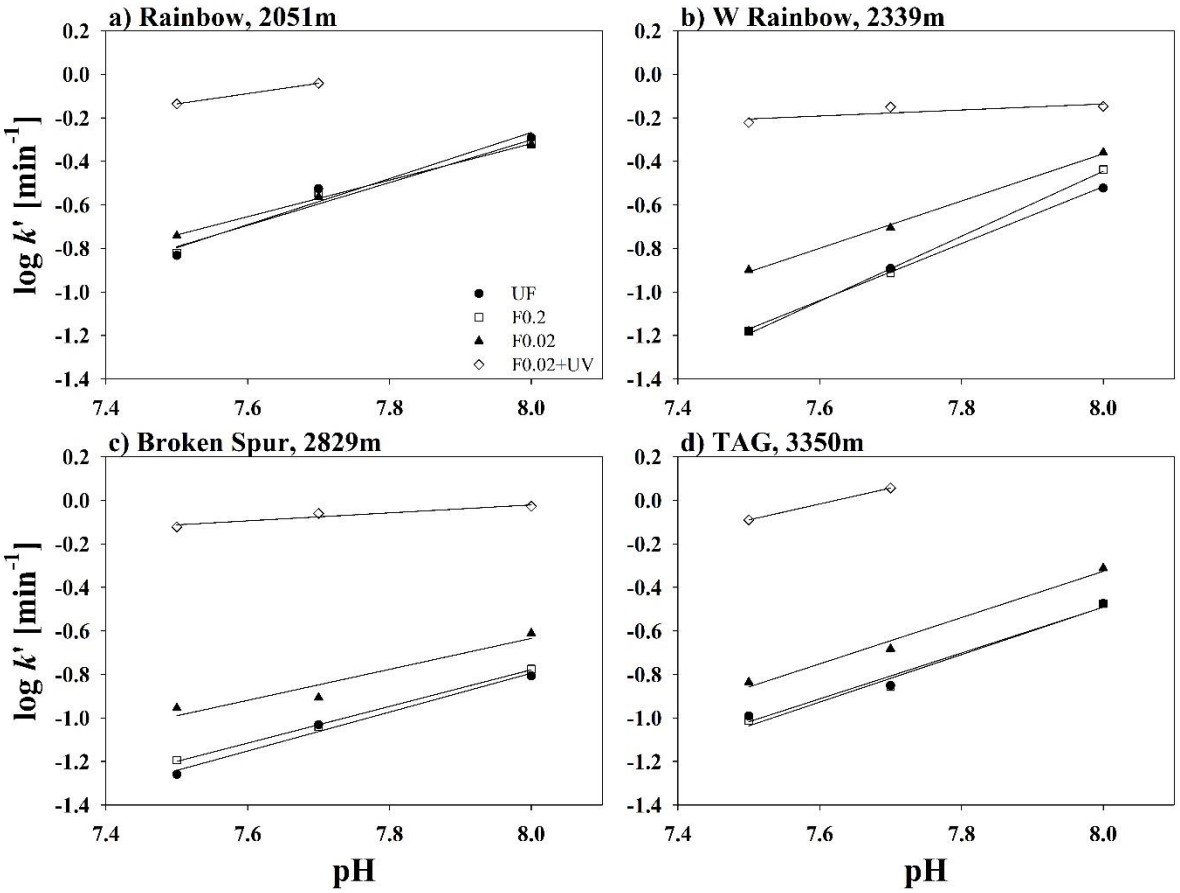

Figure 3-8. Oxidation rate constants at different pH (7.5, 7.7 and 8), for selected unfiltered (UF, filled circles), filtered through 0.2 µm (F0.2, open squares), filtered through 0.02 µm (F0.02, filled triangles) and filtered through 0.02 µm followed by UV irradiation (F0.02+UV, open diamonds) samples at a) Rainbow (Stn 16, 2051 m), b) West of Rainbow (Stn 13, 2339 m), c) Broken Spur (Stn 24, 2829 m) and d) TAG (Stn 35, 3350 m).

Experiments with samples from Rainbow (Stn 16, 2051 m), West of Rainbow (Stn 13, 2339 m), Broken Spur (Stn 24, 2829 m) and TAG (Stn 35, 3350 m) were performed to improve our understanding of the impact of particulate and organic matter on the oxidation kinetics of hydrothermal vent fluids. The Rainbow sample at 2051 m, located outside the plume, did not show any difference in the log(*k'*) due to the presence of particulates, with values at each pH unit varying by ± 0.03 and an average slope of log(*k'*) against pH of 0.96 ± 0.07 for UF, F0.2 and F0.02 treatments (Figure 3-8). For the other three samples (Figure 3-8 b to d), oxidation

rate constants for UF and F0.2 did not present significant differences, with values that were reproducible within ±0.02 for the studied pH range. However, F0.02 samples had higher oxidation rate constants, while also maintaining the pH dependence (0.95 ± 0.07). Therefore, the presence of colloidal size particles delayed the oxidation process while not affecting the pH dependence, as shown in Figure 3-8, where the intercept changes but the slope is unchanged. All of the UV irradiated samples in Figures 3-8 a to d indicate that the absence of dissolved organic matter increased the oxidation rate constants. For TAG (3350 m) and Rainbow (2051 m), the rates were so fast that it was impossible to determine them at pH = 8 under our experimental conditions.

3.5. Discussion

3.5.1. Derived oxidation rate constants as a function of pH and temperature

In the 1990s, Fe(II) oxidation kinetics variability was reported at the TAG hydrothermal field (2-3 min) (Rudnicki and Elderfield, 1993) and near the Juan de Fuca Ridge hydrothermal systems (32 h) (Chin et al., 1994; Massoth et al., 1994) using the Millero et al. (1987) equation. Nevertheless, the variability between those two sites was difficult to explain and reflected fluctuations caused by O_2, T, and pH among the different sites.

When combining the six hydrothermal vent sites on the MAR (Figure 3-9), the relationship between the measured oxidation rate constants under *in situ* conditions against the theoretically derived oxidation rate constants as a function of pH and temperature (in aerated water) can be obtained. Overall, equation 3-4 can explain 76 out of 104 data points. When color-coding the data points by stations, we observed that all the outliers corresponded to samples that were collected inside hydrothermal plumes (defined by turbidity, light scatter, and redox potential). Consequently, the results obtained from the theoretical equation (Eq. 3-4) and Figure 3-9, agree well with previous results that O_2, S, T, and pH can be used to characterize the Fe(II) oxidation rate constant in open ocean waters but not from within hydrothermal plumes.

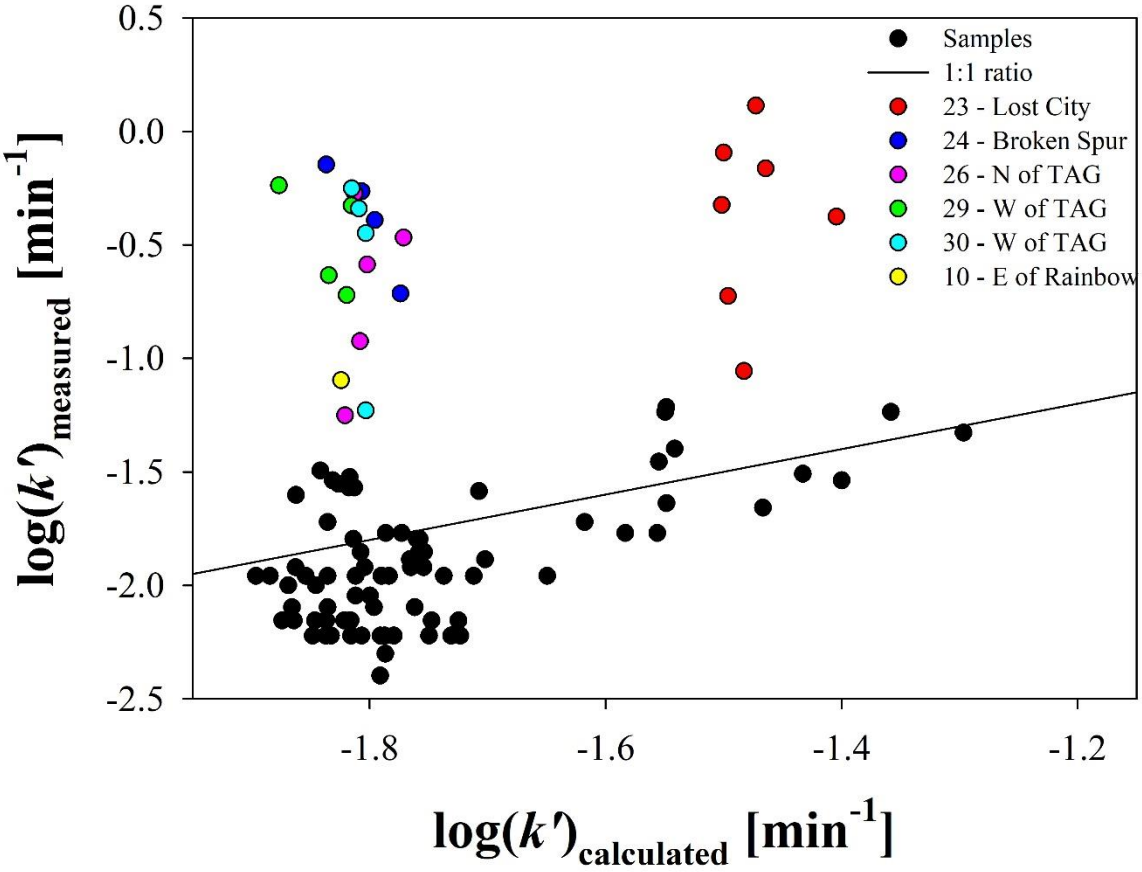

Figure 3-9. Iron (II) oxidation rate constants (log(k')) determined under *in situ* conditions against the anticipated expected theoretical value . All data points are shown in black. The black line represents a 1:1 ratio between both oxidation rate constants. Color coded data points correspond to samples with measured oxidation rate constants greater than 20% of the theoretically derived rate constants.

Our study clearly indicates (Figures 3-8 and 3-9) that the presence of both colloidal particles and dissolved organic matter increases the half-life of Fe(II) (decreased *k'*). This agrees with previous work showing a decrease in the Fe(II) oxidation rate constants in seawater in the presence of some natural organic compounds (Santana-González et al., 2019). However, organic matter can have a positive or negative effect on the oxidation rate constants of Fe(II) depending on the type of organic matter and its degree of remineralization (Rose and Waite, 2003a). The variability in the effect of total organic carbon on Fe(II) oxidation proves that total organic carbon cannot be used as a variable in an equation describing *k'* (Santana-Casiano et al., 2000; Santana-González et al., 2018, 2019). In this sense, a more detailed characterization of organic matter would be necessary, especially in a hydrothermal environment.

3.5.2. Influence of organic species on Fe(II) oxidation rate constants

The Fe(II) oxidation rate constant (Eq. 3-5) can be expressed as a function of each Fe(II) species (Fe^{2+}, $FeOH^{+}$, $Fe(OH)_2$, $FeHCO_3^{+}$, $Fe(CO_3)$, $Fe(CO_3)_2^{2-}$, $Fe(CO_3)OH^{-}$, $FeCl^{+}$, $FeSO_4$, FeH_3SiO_4 and any organically complexed Fe species). Species such as $Fe(CO_3)_2^{2-}$ and $Fe(OH)_2$ could become important at pH higher than 8 (Ussher et al., 2004; González-Davila et al., 2005; Santana-Casiano et al., 2005) in solution. Considering the side reaction coefficient for each inorganic (α_i) and organic (α_j) Fe(II) species in seawater and the associated second-order oxidation rate constant for the kinetically reactive Fe(II) species (k_i and k_j) (Eq. 3-6) (Millero and Sotolongo, 1989; King, 1998; Santana-Casiano et al., 2005), the apparent oxidation rate constant can be expressed as:

$$k_{\text{app}} = k_{Fe^{2+}}\alpha_{Fe^{2+}} + k_{FeOH^{+}}\alpha_{FeOH^{+}} + k_{Fe(OH)_2}\alpha_{Fe(OH)_2} + k_{FeHCO_3^{+}}\alpha_{FeHCO_3^{+}} + k_{Fe(CO_3)}\alpha_{Fe(CO_3)} + k_{Fe(CO_3)_2^{2-}}\alpha_{Fe(CO_3)_2^{2-}} + k_{Fe(CO_3)OH^{-}}\alpha_{Fe(CO_3)OH^{-}} + k_{FeCl^{+}}\alpha_{FeCl^{+}} + k_{FeSO_4}\alpha_{FeSO_4} + k_{FeH_3SiO_4}\alpha_{FeH_3SiO_4} + \sum_i k_{FeL_j}\alpha_{FeL_j} \quad (3\text{-}5)$$

$$k_{\text{app}} = \sum_i \alpha_i k_i + \sum_j \alpha_j k_j \quad (3\text{-}6)$$

$$\alpha_{Fe^{2+}} = 1/\left(1 + \sum K_{L_i}[L_i] + \sum K_{L_j}[L_j]\right) \quad (3\text{-}7)$$

Where $\alpha_{Fe^{2+}}$ is the fraction of free Fe(II) including inorganic and organic speciation, $[L_i]$ is the concentration of each inorganic ligand with a conditional stability constant K_i and $[L_j]$ is the concentration of each organic ligand with a conditional stability constant K_{Lj}. The inorganic site reaction coefficient at pH 8 and 25 ºC was previously determined as 0.38 (Santana-Casiano et al., 2006). For any inorganic or organic FeL complexes:

$$\alpha_{FeL} = K_{FeL}[L]\alpha_{Fe^{2+}} \quad (3\text{-}8)$$

According to our results, the presence of DOM in solution generated Fe(II)-organic complexes that were overall less reactive to oxidation and therefore, when removed by UV irradiation the resulting oxidation rate constants were higher (Figure 3-8).

The amount of dissolved organic carbon (DOC) in the samples ranged between 50 and 79 µmol kg^{-1} (data not shown) and according to O'Sullivan et al. (2005) the maximum amount of H_2O_2 produced during irradiation could be 125 to 147 nmol kg^{-1}, respectively. Following González-Davila et al. (2005) and assuming the extreme case of no H_2O_2 decay after 6 days, the UV generated H_2O_2 could theoretically accelerate the Fe(II) oxidation rates in oxygen saturated

conditions. The theoretical $t_{1/2}$ associated with the H_2O_2 oxidation was between 48 % and 53 % of the $t_{1/2}$ measured for 0.02 μm filtered samples. Nevertheless, the measured $t_{1/2}$ for UV-irradiated samples (Supplementary Table S1 and Figure 3-8) were shorter (higher *k'*), indicating that any H_2O_2 remaining in solution after 6 days was not the main factor that increased the oxidation rate constants and that the presence of dissolved organic matter was stabilizing Fe(II) in solution. Furthermore, laboratory experiments have shown that the $t_{1/2}$ of H_2O_2 in oceanic waters is shorter than 5.5 days (Yuan and Shiller, 2001), therefore the impact of H_2O_2 in the experiments would be further reduced.

The role of organically complexed Fe(II) could be calculated from the following assumptions. Firstly, the Fe(II)-L complex was assumed to not oxidize in the pH range of 7.5 to 8. Secondly, the observed increase in Fe(II) oxidation rate constants (Figure 3-8 and Supplementary Table S1) at 25 ºC between the 0.02 μm filtered and the filtered and UV irradiated samples was due to organic complexation. The computed role of organic complexation produced a 78 ± 6% decrease in the concentration of reactive inorganic Fe(II) species. The effect of organic Fe(II) species was highest at Broken Spur and TAG sites (81 ± 5 %) and lowest at Rainbow (74.1 ± 4 %). Roy et al. (2008) found a value that was slightly lower for the western subarctic Pacific water, with a 61 ± 8% decrease. As both the organic ligand concentrations and the conditional constants are unknown, only the product $K_{Lj} \cdot [L_j]$ (Eq. 3-7) can be inferred. Knowing the inorganic distribution coefficient of Fe(II), which is pH dependent but can be calculated from Santana-Casiano et al., (2005), and considering a unique class of ligand (L), the product $K_{Lj} \cdot [L_j]$ should be 9 ± 2 (higher values at Broken Spur and TAG, while lower values at Rainbow) while $1 + \sum K_{L_i}[L_i]$ in Eq. 3-7 is 2.6 (2.6 = 1/0.38, Santana-Casiano et al., (2006)).

If the concentration of Fe(II) organic ligands in seawater is on the same order as Fe(III) ligands (1 to 10 nmol L^{-1}), as assumed by Roy et al. (2008), the corresponding conditional constant should range between 10^9 to 10^{10}, (respectively for 10 and 1 nmol L^{-1} of ligands). The strength of these Fe(II) complexing ligands compared to those for Fe(III) is in the low affinity range (Gledhill and Buck, 2012; Bundy et al., 2014). However, the formation of these complexes would decrease the Fe(II) oxidation rate constant through both the effects on the side reaction coefficients (Eqs. 7-8) and because the complexes can be non-reactive to oxidation or oxidize slower than any other inorganic species. Moreover, it should be considered that organic matter could also increase the Fe(II) $t_{1/2}$ due to the reduction of organically complexed Fe(III), which would increase the Fe(II) in solution, and therefore the $t_{1/2}$ (Santana-Casiano et al., 2010).

The UV-irradiation treatment (Figure 3-8) removes the organic matter effect on the Fe-complexation, which for the studied samples resulted in an increase in the oxidation rate constants. Consequently, in these analyzed natural samples, organic matter lowered the oxidation rate constants (black data points below the straight line in Figure 3-9).

The DOM is prone to natural and thermal degradation in hydrothermal systems (Hawkes et al., 2016). Accordingly, the variety of organic-complexing ligands and their effect on oxidation could change with plume transport and distance to the vent site as observed in figures 3-6 and 3-7. In the proximities to the vent sites, samples presented greater than theoretical oxidation rate constants (above the straight line in Figure 3-9). This could be due to the presence of organic matter with ligands complexing Fe that oxidizes faster than the inorganic Fe(II) species. At these locations, the organic ligand effect would dominate over processes that lower oxidation rate constants such as nanoparticle concentrations. Similar experiments considering organic matter degradation just above the vent site should be carried out to confirm this hypothesis. Nevertheless, the complexity of the organic matter pool and the extent and nature of Fe-DOM interactions make the resulting effect on the oxidation rate constants difficult to predict.

3.5.3. Effects of physical speciation

Lough et al. (2019b) have shown that there is an Fe exchange between the different particle size fractions within the hydrothermal plume. This exchange could affect Fe(II) oxidation as found in this study for particles smaller than 0.2 µm and colloidal sized particles (0.2-0.02 µm) at different locations in TAG and in Rainbow (Figure 3-8). The results shown in Figure 3-8 seem to indicate that the size-fractionation can significantly affect Fe(II) oxidation and thus, is a factor that should be considered in future studies. In this sense, previous work has shown that particulate Fe(II), such as pyrite nanoparticles are more resistant to oxidation, with Fe(II) half-life between 4 and 48 months at 2 ˚C (Yücel et al., 2011). The presence of colloidal particles also enhances the decay of ROS allowing for longer Fe(II) permanence (Yuan and Shiller, 2001). Therefore, nanoparticles could account for a substantial fraction of the decrease in the oxidation rate constants (Figure 3-8). Another consequence of filtration is the reduction in larger size organic matter, which could also affect the stabilization of Fe(II) (Buck et al., 2015).

The variability observed in the oxidation rate constants inside the plume for the six studied hydrothermal vents indicates that changes in the composition of both the DOM and colloidal

particles, both between sites and at different distances from the vent, can strongly affect the oxidation rate constants, thus, their role requires further study.

3.6. Conclusions

This study highlights the complexity of Fe(II) chemistry in the ocean, with a focus on hydrothermal vent settings. Fe(II) oxidation rate constants, and therefore persistence in the environment, is shown to not only depend on the physico-chemical conditions (T, S, pH, O_2 content) but also the physical state (soluble, colloidal and particulate) of the inorganic and organic species that are present. Our results indicate that organic ligands can stabilize Fe(II) and that nanoparticles present in hydrothermal plumes could increase the resistance to oxidation. Both processes contribute to the observed variability in the oxidation rate constants in the proximities of vents. We were able to revise the theoretical equation for the estimation of k', and to further increase the existing temperature range to include seawater temperatures as low as 2 ºC. Future studies on iron oxidation kinetics in the marine environment should be accompanied by a characterization of the organic matter present in the medium, a size-fractionation of the samples, and a detailed description of the conventional physico-chemical factors (pH, T, and S).

3.7. Author contributions

DGS wrote the manuscript with significant contributions from all coauthors. DGS was invited to the research cruise by MCL, where DGS, MCL, and LA collected the samples. DGS analyzed the samples with support from MSC and MGD. Figures for the results were designed by HP and GS. Cruise related costs were managed by MCL and AT, while analysis costs were handled by MSC, MGD, GS, and HP.

3.8. Acknowledgements

The authors would like to thank the captain and crew of the R.R.S. James Cook as well as the scientific team during the GA13 cruise. The field work was supported by NERC (NE/N010396/1 and NE/N009525/1). This work was supported by ISblue project, Interdisciplinary graduate school for the blue planet (ANR-17-EURE-0015) and co-funded by

a grant from the French government under the program "Investissements d'Avenir". Lab work was supported by the ATOPFe CTM2017-83476-P project (Spanish Ministry of Economy and Competitiveness) awarded to MSC and MGD.

4. Dissolved iron (II) variability in the Mid Atlantic Ridge: GEOTRACES GA13

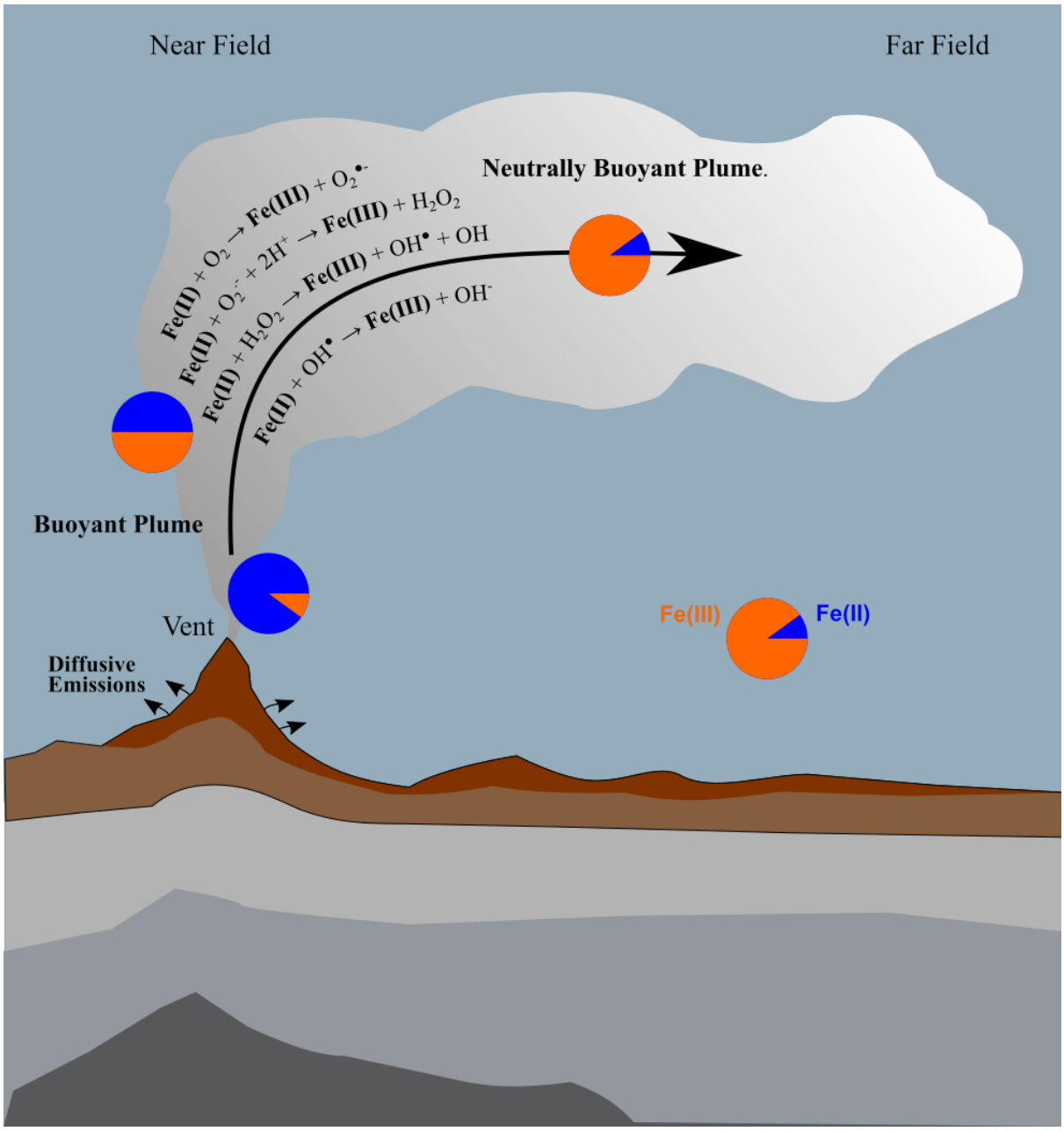

Graphical abstract of chapter 4. Hot and acidic hydrothermal sites are sources of reduced species. Iron is sourced as ferrous iron (Fe(II)) which oxidizes to ferric iron (Fe(III)) as the hydrothermal fluid mixes with the surrounding oxic seawater. Iron (II) concentrations vary both among hydrothermal vent sites and within each hydrothermal plume.

This chapter follows the same structure as a standard scientific manuscript (Introduction, Materials and Methods, Results and Discussion). It is so far focused on Fe(II) concentrations but, before submission, we will include other parameters, such as ORP data in collaboration with J. Resing.

David González-Santana[1*], Alastair J. M. Lough[2], Hélène Planquette[1], Géraldine Sarthou[1], Alessandro Tagliabue[3], Joseph A. Resing[4], and M. C. Lohan[2])

[1]Univ Brest, CNRS, IRD, Ifremer, LEMAR, F-29280 Plouzane, France.

[2]Ocean and Earth Science, University of Southampton, National Oceanography Centre, Southampton, SO14 3ZH, United Kingdom.

[3]School of Environmental Sciences, University of Liverpool, Liverpool, United Kingdom.

[4]Joint Institute for the Study of the Atmosphere and the Ocean, University of Washington and NOAA-PMEL, 7600 Sand Point Way NE, Seattle, WA 98115, USA

4.1. Abstract

Hydrothermal vent sites found ubiquitously throughout the mid-ocean ridges are sources of numerous reduced species and trace elements. In this manuscript, we determined the ferrous iron (Fe(II)) concentrations above six hydrothermal vent sites situated along the Mid Atlantic Ridge between 39.5°N and 26°N. To establish dissolved Fe(II) (dFe(II)) concentration variability in the ridge, dFe(II) was measured above Menez Gwen, Lucky Strike, Rainbow, Lost City, Broken Spur, TAG and non-hydrothermally affected stations. The dFe(II) concentrations ranged from less than 0.1 nmol L^{-1} in non-hydrothermally affected regions to values as high as 69.6 nmol L^{-1} in areas with hydrothermal activity. We used a multiparametric equation to estimate the original Fe(II) concentration at each site. Theoretical dFe(II) concentrations in the ocean were calculated considering their fast oxidation rate which are on average three times faster than the time required to transport the sample from the deep ocean to its analysis. The theoretical concentrations calculated considering the temperature, pH, salinity and time show that Fe(II) plays a more significant role than previously accounted for. This discrepancy is caused by a Fe(II) loss during sampling, where between 35 and 90% of the original dFe(II) gets oxidised by the time samples are analysed. Furthermore, in this section of the North Atlantic, variations in dissolved oxygen concentrations can account for a 60% faster Fe(II) oxidation rate, further reducing the measurable dFe(II). Consequently, dFe(II) concentrations constitute a fraction greater than 20% of the dissolved iron pool, in contrast to the previously reported less than 10%.

4.2. Introduction

Life developed before the Great Oxidation Event, approximately 2.4 billion years ago (Lyons et al., 2014), in an anoxic ocean, where anoxygenic photosynthesis with ferrous iron (Fe(II)) as the electron donor is thought to be the earliest type of photosynthetic process (Des Marais, 2000; Xiong et al., 2000). The biological significance of iron (Fe) is based upon its past availability and its redox capabilities, with Fe(II) and ferric iron (Fe(III)) operating as electron acceptors or donors, respectively, for different dissimilatory processes (e.g. Straub et al., 2001, 2004). Therefore, due to Fe availability and its redox state during the origin of life, Fe(II) is still required in diverse metabolic pathways (Raven et al., 1999).

In the current oxic seawater the reduced ferrous Fe (Fe(II)) is thermodynamically unstable (Millero et al., 1987; Santana-Casiano et al., 2006) and rapidly oxidises to its more stable redox

state Fe(III). The Fe(II) oxidation rate depends on the physical and chemical properties of seawater. The Fe(II) oxidation takes place in a period of minutes to hours forming iron oxyhydroxides with low solubility, a process depending primarily on pH and temperature of the seawater (Liu & Millero, 2002; Millero et al., 1987; Santana-Casiano et al., 2005). The immediate products of the initially soluble Fe(II) are oxidised colloidal sized (0.02 to 0.2 μm diameter) particles (Massoth et al., 1998). As such, the primary production of phytoplankton in 30–40% of the world's oceans is limited by Fe (Martin and Fitzwater, 1988) that prefer soluble iron (Shaked et al., 2005; Morel et al., 2008).

Hydrothermal vents are recognized as the most significant source of Fe to the deep ocean and act as reducing environments, delivering Fe in its reduced form. Considering that the ocean covers 70% of the Earth's surface, vent systems only make up a tiny percentage of the areal extent of the seafloor. Nevertheless, they emit substantial quantities of Fe and sulfur minerals with current estimates for Fe-release being on the order of 9×10^{8} mol yr^{-1} (Tagliabue et al., 2010). Furthermore, these Fe-rich plumes can be transported for thousands of kilometres, acting as basin-scale sources of Fe (Resing et al., 2015; Fitzsimmons et al., 2017). Within the plume Fe size fractions are modified and can be seen as free forms, Fe-oxyhydroxides, adsorbed on bigger particles or associated with organic ligands (Bennett et al., 2008). Furthermore, because of the surrounding oxic environment, Fe(II) oxidises to the insoluble form Fe(III).

Limited basin-scale dFe(II) transect data has been reported. Hansard et al. (2009) reported the first values through two CLIVAR transects across the Pacific Ocean (PO2 and P16N). The second report was performed by Sedwick et al. (2015) across the U.S. GEOTRACES GA03 transect, with this data being readily available in the GEOTRACES IDP2017. Similarly, a study for labile Fe(II), Fe(II) in unfiltered samples and Fe(II) oxidation, was reported by Sarthou et al. (2011) along the Atlantic sector of the Southern Ocean. Iron(II) has also received interest in process studies and specific oceanic regions (eg. Schallenberg et al., 2015; Vedamati et al., 2014).

In this manuscript, we report and discuss dFe(II) concentrations that were measured on samples collected during the 2017-2018 GEOTRACES GA13 section cruise, which perpendicularly crossed the GA03 transect. We focus on the distribution of Fe(II) concentrations above the Mid Atlantic Ridge (MAR) in the vicinity of six hydrothermal vents. We compare the dFe(II) concentrations to the soluble (sFe, filtered through 0.02 μm pore size filter) and dissolved (dFe,

filtered through 0.2 µm pore size filter) Fe fractions. Moreover, we use a multiparametric equation to estimate the original Fe(II) concentration at the *in situ* time of sampling. This dataset substantially increases the few studies which have reported Fe(II) distributions in hydrothermal environments.

4.3. Materials and methods

4.3.1. Sampling Sites

Sampling was performed along the MAR including six hydrothermal vent sites: Menez Gwen (37˚ 50'N; Charlou et al., 2000), Lucky Strike (37˚ 17'N; Charlou et al., 2000), Rainbow (36˚ 14'N; Douville et al., 2002), Lost City (30˚N; Kelley et al., 2001), Broken Spur (29˚N; James et al., 1995), and TAG (26˚N; Gamo et al., 1996). The six hydrothermal vent sites investigated during this cruise represent a wide range of geological conditions which affect the hydrothermal properties. Geologically, Menez Gwen and Lucky Strike present mafic basement rocks, enriched-Mid-Ocean Ridge Basalt (E-MORB, enriched with light rare earth elements, LREE), and present sulfide mounds. Rainbow also presents sulfide mounds, but its basement rocks are ultramafic. Similarly, Lost City is also situated above an ultramafic base but presents carbonate chimneys. Broken Spur and TAG present sulfide mounds and have basement rocks formed by normal-MORB (N-MORB, LREE depletion; references within Fouquet et al., 2010). In relation with the depths, Lost City and Menez Gwen are the shallowest sites, with the vent site depths located at 700-720 m and 840-850 m, respectively. Lucky Strike hydrothermal field is situated between 1560 and 1730 m depth. Rainbow vent site is found at 2270-2280 m depth, within the average range (2000 to 3000 m) of oceanic ridge depth (Searle, 2013), while Broken Spur and TAG are deep hydrothermal systems located at 3100-3300 m and 3670-3700 m, respectively. Chemically, Lost City is an alkaline hydrothermal vent, with pH ranging from 9.0 to 9.8. In comparison with the other sites, the vent fluid is cold (40-75 °C) with extremely low concentrations of most trace elements (Ludwig et al., 2006). All other hydrothermal vent sites are acidic with pH lower than 4 and act as important sources of trace metals (Charlou et al., 2000; Douville et al., 2002; Andreani et al., 2014).

The GA13 cruise stations were localized along 3 transects. Transect A was subdivided into three sections (A1, A2 and A3) starting East of Azores and following the MAR (Figure 4-1). Transects B and C were two longitudinal transects centred around Rainbow and TAG, respectively. Figure 4-1 shows the map with the sampling stations. Transect A started to the northeast of Azores (39.5 °N 23.384 °W) and ended at Broken Spur (29.167 °N 43.174 °W).

Section A1 was a 600 km section that covered the area north of the Azores in the east to west direction. The first station was performed to the east of the Azores Plateau, with ocean depth of nearly 4000 m, the second station was performed in the plateau slope, with a depth of ~2600 m, while the third station was positioned above the Azores Plateau, with an ocean depth ~2100 m. Sections A2 and A3 followed the Mid Atlantic Ridge, and the samples were collected inside the ridge valley. Section A2 was a short (275 km) section and encompassed three stations: Menez Gwen (Stn 6), Lucky Strike (Stn 8) and a station situated north of Rainbow (Stn 9). Section A3 was a 900 km long section that started at 34.53 °N and finished north of TAG.

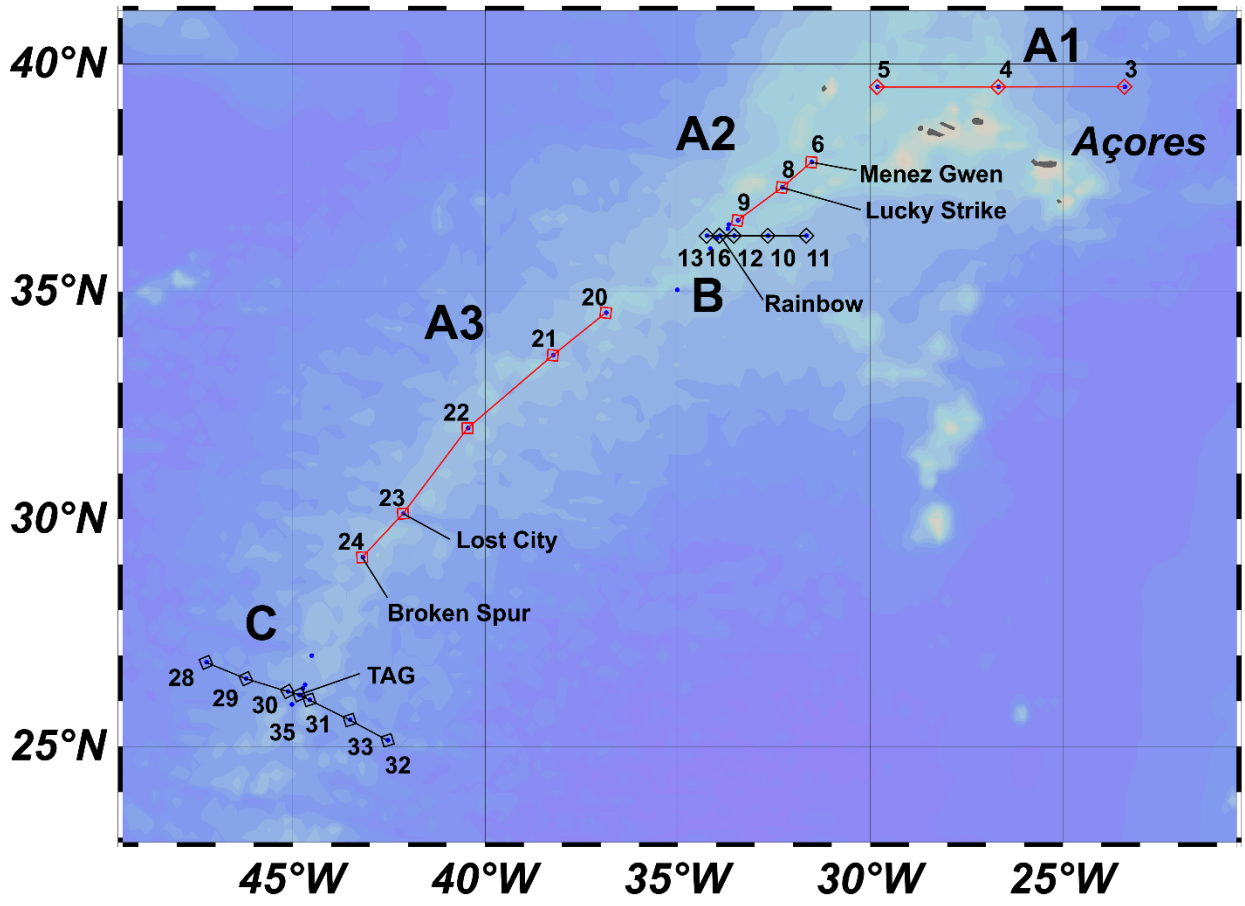

Figure 4-1. Map showing the sampling stations for the GEOTRACES transect cruise GA13. The cruise track was divided into three transects (A (red), B and C (both in black)). Station numbers are shown; hydrothermal stations also include the vent site name. See text for further details.

The longitudinal transect B was a 230 km transect starting 30 km west of Rainbow and finishing 200 km east of the hydrothermal site. It included 5 stations, the first one 30 km to the west of the vent site (Stn 13), the second one at the vent site (Stn 16), and 3 towards the east, at 30, 110 and 200 km from the vent site (Stns 12, 10, 11, respectively). Transect C was a longitudinal transect, consisting of 10 stations focusing on the TAG vent site (Stn 35). There were three stations toward the northwest and three stations towards the southeast positioned at 30, 150 and

250 km (Stns 30, 29, 28 and 31, 33, 32, respectively). Rosette deployments were also carried out in three other stations, station 37 located 5 km east of TAG, station 34 less than 250 m southwest of the vent site and a final station (Stn 39) at the same location as station 35, but with a higher emphasis in intermediate waters.

4.3.2. Sample collection

Water column samples were collected during the GA13 section cruise (JC156) along the MAR onboard the *R.R.S. James Cook*. This cruise departed Southampton, the United Kingdom on December 20th, 2017 and arrived at Guadeloupe, France on February 1st, 2018. Thirty-two stations were sampled for dFe(II), sFe, dFe and pH. Seawater samples were collected according to the GEOTRACES guidelines (http://www.geotraces.org/images/Cookbook.pdf). Briefly, a titanium rosette fitted with 24 x 10 L trace metal-clean Teflon-coated OTE (Ocean Test Equipment) bottles, a CTD profiler (Sea-bird Scientific), and a redox potential sensor (PMEL MAPR), were deployed on a conducting Kevlar wire to collect samples from the water column. Sampling depths were chosen from the continuous temperature, salinity, and redox potential data.

Upon recovery, the OTE bottles were transported into an ISO Class 6 clean air van. pH samples were collected in 125 mL borosilicate bottles and kept in the dark until analysis. Samples for dFe were filtered through 0.45/0.2 µm two-step acetate membrane cartridge filters (Sartobran-300, Sartorius) into trace metal-clean 125 ml low-density polyethylene (LDPE) bottles and acidified to pH 1.7 (0.024 mol L^{-1}) by the addition of 12 mol L^{-1} ultrapure hydrochloric acid (HCl, Romil, UpA) under an ISO Class 6 laminar flow hood (Lohan et al., 2006). Samples for sFe went through an additional in-line filtration step through 0.02 µm syringe filters (Anotop, Whatman) before acidification.

4.3.3. Analytical methods

4.3.3.1. Dissolved iron (II) analysis

Dissolved Fe(II) was determined by flow injection analysis (FIA-CL) with in-line filtration through 0.2 µm syringe filters (Anotop, Whatman), preconcentration on resin-immobilized 8-hydroxyquinoline and chemiluminescence detection, modified after the method of Bowie et al. (2002a). Luminol (Sigma-Aldrich) was cleaned using a Chelex 100 (Sigma-Aldrich) filled

column. Standards used for shipboard analyses included a primary stock solution of 0.02 mol L^{-1} dFe(II), weekly prepared by dissolving ferrous ammonium sulfate hexahydrate (Fisher) in ultrapure 0.1 N hydrochloric acid solution (ROMIL); this solution was stabilized by the addition of 100 mmol L^{-1} sodium sulfite (Sigma-Aldrich). Working standards with concentrations of 200 mmol L^{-1} and 200 nmol L^{-1} dFe(II) were prepared daily by serial dilution of the primary stock solution with ultrapure 0.01 N and 0.001 N hydrochloric acid solution, respectively. Aged, low-Fe(II) seawater (obtained over 24h before analysis from 2000 m depth and kept in the dark) adjusted to pH 5.5 with 2 mol L^{-1} ammonium acetate buffer was spiked with dFe(II) standard to obtain calibration standards generally in the range of 0-1 nmol L^{-1} dFe(II). For Fe-rich hydrothermal plume samples, preconcentration time was decreased and luminol concentration halved to not overload the resin and keep the signal within the sensor detection range. For these samples, a second calibration was performed after the sample analysis with an increasing range until all the samples were encompassed. To eliminate Fe contamination after each hydrothermal station, the FIA-CL system had to be acid-cleaned, all the tubing was replaced and the system re-cleaned using 0.5, 0.1 nmol L^{-1} HCl and UHP water for 10, 30 and 60 minutes, respectively.

The analytical limit of detection was estimated daily as the dFe(II) concentration corresponding to a signal equal to three times the standard deviation of quadruplicate analyses of the blank (Bowie et al., 2004; Sarthou et al., 2011). For the blank solution, we used filtered, aged, low-Fe(II) seawater that was stored in the dark for over 24h. The average limit of detection was 0.02 ± 0.02 nmol L^{-1} (n=42) for all of the daily shipboard analyses. Currently, there are no Fe(II) standards that can be used to ascertain the accuracy of Fe(II) concentrations. We tried to mitigate this by preparing the primary Fe(II) stock weekly instead of monthly. This allowed for the intercomparison of two 0.2 nmol L^{-1} dFe(II) standards prepared from different primary stocks.

4.3.3.2. Dissolved and soluble iron analysis

Soluble and dissolved Fe was measured by flow injection chemiluminescence (Obata et al., 1993) with measured values of 0.94 ± 0.04 for D2 reference material (n = 15). Soluble samples were measured by flow injection on-shore and initial dissolved measurements were done shipboard. High concentration dissolved samples (>0.7 nM) were re-analysed on-shore for Fe after 6 months of acidification by ICP-MS (Thermoscientific, Element XR) using a standard

addition method (Lough et al., 2017, 2019b). GEOTRACES reference material D2 with 0.96 nmol L^{-1} Fe compared well with our measured values of 0.95 ± 0.06 nmol L^{-1} Fe (n = 5). In house standards with higher concentrations of Fe in the range of hydrothermal samples were measured repeatedly with relative standard deviations of 7 %. The complete dFe dataset is reported elsewhere (Lough et al., in prep.).

4.3.3.3. pH analysis

pH was measured onboard on the free scale using a Tris buffer solution (Millero, 1986). Onboard pH samples were kept in the dark, inserted into a 25 ˚C water bath, and measured at 25 ˚C, within less than one hour after collection. The pH at *in situ* conditions were computed considering the total alkalinity for an average profile of the area (https://www.nodc.noaa.gov/ocads/oceans/GLODAPv2/, last accessed 18/05/2020) and the set of constants from Lueker et al. (2000).

4.4. Results

4.4.1. Measured dissolved iron (II) concentrations

The results of the shipboard measurements of dFe(II) are presented in Figure 4-2. Concentrations measured throughout the water-column profile were low, with 90% of the analysed samples (n=362/403) presenting values below 0.2 nmol L^{-1}. In the deep ocean, dFe(II) concentrations ranged from less than 0.1 nmol L^{-1} in non-hydrothermally affected regions to values as high as 69.6 nmol L^{-1} in areas with hydrothermal activity.

Along section A1, dFe(II) displayed constant concentrations averaging 0.07 ± 0.03 nmol L^{-1} (n=36) (Figure 4-2). In transect A2, at Menez Gwen (Stn 6), dFe(II) concentrations reached 0.25 ± 0.01 nmol L^{-1} at 829 m depth (15 m above the seafloor). Similarly, at Lucky Strike (Stn 7), dFe(II) concentrations were high in the bottom 60 m (1674-1723m), averaging 0.61 ± 0.14 nmol L^{-1} (n=4). Station 9, a station not situated above a hydrothermal vent site, did not present any dFe(II) increases, and presented concentrations in agreement with a non-hydrothermally affected station. The first four stations in section A3, (Stns 20-23, including the alkaline vent Lost City) did not present any dFe(II) anomalies, with an average dFe(II) concentration of 0.05 ± 0.03 nmol L^{-1} (n=78) (Figure 4-2). The last station of this transect was located at Broken

Spur (Stn 24), where dFe(II) was greater than 0.25 nmol L^{-1} below 2800 m (n=8), reaching 0.95 ± 0.07 nmol L^{-1} (n=2) at 2829 and 2834 m (~200 m above the seafloor).

Transect B showed a very localized dFe(II) source, with a dFe(II) concentration averaging 6±5 nmol L^{-1} (n=4; between 1.98 and 12.77 nmol L^{-1}) at depths between 2000 and 2108 m (~160-270 m above the seafloor) at the Rainbow site (Stn 16) (Figure 4-2). A second plume specific cast at this station, revealed dFe(II) concentrations ranging from 44.1 to 69.6 nmol L^{-1} (n=3) between 2242 and 2252 m depth (~20-30 m above the seafloor; within the ascending plume). At the four other stations of this transect, dFe(II) concentrations were similar to deep ocean background values (below 0.1 nmol L^{-1}) averaging 0.04 ± 0.03 nmol L^{-1} (n=52).

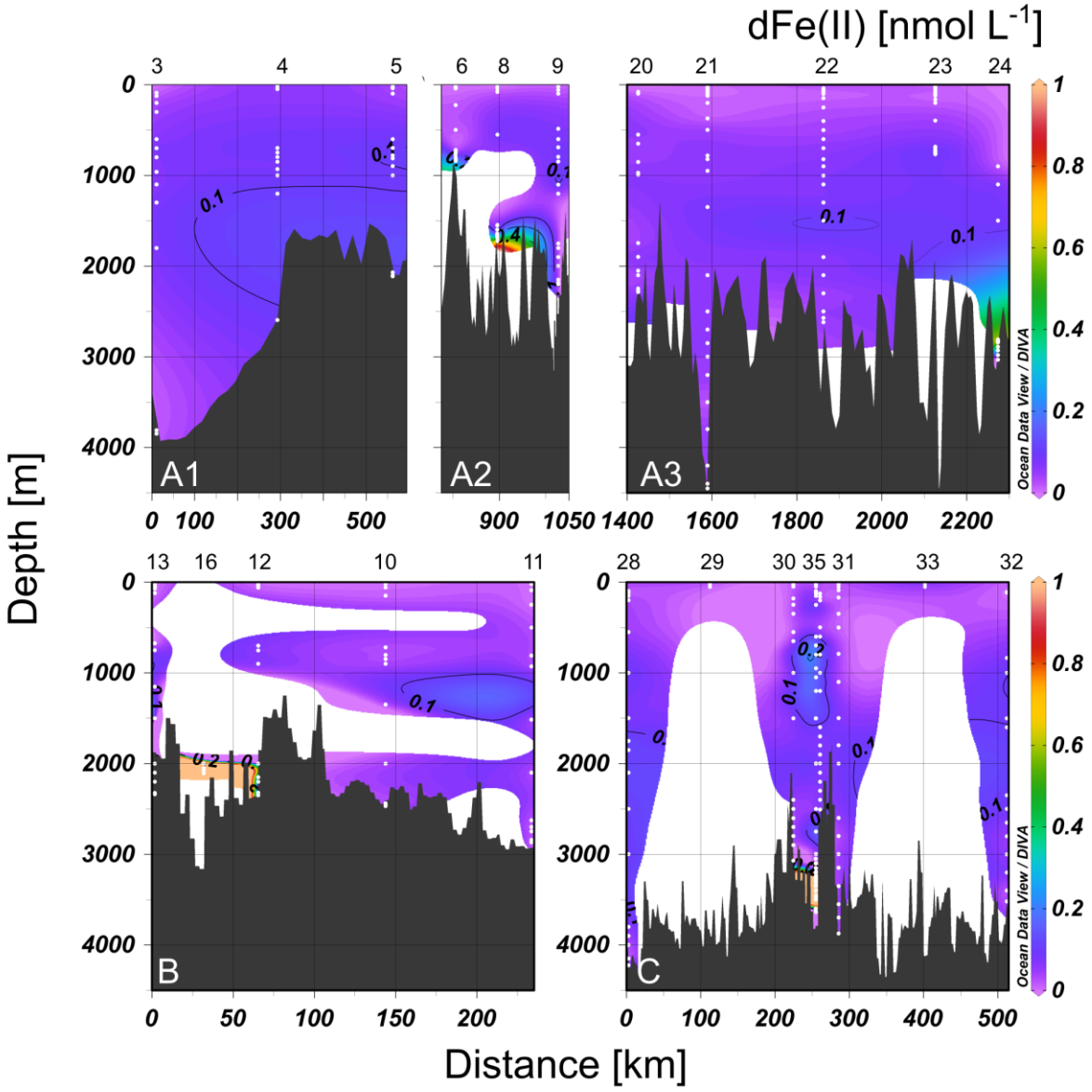

Figure 4-2. Contoured vertical sections of dissolved iron(II) (dFe(II)) concentration along the three transects of GEOTRACES cruise GA13 (refer to Figure 4-1). Note that the maximum value of the colour scale is 1 nmol L^{-1}. Black contours present dFe(II) concentrations. Top x-axis presents the station numbers.

From the 10 stations (n=137) of transect C (Figure 4-2), only the TAG site (Stn 35) presented higher dFe(II) concentrations than background concentrations, averaging 8 ± 1 nmol L^{-1} (n=6) at the neutrally buoyant plume depth (3263-3453 m), but also high concentrations below the plume 4.1±0.9 nmol L^{-1} (n=2) were measured. Moreover, at station 39 the ship was positioned at the same latitude and longitude as station 35, yet no hydrothermal dFe(II) signal could be observed in the deep samples. In transect C, a regional maximum (0.22 ± 0.01 nmol L^{-1}, n=4) was observed between 1000 and 1500m depth, coinciding with the oxygen minimum zone.

4.4.2. Corrected dissolved iron (II)

Measured dissolved Fe(II) concentrations ($dFe(II)_{measured}$) were corrected for the elapsed time (t) from the sample collection using the rosette to the measurement in the laboratory. The original dFe(II) concentration in the ocean ($dFe(II)_0$) can be related to the measured dFe(II) in the sample considering the elapsed time and the oxidation rate constant (*k'*) (Equations 4-1,4-3 and 4-4). The time that elapses from the moment the sample was collected in the water column until it is analyzed was divided into four periods: *a*) from the sample collection by the rosette to the transport of the OTE bottles inside the sampling van, *b*) from the end of the previous step to the insertion of the subsample into the cooler box, *c*) time required to collect other Fe(II) samples *d*) time spent in the laboratory inside the cooler box before analysis. Time steps a-d were different for each sample and were all taken into account. We assumed that the oxidation rate of steps *a* and *b* occurred at *in situ* temperature in a time $t_1 = t_a + t_b$, while steps *c* and *d* occurred at 2 °C (inside the cooler box) in a time $t_2 = t_c + t_d$.

The Fe(II) oxidation was considered to be well represented by a pseudo-first-order rate constant, *k'* (Equations 4-1 and 4-2) computed using the updated multiparametric equation from González-Santana et al. (in rev.) calculated using the same samples as in this work. These computed *k'* values were determined at saturated oxygen concentrations. To consider the effect of the oxygen concentration variability in the Fe(II) oxidation, the oxidation rate constant *k* was calculated from Equation 4-2 using the saturated oxygen *k'*. A new *k'* for the *in situ* oxygen concentration was then recalculated reapplying Equation 4-2 using the newly obtained *k* and the *in situ* O_2 concentration. For non-hydrothermally affected samples, the experimental data and the theoretically derived data presented a standard error of estimate of log *k'* = 0.2287 (*k'* in min^{-1}), which corresponds to a half-life error of less than one minute. The multiparametric equation is temperature, pH and salinity dependent. We assumed constant oxygen

concentration and salinity and used two temperatures, *in situ* temperature of the sample that was assumed to be constant until sampling (period t_1) and 2 °C for the samples inside the cooler box until measurement (period t_2) and the corresponding pH values. Equation 4-3 was modified to compute the original *in situ* concentrations ($dFe(II)_0$) considering the two oxidation rates (Equation 4-4).

$$-d[Fe(II)]/dt = k'[Fe(II)] \quad (4\text{-}1)$$

$$k' = k[OH^-]^2[O_2] \quad (4\text{-}2)$$

$$\ln(dFe(II)_{measured}) = \ln(dFe(II)_0) - k' \cdot t \quad (4\text{-}3)$$

$$\ln(dFe(II)_0) = \ln(dFe(II)_{measured}) + k'_{sal,(pH,T,O_2)_{in\ situ}} \cdot t_1 + k'_{sal,O_{2,in\ situ},(pH,T)_{2°C}} \cdot t_2 \quad (4\text{-}4)$$

The *k'* is pH, salinity (sal) and temperature (T) dependent, with T and pH being the main influencing factors. In congruence with previous dFe(II) work, hereafter measured dFe(II) concentrations will be reported as dFe(II), while corrected dFe(II) concentrations will be defined as $dFe(II)_0$.

Figure 4-3 depicts the distribution of the variables affecting the oxidation rate. Surface temperatures (Figure 4-3A) increased from north to south, from 18 to 22°C. Accordingly, subsurface temperatures deepened their thermolines. Values close to the bottom ranged from 2.7 and 2.8 °C at TAG and Broken Spur to 8.6 and 10.2 °C at Menez Gwen and Lost City. The *in situ* pH (pH_{is}) in the surface samples was greater than 8.2, with a deepening in the isolines towards the south (Figure 4-3B). A surface discrepancy was observed south of station 22 with pH_{is} values below 7.95. This discrepancy was caused by rain, with an associated 0.4 decrease in salinity (data not shown). Central waters presented pH_{is} below 8.2, as a result of remineralization. The pH is temperature-dependent, and when the pH is normalised to a constant temperature, we observed that the pH_{25} increased towards the south. This variation is related to increases in biological activity. pH_{25} above 8.2 was found in surface waters shallower than 60-80 m at 49.5°N and deepened to 560 m by 30°N. Dissolved oxygen (O_2) in the water column varied from North to South following the distribution of the different water masses in the area (Liu and Tanhua, 2019). Surface waters in the North (49.5 °N) had O_2 concentrations above 240 µmol kg^{-1} but decreased to 220 µmol kg^{-1} by 30°N (Figure 4-3C). Similarly, O_2 concentrations in the water column were affected, with O_2 concentrations below 220 µmol kg^{-1} being found between 500 and 1000 m in the north, reaching 195 µmol kg^{-1} at 800 m depth,

and expanding from 0 to 1250 m south of 35 °N, with concentrations below 175 μmol kg^{-1} at 800 m depth in the northeast central waters. Other factors affecting the oxidation rate were not considered as they have a positive or negative effect depending on seawater composition (Theis and Singer, 1974; Santana-Casiano et al., 2000). The equation does not include biological interactions, such as organic matter, which depending on its composition can accelerate or retard the oxidation rate. Due to a higher temperature and pH_{is} values for the central and surface water (the top 800 m) with half-life times of a few minutes, the extrapolation to compute the $dFe(II)_0$ for the top 800 m of the water column has not been shown.

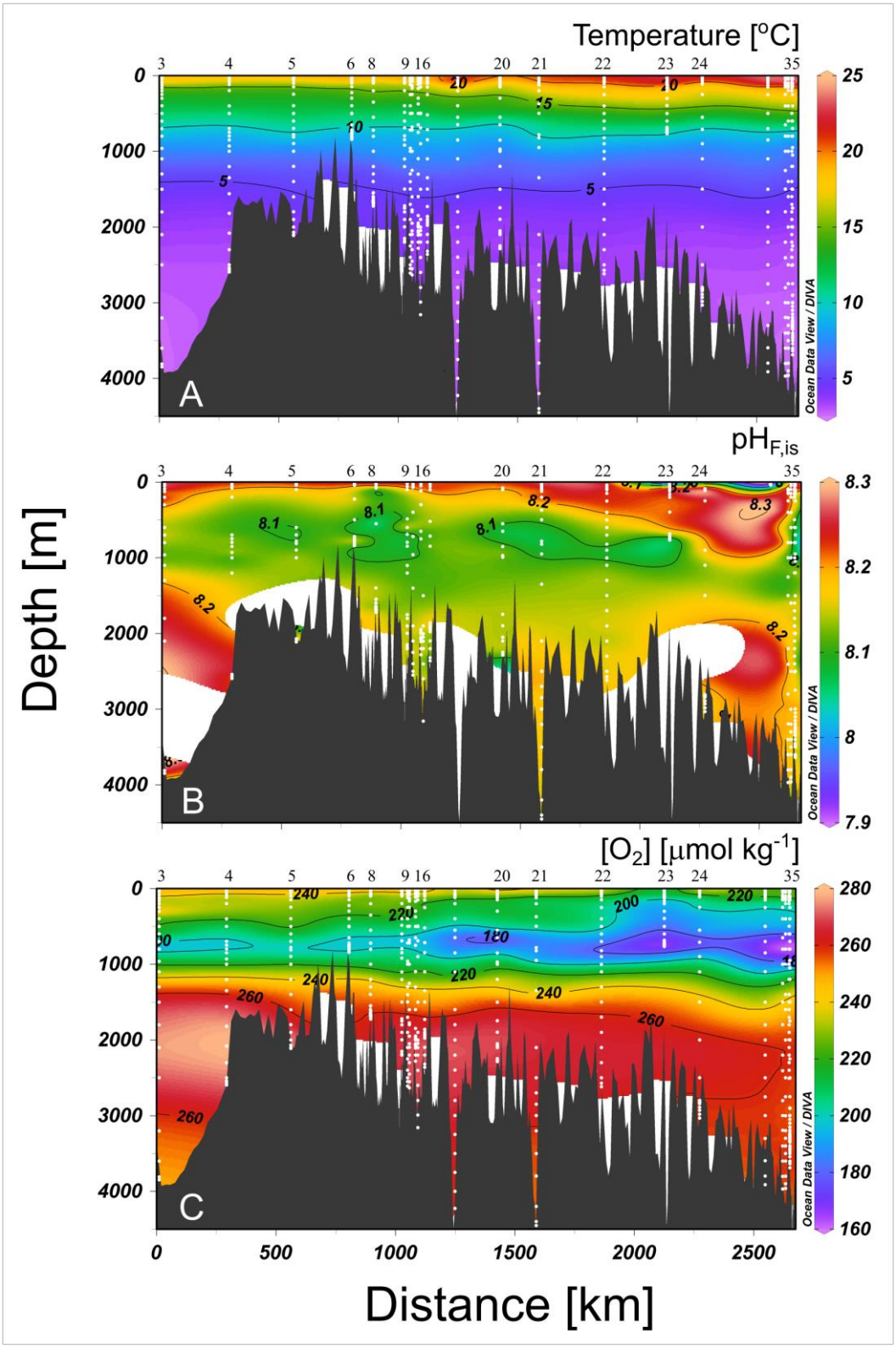

Figure 4-3. Contoured vertical sections of A) Temperature (°C), B) pH in the free scale at *in* situ temperature ($pH_{F,is}$), and C) oxygen concentration (µmol kg^{-1}) along transect A of the GEOTRACES cruise GA13 (refer to Figure 4-1) . Top x-axis presents the station numbers.

4.4.2.1. Corrected dissolved iron (II) concentrations

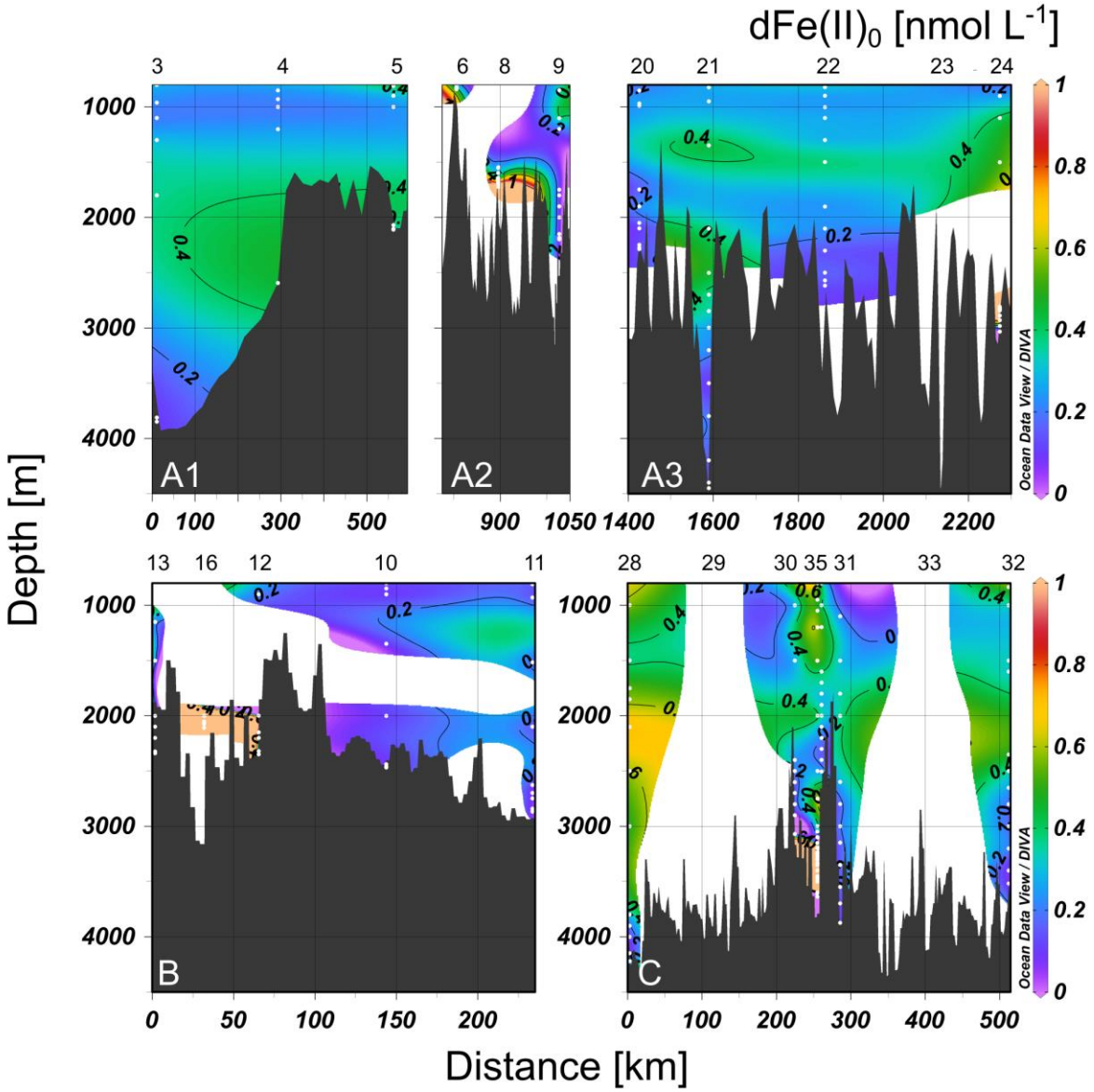

Figure 4-4. Contoured vertical sections of the corrected dissolved iron (II) ($dFe(II)_0$) concentration along the three transects of GEOTRACES cruise GA13 (refer to Figure 4-1) . Note that top 800 m of the profile have not been included. The maximum value of the colour scale is 1 nmol L^{-1}. Top x-axis presents the station numbers.

The theoretical $dFe(II)_0$ concentrations were computed for the water profile between 800 to 4500 m depth (Figure 4-4). These computed concentrations show a more variable and more dFe(II) concentrated ocean. The average concentration of section A1 ascended to 0.27±0.10 nmol L^{-1} (n=19). In transect A2 at Menez Gwen (Stn 6) $dFe(II)_0$ ascended from 0.25±0.01 nmol L^{-1} at 829 m depth to 0.53 nmol L^{-1}. In the bottom 60 m of Lucky Strike (Stn 8) $dFe(II)_0$ raised to 1.54±0.39 nmol L^{-1}. In the first three stations of section A3 (Stns 20-22, Lost City (Stn 23) is shallower than 800m) the $dFe(II)_0$ concentration increased to 0.23±0.10 nmol L^{-1} (n=36). The maximum $dFe(II)_0$ signal at Broken Spur (Stn 24) was five times higher, reaching 4.79±0.15 nmol L^{-1} after the oxidation correction. Transect B still showed a localized $dFe(II)_0$

source at the Rainbow vent site (Stn 16). At depths between 2000-2108 m, the oxidation correction increased $dFe(II)_0$ concentration range to between 6.01 and 27.62 nmol L^{-1}. In transect C, the neutrally buoyant of TAG (Stn 35) had $dFe(II)_0$ concentrations up to 46.7 nmol L^{-1}, with concentrations above 30 nmol L^{-1} between 3250 and 3450 m. At the other four stations, $dFe(II)_0$ concentrations were 0.27±0.17 nmol L^{-1}, with the highest concentrations observed at 2000 m depth. The regional maximum between 1000 and 1500 m depth above TAG (Stn 35) was still visible after the $dFe(II)_0$ correction (0.76±0.12 nmol L^{-1} (n=3)).

4.4.2.2. Dissolved iron (II) underestimations

The measured dFe(II) as a percentage of $dFe(II)_0$ represents the theoretical dFe(II) that could be measured in the laboratory considering the oxidation of Fe(II) (Figure 4-5). Overall, less than 65% of the $dFe(II)_0$ was measured as dFe, which decreases to less than 45% if the hydrothermal vent sites are not considered. The lowest losses of dFe(II) (highest percentages in Figure 4-5) were computed for waters sampled between 1000 and 2000 m. The limited underestimations were a combination of the effect of low seawater temperatures (Figure 4-3A), low pH (Figure 4-3B), low oxygen concentrations (Figure 4-3C) and reduced sampling time including the displacement of the rosette. Stations 4 and 5 were the least affected due to the limited ocean depth. The highest losses, greater than 90%, were obtained in samples shallower than 800 m.

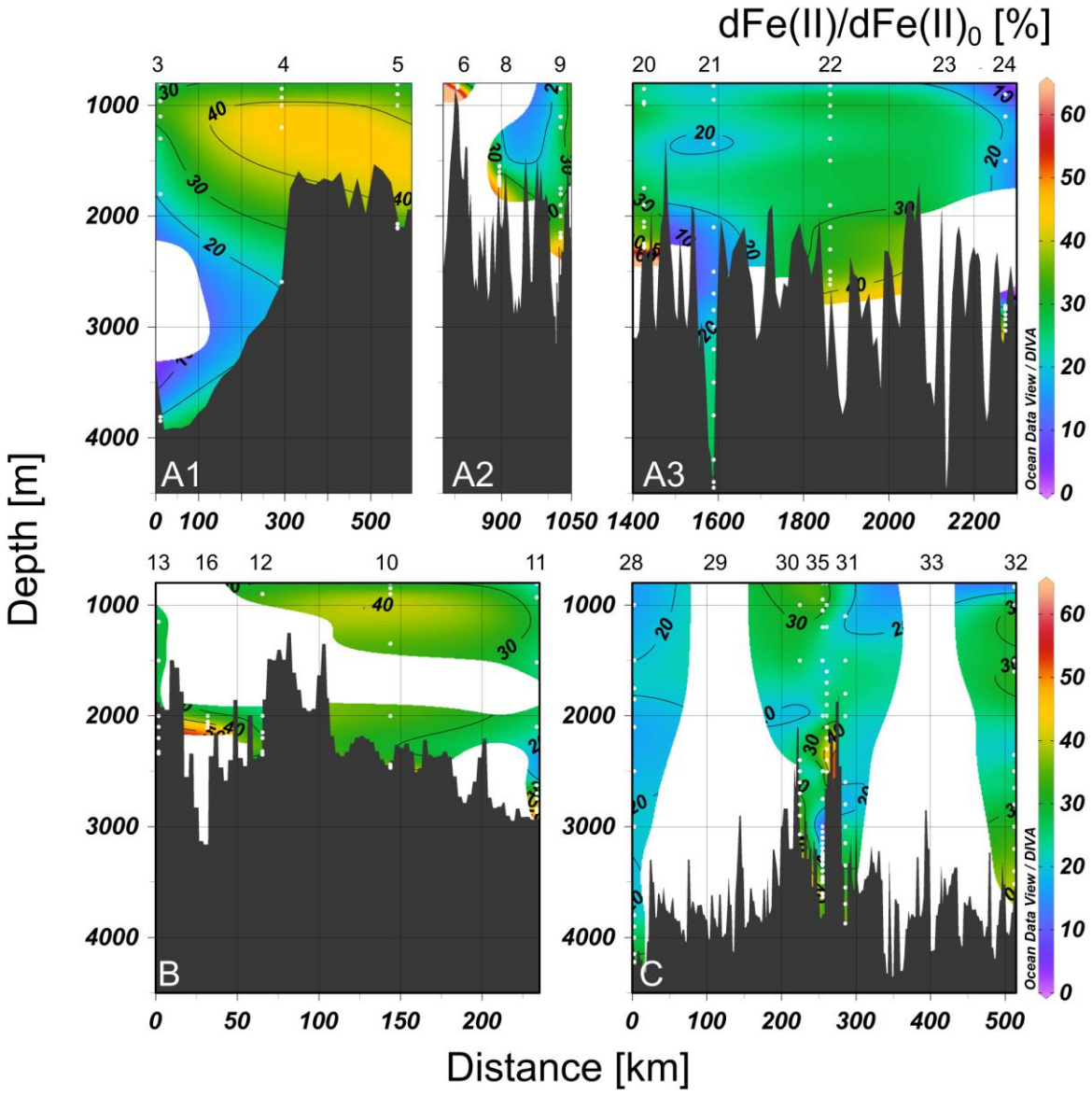

Figure 4-5. Contoured vertical sections of the measured dissolved iron (II) as a percentage of the corrected dissolved iron (II) ($dFe(II)_0$) concentration along the three transects of GEOTRACES cruise GA13 (refer to Figure 4-1). Note that top 800 m of the profile have not been included. The maximum value of the colour scale is 65 %. Top x-axis presents the station numbers.

4.4.3. Dissolved iron (II) relevance

4.4.3.1. Dissolved iron (II) in relation with the dissolved iron pool

The $dFe(II)_0$ concentrations were compared to the absolute presence of dFe (dFe = dFe(II) + dFe(III)). The $dFe(II)_0$/dFe presented four distinct regions (Figure 4-6). First, a surface region in the photic zone (not shown); second, the central waters with the highest remineralisation region at depths within the minimum oxygen concentration zone of the Eastern North Atlantic Intermediate Central waters (mixed with Subarctic Intermediate Waters and Mediterranean

Overflow Seawater); third, a deep ocean region inside the North Atlantic Deep Waters and fourth, the hydrothermally affected region.

In the central waters, $dFe(II)_0$ concentrations increased from north to south. Nevertheless, dFe concentrations did not vary in the same proportion, as such, there is a north to south gradient in the $dFe(II)_0/dFe$ ratio varying from 20-40% in section A1 to 50-80% in the second half of section A3.

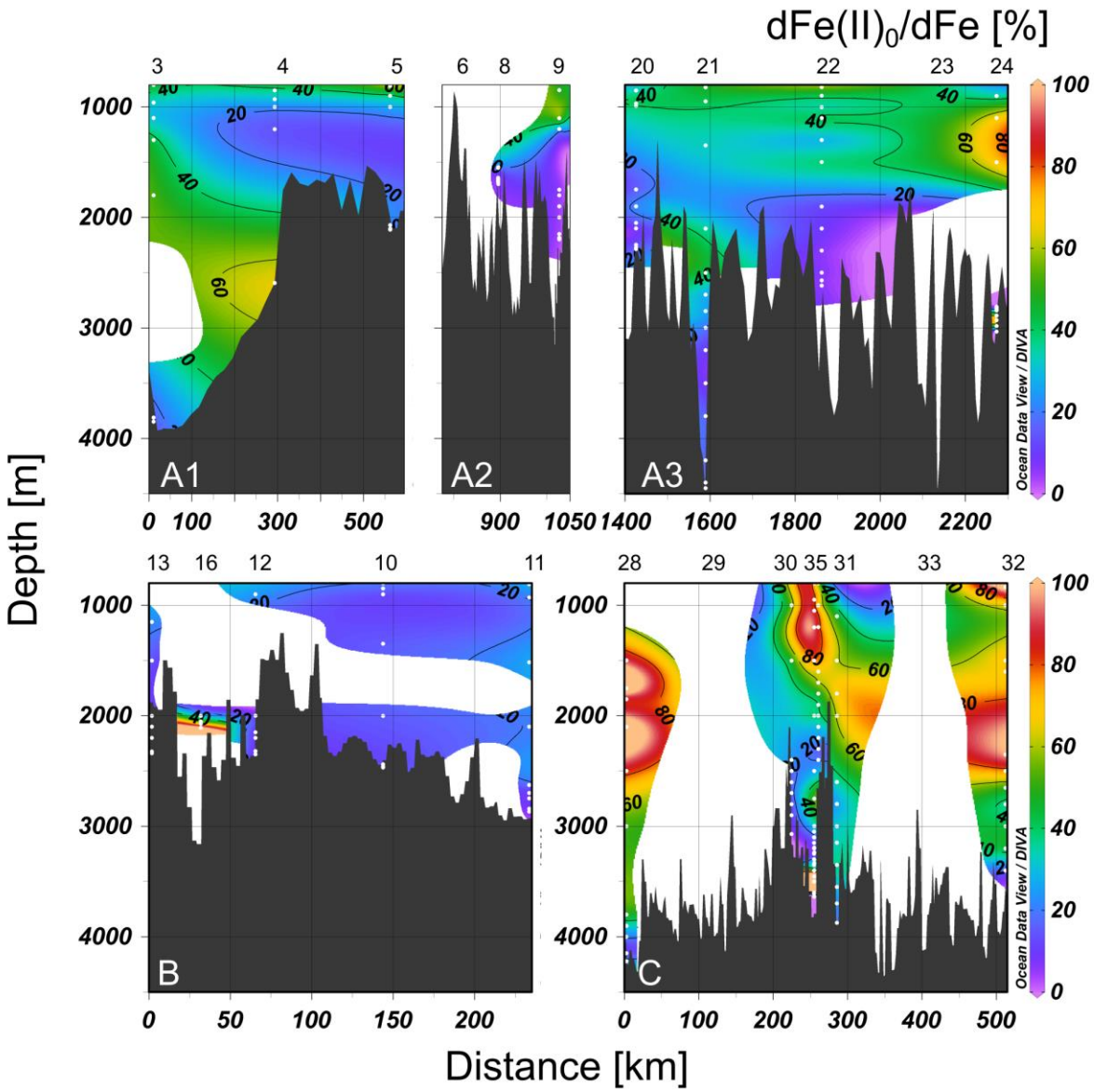

Figure 4-6. Contoured vertical sections representing the proportion of $dFe(II)_0$ in the dFe pool ($dFe(II)_0/dFe$ [%]) along the three transects of GEOTRACES cruise GA13 (refer to Figure 4-1). Note that the maximum value of the colour scale is 100%. Top x-axis presents the station numbers.

4.4.3.2. Dissolved iron (II) in relation with the soluble iron pool

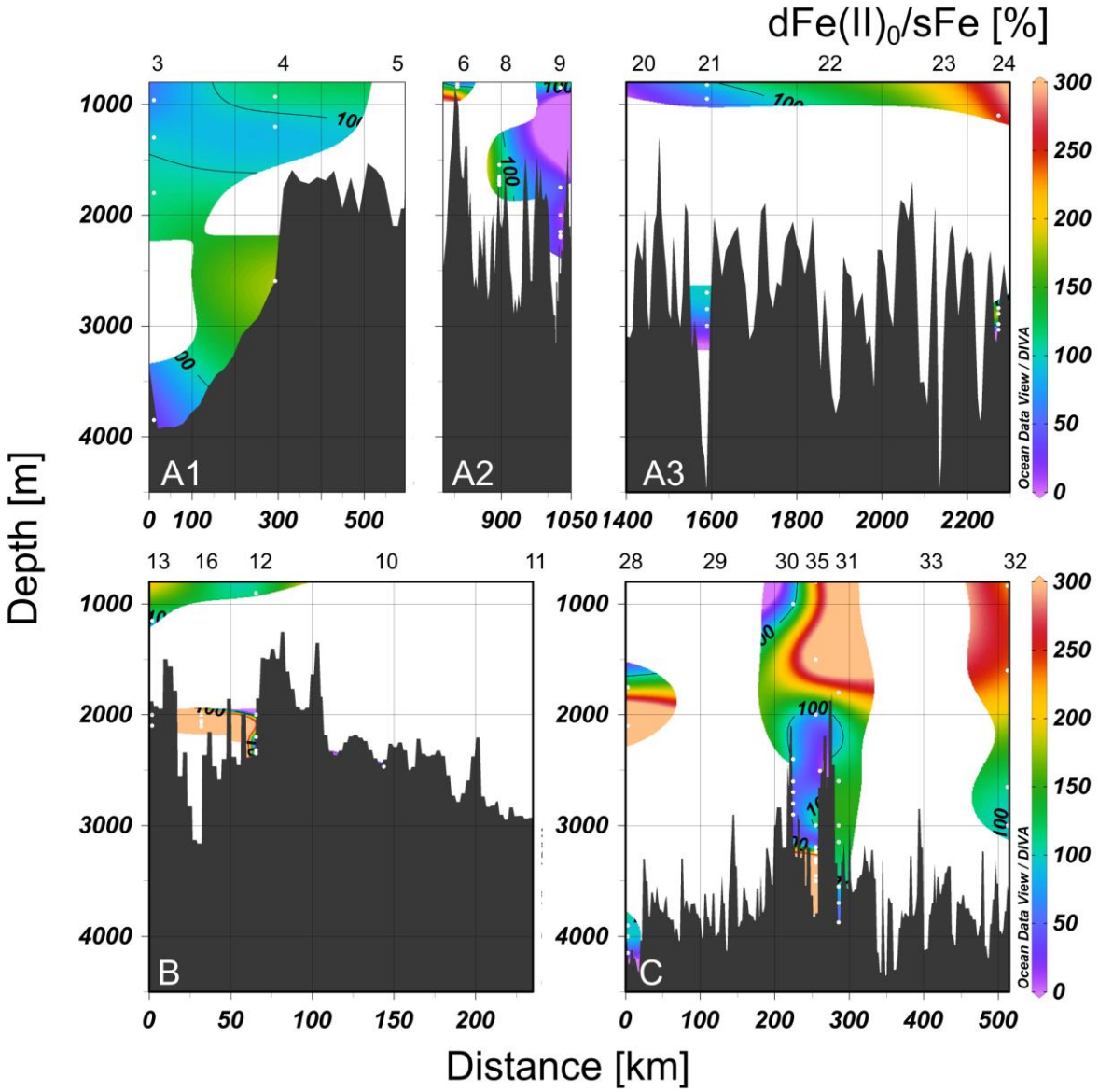

Figure 4-7. Contoured vertical sections of corrected dissolved Fe(II) divided by the soluble Fe pool as a percentage ($dFe(II)_0/sFe$ [%]) along the three transects of GEOTRACES cruise GA13 (refer to Figure 4-1). Note that the maximum value of the colour scale is 300%, with the contour at 100%. Top x-axis presents the station numbers.

The dFe(II)/sFe and $dFe(II)_0/sFe$ percentages were scarce due to sampling limitations. Nevertheless, percentages above 100% are prevalent throughout the whole water column (Figure 4-7), with the highest percentages in the hydrothermal neutral buoyant plumes. Menez Gwen (Stn 6) and Lost City (Stn 23) presented the lowest percentages 40±20% (n=8 and n=2, respectively). However, all other hydrothermal plumes presented $dFe(II)_0/sFe$ percentages above 100%. Broken Spur (Stn 24) and Lost City (Stn 23) presented higher $dFe(II)_0$ concentration than sFe at 120 and 140±50% (n=4), respectively. Moreover, at TAG (Stn 35), concentrations of $dFe(II)_0$ were tens of times higher than sFe (1260±60%; n=3). Similar percentages were determined between 2001 and 2072 m at the Rainbow vent site (Stn 16)

averaging 1120±510 % (n=3), but peaking at 3497% at 2108 m depth, where the maximum dFe(II) concentration was measured.

4.5. Discussion

The chemical speciation of Fe in the ocean is dominated by Fe(III) complexed with organic ligands (Rue and Bruland, 1997; Bennett et al., 2008; Hawkes et al., 2013; Kleint et al., 2016). Iron (II) species have largely been assumed to have an ephemeral presence. This Fe(II) is thought to be mainly in the soluble phase (O'Sullivan et al., 1991; Millero et al., 1995; Massoth et al., 1998; Klar et al., 2017). Unlike other trace metals, or even compared to its oxidized form of Fe(III), Fe(II) is a highly unstable metal in the ocean. The determination of dFe(II) in the marine environments involves a degree of uncertainty which can be higher or lower depending on the specific zone within the water column in which it is measured. Iron(II) tends to rapidly oxidize to its more thermodynamically stable redox state Fe(III) (Millero et al., 1987; Santana-Casiano et al., 2005). The Fe(II) oxidation rate depends on many factors, the most important being oxygen and hydrogen peroxide concentrations, temperature, pH and to a lesser extent salinity if we consider the narrow range of variation in the ocean (Millero and Sotolongo, 1989; González-Dávila et al., 2006; Santana-Casiano et al., 2006). Organic matter also plays an important role in controlling the oxidation rate of Fe(II), both accelerating or retarding it, even complexing Fe(II) and thus keeping it in the solution (González-Santana et al., in rev.; Santana-Casiano et al., 2000, 2004a). Speciation based on size is also very important, colloidal particles have been shown to reduce the oxidation rate (González-Santana, in rev.). Recent studies suggest that sFe and colloidal Fe (cFe; between 0.02 µm and 0.2 µm) are composed of inorganic colloids (FeS_2 or Fe oxyhydroxides) (Yücel et al., 2011; Gartman et al., 2014; Fitzsimmons et al., 2017), organic Fe complexes (Bennett et al., 2008; Hawkes et al., 2013; Kleint et al., 2016) and/or other Fe(II) species (Sedwick et al., 2015). Furthermore, colloid aggregation is important in the control of the amount of dFe added to the ocean by hydrothermal vents (Lough et al., 2019b). In hydrothermal plumes, 30 ± 21% of dFe is stabilised by chemically labile binding to ligands (Hawkes et al., 2013). Work started by Roy et al. (2008) demonstrated that dFe(II) can comprise a significant proportion of dFe in the ocean. Hence, there is the need to define well the conditions in which Fe(II) is measured, the *in situ* conditions of the sample and the time that the process takes.

4.5.1. Variables under control

The variables that can be controlled which affect Fe(II) oxidation rate and used to define the conditions in which Fe(II) is measured are a) light, by keeping the samples in the dark limiting photoproduction of Fe(II), b) temperature, by keeping the samples in a cooler box full of ice reducing the sample temperature slowing down the Fe(II) oxidation rate, c) oxygen, by collecting samples in bottles without producing and leaving air bubbles limiting oxidation and d) time, by analysing the samples as soon as possible since there is no Fe(II) preserving method. As such, samples collected thousands of meters below sea level, have to be transported to surface inside a rosette. The rosette or the rosette bottles have to be transported into the trace metal sampling van, the samples are then carefully collected and inserted into a portable cooler box, and after all the dFe(II) samples have been obtained, they are transported to a clean laboratory, where they are kept in the cooler box until analysis.

The relative high seawater temperatures found in surface samples compared to deep ocean samples produces faster Fe(II) oxidation rates, with a $t_{1/2}$ ranging between 2 and 4 minutes. Cooling the surface samples by introducing them into a cooler box slows down the oxidation rate. However, the oxidation rate is also dependent on the pH. When a sample is cooled down, its pH increases and as a result the oxidation rate increases. The temperature dependence of the Fe(II) oxidation rate is greater than the pH effect, therefore, cooling surface samples slows down the oxidation rate, but the final effect is moderate, with $t_{1/2}$ at 2 °C increasing to 12 to 20 min. When sampling is considered for surface samples, just the time required to transport the samples from their original depth to the clean laboratory accounts for 5 to 10 times the $t_{1/2}$. Under these circumstances, the applicability of the linearity of Fe(II) oxidation is questionable. On that account, future sampling in the mixed layer depth should consider the effects the oxidation has on reactive species such as redox-dependent variables. We suggest that sampling focus should attempt to prioritise these samples, particularly when considering size fractionation and redox states. Furthermore, alternative fast subsampling methods such as the use of centrifuges (Schlosser et al., 2013) could potentially give a better understanding of the real size fractionation. If they are capable of filtering samples fast enough that oxidation is reduced, the soluble size fraction could potentially be more significant than what is currently being acknowledged. Alternatively, the use of Teflon pumps which would transport the water directly to the laboratory could significantly reduce the sampling time of surface samples, by eliminating the rosette time.

4.5.2. Knowledge of the iron (II) oxidation kinetics

As a result of more than forty years of studying the oxidation kinetics of Fe(II) in seawater and the physical-chemical factors that control it (González-Santana et al., in rev.; Millero et al., 1987; Santana-Casiano et al., 2005), nowadays the Fe(II) oxidation rate can be theoretically calculated for different pH, temperature and salinity conditions, with reasonable certainty. However, factors such as the characteristics and degree of natural and remineralised organic matter (Rose and Waite, 2002; Santana-González et al., 2018, 2019), nutrient concentrations as high silicate (Samperio-Ramos et al., 2016), the subtle differentiation in size between truly soluble and colloidal (González-Santana et al., in rev.), the presence of other metallic species such as copper which could catalyze the redox process of Fe (Pérez-Almeida et al., 2019) or the greater presence of reactive oxygen species due to the photooxidation (Voelker et al., 1997; Rose and Waite, 2003b) are factors that cannot be generalized in an equation and that must be considered in each particular case. Moreover, even when several types of conditions that control the oxidation process could be involved, first-order kinetics concerning Fe(II) has been observed and pseudo-first-order kinetics has been considered (González-Santana et al., in rev.). Overall, González-Santana et al. (in rev.) observed that first-order linearity was observed for times longer than more than 3 half-live times (3 $t_{1/2}$) in the MAR and that the theoretical Fe(II) oxidation equation could be used for most of the marine environments. Discrepancies appeared in highly active environments such as regions with high organic matter, and colloids. The highest discrepancies between theoretical and analysed oxidation rates were observed in the proximities of hydrothermal vent sites where oxidation rates were generally faster. For example, in the neutrally buoyant plume of Menez Gwen (Stn 6) theoretical $t_{1/2}$ were 34 ± 1 minutes; however, the measured $t_{1/2}$ were as fast as 12 minutes. The highest differences were observed at Broken Spur (Stn 24), where the measured $t_{1/2}$ was ten times faster than the theoretical $t_{1/2}$ (less than 5 and greater than 50 minutes, respectively). However, at TAG (Stn 35), the theoretical $t_{1/2}$ were on average smaller than the measured $t_{1/2}$ (58 ± 3 min and between 35 and 131 min, respectively). Nevertheless, González-Santana et al. (in rev.) reported that the oxidation kinetics equation properly describes the oxidation rate outside of the neutrally buoyant plumes, where colloidal particles and organic matter plays a less pivotal role in the oxidation rate.

In this work, the theoretical oxidation rates were variable through the water column and were highly dependent on temperature on the upper 800 m water samples. During the analysis, the emphasis was on the deep ocean waters as such surface water samples could remain in the

cooler box between 1 and 1.5 h before analysis. Furthermore, surface water samples had higher *in situ* temperatures which drastically increase the oxidation rate and reduce the associated Fe(II) $t_{1/2}$. Furthermore, the dFe(II) could be maintained due to biological activity. Consequently, samples collected at depths shallower than 800 m have not been presented in Figures 4-4 to 4-7.

4.5.3. Iron (II) corrections

As stated in the results section 4.4.2., dFe(II) corrections are an important improvement in dFe(II) determination. Furthermore, the use of the corrected concentrations agrees with the consensus that Fe(II) is mainly found in its free form with dFe(II) concentration within the sFe concentration range. Nevertheless, it is within hydrothermal environments were divergences with the theoretical oxidation rates are most observed (González-Santana et al., in rev.). These discrepancies have a far-reaching effect on the collection and use of sFe samples and data. Considering that hydrothermal vent sites are a source of Fe(II) into the marine environment and that Fe(II) is mainly found in the soluble size fraction, dFe(II) concentrations should be equal to or below dFe concentrations and sFe if the sampling process is fast enough that the free Fe(II) is not adsorbed by particles (including colloids) or oxidised to Fe(III) and became part of the Fe oxyhydroxide particulate phase. To confirm this hypothesis, $dFe(II)_0/dFe$ (Figure 4-6) and $dFe(II)_0/sFe$ (Figure 4-7) were considered.

4.5.4. Iron (II) in the water column

The $dFe(II)_0$ contours in Figure 4-4 present both higher concentrations and a more variable water profile than what is measured (Figure 4-2). Due to oxidation during transport, measured dFe(II) concentrations decreased with respect to what is theoretically expected (Figure 4-5). The $dFe(II)_0$ values indicated that even though deep samples were the first to be collected, the cold temperatures counterbalanced the oxidation of the Fe(II). As a result, samples collected from depths deeper than 1000 m theoretically maintained 20 to 45% of their initial Fe(II) concentration even when the deepest samples were collected at depths beyond 4000 m.

4.5.4.1. Iron (II) in surface waters

Surface waters, between 0 and 200 m depth are characterised by their high pH and temperature. These conditions result in fast oxidation rates with short Fe(II) $t_{1/2}$ (theoretical $t_{1/2}$ 3.3±0.4 min, n=212). These waters are in the photic zone, so they are also affected by two processes which can significantly influence Fe(II) concentrations. First, light can cause photoreduction. This process will transform Fe(III) complexed with ligands to the reduced Fe(II) but also create a higher concentration of photoproduced H_2O_2 will affect both the Fe(II) and Fe(III) concentrations (Millero and Sotolongo, 1989; King et al., 1995). Second, there is biological influence, where primary production conditions the available Fe(II). Generally, chlorophyll maxima are characterised by presenting the lowest Fe(II) concentrations. However, the opposite has also been described and is attributed to an increase in organic matter from biological activity (Bowie et al., 2002b).

4.5.4.2. Iron (II) in central waters

Central water, situated at depths between 800 and 1500 m, conform the water depths at which the maximum of remineralization occurs. Remineralization of the surface waters generated organic matter consumes dissolved oxygen, affecting the dissolved oxygen profile. Consequently, apparent oxygen utilisation increased from north to south. The reduction in available oxygen influences Fe(II) oxidation kinetics, by decreasing the oxidation rate. Differences in oxygen concentrations between ocean basins such as the more aerated North Atlantic compared to the North Pacific have been suggested as the factor increasing the oxidation rate in the North Atlantic basin (Statham et al., 2005). This phenomenon could explain why the more O_2 concentrated central waters found in the north (section A1) presented lower $dFe(II)_0$ concentrations than the further south samples (section A3 and transect C). The Fe(II) half-life time of a sample with the same temperature, salinity and pH and with dissolved oxygen corresponding to the maximum (250 µmol kg^{-1}) and to the minimum (156 µmol kg^{-1}) concentrations in the studied region is 60% higher in the low oxygen condition (according to Equation 4-2).

Through transects A, B and C, one regional maximum is observed at a depth between 1000 and 1500m. This regional maximum is found above the TAG vent site (Stn 35) and presents concentrations averaging 0.22 ± 0.01 nmol L^{-1} ($dFe(II)_0$ = 0.76±0.12 nmol L^{-1}). This regional maximum coincides with the maximum observed by Sedwick et al. (2015) at this specific

location. These authors described two hypotheses to explain the anomaly. The first hypothesis considered secondary hydrothermal shallow hydrothermal sources located close to TAG. Their second hypothesis explained the anomaly as a result of upwelling from the TAG hydrothermal vent site. Although in this work, we cannot explain how the hydrothermal upwelling could reach 2000 m above the vent site, we find this hypothesis more reasonable, since our oxidation kinetics calculations could not account for the transport of a dFe(II) hydrothermal plume from another of the close by studied vent sites.

4.5.4.3. Iron (II) in deep waters

Deep waters, depths greater than 1500 m present cold *in situ* temperatures. These conditions allow for slower oxidation of the samples (theoretical $t_{1/2}$ of 53 ± 7 min, n=377), with $dFe(II)/dFe(II)_0$ presenting the highest percentages in a non-hydrothermally affected water profile (Figure 4-5). Nevertheless, measured dFe(II) concentrations were always below 0.1 nmol L^{-1}.

4.5.4.4. Iron (II) in hydrothermal areas

The presence of colloidal particles and complexation of the oxidised Fe(II), dominant during buoyant plume rise, would affect the rate of Fe(II) oxidation enabling the dissolved Fe(II) to be exported to the non-buoyant plume. Although Fe-ligand complexes have been studied for the colloidal and soluble pool (Cullen et al., 2006), at present no methods exist for the measurement of dissolved Fe(II)-ligand complexes and, similarly, there are no Fe(II) oxidation rate equations considering the organic matter content, type of organic matter, and colloidal particle effects.

The highest measured dFe(II) concentration at the Rainbow site (Stn 16; 2051 m depth) was 12.76 nmol L^{-1} ($dFe(II)_0$ = 27.6 nmol L^{-1}) it corresponded to 54% of the dFe ($dFe(II)_0/dFe$ = 116%), although when compared to the sFe, it was 16 times higher (1615%; $dFe(II)_0/sFe$ = 3500%). This discrepancy could be caused by oxidation of Fe(II) to Fe(III) which forms Fe-oxyhydroxides. Furthermore, colloid aggregation in filters could then influence the dFe proportion during the filtration (Massoth et al., 1998). This would explain that less than 5% of the dFe was in the soluble size fraction. The loss of Fe(II), a component of sFe, is seen in Figure 4-5. Therefore, the information obtained from the dFe and, particularly, from the sFe fractions

should consider sample transformation from *in situ* conditions to the measured ones and sFe only informs about how much sFe is present, in most of the cases, hours after sampling.

The dFe(II) concentration profiles (Figures 4-2) and the $dFe(II)_0$ (Figure 4-4) display an important behaviour in Fe transport. In the stations surrounding the hydrothermal vent sites, at distances of 30 km, dFe(II) concentrations had decreased to background levels. Therefore, most of the oxidation of dFe(II) should occur within the first kilometres from the vent sites. This is in agreement with the fast oxidation rates reported in these hydrothermal vent sites (González-Santana et al., in rev).

Nevertheless, some of our hydrothermal samples presented higher dFe(II) concentrations than sFe (Figure 4-7). A possible explanation for this phenomenon is related to the sampling procedure currently used (http://www.geotraces.org/images/Cookbook.pdf). The accepted and most common method follows a two-step filtration process. First, samples are filtered through a 0.2 or 0.45 μm filter by pressuring the rosette bottles, obtaining the dissolved fraction. Secondly, the dissolved samples are filtered through a 0.02 μm filter, generally using a multi-channel peristaltic pump. These procedures are carried out inside laboratories with room temperatures around 20 °C, which will accelerate Fe(II) oxidation kinetics. The oxidised Fe(II) would transform to cFe and then be prone to processes such as coagulation and flocculation, changing their size and acting as a filter for the available sFe (Massoth et al., 1998). Furthermore, the presence of some iron oxides such as hematite has been shown to exchange the initially free Fe(II) by Fe(III) in experiments carried out at room temperatures and pH ranging from 7.0 to 8.0 (Frierdich et al., 2015).

4.6. Conclusions

The GA13 cruise has provided invaluable data of the North MAR. Although exact trace metal concentrations are variable between different cruises, the overall distribution remains. Measured dFe(II) concentrations through the whole water column are low, with concentration below 0.2 nmol L^{-1}, with concentration decreasing in the deep ocean to less than 0.1 nmol L^{-1}. In this manuscript, we have identified some sources and physico-chemical conditions which change the homogenous profile. Over the whole water profile, Fe(II) oxidation is the main limiting factor, with measured dFe(II) concentrations only accounting for 10 to 65% of the theoretical original Fe(II) concentration. When considering individual ocean layers, surface waters include the photic zone, where photoreduction of Fe(III) forms Fe(II). Nevertheless, the

main physico-chemical parameters, high seawater temperature above 15 °C, high pH and highly oxic waters influence the Fe(II) half-life in the surface layer, shortening the $t_{1/2}$ to multiple times shorter than the time required to analyse the samples. Concurrently, biological activities excrete organic matter affecting the Fe(II) concentrations and residence time. Therefore, theoretical original Fe(II) concentrations currently cannot be determined. In the central waters, where the minimum oxygen zone is produced as a result of organic matter remineralization, the conditions allow for a slower oxidation rate, where measured dFe(II) concentrations increase. Oxygen variations within this section accounted for a Fe(II) half-life variation of up to 60%. Finally, in the interface between the ocean and the sediment, hydrothermal activity acts as a source of Fe(II), whose concentrations will be dependent on the vent site, the distance from the vent to the sampling point and the oxidation rate. Furthermore, the oxidation rate is also dependent on the specific organic matter found and the colloidal size particles. These two variables have not been considered in this manuscript, since the oxidation rate equation can only account for some inorganic processes. Nevertheless, previous oxidation kinetic studies at these hydrothermal vent sites show that hydrothermal environments produce highly variable oxidation rates, with Broken Spur producing faster than theorised oxidation rates, while TAG presents the opposite behaviour.

This work has shown that $dFe(II)_0$ could account for more than 20% of the dFe pool and not only <10% as previously reported (Sedwick et al., 2015) when the oxidation during sampling and analysis time is taken into account. The importance of Fe(II) oxidation is not only related to Fe(II) concentrations and its proportion to the Fe pool but the effect on the quantification of other Fe cycle parameters. The fast oxidation rate of Fe(II) makes Fe speciation difficult to establish, and its oxidation can influence its size fractionation. As such, the mainly soluble sized Fe(II) will oxidize to the colloidal size fraction or get adsorbed by bigger particles explaining the higher than 100% percentages of $dFe(II)_0$/sFe (Figure 4-7). Resultantly, oxidation of Fe(II) will affect more predominant measurements such as sFe, cFe and dFe. This work has encountered problems when calculating the theoretical dFe(II) concentration in waters shallower than 800 m due to the presence of high temperatures, pH, organic matter and biological activity. Therefore, future work should focus on this rapidly evolving environment, where theoretical oxidation rates are fast enough that it requires sampling and analysis to start with these samples.

4.7. Author contributions

DG-S analysed the dFe(II) and pH samples. AJML analysed the sFe and dFe samples. ML was in charge of the trace metal sampling team. DG-S, HP and GS wrote the manuscript with significant contribution from all co-authors. All the authors contributed to the article and approved the submitted version.

4.8. Acknlowledgements, Samples, and Data

The authors would like to thank the captain and crew of the *R.R.S. James Cook* as well as the scientific team during the FRidge cruise. The authors declare that there are no financial or non-financial conflicts of interests.

5. Processes driving iron and manganese dispersal from the TAG hydrothermal plume (Mid-Atlantic Ridge): results from a GEOTRACES process study

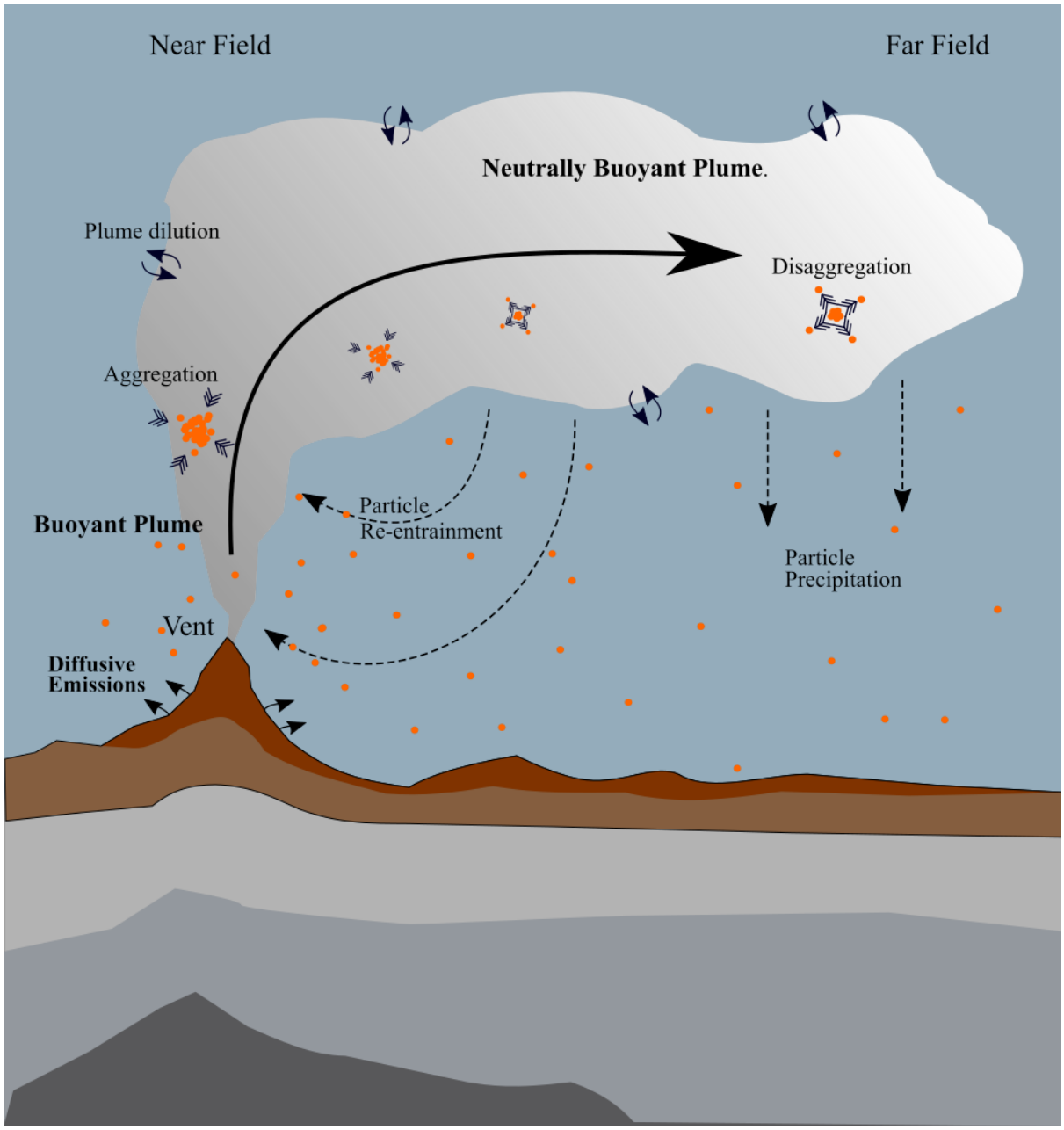

Graphical abstract of chapter 5. Hydrothermally Fe is emitted from the vent site forming the buoyant plume which ascends becoming the neutrally buoyant plume. During the first two kilometres, aggregation of small size particles predominates. As the plume is transported and diluted with the surrounding seawater, disaggregation of Fe-containing particles maintains the dissolved Fe concentrations. Meanwhile, particles precipitate, with higher precipitation rates close to the vent site. A fraction of the particles precipitating close to the vent site can be re-entrained in to the ascending plume.

This chapter is published in *Frontiers in Marine Science - Marine Biogeochemistry (https://doi.org/10.3389/fmars.2020.00568)*. See appendix C for the original article. The Supplementary Material (a table with all the measured dFe and dMn concentrations and errors) for this article can be found online at: *https://www.frontiersin.org/articles/10.3389/fmars.2020.00568/full#supplementary-material.*

González-Santana, D.[1], Planquette, H. [1], Cheize, M.[1,2], Whitby, H.[1], Gourain, A.[3], Holmes, T.[4], Guyader, V.[2], Cathalot, C.[2], Pelleter, E.[2], Fouquet, Y.[2], & Sarthou, G.[1] (2020). Processes Driving Iron and Manganese Dispersal From the TAG Hydrothermal Plume (Mid-Atlantic Ridge): Results From a GEOTRACES Process Study. Frontiers in Marine Science, 7, 568.

[1]Univ Brest, CNRS, IRD, Ifremer, LEMAR, F-29280 Plouzane, France.

[2]Ifremer, Géosciences Marine, LCG, Plouzané, France

[3]Department of Ocean Sciences, School of Environmental Sciences, University of Liverpool, Liverpool, United Kingdom

[4]The Institute for Marine and Antarctic Studies, University of Tasmania, Hobart, TAS, Australia

5.1. Abstract

Hydrothermal vents are a recognized source of trace elements to the ocean inventory. Nevertheless, the contribution of slow-spreading ridges remains poorly resolved. To address this, high-resolution dissolved (<0.45µm) iron (dFe) and manganese (dMn) samples were collected during the GEOTRACES HERMINE GApr07 process study at the Mid Atlantic Ridge. Samples were collected at nine stations, from the TAG vent site to 75 km south-southwest following the neutrally buoyant plume. Concentrations of dMn and dFe ranged from 71 ± 6 and 51 ± 2 nmol kg^{-1} right above the vent site to 0.43 ± 0.01 and 1.56 ± 0.02 nmol kg^{-1} at the most distal station, respectively. Using a 5-box model coupled with our data, we show that as the plume travelled away from the vent, aggregation processes controlled dFe concentrations in the first 2 km, with an aggregation rate averaging between 8.0 ± 0.6 and 0.11 ± 0.04 nmol L^{-1} d^{-1}, respectively in the first and second kilometer. Aggregation, likely of small colloidal particles, led to partitioning of the size fractionated Fe pool, as 6% of the dFe was moved into the particulate size fraction. Further away, disaggregation processes became more prevalent, with rates ranging from 0.27 ± 0.02 to 0.008 ± 0.001 nmol L^{-1} d^{-1}, enriching the dFe pool by 10 %. The computed decrease of hydrothermal Fe within the neutrally buoyant plume was likely caused by flocculation of small Fe oxyhydroxide particles. This process resulted in Fe aggregate formation with radii estimated to range between 14 and 20 µm in the first km from TAG. Between 2 and 30 km from the vent site, the radii ranged between 2 and 4 µm.

5.2. Introduction

The Trans-Atlantic Geotraverse (TAG) active mound is situated on the Mid Atlantic Ridge (MAR) (26° 8′ N, 44° 50′ W) at a depth of around 3620 m and corresponds to a seafloor massive sulfide mound measuring 250 m in diameter and 50 m in height. TAG active mound was the first high-temperature hydrothermal vent found at a slow-spreading oceanic ridge during the NOAA Trans-Atlantic Geotraverse project in 1985 (Rona et al., 1986). Since then, TAG has become one of the most comprehensively studied seafloor hydrothermal fields and is well characterized in terms of activity (e.g. Lalou et al., 1995), fluid composition (e.g. Von Damm, 1995), and deposits (e.g. Mills et al., 2001).

Since the widespread interest in oceanic iron (Fe) started in the late 1980s (Martin and Fitzwater, 1988), multiple "new" Fe sources (Boyd and Ellwood, 2010) have been investigated, including atmospheric dust, resuspension of coastal and shallow sediments, ice melting,

vertical diffusive flux, volcanism, bottom pressure torque, and hydrothermal activity (e.g. Tagliabue et al., 2017). Recently, the observed basin-scale impact of the East Pacific Rise hydrothermal site has revived interest in hydrothermal sites, pointing them out as a far-field source of some trace elements and isotopes (TEIs) (Resing et al., 2015; German et al., 2016; Fitzsimmons et al., 2017). Nevertheless, to date, the contribution of slow-spreading ridges to the trace metal pools is poorly constrained (German et al., 2016). The persistence of the hydrothermal anomaly in the water column is affected by physical and chemical speciation processes, including complexation with organic ligands and the formation of iron-sulfide colloidal nanoparticles (Luther et al., 1992; Fitzsimmons et al., 2017). This last process is even more favorable at TAG than in other close-by hydrothermal sites at the MAR, due to its high-sulfide content (Rona, 2005).

In the absence of important external sources, the vertical distribution of dissolved iron (dFe) in the ocean presents a nutrient-like profile, indicative of its biological role, with near constancy at depths below 1000 m (~0.7 nmol L^{-1}, Boyd and Ellwood, 2010; Johnson et al., 1997). In contrast, dissolved manganese (dMn) concentrations in deep waters, in the absence of submarine manganese sources such as hydrothermal activity and sediment inputs, are low and uniform (Statham et al., 1998), ranging from 0.1 to 0.2 nmol kg^{-1} in the Central Atlantic Ocean (Hatta et al., 2015). Since 1985, the combination of positive anomalies of dMn and increases in suspended matter have been used as a tracer for hydrothermal plumes including the TAG neutrally buoyant plume (Klinkhammer et al., 1986; Speer and Marshall, 1995).

Hydrothermal vents act as potentially major sources of trace metals (TMs) to the deep Atlantic Ocean (e.g. Tagliabue et al., 2010). Previously, models have tried to represent the relative role played by ridges in different ocean basins. However, they have encountered significant uncertainties caused by the scarcity of data from slow-spreading ridges (German et al., 2016; Tagliabue and Resing, 2016) especially at distances further than 1 km from high-temperature vent sites. This was previously described during the 1990s when German and Sparks (1993) emphasized the need to study the TAG hydrothermal plume over scales of 1 to 10 km, based on the re-entrainment results from their particle recycling model, where sinking particles can get reintroduced into the plume, potentially desorbing Fe. The combination of TAG's location and its hydrothermal venting results in an input of numerous chemical components into the relatively newly formed North Atlantic Deep Water with an important dispersion potential due to the global thermohaline conveyor (Statham et al., 2005).

Recent studies have indicated that hydrothermal plumes present a nearly conservative dFe behavior (Resing et al., 2015), with plumes extending from short distances in the Atlantic, Indian, Arctic, and Southern oceans (Middag et al., 2009, 2011; Nishioka et al., 2013; Saito et al., 2013; Conway and John, 2014; Measures et al., 2015) to long in the Pacific (Resing et al., 2015; Fitzsimmons et al., 2017). Both Fe-stabilizing ligands (Bennett et al., 2008; Sander and Koschinsky, 2011) and unreactive Fe nanoparticles or colloids (Yücel et al., 2011) should regulate the stabilization of Fe against loss from solution. High- and low-temperature vents have different discharged metal concentrations, hydrogen sulfide concentrations and high biological activity, together with degradation of biomass, specific synthesis by microbial activities and abiotic formation of organic molecules that could be potential sources of dissolved organic molecules in both types of vents (Sander and Koschinsky, 2011). Ligands also form organically complexed Fe(II) species present during buoyant plume rise, potentially lowering the Fe(II) oxidation rate (Bennett et al., 2008). Stimulated by observations of Fe distributions in the near-field neutrally buoyant plume at 9°45'N on the Northern East Pacific Rise, Field and Sherrell (2000) calculated Fe(II) oxidation rates for a variety of vent sites in the Atlantic and Pacific as a function of ambient deep water pH, oxygen, temperature, salinity and pressure, based on inorganic kinetic rate constant data of Millero et al. (1987), and concluded that half-live time for Fe(II) oxidation and the resultant formation of Fe oxyhydroxide particles should vary substantially among vent sites in different ocean basins, from 20 minutes to >6 hours. The only field study to test this prediction was carried out at Indian Ocean vent sites, and the rate observations largely supported these predictions, while suggesting the possibility that Fe(II) interactions with dissolved organic matter may slightly modify the governing equations (Statham et al., 2005).

In this context, one of the primary goals of the HERMINE process study cruise (GEOTRACES GApr07; DOI 10.17600/17000200) was to understand the dispersal and biogeochemical reactivity of Fe and Mn within the TAG hydrothermal plume, along the mixing continuum with seawater. Here, we present the concentrations of dFe and dMn measured at 9 stations in close vicinity to TAG in order to describe their variability inside the neutrally buoyant plume (NBP). This unprecedented high sampling resolution provides an in-depth view of the reversible exchanges occurring within the NBP. The model presented in this paper takes into account most of the state-of-the-art processes controlling Fe behavior along hydrothermal plumes in the oceans and could be applied to characterize its distribution in slow spreading ridges.

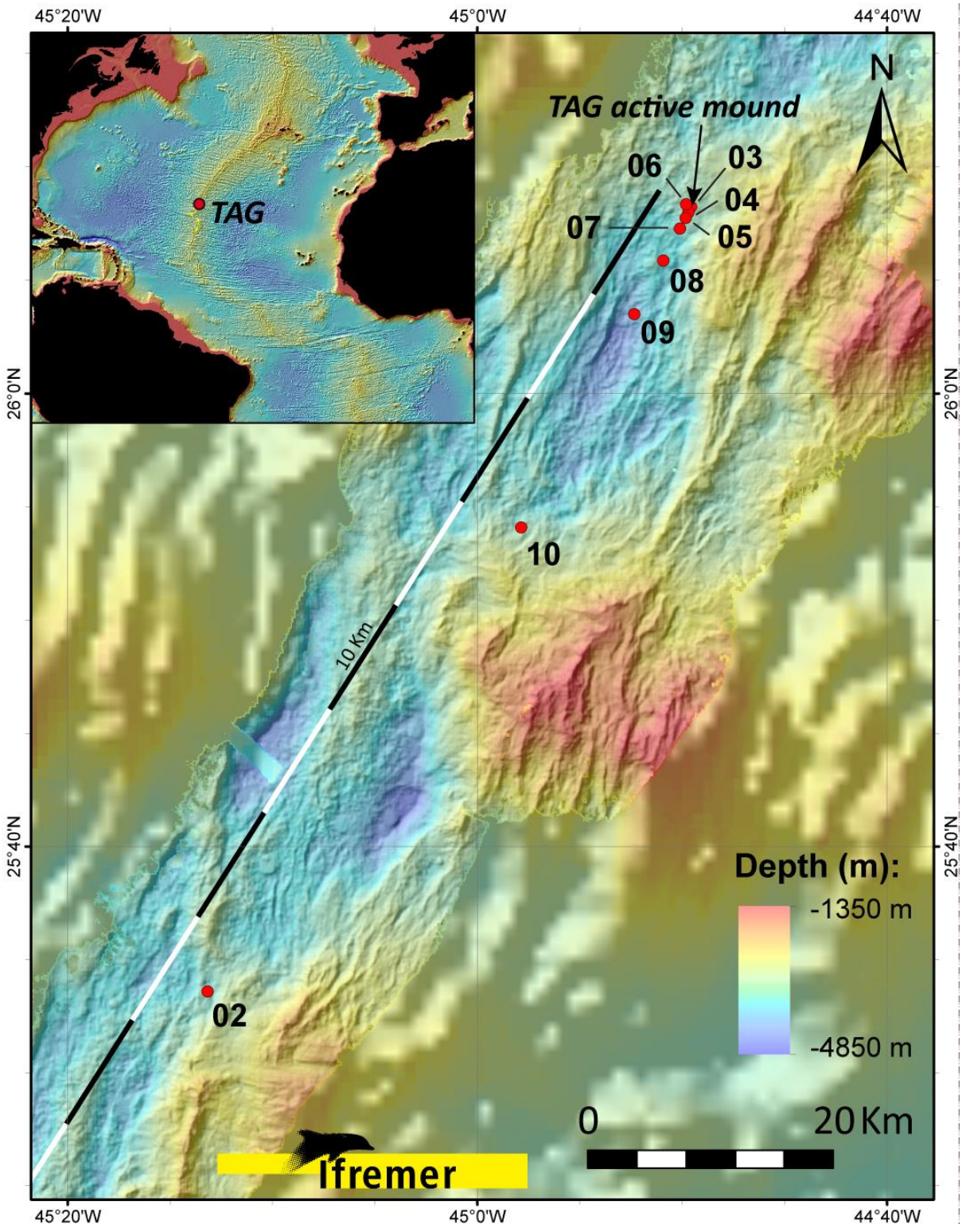

Figure 5-1. Bathymetric map of the Mid-Atlantic Ridge around the TAG hydrothermal mound. Red circles represent stations where the trace metal rosette was deployed. Station 3 was deployed at the mound, station 6 was deployed 0.5 km to the west. Stations 4, 5, 7, 8, 9, 10 and 2 were respectively deployed 0.5, 1, 2, 5, 10, 30 and 75 km SSW of TAG. Inset is an index map of the location of the TAG hydrothermal site in the North Atlantic Ocean.

5.3. Materials and methods

Seawater samples were collected during the HERMINE GApr07 process study cruise around the TAG hydrothermal site (Figure 5-1). The cruise took place during spring 2017 (13th March to 28th April) onboard the French Research Vessel N/O *Pourquoi Pas?*.

5.3.1. Sampling strategy

The sampling strategy allowed for high-resolution sampling within the TAG rising and distal NBP. Onboard Lowered Acoustic Doppler Current Profiler (L-ADCP) combined with the TM-clean rosette fitted with a conductivity temperature depth sensor (CTD, Seabird 911plus) and suspended matter data were processed in real time so that the NBP could be followed while maintaining the highest possible spatial resolution. The highest suspended matter values (0.089 NTU) were measured at the NBP depths at station 6, located 0.5 km west (W) from the vent site (26° 8.4′ N, 44° 49.8′ W). However, TAG is situated in the rift valley of the MAR. As a result, while the plume is initially transported westward the ridge blocks its pathway and thus the plume does not follow a straight, uninterrupted path (Figure 5-1). This is especially prevalent at depths deeper than 3000 m.

After deploying a L-ADCP at TAG, a clear 229° angle was observed in the current direction at the depth of maximum suspended matter signal (Cathalot et al., in prep). In light of these results, it was thus decided to follow the south-southwest (SSW) direction, with NBP suspended matter values reaching 0.086 NTU 0.5 km from the vent site. Stations were therefore arranged along the current flow path, with increasing distance SSW from the vent site, at 0.5, 1, 2, 5, 10, 30, and 75 km (Figure 5-1). For this study, sampling efforts concentrated on the NBP, with half of the sampling depths encompassed inside the NBP (between 2965 and 3607 m), and almost two-thirds of the chosen depths being deeper than 2500 m.

5.3.2. Sample collection and analysis

Seawater samples were collected according to the GEOTRACES guidelines (http://www.geotraces.org/images/Cookbook.pdf), using a TM-clean polyurethane powder-coated aluminum frame rosette equipped with twenty-four 12-L, externally closing, Teflon-lined, GO-FLO bottles (General Oceanics) and attached to a Kevlar® line. The cleaning protocols for sampling bottles and equipment also followed the GEOTRACES Cookbook.

Upon recovery of the TM rosette, GO-FLO bottles were transported to a class ISO 6 TM-clean sampling van equipped with a ISO 5 laminar flow hood. The bottles were inverted three times to avoid settling of particles and pressurized to < 50 kPa with 0.2 µm filtered dinitrogen (N_2, Air Liquide). Sub-samples for dissolved TMs were collected in TM-clean low-density polyethylene bottles (Nalgene®) after filtration through acid-cleaned 0.45 µm pore-size polyethersulfone filters (Supor®, 25 mm) mounted on Swinnex® filter holders, following Planquette and Sherrell (2012). Seawater samples were then acidified to ~ pH 1.7 using hydrochloric acid (HCl, Ultrapure® Merck) under the class 100 laminar flow hood, double bagged, and stored at ambient temperature in the dark before shore-based analysis.

Trace metal measurements were carried out within 12 months after collection on a SF-HR-ICP-MS Element XR instrument (Thermo Fisher, Bremen, Germany), at Pôle Spectrométrie Océan (IFREMER, France). The spectrometer was coupled to an ESI seaFAST-pico™ introduction system and run with a method analytically similar to that of Lagerström et al. (2013). Calibrations were performed using low trace metal concentration internal seawater with known standard additions of a mixed solution containing Fe, Mn, Cu, Co, Ni, Pb and Zn. Nine-point calibrations were performed at the beginning, half-way and at the end of the run. The average slope of the first and second calibrations was used for the first half of the samples, while the second and third calibration were used for the second half of the samples. This standard addition technique effectively minimized the sensitivity differences caused by the matrix effect. We performed an internal standardization using 10 ppb In (indium) in order to correct the changes of sensitivity of our instrument. Four triplicate reference materials (SAFe S, SAFe D2, GSC and GSP, Table 5-1) were analyzed daily during each analytical run to ascertain accuracy and precision. Analyzed SAFe standards were validated with the consensus values, but we could not validate for the GSC and GSP standards. Precision was further assessed through duplicate samples (every 10^{th} sample was a duplicate). The computed average dMn and dFe deviation from duplicate measurements of the same sample with concentrations < 1.5 nmol kg^{-1} was 64 and 66 pmol kg^{-1}, respectively (n = 44). The standard deviation of the reported concentrations was calculated from the duplicate analysis of samples combined with the concentration determination from the three daily calibration curves. The detection limit (defined as three times the standard deviation of the blank) was 0.018 nmol L^{-1} for both elements.

CRM		SAFE D2			SAFE S			GSP			GSC		
		Average	SD	n	Average	SD	n	Average	SD	n	Average	SD	n
dMn (nmol kg^{-1})	This study	0.34	0.07	20	0.76	0.07	9	0.18	0.08	4	0.61	0.08	18
	Consensus	0.35	0.05		0.79	0.06		0.78	0.03	9	2.18	0.08	8
dFe (nmol kg^{-1})	This study	0.96	0.08	20	0.16	0.01	9	0.26	0.01	4	1.09	0.11	18
	Consensus	0.93	0.02		0.09	0.01		0.16	0.05	11	1.54	0.12	13

Shown are the average concentrations in nmol kg^{-1}, standard deviation in nmol kg^{-1} and the number of replicates.

Table 5-1. Intercomparison reference material values obtained during the analysis of the samples. Shown are the average concentrations in nmol kg^{-1}, standard deviation in nmol kg^{-1} and the number of replicates.

5.4. Results

5.4.1. Gauging hydrothermal imprint using physical properties

Physical properties such as potential temperature (θ), salinity (S), potential density (σ), and suspended matter were closely monitored to identify the hydrothermal signal (θ and σ have been computed using ocean surface as the reference value). At the vent site station, at depths greater than 3145 m, variations in the physical properties of seawater were associated with hydrothermal activity (Figure 5-2 a). The hydrothermal source produced a plume, the buoyant plume (BP), that was less dense than the surrounding water. The BP ascended until its density reached the density of the surrounding water, thereby transforming into the NBP. A θ-S plot (Figure 5-3 a) shows three main differences with respect to a profile of a non-hydrothermally affected station. The hydrothermal imprint on the water column was still clearly visible 0.5 and 1 km SSW of TAG (Figure 5-3 b and c), with increases in θ-S at both stations. At these distances, the NBP was better mixed, as interpreted from the lack of crossover of deeper waters in the θ-S plot (Figure 5-3 a inside the ellipse compared to Figure 5-3 b-d). The hydrothermal θ-S signal was lost 2 km SSW of TAG (Figure 5-3 d).

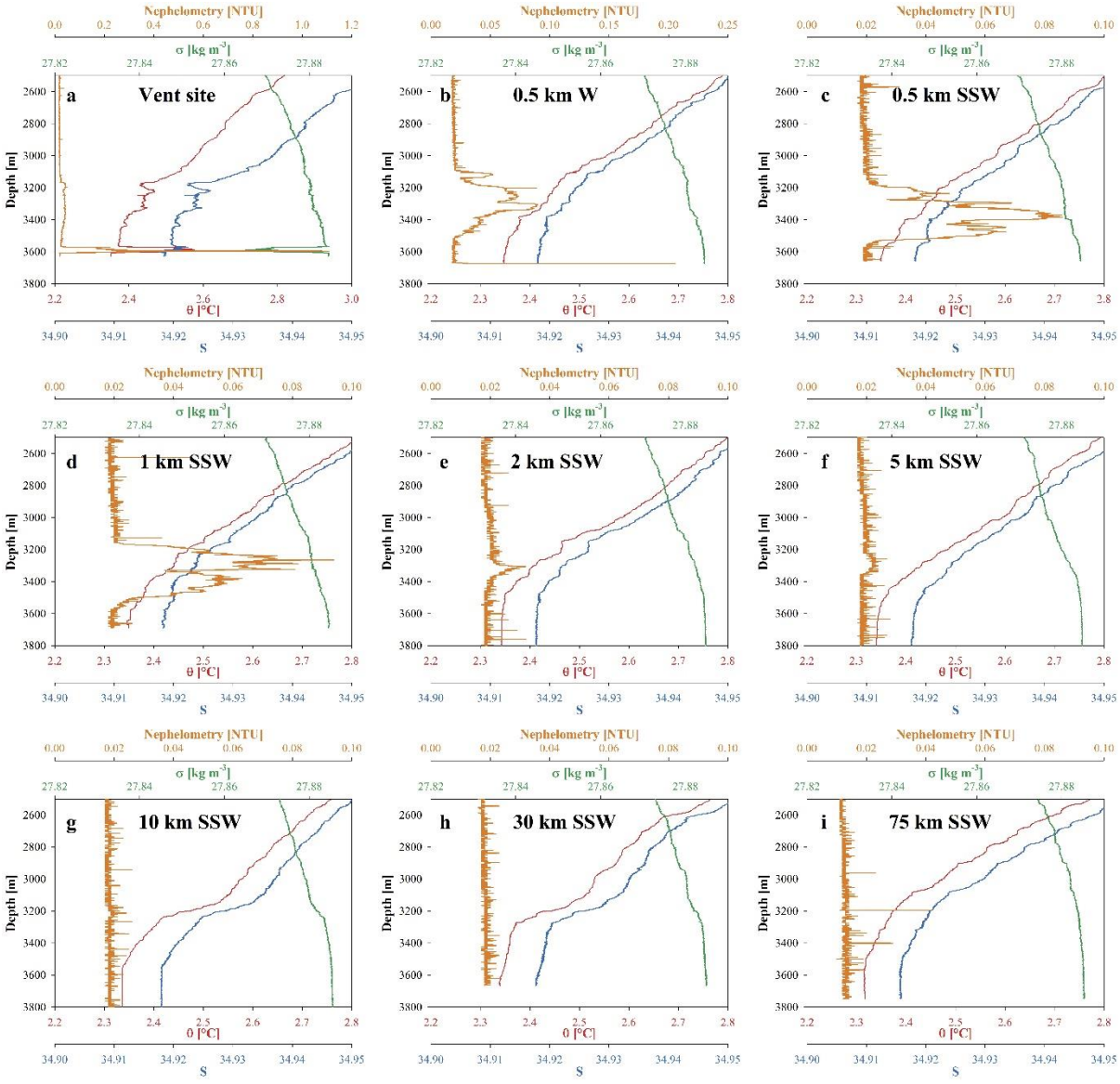

Figure 5-2. Vertical profiles for depths deeper than 2500 m of potential temperature θ (red), salinity S (blue), potential density σ (green), and suspended matter/nephelometry (orange) for station situated at TAG vent site (a; Stn 3), 0.5 km W (b; Stn 6), 0.5 km SSW (c; Stn 4), 1 km SSW (d; Stn 5), 2 km SSW (e; Stn 7), 5 km SSW (f; Stn 8), 10 km SSW (g; Stn 9), 30 km SSW (h; Stn 10) and 75 km SSW of TAG (i; Stn 2).

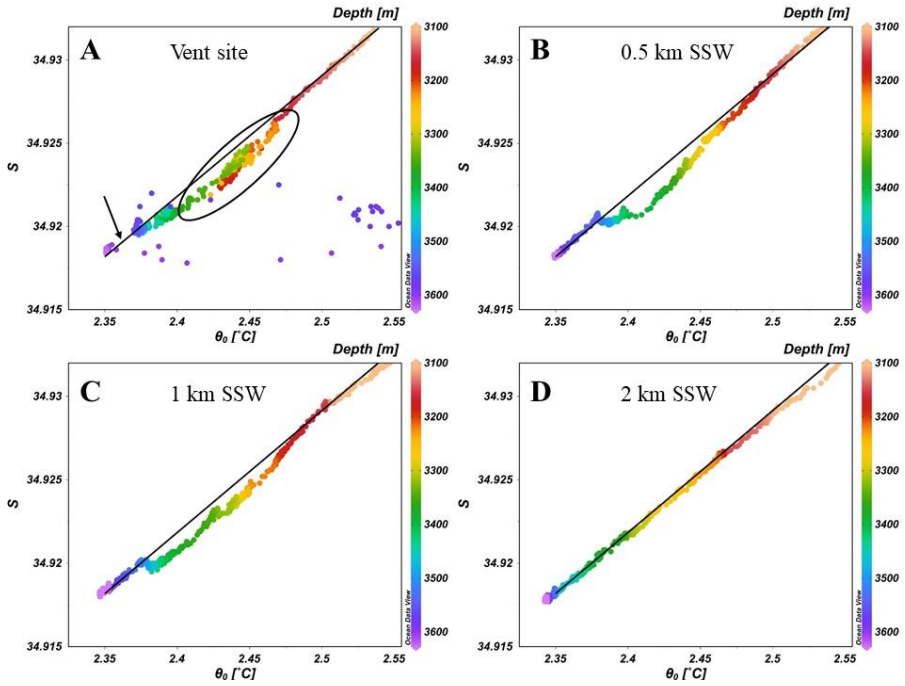

Figure 5-3. θ-S relation in the water column at the TAG site (A), 0.5 km SSW (B), 1 km SSW (C) and 2 km SSW (D). The potential temperatures increased with respect to background levels as a response to the introduction of warm hydrothermal fluid (datapoints diverge from the straight line). The arrow points to a missing section located around 3607 m as a result of sampling close to the hydrothermal vent, which showed 0.5 ˚C warmer (up to 2.85 ˚C) and saltier water than background level values, but in agreement with a hydrothermal source (Rudnicki and Elderfield, 1993; Goto et al., 2007). The hydrothermal source produced a plume, the buoyant plume (BP), that was less dense than the surrounding water. The ascension of the BP caused a non-linearity in θ-S with depth between 3165 and 3370 m. The BP ascended until its density reached the density of the surrounding water, thereby transforming into the NBP (ellipse).

Higher than background levels of suspended matter observed hundreds of meters above the sea floor indicated the presence of increased concentrations of suspended particulate matter, which are characteristic of hydrothermal plumes (German et al., 1996). At the vent site, two suspended matter maxima were observed. A deep maximum next to the vent site between 3563 and 3607 m (1.11 NTU) and a shallower maximum between 3167 and 3475 m (0.05 NTU) corresponding to the NBP signal (Figure 5-2 a). The maximum suspended matter signal, observed close to the sediment bed, does not result solely from hydrothermal activity, but instead reflects a combination of hydrothermal particles and resuspended sediments. Following the SSW direction, pronounced increases with respect to background levels in suspended matter were observed in the first 10 km from the TAG site (Figure 5-2 a to g). At 30 km SSW, the suspended matter signal was reduced by 98 % with respect to the maximum observed at the vent sites' BP which made it impossible to clearly differentiate the depth at which the NBP was located.

Previous studies have reported TAG's NBP to ascend 300 to 400 m above the seafloor (Klinkhammer et al., 1986; Rona and Speer, 1989; German et al., 1991a), with the core of the plume detected at depths of 3200-3500 m (German et al., 1991b; Goto et al., 2007; Hatta et al., 2015). In this study, the maximum suspended matter signal in the NBP ranged from 3385 m deep at 0.5 km SSW of TAG (Figure 5-2 b) to 3210 m at 10 km SSW (Figure 5-2 g), remaining within the previously reported depth ranges, but ascending 175 m in the first 10 km. We attribute the ascension of the plume to water mass transport. The high suspended matter signal at the NBP was bordered by water masses of two densities, of $\sigma = 27.880$ kg m^{-3} and $\sigma = 27.883$ kg m^{-3} above and below, respectively. At the vent site, the BP was situated between 3455 and 3555 m, while the NBP was found between 3165 and 3455 m. The NBP could be located using the changes in the gradients of θ, S, and σ ($\sigma = 27.880$ and 27.883 kg m^{-3}, Figure 5-2 h and i). This confirmed that its upper limit continuously shallowed from 3165 to 3110 m and its thickness decreased from 442 m at the vent site (Stn 3), to 138 m 5 km from the vent site (Stn 8), followed by an increase up to 205 m 10 km from the vent site (Stn 9). The variable thickness can be caused by internal waves generated from having two water masses, the plume and the surrounding water, which have different densities and could move at different speeds, as can be observed at the Rainbow hydrothermal site (van Haren et al., 2017).

Suspended matter results also showed the existence of a deep nepheloid layer, below 3800m, from 2 km SSW of TAG and extending through until 10 km SSW of TAG (Figure 5-4 a). This left a vertical "buffer" zone greater than 400 m between the NBP and the benthic nepheloid layer, preventing any direct interactions between the pools of particles. Dissolved Fe and dMn concentrations in the buffer zone were significantly lower than in the bottom section of the NBP (see Figure 5-4 a-b), further confirming there was no interference from the nepheloid layer on the NBP.

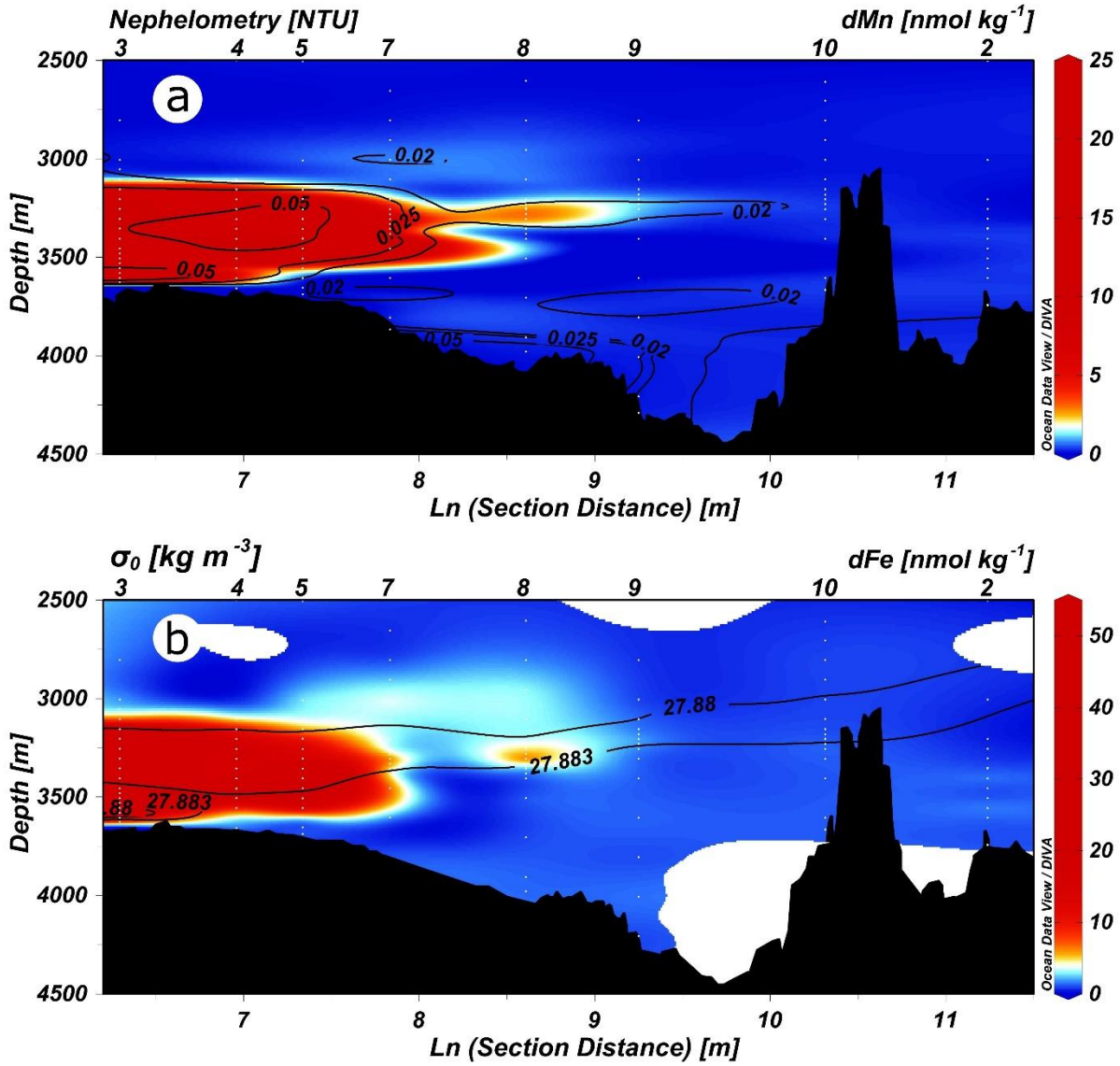

Figure 5-4. Zonal concentration distribution for dissolved manganese with nephelometry contours (a), and dissolved iron with the 27.880 and 27.883 kg m^{-3} isopycnals (b) , following the SSW TAG hydrothermal neutrally buoyant plume. In the bottom x-axis, a natural logarithmic scale of the distance in meters is used in order to provide better visual resolution of the station properties. Station numbers are shown on the top x-axis. White dots represent depths at which there is a data point for the specific variable. For Figures. c-e, 1 m-binned CTD sensor data is displayed.

5.4.2. Hydrothermal imprint on trace metal distribution

The vertical and horizontal distribution of TMs can help us to understand Fe and Mn residence times in the water column and their transport across ocean basins. Past work at the fast-spreading East Pacific Rise, revealed a hydrothermal plume which transported dFe over 4000 km (Resing et al., 2015; Fitzsimmons et al., 2017). Similarly, in the South Atlantic Ocean, slow-spreading ridges have been suggested to export dFe over 1000 km, reaching the Southern Ocean (Saito et al., 2013). Although geological conditions differ between these sites, previous

existing datasets at TAG describe a hydrothermal plume with a potential impact between 20 and 1000 km away from its source (Rona, 1980; Klinkhammer et al., 1986; Conway and John, 2014).

The mixing of hydrothermal fluid with seawater results in the production of particulate matter. In the NBP, the most common precipitates are collectively referred to as oxyhydroxides, which are characteristic components of marine sediments in hydrothermal zones (Nelsen et al., 1987). Due to their chemical composition, these hydrothermally produced particles act as efficient scavengers for many trace elements from the surrounding seawater (Pichler and Veizer, 1999).

In 2010–2011, the U.S. GEOTRACES North Atlantic Cruises: GEOTRACES GA03w (Hatta et al., 2015) crossed the North Atlantic Ocean, zonally crossing the TAG hydrothermal vent during the transect. Stations unaffected by coastal and shelf margins or hydrothermal emissions showed an average background dFe and dMn concentrations for the deep ocean (>2500 m) from 0.6 to 0.8 nmol kg^{-1} and from 0.1 to 0.2 nmol kg^{-1}, respectively.

In contrast, the concentrations of both of these metals within the TAG hydrothermal fluids can be orders of magnitude higher, with end member concentrations of 5.1 ± 0.5 mM and 0.69 ± 0.02 mM respectively for Fe and Mn (Chiba et al., 2001). Within the NBP, dFe and dMn concentrations of up to 68 nmol L^{-1} and 33 nmol L-1were measured during the GA03w cruise (Hatta et al., 2015). According to previous work (Edmonds et al., 1996; Chiba et al., 2001), the black smoker fluid composition has not shown any significant changes over time.

5.4.2.1. Dissolved manganese distribution

At the vent site station, the dMn maximum was found at 3605 m depth (approximately 45 m above the seafloor), reaching 71.2 ± 5.6 nmol kg^{-1} (Figure 5-5 a). This high dMn concentration could be due to hydrothermal activity and/or caused by sediment interactions, such as diffusion, tidal pumping of porewaters and bioirrigation (Elderfield, 1977; Noble et al., 2012; Cheize et al., 2019), although there was no increase in pMn. At 3580 m depth, dMn concentrations decreased to 0.14 ± 0.01 nmol kg^{-1}, which is in the upper range of dMn background level concentrations (0.10-0.15 nM, Hatta et al., 2015; van Hulten et al., 2016). Ascending from 3555 m to 3204 m, dMn concentrations in the BP and the NBP increased to a local maximum of 35.6 ± 2.8 nmol kg^{-1}. From 3204 m to 3104 m concentrations decreased to background levels.

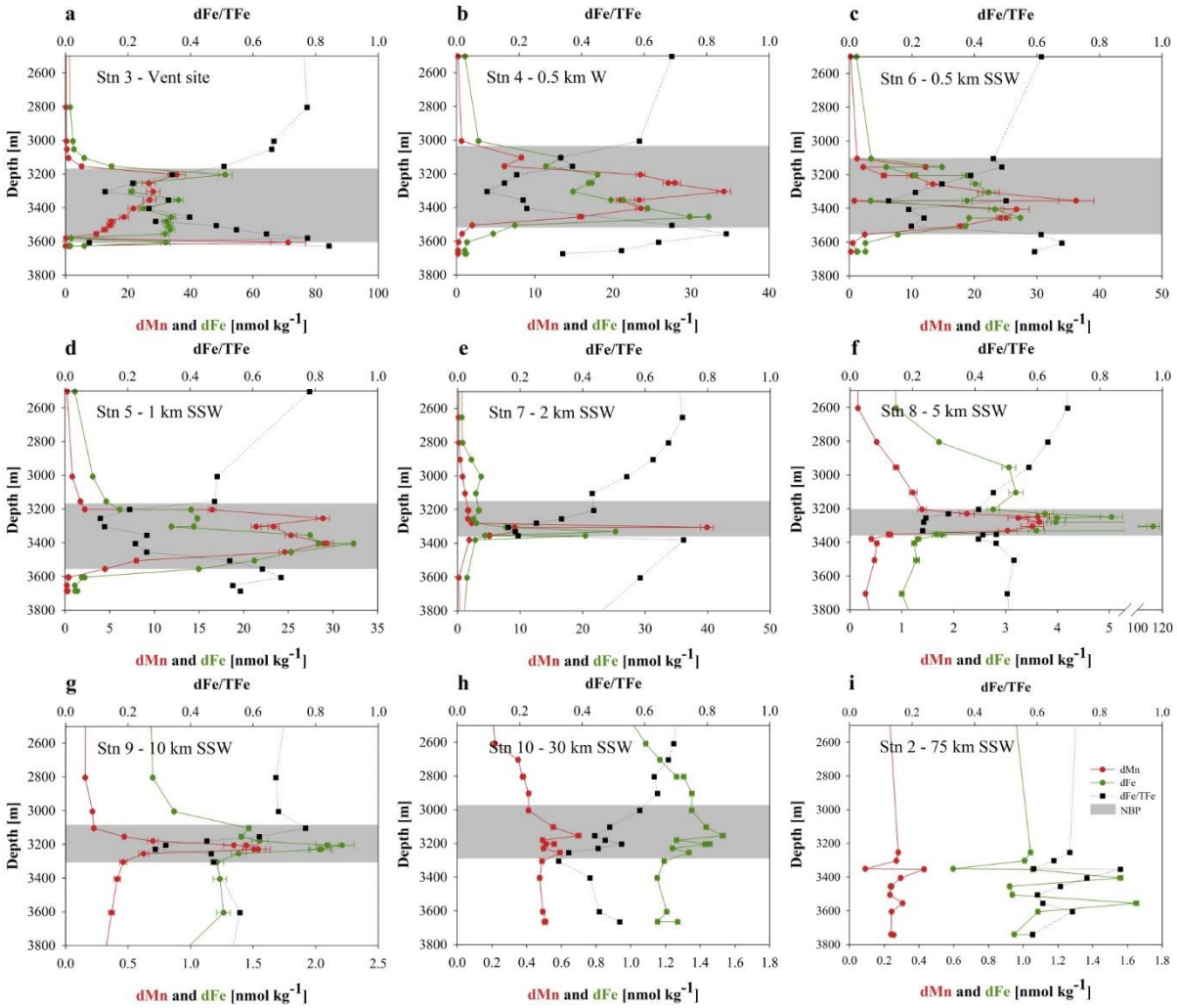

Figure 5-5. Vertical profiles for dMn (red circles), dFe (green circles), and the fraction of dFe as the total Fe pool (black squares) at stations located at TAG vent site (a; Stn 3), 0.5 km W (b; Stn 6), 0.5 km S (c; Stn 4), 1 km SSW (d; Stn 5), 2 km SSW (e; Stn 7), 5 km SSW (f; Stn 8), 10 km SSW (g; Stn 9), 30 km SSW (h; Stn 10) and 75 km SSW of TAG (i; Stn 2). The grey shading shows the NBP depth using σ = 27.880 and 27.883 kg m^{-3}.

Half a kilometer west of TAG (Figure 5-5 b), three variations within the plume were observed with maximum dMn concentrations located between 3100 and 3410 m (Figure 5-5 b). Similarly, 0.5 km SSW of TAG (Figure 5-5 c), three plume variations were observed, although the two shallowest variations were located 50 meters deeper than their counterparts to the west (Figure 5-5 c). At the station situated 1 km SSW (Figure 5-5 d), the lower plume variation remained at the same depth (3404 m), while the upper two plume variations combined and were situated at 3255 m. Further away, at 2 km SSW, there were no variations within the plume (Figure 5-5 e), and the dMn maximum was located at 3305 m depth. The dMn profile shape at these stations followed the same trend as nephelometry (Figure 5-4a), adding further evidence that we sampled multiple plume sections.

Dissolved Mn concentrations reached up to 0.43 ± 0.01 nmol kg^{-1} (maximum at 3355 m) 75 km SSW of TAG, more than twice the expected background concentrations (0.10-0.15 nM) (van Hulten et al., 2016). The persistence of dMn 75 km away from the vent site, suggests slow oxidation rates of dMn along the spatial scales considered in our study. Previous work performed at TAG has used dMn as a hydrothermal tracer for the TAG neutrally buoyant plume (Klinkhammer et al., 1986; Speer and Marshall, 1995). To evaluate the possibility of using dMn as a hydrothermal tracer, we considered that precipitation processes could affect the distribution of dMn through transfer to the particulate pool. As pMn concentrations remained orders of magnitude lower than dMn through all stations (58 ± 30 pmol kg^{-1}, n = 196; Cheize, in prep.), and in agreement with the global deep ocean pMn concentration ~25 pM (van Hulten et al., 2016), it seems that, at the spatial scale of our study, precipitation of dMn is therefore unlikely to be a major loss term of dMn with respect to dilution of the NBP. Accordingly, and in agreement with previous studies (eg. Field and Sherrell, 2000), we considered dMn as a conservative tracer at the TAG NBP, whose only loss term was dilution and dispersion.

5.4.2.2. Dissolved iron distribution

Overall, dFe profiles exhibited similar behavior to dMn profiles, with some discrepancies between dFe and dMn observed at the vent site station (Figure 5-5 a). In contrast to dMn and turbidity maxima, the dFe maximum was not observed at the vent depth (3605 m; 32.1 ± 1.4 nmol kg^{-1}), but was found higher in the water column at the top of the NBP. The lack of dFe maximum at the vent depth can be explained by aggregation/adsorption of Fe into the particulate Fe (pFe; grain/mineral or aggregate collected on the 0.45 µm pore size filter), leaving only 8 % of the total Fe (TFe = dFe + pFe) in the dissolved phase, compared to 34 % at the dFe maximum. Nevertheless, the apparently "low" dFe:dMn ratio could also be explained from manganese enriched sediments (Noble et al., 2012; Cheize et al., 2019). Entrainment of Mn rich sediment porewaters, diffusion into overlying bottom waters and recycling of Mn oxides could create and maintain the elevated dMn that we measured. In parallel, these Mn oxides could also scavenge any surrounding dFe (Machado-Infante et al., 2016).

The vertical dFe profile at the TAG vent station presented more homogeneous concentrations in the BP (3555 m to 3455 m; 33 ± 1 nmol kg^{-1}; n = 5) than in the shallower NBP (3405 m to 3165 m; 31 ± 13 nmol kg^{-1}; n = 5), as observed in the θ and S profiles (Figure 5-2 a). Water tank experiments of multi-phase plumes (including gas, different density and size of particles

(including the colloidal size) and the soluble phase) in uniform and stratified crossflows have shown that multi-phase plumes behave as mixed single-phase plumes up to a critical height, after which the particulate phase separates from the plume (Socolofsky and Adams, 2002). This would explain the more homogeneous concentrations in the BP and the variability in the NBP. To corroborate this hypothesis, future studies could determine the chemical composition of colloids and particles collected at different depths within the NBP, and combine this information with the physical properties. Dissolved Fe concentrations were still elevated compared to background levels 75 km SSW of TAG (Figure 5-5 i) following the NBP dispersion direction. Even though the maximum dFe concentration (1.65 ± 0.02 nmol kg^{-1}) was less than 2 % of the maximum concentration measured at the hydrothermal vent site, the values in the bottom 500 m of the profile (1.11 ± 0.25 nmol kg^{-1}) were double the reported background level concentration. Analogous studies found transport over greater distances (Saito et al., 2013; Fitzsimmons et al., 2015; Hatta et al., 2015) suggesting the elevated dMn and dFe concentrations detected 75 km from the vent site at depths deeper than 3200m could be a result of the hydrothermal transport from TAG. Previous research in hydrothermal environments has shown that the dFe would mainly comprise of colloidal species, while the dMn would be predominantly soluble (Fitzsimmons et al., 2017), though we could not determine with certainty the origin and pathway of these elevated concentrations due to lack of ancillary hydrothermal tracers.

5.5. Discussion

Our results demonstrated that the transport of both dMn and dFe could be observed at least up to 30 km from the vent site. Nevertheless, the discrepancies between dFe and dMn profiles pointed to possible divergences in the transport of these two dTMs. Basin-scale transport of hydrothermally generated TM in fast-spreading ridges has previously been attributed to the reversible exchange dynamics between dissolved and particulate phases that may occur in the NBP (Fitzsimmons et al., 2017). With this in mind, we developed a 5-box model to reveal the importance of distinctive processes that could affect both TMs differently. Consequently, this model presents the evolution of Fe within the plume and the contribution of each loss term as the NBP was transported away from the vent site.

5.5.1. Model assumptions

The design of the model follows a simple 5-box model (Figure 5-6). The box height was calculated from the NBP using the σ = 27.880 and 27.883 kg m^{-3} isopycnals. The lengths of the boxes were chosen from the sampled stations situated at the vent site, and at 1, 2, 5, 10, and 30 km away. The third dimension was given to the model by fixing its width to 1 m, to obtain the TM inventory in m^3. With this we eliminated extra assumptions on how the transverse horizontal concentrations of the NBP varied. To better constrain the width of the NBP, transversal tow-yos would have been required.

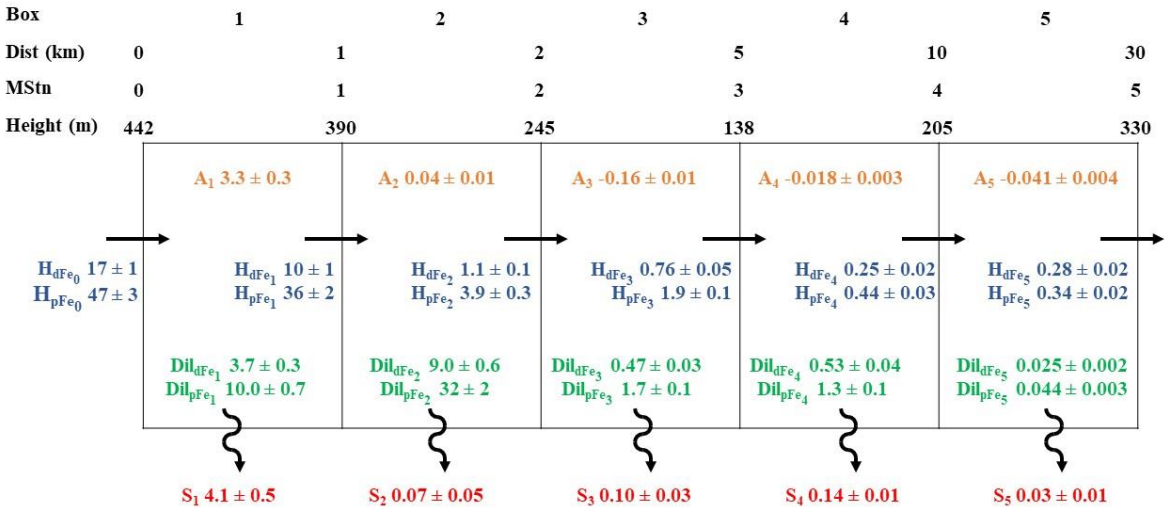

Figure 5-6. Dissolved and particulate iron 5-box budget of the TAG NBP . Numbers 1 to 5 on the top correspond to the number of the boxes. Below are depicted the distance from the TAG site, the number of the modelled stations, and the height of the NBP using σ = 27.880 and 27.883 kg m^{-3}. The box-model's $H_{i_{|n|}}$ (in blue), $Dil_{i_{|n|}}$ (in green), $A_{|n|}$ (in orange), and $S_{|n|}$ (in red) are followed by the modelled rate and error from the resolution of model equations combined with a Monte Carlo Method of error propagation. Units are in mol d^{-1}.

During the HERMINE cruise, all sampling stations followed the hydrothermal plume and no stations were carried out in non-hydrothermally affected waters. Consequently, water situated above and below the NBP, could potentially be affected by the hydrothermal signal. Therefore, to calculate the excess of dMn and dFe in the water column, we subtracted the background level concentrations using the 2010–2011 U.S. GEOTRACES North Atlantic Cruises: GEOTRACES GA03w (Hatta et al., 2015) which took place at the same latitude (crossing the TAG vent field) and assumed background dFe to be 0.70 nmol kg^{-1} and dMn to be 0.15 nmol kg^{-1}. To account for aggregation and disaggregation, all pFe and particulate Mn (pMn) concentrations were obtained from Cheize (unpublished data). Due to the low and stable pMn concentrations through all the samples (58 ± 30 pmol kg^{-1}, n = 196), we assumed that the interactions between the dissolved and particulate pools of Mn are negligible (Field and

Sherrell, 2000). Dissolved Mn was used as a conservative tracer, to identify the processes affecting the Fe distribution.

The model considers that the deep ocean is in steady state. Background level concentrations were considered constant throughout the water column. Only one source of TMs was considered to influence the system: the TAG source located at distance 0 km. With respect to the TM data, two assumptions were required. First, that the rosette was deployed crossing the core axis of the NBP. Second, we assumed that linear interpolation between the different data points in a profile faithfully represented the NBP concentrations (straight lines in Figure 5-5).

Finally, based on L-ADCP data (Cathalot et al., *in prep*), the horizontal velocity was rounded to 1.5 cm s^{-1} throughout the whole model to calculate the horizontal fluxes between boxes. This horizontal velocity agrees with the average value computed by Wichers (2005) from 50 hours of results from a deployed ADCP.

5.5.2. Model design

Modeled stations (MStns) were renamed by their location in the model (vent site, 1, 2, 5, 10, 30 km SSW of TAG as MStn 0 to 5. This produced five boxes ($1 < |n| < 5$), with sides $h_{|n-1}$ (left side, Figure 5-6) and $h_{|n}$ (right side) calculated from the NBP height; the length ($l_{|n|}$; m) calculated from the distance between the stations, and the width (w = 1 m) was assumed to be constant. Thus, the plume is modeled as a tall narrow wall of varying height with distance from the plume.

Each box had an average concentration ($[I_{|n|}]$; mol m^{-3}; Eq. 5-1), a volume $V_{|n|}$ (Eq. 5-2), and a total inventory ($Q_{i_{|n|}}$; mol; Eq. 5-3) of element *i*,

$$[I_{|n|}] = \frac{1}{h_{|n}} \int_{NBP_{bottom}}^{NBP_{top}} \rho \cdot ([i_{|nh}] - [i_{bg}])\ dh_{|n} \qquad (5\text{-}1)$$

$$V_{|n|} = \frac{h_{|n-1} + h_{|n}}{2} \cdot l_{|n|} \cdot w \qquad (5\text{-}2)$$

$$Q_{i_{|n|}} = [I_{|n|}] \cdot V_{|n|} \qquad (5\text{-}3)$$

Where $[I_{|n|}]$ is calculated from the integrated excess inventory (Eq. 5-1) using the measured concentration ($[i_{|nh|}]$; mol m^{-3}) at station n and depth h on the right side of the box, the background concentration ($[i_{bg}]$; mol m^{-3}), the potential density (ρ; kg m^{-3}) and the height of

the integrated area ($h_{|n}$; m). The data point at 3305 m at MStn 3 (5 km from TAG) was flagged as an outlier and therefore not considered due to its significantly higher concentration, compared to both the surrounding concentrations and compared to the vent site station.

	0	1 (0–1 km)	2 (1–2 km)	3 (2–5 km)	4 (5–10 km)	5 (10–30 km)
Volume (x10^6 m^3)		**0.416**	**0.318**	**0.668**	**1.620**	**5.350**
H_{dMn} (mol d^{-1})	13.488 ± 0.905	10.606 ± 0.712	1.162 ± 0.078	0.652 ± 0.044	0.201 ± 0.014	0.189 ± 0.013
H_{dFe} (mol d^{-1})	17.120 ± 1.149	10.124 ± 0.680	1.073 ± 0.072	0.761 ± 0.051	0.253 ± 0.017	0.278 ± 0.019
H_{pFe} (mol d^{-1})	46.910 ± 3.149	36.095 ± 2.423	3.915 ± 0.263	1.944 ± 0.131	0.442 ± 0.030	0.344 ± 0.023
H_{TFe} (mol d^{-1})	64.030 ± 4.293	46.219 ± 3.100	4.988 ± 0.334	2.705 ± 0.181	0.694 ± 0.047	0.622 ± 0.042
Dil_{dMn} (mol d^{-1})		2.882 ± 0.211	9.445 ± 0.635	0.509 ± 0.035	0.451 ± 0.030	0.013 ± 0.002
Dil_{dFe} (mol d^{-1})		3.657 ± 0.264	9.015 ± 0.605	0.470 ± 0.032	0.526 ± 0.035	0.016 ± 0.002
Dil_{pFe} (mol d^{-1})		10.022 ± 0.722	32.142 ± 2.158	1.716 ± 0.116	1.344 ± 0.090	0.028 ± 0.004
Dil_{TFe} (mol d^{-1})		13.679 ± 0.984	41.157 ± 2.760	2.186 ± 0.148	1.870 ± 0.126	0.044 ± 0.006
A_{dFe} (µmol m^{-3} d^{-1})		8.025 ± 0.622	0.112 ± 0.036	−0.275 ± 0.022	−0.013 ± 0.002	−0.008 ± 0.001
S_{pFe} (µmol m^{-2} d^{-1})		4130 ± 53	73 ± 46	33 ± 9	17.6 ± 1.6	1.4 ± 0.4

Table 5-2. Box model outputs (horizontal hydrothermal advective fluxes, $H_{i_{|n|}}$ (mol d^{-1}); dispersion and dilution fluxes, $Dil_{i_{|n|}}$ (mol d^{-1}); aggregation/disaggregation fluxes, $A_{|n|}$ (µmol m^{-3} d^{-1}); and sinking fluxes, $S_{|n|}$ (µmol m^{-2} d^{-1}) with errors computed from equations 1-11 using the Monte Carlo method of error propagation.

Four types of fluxes were considered in the model and reported on Eqs. 5-4 to 5-8 (units and results shown in Table 5-2). For each species *i*, a horizontal hydrothermal advective flux ($H_{i_{|n|}}$) in the export direction of the plume (positive x-axis (Figure 5-6)) was implemented. This flux went both in ($H_{i_{|n-1|}}$) and out ($H_{i_{|n|}}$) of each box (Eq. 5-4) and was calculated using the horizontal velocity $\vec{u}$, the concentration at the left side of the box $[i_{|nh|}]$ and the area of the left side of the box ($h_{|n-1} \cdot w$).

$$H_{i_{|n|}} = [I_{|n|}] \cdot \vec{u} \cdot h_{|n} \cdot w \quad (5\text{-}4)$$

We considered the existence of two endmembers, the hydrothermally affected seawater from the vent site, and the non-hydrothermally affected seawater. A conservative mixing of both of these two endmembers, could be computed using the excess dMn as the tracer found in the hydrothermally affected endmember which would be diluted (i.e. decreasing its concentration by mixing with seawater) and/or dispersed (i.e. physical transport of high concentrated water mass to less concentrated areas) ($Dil_{i_{|n|}}$; Eq. 5-5 and 5-6) with the non-hydrothermally affected seawater. Since $Dil_{i_{|n|}}$ represented the conservative mixing of the two endmembers, $Dil_{i_{|n|}}$ of dFe and pFe was proportional to the percentage decrease of dMn (Eq. 5-6).

$$Dil_{dMn_{|n|}} = H_{i_{|n-1|}} - H_{i_{|n|}} \quad (5\text{-}5)$$

$$Dil_{i_{|n|}} = Dil_{dMn_{|n|}} \cdot \frac{Q_{i_{|n|}}}{Q_{dMn_{|n|}}} \quad (5\text{-}6)$$

In the case of Fe, two more fluxes were considered, an aggregation/disaggregation process ($A_{|n|} > 0$ and $A_{|n|} < 0$, respectively) between dFe and pFe pools and the sinking of pFe ($S_{|n|}$). Both processes produced non-conservative behaviors. We used aggregation and disaggregation in their broad definition. The operationally defined dissolved fraction (<0.45μm), is the sum of the soluble fraction (<0.02 μm) and the colloidal fraction (between 0.02 and 0.45 μm). In the soluble fraction Fe(II) oxidizes in minutes to Fe(III), which is less soluble (Santana-Casiano et al., 2005). Iron(III) can adsorb to particles in the plume, therefore increasing the Fe content in the measured particulate phase. This would be accounted for in the aggregation process. Conversely, the desorption of Fe from large particles (particulate fraction, > 0.45 μm) would be accounted for as a negative aggregation value (disaggregation). In the hydrothermal plume, most of the Fe has been found in the colloidal size fraction (Fitzsimmons et al., 2017; Lough et al., 2019b). These nanoparticles can combine, resulting in greater than 0.45 μm particles which would be operationally defined as particulates. As such, the dFe pool depends on the balance between stabilization processes and the reversibility of exchange onto small, sinking particles.

Since the model is assumed to be at steady state, $A_{|n|}$ and $S_{|n|}$ were calculated as follows (Eq. 5-7 and 5-8).

$$A_{|n|} = H_{dFe_{|n-1|}} - H_{dFe_{|n|}} - Dil_{dFe_{|n|}} \quad (5\text{-}7)$$

$$S_{|n|} = H_{pFe_{|n-1|}} - H_{pFe_{|n|}} - Dil_{pFe_{|n|}} + A_{|n|} \quad (5\text{-}8)$$

Equations 5-7 and 5-8 are obtained from the assumption that dMn is a conservative tracer. From this assumption, an excess decrease in dFe that is not proportional to the decrease in dMn is due to aggregation. Similarly, sinking is the excess loss of pFe with respect to dMn, but it also considers aggregation.

The resulting dMn, dFe and pFe fluxes estimated in our box model are shown in Eqs. 5-9 to 5-11.

$$\frac{d(dMn)}{dt}_{|n|} = \frac{1}{V_{|n|}} \cdot \left(H_{dMn_{|n-1|}} - H_{dMn_{|n|}} - Dil_{dMn_{|n|}}\right) \quad (5\text{-}9)$$

$$\frac{d(dFe)}{dt}_{|n|} = \frac{1}{V_{|n|}} \cdot \left(H_{dFe_{|n-1|}} - H_{dFe_{|n|}} - Dil_{dFe_{|n|}} - A_{|n|}\right) \quad (5\text{-}10)$$

$$\frac{d(pFe)}{dt}_{|n|} = \frac{1}{V_{|n|}} \cdot \left(H_{pFe_{|n-1|}} - H_{pFe_{|n|}} - Dil_{pFe_{|n|}} - S_{|n|} + A_{|n|}\right) \quad (5\text{-}11)$$

5.5.3. Model results and discussion

The analyzed trace metal data, and equations 5-1 to 5-11 were used as the input for a custom MATLAB 9.1 (MathWorks, R2016b) script. To understand the possible uncertainties of our model, we carried out the Monte Carlo method of error propagation. Fluxes and error obtained using the Monte Carlo method, are reported in Table 5-2 and displayed in Figure 5-6.

5.5.3.1. Fate of the plume signal

The plume signal rapidly decreased with the increase in distance from the vent site. Dilution and dispersion were responsible for a 21% decrease in the dMn concentration in the first km, which drastically increased to 91% decrease 2 km from the vent site, with $Dil_{dMn_{|n|}}$ rates of 2.9 ± 0.2 and 9.4 ± 0.6 mol d^{-1}, respectively (Table 5-2).

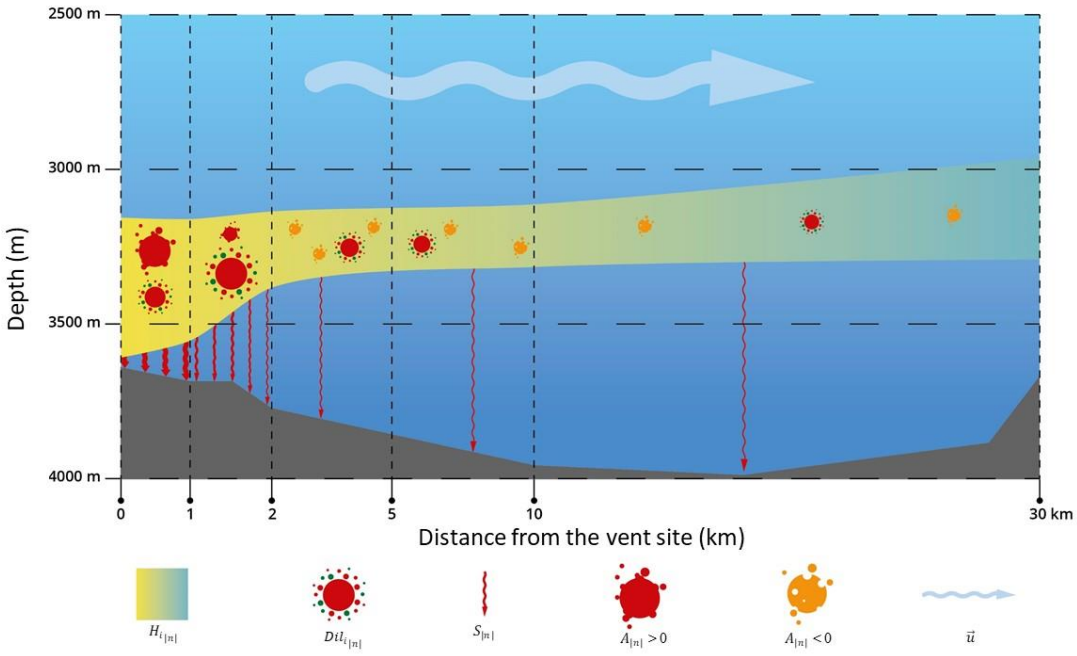

Figure 5-7. Schematic diagram of the main processes occurring inside the neutrally buoyant plume . The symbol size is representative of the importance of the process with respect to each section of the plume but are not to scale.

Three plume concentration loss processes, dilution and dispersion, aggregation, and sinking, were identified in our box model as processes affecting the Fe behavior. Where dilution and dispersion caused a concentration loss of dFe and pFe in all boxes; aggregation produced a dFe loss in boxes 1 and 2, and a pFe loss in boxes 3 to 5; and sinking only affected pFe (Figure 5-

7). In the first 30 km, dilution and dispersion of the NBP caused > 99 % of the dFe decrease from the NBP, except in the first km from the vent site, where aggregation was responsible for 47 % of the dFe decrease. Similarly, dilution and dispersion were the main pFe loss term. Sinking contributed 29 % of pFe decrease in the first km, while disaggregation (A < 0) combined with sinking caused a 62 % pFe decrease in the 10 to 30 km box.

These NBP loss terms influenced the fate of the plume. When looking at the evolution of its horizontal advection ($H_{dFe_{|n|}}$ and $H_{pFe_{|n|}}$), our results suggest that 93.7 % and 91.7 % of the hydrothermal dFe and pFe, respectively, had been lost within just 2 km from the vent site. The loss increased to 98.5 % and 99.1 %, respectively, 10 km from the vent site, and to 98.4 % and 99.3 % a further 20 km away. These Fe decreases may be due to reversible exchange processes between the dissolved and particulate phases and/or sinking of suspended particles.

5.5.3.2. Aggregation/disaggregation between dissolved and particulate iron

To observe whether reversible exchange dynamics played any role in TAG's NBP dispersal, the dFe/TFe ratio was considered. The dFe/TFe ratio varied through the NBP. At the vent site, aggregation was observed, with the dFe/TFe ratio decreasing from 0.77 at 3580 m to 0.21 at 3255 m (Figure 5-5). Overall, at the vent site inside the NBP, the ratio averaged 0.27. As the NBP dispersed (1 and 2 km away), the dFe/TFe ratio kept decreasing (0.22 and 0.21). At 5, 10, and 30 km away from the vent site, the dFe/TFe ratio increased to 0.28, 0.36 and 0.45, respectively.

This dFe/TFe ratio variability was controlled by changes in the fraction of dFe and/or pFe that was present in the TFe pool. An increase in the ratio may indicate the sinking of pFe (reducing the TFe pool), or the disaggregation of pFe into dFe (maintaining the TFe pool). On the other hand, a decrease in the ratio could also be caused by a decrease in dFe due to aggregation combined with limited sinking. Therefore, dFe/TFe can be used as a first indicator of aggregation or disaggregation processes without any prior information on rates and sources or losses of dFe and pFe.

In the model, the sign of $A_{|n|}$ follows the same pattern as the dFe/TFe ratio, $A_{|n|}$ > 0 when the dFe/TFe ratio decreases and vice-versa. This shows that aggregation of dFe predominates in the first km and persists into the second km away from the hydrothermal site, with rates of 8.0 ± 0.6 and 0.11 ± 0.04 nmol L^{-1} d^{-1} respectively. Between 2 and 5 km from the vent site,

disaggregation ($A_{|n|} < 0$, -270 ± 20 pmol L^{-1} d^{-1}) becomes more predominant than aggregation. Disaggregation is continuously observed after 5 and 10 km (-13 ± 1 and -8 ± 1 pmol L^{-1} d^{-1}, respectively), although at a much lower rate due to the decrease in the concentration of pFe.

Cheize et al., (2019) calculated the suspended particle dissolution rate during a 14-month period, following the addition of three sediment types collected around Kerguelen Island in the Southern Ocean. During their experiments, they observed net dissolution rates ranging from 1.74 to 7.77 pmol L^{-1} d^{-1}. Even though different minerals were involved in the two different regions, their dissolution rate is in the same order of magnitude as the disaggregation rate calculated in our model between 10 and 30 km from TAG (8 ± 1 pmol L^{-1} d^{-1}), supporting the validity of the hypotheses considered in our model.

5.5.3.3. Particulate iron sinking fluxes

Particle loss is responsible for the distal metalliferous sediments found below the dispersal trajectories of hydrothermal plumes (Gurvich, 2006). Dividing $S_{|n|}$ by the bottom surface area ($l_{|n|} \cdot w$) of each box, we obtained the average sinking flux in µmol m^{-2} d^{-1} in each box (Table 5-2). The highest pFe sinking flux ($S_{|n|}$) occurred in the first km from the vent site and exponentially decreased as the distance from the vent site increased. High suspended matter was observed in the four stations deployed in the first km (Figure 5-2 a-d). The high suspended matter identified an elevated particle load in the seawater, which likely caused the high sinking flux of 4130 ± 530 µmol m^{-2} d^{-1}. In contrast, 10 to 30km from the vent site, were the turbidity signal was reaching its limit of detection due to the decrease in particle abundance, the sinking flux decreased three orders of magnitude to 1.4 ± 0.4 µmol m^{-2} d^{-1}. Using dynamic curve fitting, two empirical equations (Eqs. 5-12 and 5-13; µmol m^{-2} d^{-1}) were computed to define the sinking flux by considering the distance at the limits of the boxes and the modelled average sinking rate within each box. S' considers the sinking rate by using the near boundary of each box ($l_{|0|}$ to $l_{|n-1|}$), therefore producing the fastest sinking rate; while S'' considers the sinking rate using the far boundary of each box ($l_{|1|}$ to $l_{|n|}$), with the corresponding slower sinking rate. These two equations create an envelope were the theoretical sinking rate at a distance (dist; in m) from the vent site could stand between S' and S''.

$$S' = 38 + 4093 \times e^{-4.7 \times dist} - 3.8 \times dist \quad (5\text{-}12)$$

$$S'' = 34 + 400000 \times e^{-4.6 \times dist} - 1.1 \times dist \quad (5\text{-}13)$$

Equations 5-12 and 5-13 were tested against the available Fe fluxes obtained from sediment trap measurements situated below a NBP. Toner et al. (2009) presented particle mass flux and total Fe weight % collected in sediment traps deployed ~5 m above the sea floor (~2,500 m depth) and ~100 m west of the Tica vent on the East Pacific Rise, a vent situated in a fast spreading ridge in the Pacific Ocean. Using their maximum particle flux (29.9 mg m^{-2} d^{-1}) and average total Fe weight % (2.69 %) we obtained a flux of 14.4 µmol m^{-2} d^{-1}. This flux is in the same range of variation as our estimated sinking flux, which provides some certainty in the order of magnitude of our results and further highlights the importance of studying the Fe-rich particle loss from the NBP which might affect other particle-reactive TEIs (German et al., 2016). Using Eqs. 12 and 13, the observed flux would be achieved in a sediment trap just below the NBP at a distance between 6.2 and 17.8 km from the vent site. For this sediment trap situated in a fast spreading ridge, Eqs. 5-12 and 5-13 underestimate the sinking flux, likely due to the difference in geology and chemistry between the vents from two contrasting spreading ridges, the vertical separation between the NBP and the sediment trap, and the faster dissipation of TAG's hydrothermal plume.

5.5.3.4. Size and sinking velocity of pFe loss

The sinking velocity of pFe could be estimated using Eq. 5-14.

$$v_{|n|} = \frac{S_{|n|}}{[I_{|n|}] \cdot \iota_{|n|} \cdot w} \qquad (5\text{-}14)$$

Values were equal to 45 ± 6 m d^{-1} in the first km and decreased to 5 ± 2 m d^{-1} between 1 and 10 km from TAG. Our settling velocity were in the same order of magnitude as those obtained by German and Sparks (1993), who estimated settling velocities (v) from 4 to 8 m d^{-1} for coarse particles (5 µm radius) and from 0.2 to 0.3 m d^{-1} for fine-grained particles (1 µm radius).

Using Stokes' Law (Eq. 5-15) and our $v_{|n|}$ values, we could estimate particle sizes.

$$v = \frac{2 \cdot g \cdot r^2 \cdot \Delta\rho}{9 \cdot \mu_w} \qquad (5\text{-}15)$$

Where g = gravitational acceleration (9.81 m s^{-2}); r = particle radius (m); $\Delta\rho$ = the density difference between the particle and the fluid; and μ = the dynamic viscosity of water (kg m^{-1} s^{-1}).

μ_W was obtained from Sharqawy et al. (2010) equations (Eqs. 5-16 to 5-19)

$$\mu_{SW} = \mu_W \cdot \left(1 + A \cdot \frac{sal}{1000} + B \cdot \left(\frac{sal}{1000}\right)^2\right) \quad (5\text{-}16)$$

$$\mu_W = 4.2844 \times 10^{-5} + (0.157 \cdot (t + 64.993)^2 - 91.296)^{-1} \quad (5\text{-}17)$$

$$A = 1.541 + 1.998 \times 10^{-2} \cdot t - 9.52 \times 10^{-5} \cdot t^2 \quad (5\text{-}18)$$

$$B = 7.974 - 7.561 \times 10^{-2} \cdot t + 4.724 \times 10^{-4} \cdot t^2 \quad (5\text{-}19)$$

Where sal = Salinity; t = temperature (°C).

To evaluate $\Delta\rho$, we used the same range of particle densities (2400 – 3600 kg m^{-3} for goethite and amorphous Fe oxyhydroxides) as German and Sparks (1993), who calculated particles ranging between 1 and 10 µm. The resulting modelled particle radii ranged between 14 and 20 µm in the first km from TAG and decreased to 2 to 4 µm between 2 and 30 km from TAG. Our particle size ranges also agree at distances greater than 1 km with aggregates observed by SEM-EDS imaging on filters collected during our cruise (unpublished data).

5.5.3.5. Particle re-entrainment

Another fate of particulate material from hydrothermal plumes is re-entrainment and recycling, by which precipitating particles are re-incorporated into the BP. Re-entrainment is proportional to the volume flow rate of the plume (volumetric flow rate into the base of the radially spreading plume) (German and Sparks, 1993). Due to TAG's volume flow rate, re-entrainment affects the particulate matter transport. Re-entrainment of suspended particulate matter from the TAG hydrothermal plume has been calculated previously as ranging from 31 to 77 % (Rudnicki and Elderfield, 1992) and from 43 to 89 % (Speer and Rona, 1989) which led to the conclusion that more than 50 % of the suspended particulate matter at the TAG hydrothermal plume was being re-entrained (German and Sparks, 1993). Based on this conclusion, and assuming that 50 % of $S_{|1|}$ was re-entrained into $H_{pFe_{|1|}}$, ~5% of the pFe influx in the vent site station does not come directly from the hydrothermal vent, but has been re-entrained. This means that re-entrainment could be a significant source of particulate material in NBP dispersion models. This can of course have profound effects on both the concentrations and residence times of elements within the plume.

5.6. Conclusions

The HERMINE cruise was a GEOTRACES process study (GApr07), which focused on the 75 km range horizontal transport of the TAG hydrothermal plume. This allowed for the positioning of 4 profile stations 1 km or closer to the vent site. At these four stations, θ, S, nephelometry and TM concentrations varied within the plume. A possible explanation is that these observations result from having a multi-phase plume which separated them due to the horizontal current.

During the first 10 km of the NBP transport, it ascended 45 m and its vertical spread decreased to 205 m (a 54% reduction), following local water masses, as identified by σ. This behavior shows that water mass characterization should be taken into account when modelling the dispersion of the NBP. Furthermore, the dominance of the dilution and diffusion flux determined using dMn as a conservative tracer in a steady-state box model (Section 5.5.3.1), showed the importance of transport in the NBP transverse axis, therefore, future work considering not only the vertical axis but the transverse axis in NBP should be undertaken, giving a spatial view on the variation of the width of the NBP.

Our box model, schematically summarized in Figure 5-7, was able to define the distance range where the main reversible exchange direction between the dissolved and the particulate phases starts taking place, somewhere between 1 and 5 km from the vent site (Section 5.5.3.4.). Aggregation predominates in the first 2 km while disaggregation outweighs aggregation further away. Our model results also suggest that the Fe loss by sinking was due to particles with radii ranging from 1.9 to 19.6 µm, with decreasing sizes as the NBP was transported away from the vent site. Even though there was a fast decrease in the particulate content in the first 2 km, and the loss rate followed an exponential decrease equation (Eqs. 5-12 and 5-13) as observed in other hydrothermal systems (Field and Sherrell, 2000; Fitzsimmons et al., 2017), the hydrothermal dFe and dMn signal could still be seen 75 km from the TAG vent site.

Limited work has been carried out in slow-spreading ridges compared to fast-spreading ridges, consequently, the lack of data makes it difficult to constrain models for these regions (German et al., 2015). The approach presented here could allow better modelling of hydrothermal sources and the computed equations should be tested in other sites situated in the MAR, such as the ultramafic-hosted hydrothermal Rainbow site (36˚ 15'N) (German et al., 1996) to elucidate the aggregation and particle dispersion processes at play in a different geodynamic context. This northward site has particle enrichment similar to TAG, where nephelometry

shows hydrothermal anomalies extending 10 - 15 km, comparable to our suspended matter anomaly (10 - 30 km). Therefore, the coupling of the model described in this study with ocean circulation models could further define the NBP dispersion from similar vent sites, improving hydrothermal modelling and constraining the station spacing in future research depending on the research goals. Furthermore, we provide the required data for future modelling studies on the relatively unknown contribution of slow-spreading ridges, with respect to fast-spreading ridges, as sources of trace metals (German et al., 2016).

5.7. Conflict of interest

The authors declare that the research was conducted in the absence of any commercial or financial relationships that could be construed as a potential conflict of interest.

5.8. Author contributions

YF, EP and CC acquired the funding for the cruise and supervised the research cruise. HP was in charge of the trace metal sampling while HW, AG and TH collected the samples at sea. DGS and HP analyzed the dTM samples while HP and MC analyzed the pTM samples. DGS, GS, HP and MC developed the box-model. DGS wrote the paper with significant contributions from all co-authors.

6. Conclusion

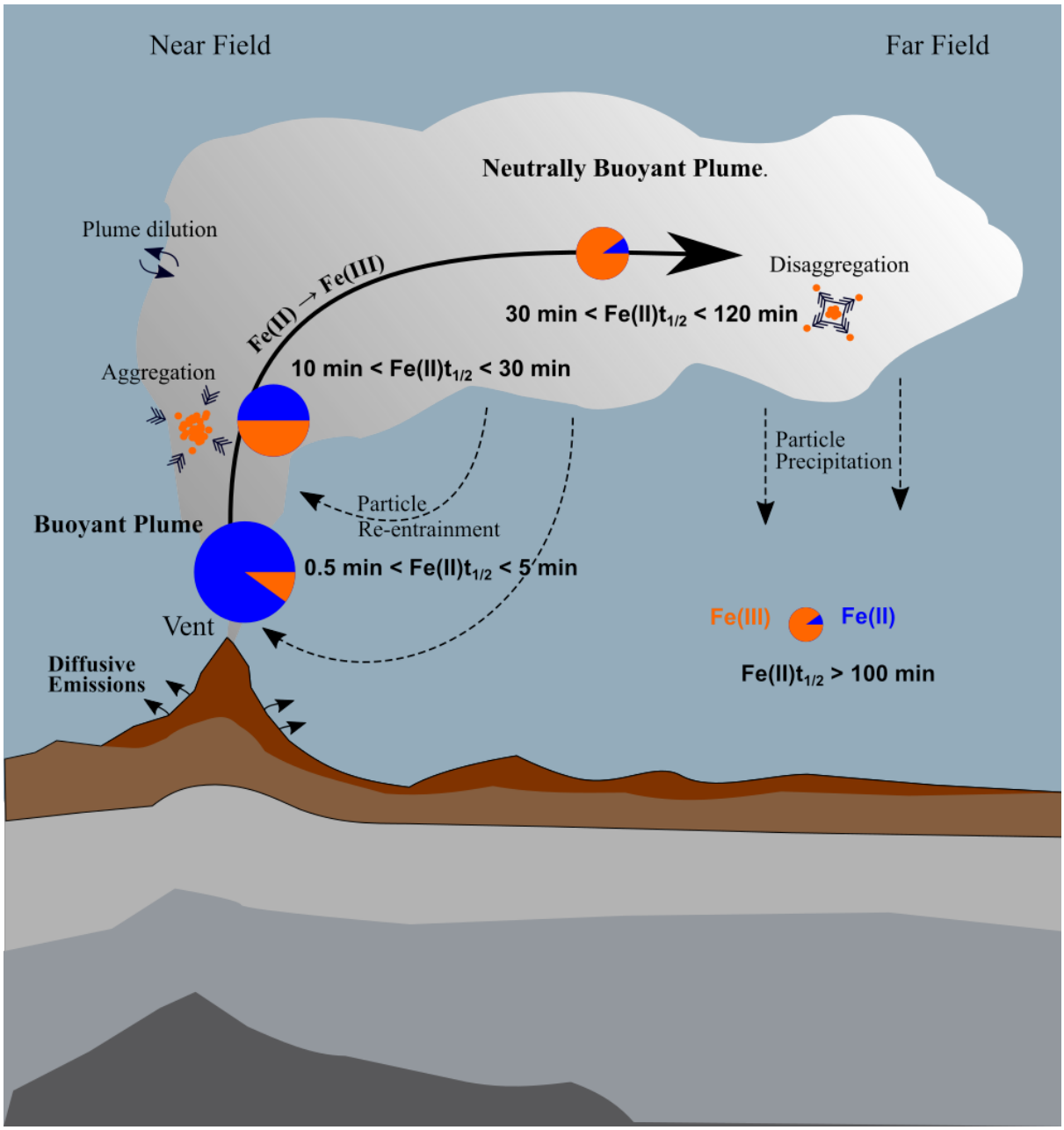

This graphical abstract represents the Fe cycle within the hydrothermal plume and summarizes the previous three chapters. The figure includes 4 pie charts, which decrease in size with the evolution of the plume. These pie charts represent Fe concentrations (which decrease with the plume dispersion, represented with the smaller pie charts; not to scale). The pie charts present Fe(III) (orange) and Fe(II) (dark blue) and show that their relative proportion changes with the plume age, as Fe(II) oxidises to Fe(III). Moreover, the Fe(II) oxidation rates vary within the plume, with the shortest $t_{1/2}$ close to the vent site, and the longest $t_{1/2}$ far from the vent and in the non-hydrothermally affected seawater. Finally, it also shows the processes that affect the Fe(III) size distribution and concentration, including the plume dilution, aggregation close to the vent site, disaggregation far from the vent site, precipitation and particle re-entrainment if the sinking occurs close to the vent site.

6.1. Synthesis

Hydrothermalism is a major trace metal source to the deep ocean and recent studies have shown it can act as a basin-scale Fe source (Fitzsimmons et al., 2017). As hydrothermal environments are a source of reduced species, it is important to investigate their chemical speciation. Indeed, Fe is initially sourced as Fe(II) mainly in soluble size fraction and quickly oxidised to Fe(III), hosted in colloidal size particles. Previously published studies have tried to circumvent this problem with *in situ* filtration and/or measurements or theoretically considering the oxidation rate. However, the available oxidation kinetic rate data in hydrothermal environments are extremely limited and therefore the theoretical equation commonly used was based on an open ocean oxidation rate (Millero et al., 1987; González-Davila et al., 2005; Santana-Casiano et al., 2005). In this context, focusing on the hydrothermal near field (less than 30 km from the vent site) Fe cycle along the MAR, I investigated the following points:

- **In Chapter 3, I studied the Fe(II) oxidation rates within the deep ocean and variations caused by hydrothermal activity**:

Firstly, **I updated the Fe(II) oxidation kinetics equation** from Santana-Casiano et al. (2005), **which increases the applicability range of the equation from 10-25 °C to 2-25 °C**. *This improvement in the equation was required to better theoretically determine the oxidation rate in deep ocean waters, which have seawater temperatures below 10 °C.* This allows to theoretically calculate the rate at which Fe(II) is oxidised and determine the initial concentration of Fe(II) *in situ* if it is not affected by specific factors such as an excess of organic matter or colloids, using the always available ancillary data (salinity, temperature, oxygen concentration and depth).

Furthermore, we were able to **demonstrate the high variability in oxidation rates between different hydrothermal vent sites** in the MAR. Thanks to the high depth frequency of the samples, we could also demonstrate that these oxidation rates vary significantly **within each hydrothermal plume**. We showed that underlying processes such as Fe(II) stabilization by organic ligands and nanoparticles (0.02-0.2 µm) present in hydrothermal plumes can increase the resistance to oxidation and contribute to the observed variability in the oxidation rates.

Very recently, Gartman and Findlay (2020) suggested that characterizing the plume based on regions that retain some reduced components versus those that are fully oxidized would better display the dominant processes occurring within the different sections of the hydrothermal plume. I completely agree with this approach as the chemical properties of Fe will directly

affect the physical characteristics (oxidation of soluble Fe(II) will produce colloidal sized Fe(III)).

It is important to highlight current uncertainties in our knowledge of hydrothermal Fe(II) oxidation kinetics. Before this Thesis, Fe(II) oxidation kinetics had been studied in thirteen hydrothermal sites summarised in Table 6-1 (Gartman and Findlay, 2020). Ten oxidation rates were obtained using the first theoretical oxidation rate equation (Millero et al., 1987), three using Fe(II) spikes in the rosette bottles with concentrations orders of magnitude higher than the measured Fe(II) without controlling pH and oxygen conditions and one following the oxidation of the Fe(II) collected in the plume (maintaining the seawater sample inside the rosette bottle).

Location	Oxidation half-life (h)	O_2 (µM)	Measurement method	Reference
Kairei, Indian Ocean	2.3	180	Fe(II) spikes	Statham et al. (2005)
TAG, Atlantic Ocean	0.35	255	Bottles in the plume	Rudnicki and Elderfield (1993)
TAG, Atlantic Ocean	0.45	255	Calculated	Field and Sherrell (2000)
Rainbow, Atlantic Ocean	0.29	269	Calculated	Field and Sherrell (2000)
EPR, Pacific Ocean 9° N	3.3	104	Calculated	Field and Sherrell (2000)
EPR, Pacific Ocean 21° N	3.7	108	Calculated	Field and Sherrell (2000)
Juan de Fuca, Pacific Ocean	6.38	64	Calculated	Field and Sherrell (2000)
Southern EPR, Pacific Ocean	1.8	153	Calculated	Field and Sherrell (2000)
SWIR, Indian Ocean	1.31	204	Calculated	Field and Sherrell (2000)
SWIR, Indian Ocean	1.6−1.8	200	Fe(II) spikes	Wang et al.(2012)
Gorda, Pacific Ocean	3.1	102	Calculated	Field and Sherrell (2000)
North Gorda, Pacific Ocean	39	180	Fe(II) spikes	Massoth et al. (1998)
Cleft Segment, Juan de Fuca, Pacific Ocean	32	70	Calculated	Chin et al. (1994)
Cleft Segment, Juan de Fuca, Pacific Ocean	9	70	Calculated	Coale et al. (1991)

Table 6-1. Measured and calculated Fe(II) oxidation half-life in hydrothermal plumes before this Thesis . Table from Gartman and Findlay (2020).

- **In Chapter 4**, **I combined the analysed Fe(II) concentrations with the knowledge gained during Chapter 3 and calculated the initial Fe(II) ($dFe(II)_0$) concentrations along the MAR in the deep ocean and six different vents.**

I determined low dFe(II) concentrations through the whole water column, with concentrations below 0.2 nmol L^{-1}, even down to less than 0.1 nmol L^{-1} in the deep ocean. We showed that Fe(II) has a short half-life in oxic waters ranging from minutes to hours mainly depending on temperature and pH (Millero et al., 1987; Santana-Casiano et al., 2005). However, this initially inconspicuous knowledge causes far-reaching effects. Firstly, **measured Fe(II) concentrations in the deep ocean are a maximum 65% of the original Fe(II) concentration;** however, **they could potentially be as low as 10% when temperature, pH, oxygen, or sampling time is increased**. Also, **the fast oxidation rate of Fe(II) makes Fe speciation difficult to establish, and its oxidation can influence its size fractionation**. As such, the mainly soluble sized Fe(II) will oxidize to the colloidal size fraction or get adsorbed by bigger particles. As a result, $dFe(II)_0$ concentrations can be higher than measured sFe concentrations and we showed that $dFe(II)_0$ in the Atlantic Ocean could account for more than 20% of the dFe pool and not only <10% as previously reported (Sedwick et al., 2015), when the oxidation during sampling and analysis time are taken into account.

- **In Chapter 5, I looked into the transport of the hydrothermally sourced Fe from the TAG neutrally buoyant plume.** To my knowledge, this is the first trace metal process study with such detail along a slow-spreading ridge. Dissolved (<0.45 μm) and particulate size fractions (>0.45 μm) were considered and combined with dissolved manganese concentrations in order to build a box model. **This model identifies the relative effect of the processes affecting the fate of the plume signal.** I showed that the dilution of the plume was the main process affecting the dFe concentration within the plume, causing 99% of the NBP dFe loss. The model also allowed the identification of other dFe sinks, such as aggregation of dFe into the particle size fraction which is responsible for 47% of the dFe loss within the first kilometre from the vent site.

With this model, it was possible to define the distance range where the main reversible exchange direction between the dissolved and the particulate phases starts taking place, between 1 and 5 km from the vent site. We showed that aggregation predominates in the first 2 km while disaggregation outweighs aggregation further away.

The model results also suggest that the Fe loss by sinking was due to particles with radii ranging from 1.9 to 19.6 mm, with decreasing sizes as the neutrally buoyant plume (NBP) was transported away from the vent site. Even though there was a fast decrease in the particulate content in the first 2 km, and the loss rate followed an exponential decrease equation as observed in other hydrothermal systems, the hydrothermal dFe and dMn signal could still be seen 75 km from the TAG vent site.

With the increase in knowledge obtained from these three chapters, I have highlighted below where I think further research is required.

6.2. Perspectives

The quote "The more I learn, the more I realize how much I don't know" is attributed to Albert Einstein. However, this sentence is missing the key aftermath, which is that the more I realize how much I don't know, the more I want to learn. The end of the PhD is a great moment to think about what you have done and what would you have done differently if you could restart the project knowing what you have learned. Luckily, science is not a one-time project, but a continuous process with numerous future opportunities to expand on with the gained knowledge and experience. With this in mind, I have thought about the main future goals and some possible ways to implement the ideas.

6.2.1. Iron (II) perspectives

Iron (II) concentrations in the marine environment are generally low (~0.1 nmol L^{-1} in the deep ocean) however Fe(II) concentrations can be highly variable due to the presence of Fe(II) sources and these concentrations remain for different periods of times depending on the seawater matrix. The effects of the inorganic interactions on the oxidation of Fe(II) are relatively well known (Millero, 1985; Liu and Millero, 2002; González-Dávila et al., 2006). It is also possible to know the $t_{1/2}$ as a function of pH, temperature and salinity in a typical seawater matrix (Santana-Casiano et al., 2005). However, the effect that factors such as particle content and organic matter have on the Fe(II) concentrations and oxidation rates are very complex and still remains to be determined in detail.

6.2.1.1. The effect of particles on Fe(II) oxidation kinetics

Previous work revealed that particulate Fe(II) like pyrite nanoparticles are more resistant to oxidation, with Fe(II) half-life between 4 and 48 months at 2 ˚C (Yücel et al., 2011). However, this Thesis (chapter 3) shows that colloidal particles also affect the overall Fe(II) oxidation rates. Future work should try to quantify this colloidal particle effect. An option could be the use of liquid nanoparticle sizing systems capable of measuring the sizes and concentrations of particles in a colloidal suspension (Van Schooneveld et al., 2011) (e.g. LNS 9310 from Kanomax FMT). Currently there are no oceanographical manuscript using this system, although the staff at Kanomax FMT have confirmed that the system could be used for seawater samples (pers. comm. with Dr Siqin He, Senior staff scientist at Kanomax FMT).

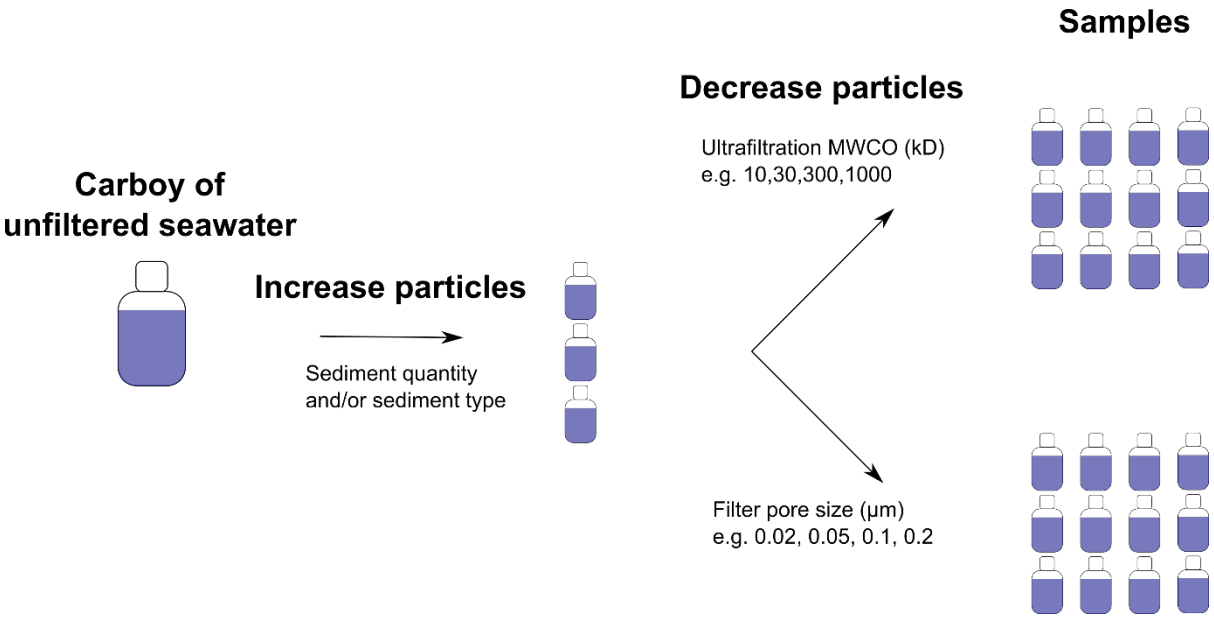

Figure 6-1. Possible experimental design to obtain multiple samples to study the effect of particles on Fe(II) oxidation kinetics. The increase particles step can be skipped to reduce possible seawater matrix changes. The samples would be analysed at constant pH and temperature.

This data could potentially be used in the updated Fe(II) oxidation kinetics equation. The current equation only considers pH, temperature and salinity. However, Chapter 3 clearly shows that colloidal-sized particles affect the oxidation rate. Iron(II) oxidation kinetics studies should be performed at constant pH and temperature with variations in colloidal particle size (quantified using liquid nanoparticle sizing systems) and composition (organic-inorganic) (Figure 6-1). The particle variations could be produced by reducing particle concentration (e.g. using different pore-size and types of filters) and/or by the addition of particles (e.g. similar to what is done in particle resuspension experiments). The main advantage of producing changes in the particle load of one sample instead of collecting multiple samples is that the seawater

matrix would have less variability and there is higher certainty that samples will have higher variations in particle load. Furthermore, to understand the natural variability different types of sediments could be used including mineral particles (Holmes et al., 2020).

6.2.1.2. The effect of organic matter on Fe(II) oxidation kinetics

Organic matter is also known to affect the Fe(II) oxidation rate (Rose and Waite, 2003a; Statham et al., 2005). The measurement of organic matter includes all organic compounds from microbial, plant or animal origin smaller than 0.45 µm and does not differentiate its stage of decomposition (Swift, 1996). We have shown in chapter 3 that the overall effect of organic matter is to reduce the Fe(II) oxidation rate. However, this variable was inadequate to better correlate the measured oxidation rate with the theoretical oxidation rate. This is probably due to the vast structural diversity of organic matter.

An easily performed experiment would be to combine the studies on the effects of colloids/particles and organic matter, by measuring colloidal organic matter or carbon (COM/COC) and comparing the results with filtered and UV-irradiated samples (Figure 6-2). COC may account for 8-19% of the dissolved organic carbon (DOC) (Dulaquais et al., 2018) and, as a result of adding an organic component factor to the theoretical equation, could potentially better constrain the Fe(II) oxidation kinetics equation. However, COM/COC would still represent a diverse range of compounds. Resultantly, it might be more effective to identify the effect of specific organic compounds. This approach has been followed by multiple researchers; however, it would be useful to identify not only the effect of the compounds on the oxidation rates but also its relative importance. This would require analysing the original seawater sample, the UV-irradiated sample and a UV-irradiated sample to which the same concentration of the specific organic compound is added.

Thus, future Fe(II) oxidation kinetics work should be accompanied by a characterization and quantification of the organic matter present in the medium and the current physico-chemical factors (pH, T, dissolved oxygen and salinity). Some methods capable of obtaining the required data are ultrahigh-resolution mass spectrometry by means of Fourier transform ion cyclotron resonance (FT-ICR-MS) (Koch et al., 2005; Dittmar and Paeng, 2009), the size-exclusion chromatography with organic carbon, ultraviolet and organic nitrogen detectors method (SEC-OCD-UVD-OND) (Dulaquais et al., 2018) and the differential pulse cathodic stripping voltammetry method (DP-CSV) (Pernet-Coudrier et al., 2013).

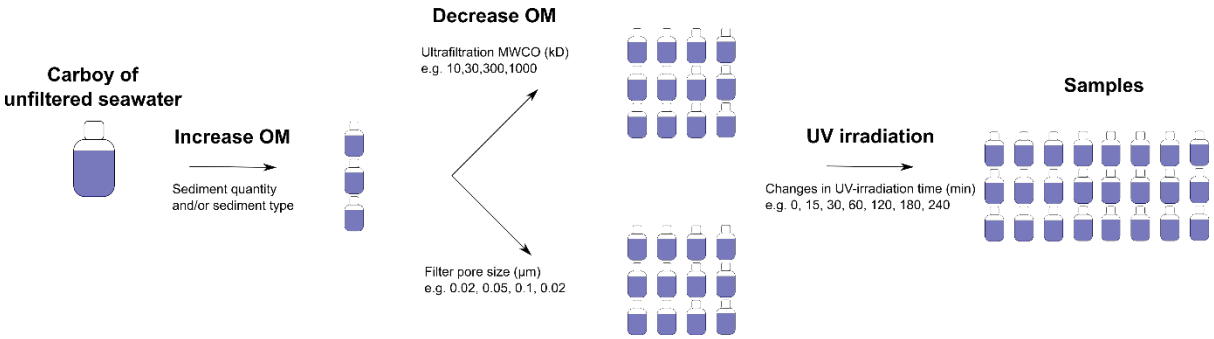

Figure 6-2. Possible experimental design to obtain multiple samples to study the effect of organic matter (OM) on the Fe(II) oxidation kinetics. The increase OM step can be skipped to reduce possible seawater matrix changes. The samples would be analysed at constant pH and temperature. Samples would require OM quantification and characterization.

6.2.1.3. Effect of oxidation and filtration time on sFe and cFe determination

The $dFe(II)_0$/sFe results from chapter 5 have suggested a possible methodological biais in the currently accepted method for sampling soluble trace metal. When Fe(II) (which is mainly found in the soluble size fraction) oxidises, it forms colloidal sized Fe(III). Consequently, in environments with high Fe(II) concentrations, sFe and cFe concentrations could potentially significantly be affected by the Fe(II) oxidation rate. This effect could be reduced by faster filtration methods or mitigated using *in situ* filtration (Cotte et al., 2015; Waeles et al., 2017). For the former, one potential method is the use of fast ultrafiltration systems such as Vivaspin® Centrifugal Concentrators (Schlosser et al., 2013). For the latter, samples can be filtered *in situ* using equipment such as the PEPITO sampler (Cotte et al., 2015; Waeles et al., 2017). This sampler requires to be deployed using a remotely operated vehicle (ROV). It could potentially be deployed on a trace metal clean rosette, but sampling would require to stop the rosette (for about 10 minutes), a method not recommended in the GEOTRACES protocols (https://geotracesold.sedoo.fr/Cookbook.pdf) because of potential contamination. Nevertheless, Cotte et al. (2015) proved that *in situ* filtration was required to reduce the underestimation of dissolved samples in eight of the twelve tested elements (underestimations in V, As, Fe, Zn, Ba, Cd, Pb and Cu; on board filtration was acceptable for Mn, Mg, Li and U).

6.2.1.4. Iron (II) oxidation kinetics in the "surface" ocean

Estimating the theoretical $dFe(II)_0$ concentration in waters shallower than 800 m is problematic due to high temperatures and pH, and the presence of organic matter, ROS and biological activity. Therefore, future work should focus on this rapidly evolving environment, where

theoretical oxidation rates are very fast and require a minimum amount of time between sampling and analysis. Experiments to potentially reduce this uncertainty could compare the sampling method, by comparing the trace metal rosette with its relatively long sampling time (the steps are i) ascend the rosette through the water column, ii) put the rosette on the vessel deck, iii) transfer the GO-FLO bottles to the sampling van, iv) collect sample v) transport samples to the analysis lab vi) sample analysis) to a Teflon pump system (e.g. lowering the tow-fish from the ocean surface to the maximum pump capacity, the steps would be i) pump water from the ocean to the analysis lab ii) sample analysis). The main benefit of lowering the tow-fish is that other deployments can be performed in the main winch (e.g. rosette, pumps or net deployments) during the tow-fish deployment; however this method is limited by the Teflon pump suctioning force. A future option could be the use of *in situ* analysis (on board the rosette). This method requires an adapted FIA system, stopping the rosette in the water (which increases the cast/station time) and currently requires high metal concentrations (due to the elevated limit of detection) (Sarradin et al., 2005; Grand et al., 2019).

6.2.1.5. Iron (II) oxidation kinetics in other hydrothermal vent sites and diffusive emissions

Hydrothermal supply of Fe to the global deep ocean is distributed extensively through all ocean basins; however, most of the previous work has focused on examining high temperature, acidic, focused flow on ridge axes forming black smoker plumes. The contribution of other types of venting to the global ocean Fe cycle has received little attention. Future work should study hydrothermal fields at larger scales, including the focused hydrothermal venting, auxiliary vents and diffusive emissions. In Chapter 3, samples for Fe(II) oxidation kinetics were collected at the Lost City hydrothermal site. This hydrothermal site has antagonistic physico-chemical characteristics compared to the other studied hydrothermal vent sites. It has a basic pH averaging 9.0 to 9.8 (Kelley et al., 2005), the vent fluid is relatively cold (40-75 °C), and presents extremely low concentrations of most trace elements (Ludwig et al., 2006). Lost City presented the biggest measured Fe(II) oxidation kinetic rate constants which would affect background Fe(II) concentrations.

Auxiliary vents which include lower temperature clear smokers, flanges, cracks, and diffusive sources constitute an important source of heat (Baker et al., 1993; Trivett and Williams III, 1994; Kinoshita et al., 2006) and Fe (German et al., 2015) on a larger spatial scale than

localized black smoker discharges. Secondary venting is characterized by systematically and significantly lower dFe:dMn ratios than those of their relative main black smoker vents (Waeles et al., 2017). Secondary venting is a source of Fe-depleted hydrothermal solutions that can get entrained with the main hydrothermal vent. Therefore, future research should also focus on auxiliary vent systems where oxidation kinetic rate constants could potentially be different than in the main black smoker discharges.

6.2.2. Mesoscale eddies and their implications in long distance trace metal transport

Throughout this Thesis, the neutrally buoyant plume has been represented by a constant cloud transported through the ocean. However, physical modellers represent hydrothermal plumes with a more complex structure formed by mesoscale eddies. The first difference between these two plume representations is that the trace metal distribution would be drastically affected, with higher concentrations within eddies than outside the eddies even when sampling within the transport path, which could result in erroneous hydrothermal transport ranges if the sampling occurs outside an eddy. Secondly, physical models of the transport of larvae generated in hydrothermal vent sites indicated that larvae can remain within the water column for long distances (Adams and Flierl, 2010). Future research should try to follow a hydrothermal eddy characterising the Fe composition within the eddy and in its boundaries as it is transported from the vent site to the far field.

6.2.3. Secondary sources of trace metals

The TAG vent site is situated on the Mid Atlantic Ridge, in the ridge valley. As such, the neutrally buoyant plume could be affected by secondary sources of trace metals, such as sediment resuspension from the bottom of the valley or mixing with seawater influenced by the valley flanks. Iron isotopes can provide a more in-depth view of the processes partaking in the plume dispersion and dilution. This can be achieved by observing the evolution of the isotopic composition of seawater and comparing it with other tracers, e.g. evolution of ^{3}He and Fe isotopes (Figure 6-3) to identify if there is just dilution with open ocean seawater or if there is a signal interference caused by a secondary iron source.

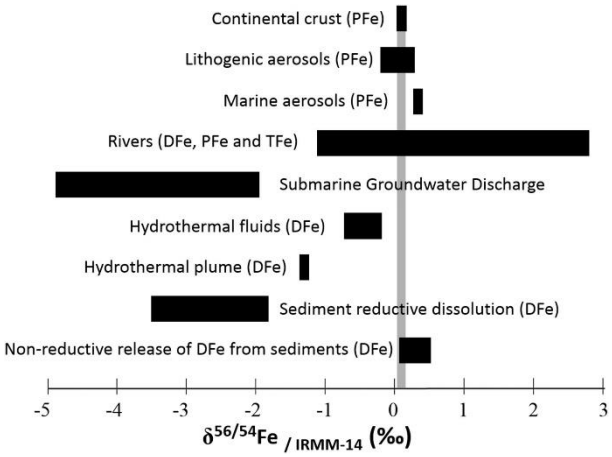

Figure 6-3. Isotopic composition of iron sources to the ocean (in per mill relative to IRMM-014). DFe, PFe, and TFe stand for dissolved, particulate, and total iron, respectively. Figure from Abadie et al, (2017).

6.2.4. Particle size distribution

Currently, rosettes are deployed with turbidimeters and light scattering sensors. The development of new particle determination techniques such as Underwater Vision Profilers (UVP) capable of determining particles greater than 100 mm and laser-diffraction based particle size analysers (e.g. LISST-200X) which can characterize particles between 1 and 500 µm will further improve the particle size characterization. These particle characterizations could be further improved to include colloidal sized particles. With this objective in mind, laser diffraction particle size analysers and liquid nanoparticle sizing systems could provide very valuable data. Samples would be collected using the rosette and the particle quantification and size classification could be combined with the currently sampled data and implemented in more complex models. One example would be combining the particle size with Stoke's Law to obtain sinking speeds, and therefore cFe and pFe loss similar to what was done in chapter 5 in the section titled "Size and Sinking Velocity of pFe Loss".

6.3. Application of the perspectives

During the last year of my PhD I had the opportunity to participate in the TONGA (GPpr14) cruise (PI Cécile Guieu and Sophie Bonnet; 31/10/2019-06/12/2019). Throughout the research cruise I analysed dFe(II) on board the ship and collected samples for future Fe(II) oxidation kinetics experiments. One of the objectives of this cruise was to study the impact of the shallow (<500 m) submarine volcanoes along the Tonga arc and associated hydrothermal venting on the input of micronutrients (especially Fe) to the photic layer of the ocean potential impact on

the biological productivity and biological carbon pump. Samples were also collected for Fe(II) oxidation kinetics and trace metal distribution on the dissolved phase, that I would like to analyse in the next few months. As such, the samples collected along the Tonga trench above shallow submarine volcanoes will allow to study the biological impact on the hydrothermally affected samples adding new parameters.

In addition, early next year, I will be participating in a South West Indian GEOTRACES section cruise (SWINGS, GS02, 10/01/2021-08/03/2021, PIs Catherine Jeandel and Hélène Planquette). The aims of the SWINGS cruise are:

1) Establishing the relative importance of sedimentary, atmospheric and hydrothermal sources of trace elements and isotopes (TEIs) in the Indian sector of the SO.
2) Investigating the drivers of the internal trace element cycles: biogenic uptake, remineralization, particle fate, and export.
3) Quantifying TEI transport by the Antarctic Circumpolar Current and the complex frontal areas at the confluence between Indian and Atlantic Oceans.

During the cruise, I will be analysing dFe on board the ship and collecting soluble trace metal samples (which I will analyse back on land using a SF-ICP-MS) and Fe(II) oxidation kinetics samples (which I will analyse back on land using a FeLUME system). This cruise will be a great opportunity to implement some of the perspectives. Firstly, on-board dFe analysis will allow us to identify if there are any Fe sources, such as continental sources coming from Africa, island sources from the Crozet, Kerguelen and Heard islands and hydrothermal sources. Moreover, I will modify the box model developed in chapter 5 to evaluate Fe fractionation (sFe, cFe, and pFe) within the different fronts (e.g. Sub-Tropical front (STF) Sub-Antarctic Front (SAF), Polar Front (PF)), the Agulhas Current (AC) and the Agulhas Return Current (ARC), and at the vicinity of various islands (Crozet, Kerguelen and Heard). Second, I will collect and perform Fe(II) oxidation kinetics experiments in all the water masses. With this in mind, 1 L Fe(II) oxidation kinetics samples will be collected instead of the usual 250 mL samples. The extra sample volume will allow for a greater number of experiments which will better constrain the organic matter and particulate content effect, therefore implementing a greater number of ideas developed during this PhD Thesis.

Bibliography

Abadie, C., Lacan, F., Radic, A., Pradoux, C., and Poitrasson, F. (2017). Iron isotopes reveal distinct dissolved iron sources and pathways in the intermediate versus deep Southern Ocean. *Proc. Natl. Acad. Sci.* 114, 858–863.

Adams, D. K., and Flierl, G. R. (2010). Modeled interactions of mesoscale eddies with the East Pacific Rise: Implications for larval dispersal. *Deep Sea Res. Part I Oceanogr. Res. Pap.* 57, 1163–1176. doi:10.1016/j.dsr.2010.06.009.

Andreani, M., Escartin, J., Delacour, A., Ildefonse, B., Godard, M., Dyment, J., et al. (2014). Tectonic structure, lithology, and hydrothermal signature of the Rainbow massif (Mid-Atlantic Ridge 36°14′N). *Geochemistry, Geophys. Geosystems* 15, 3543–3571. doi:10.1002/2014GC005269.

Ardyna, M., Lacour, L., Sergi, S., D'Ovidio, F., Sallée, J.-B., Rembauville, M., et al. (2019). Hydrothermal vents trigger massive phytoplankton blooms in the Southern Ocean. *Nat. Commun.* 10, 1–8. doi:10.1038/s41467-019-09973-6.

Armstrong, R. A., Lee, C., Hedges, J. I., Honjo, S., and Wakeham, S. G. (2001). A new, mechanistic model for organic carbon fluxes in the ocean based on the quantitative association of POC with ballast minerals. *Deep Sea Res. Part II Top. Stud. Oceanogr.* 49, 219–236. doi:10.1016/S0967-0645(01)00101-1.

Baker, E. T., Massoth, G. J., Walker, S. L., and Embley, R. W. (1993). A method for quantitatively estimating diffuse and discrete hydrothermal discharge. *Earth Planet. Sci. Lett.* 118, 235–249.

Baumgartner, R. J., Van Kranendonk, M. J., Wacey, D., Fiorentini, M. L., Saunders, M., Caruso, S., et al. (2019). Nano-porous pyrite and organic matter in 3.5-billion-year-old stromatolites record primordial life. *Geology* 47, 1039–1043. doi:10.1130/G46365.1.

Beaulieu, S. E., and Szafrański, K. M. (2020). InterRidge Global Database of Active Submarine Hydrothermal Vent Fields Version 3.4. doi:10.1594/PANGAEA.917894.

Bennett, S. A., Achterberg, E. P., Connelly, D. P., Statham, P. J., Fones, G. R., and German, C. R. (2008). The distribution and stabilisation of dissolved Fe in deep-sea hydrothermal plumes. *Earth Planet. Sci. Lett.* 270, 157–167. doi:10.1016/j.epsl.2008.01.048.

Betts, H. C., Puttick, M. N., Clark, J. W., Williams, T. A., Donoghue, P. C. J., and Pisani, D. (2018). Integrated genomic and fossil evidence illuminates life's early evolution and eukaryote origin. *Nat. Ecol. Evol.* 2, 1556–1562. doi:10.1038/s41559-018-0644-x.

Birchill, A. J., Hartner, N. T., Kunde, K., Siemering, B., Daniels, C., González-Santana, D., et al. (2019). The eastern extent of seasonal iron limitation in the high latitude North Atlantic Ocean. *Sci. Rep.* 9, 1435. doi:10.1038/s41598-018-37436-3.

Bischoff, J. L., and Rosenbauer, R. J. (1984). The critical point and two-phase boundary of seawater, 200–500°C. *Earth Planet. Sci. Lett.* 68, 172–180. doi:10.1016/0012-821X(84)90149-3.

Blain, S., Sarthou, G., and Laan, P. (2008). Distribution of dissolved iron during the natural iron-fertilization experiment KEOPS (Kerguelen Plateau, Southern Ocean). *Deep Sea Res. Part II Top. Stud. Oceanogr.* 55, 594–605. doi:10.1016/j.dsr2.2007.12.028.

Bogdanov, Y. A., Bortnikov, N. S., Vikent ev, I. V, Lein, A. Y., Gurvich, E. G., Sagalevich, A. M., et al. (2002). Mineralogical-Geochemical Peculiarities of Hydrothermal Sulfide Ores and Fluids in the Rainbow Field Associated with Serpentinites, Mid-Atlantic Ridge (36^ o14'N). *Geol. ORE Depos. C/C Geol. Rudn. MESTOROZHDENII* 44, 444–473.

Bowie, A. R., Achterberg, E. P., Sedwick, P. N., Ussher, S. J., and Worsfold, P. J. (2002a). Real-Time Monitoring of Picomolar Concentrations of Iron(II) in Marine Waters Using Automated Flow Injection-Chemiluminescence Instrumentation. *Environ. Sci. Technol.* 36, 4600–4607. doi:10.1021/es020045v.

Bowie, A. R., Sedwick, P. N., and Worsfold, P. J. (2004). Analytical intercomparison between flow injection-chemiluminescence and flow injection-spectrophotometry for the determination of picomolar concentrations of iron in seawater. *Limnol. Oceanogr. Methods* 2, 42–54. doi:10.4319/lom.2004.2.42.

Bowie, A. R., Whitworth, D. J., Achterberg, E. P., Mantoura, R. F. C., and Worsfold, P. J. (2002b). Biogeochemistry of Fe and other trace elements (Al, Co, Ni) in the upper Atlantic Ocean. *Deep Sea Res. Part I Oceanogr. Res. Pap.* 49, 605–636. doi:10.1016/S0967-0637(01)00061-9.

Boyd, P. W., and Ellwood, M. J. (2010). The biogeochemical cycle of iron in the ocean. *Nat. Geosci.* 3, 675–682. doi:10.1038/ngeo964.

Boyd, P. W., Jickells, T. D., Law, C. S., Blain, S., Boyle, E. A., Buesseler, K. O., et al. (2007). Mesoscale iron enrichment experiments 1993-2005: Synthesis and future directions. *Science (80-.).* 315, 612–617. doi:10.1126/science.1131669.

Boyd, P. W., Watson, A. J., Law, C. S., Abraham, E. R., Trull, T., Murdoch, R., et al. (2000). A mesoscale phytoplankton bloom in the polar Southern Ocean stimulated by iron fertilization. *Nature* 407, 695–702.

Boyle, E. A., Edmond, J. M., and Sholkovitz, E. R. (1977). The mechanism of iron removal in estuaries. *Geochim. Cosmochim. Acta* 41, 1313–1324.

Brand, L. E. (1991). Minimum iron requirements of marine phytoplankton and the implications for the biogeochemical control of new production. *Limnol. Oceanogr.* 36, 1756–1771. doi:10.4319/lo.1991.36.8.1756.

Bruland, K. W., Franks, R. P., Knauer, G. A., and Martin, J. H. (1979). Sampling and analytical methods for the determination of copper, cadmium, zinc, and nickel at the nanogram per liter level in sea water. *Anal. Chim. Acta* 105, 233–245. doi:10.1016/S0003-2670(01)83754-5.

Bruland, K. W., Rue, E. L., and Smith, G. J. (2001). Iron and macronutrients in California coastal upwelling regimes: Implications for diatom blooms. *Limnol. Oceanogr.* 46, 1661–1674.

Buck, K. N., Sohst, B., and Sedwick, P. N. (2015). The organic complexation of dissolved iron along the U.S. GEOTRACES (GA03) North Atlantic Section. *Deep Sea Res. Part II Top. Stud. Oceanogr.* 116, 152–165. doi:10.1016/j.dsr2.2014.11.016.

Bundy, R. M., Abdulla, H. A. N., Hatcher, P. G., Biller, D. V, Buck, K. N., and Barbeau, K. A. (2015). Iron-binding ligands and humic substances in the San Francisco Bay estuary and estuarine-influenced shelf regions of coastal California. *Mar. Chem.* 173, 183–194.

Bundy, R. M., Biller, D. V, Buck, K. N., Bruland, K. W., and Barbeau, K. A. (2014). Distinct

pools of dissolved iron-binding ligands in the surface and benthic boundary layer of the California Current. *Limnol. Oceanogr.* 59, 769–787. doi:10.4319/lo.2014.59.3.0769.

Butterfield, D. A., Nakamura, K., Takano, B., Lilley, M. D., Lupton, J. E., Resing, J. A., et al. (2011). High SO2 flux, sulfur accumulation, and gas fractionation at an erupting submarine volcano. *Geology* 39, 803–806.

Camacho, A., Walter, X. A., Picazo, A., and Zopfi, J. (2017). Photoferrotrophy: remains of an ancient photosynthesis in modern environments. *Front. Microbiol.* 8, 323.

Charlou, J. L., Donval, J. P., Douville, E., Jean-Baptiste, P., Radford-Knoery, J., Fouquet, Y., et al. (2000). Compared geochemical signatures and the evolution of Menez Gwen (35°50N) and Lucky Strike (37°17N) hydrothermal fluids, south of the Azores Triple Junction on the Mid-Atlantic Ridge. *Chem. Geol.* 171, 49–75. doi:10.1016/S0009-2541(00)00244-8.

Cheize, M., Planquette, H., Fitzsimmons, J. N., Pelleter, E., Sherrell, R. M., Lambert, C., et al. (2019). Contribution of resuspended sedimentary particles to dissolved iron and manganese in the ocean: an experimental study. *Chem. Geol.* 511, 389–415. doi:10.1016/j.chemgeo.2018.10.003.

Chever, F., Sarthou, G., Bucciarelli, E., Blain, S., and Bowie, A. R. (2010). An iron budget during the natural iron fertilisation experiment KEOPS (Kerguelen Islands, Southern Ocean). *Biogeosciences* 7, 455–468. doi:10.5194/bg-7-455-2010.

Chiba, H., Masuda, H., Lee, S. Y., and Fujioka, K. (2001). Chemistry of hydrothermal fluids at the TAG active mound, MAR 26, in 1998. *Geophys. Res. Lett.* 28, 2919–2922. doi:10.1029/2000GL012645.

Chin, C. S., Coale, K. H., Elrod, V. A., Johnson, K. S., Massoth, G. J., and Baker, E. T. (1994). In situ observations of dissolved iron and manganese in hydrothermal vent plumes, Juan de Fuca Ridge. *J. Geophys. Res. Solid Earth* 99, 4969–4984.

Coale, K. H., Chin, C. S., Massoth, G. J., Johnson, K. S., and Baker, E. T. (1991). In situ chemical mapping of dissolved iron and manganese in hydrothermal plumes. *Nature* 352, 325–328.

Conway, T. J., and John, S. G. (2014). Quantification of dissolved iron sources to the North Atlantic Ocean. *Nature* 511, 212–215. doi:10.1038/nature13482.

Corliss, J. B., Lyle, M., Dymond, J., and Crane, K. (1978). The chemistry of hydrothermal mounds near the Galapagos Rift. *Earth Planet. Sci. Lett.* 40, 12–24. doi:10.1016/0012-821X(78)90070-5.

Cotte, L., Waeles, M., Pernet-Coudrier, B., Sarradin, P.-M., Cathalot, C., and Riso, R. D. (2015). A comparison of in situ vs. ex situ filtration methods on the assessment of dissolved and particulate metals at hydrothermal vents. *Deep Sea Res. Part I Oceanogr. Res. Pap.* 105, 186–194. doi:10.1016/j.dsr.2015.09.005.

Croot, P. L., Bowie, A. R., Frew, R. D., Maldonado, M. T., Hall, J. A., Safi, K. A., et al. (2001). Retention of dissolved iron and Fe II in an iron induced Southern Ocean phytoplankton bloom. *Geophys. Res. Lett.* 28, 3425–3428. doi:10.1029/2001GL013023.

Cullen, J. T., Bergquist, B. A., and Moffett, J. W. (2006). Thermodynamic characterization of the partitioning of iron between soluble and colloidal species in the Atlantic Ocean. *Mar. Chem.* 98, 295–303. doi:10.1016/J.MARCHEM.2005.10.007.

de Baar, H. J. W., Boyd, P. W., Coale, K. H., Landry, M. R., Tsuda, A., Assmy, P., et al. (2005). Synthesis of iron fertilization experiments: From the iron age in the age of enlightenment. *J. Geophys. Res. C Ocean.* 110, 1–24. doi:10.1029/2004JC002601.

de Baar, H. J. W., and De Jong, J. T. M. (2001). "Distributions, sources and sinks of iron in seawater," in *The Biogeochemistry of Iron in Seawater*, eds. D. Turner and K. A. Hunter (Chichester, UK: John Wiley & Sons Ltd.), 125–253. doi:10.1152/jn.90941.2008.

Demina, L. L., Lein, A. Y., Galkin, S. V, and Lisitzin, A. P. (2015). Features of trace metal distribution in the components of the ecosystem of the Lost City hydrothermal vent field (North Atlantic). *Dokl. Earth Sci.* 465, 1312–1316. doi:10.1134/S1028334X1512017X.

Des Marais, D. J. (2000). When did photosynthesis emerge on Earth? *Science (80-.).* 289, 1703–1705.

Ding, K., and Seyfried, W. E. (2007). In situ measurement of pH and dissolved H2 in mid-ocean ridge hydrothermal fluids at elevated temperatures and pressures. *Chem. Rev.* 107, 601–622.

Dittmar, T., and Paeng, J. (2009). A heat-induced molecular signature in marine dissolved organic matter. *Nat. Geosci.* 2, 175–179.

Dodd, M. S., Papineau, D., Grenne, T., Slack, J. F., Rittner, M., Pirajno, F., et al. (2017). Evidence for early life in Earth's oldest hydrothermal vent precipitates. *Nature* 543, 60–64. doi:10.1038/nature21377.

Douville, E., Charlou, J. L., Oelkers, E. H., Bienvenu, P., Jove Colon, C. F., Donval, J. P., et al. (2002). The rainbow vent fluids (36°14′N, MAR): The influence of ultramafic rocks and phase separation on trace metal content in Mid-Atlantic Ridge hydrothermal fluids. *Chem. Geol.* 184, 37–48. doi:10.1016/S0009-2541(01)00351-5.

Duckworth, R. C., Knott, R., Fallick, A. E., Rickard, D., Murton, B. J., and Van Dover, C. (1995). Mineralogy and sulphur isotope geochemistry of the Broken Spur sulphides, 29 N, Mid-Atlantic Ridge. *Geol. Soc. London, Spec. Publ.* 87, 175–189.

Dulaquais, G., Breitenstein, J., Waeles, M., Marsac, R., and Riso, R. (2018). Measuring dissolved organic matter in estuarine and marine waters: size-exclusion chromatography with various detection methods. *Environ. Chem.* 15, 436–449.

Edmond, J. M., Measures, C., McDuff, R. E. E., Chan, L. H. H., Collier, R., Grant, B., et al. (1979). Ridge crest hydrothermal activity and the balances of the major and minor elements in the ocean: The Galapagos data. *Earth Planet. Sci. Lett.* 46, 1–18. doi:10.1016/0012-821X(79)90061-X.

Edmonds, H. N., German, C. R., Green, D. R. H., Huh, Y., Gamo, T., and Edmond, J. M. (1996). Continuation of the hydrothermal fluid chemistry time series at TAG, and the effects of ODP drilling. *Geophys. Res. Lett.* 23, 3487–3489. doi:10.1029/96GL01597.

Elderfield, H. (1977). "Chapter 9 The Form of Manganese and Iron in Marine Sediments," in *Marine Manganese Deposits*, ed. G. P. B. T.-E. O. S. Glasby (Elsevier), 269–289. doi:10.1016/S0422-9894(08)71023-7.

Elderfield, H., and Schultz, A. (1996). Mid-ocean ridge hydrothermal fluxes and the chemical composition of the ocean. *Annu. Rev. Earth Planet. Sci.* 24, 191–224.

Elrod, V. A., Berelson, W. M., Coale, K. H., and Johnson, K. S. (2004). The flux of iron from

continental shelf sediments: A missing source for global budgets. *Geophys. Res. Lett.* 31. doi:10.1029/2004GL020216.

Emmenegger, L., King, D. W., Sigg, L., and Sulzberger, B. (1998). Oxidation kinetics of Fe (II) in a eutrophic Swiss lake. *Environ. Sci. Technol.* 32, 2990–2996.

Falkowski, P. G., Barber, R. T., and Smetacek, V. (1998). Biogeochemical controls and feedbacks on ocean primary production. *Science (80-.).* 281, 200–206.

Field, M. P., and Sherrell, R. M. (2000). Dissolved and particulate Fe in a hydrothermal plume at 9°45'N, East Pacific Rise: Slow Fe (II) oxidation kinetics in Pacific plumes. *Geochim. Cosmochim. Acta* 64, 619–628. doi:10.1016/S0016-7037(99)00333-6.

Fitzsimmons, J. N., Boyle, E. A., and Jenkins, W. J. (2014). Distal transport of dissolved hydrothermal iron in the deep South Pacific Ocean. *Proc. Natl. Acad. Sci.* 111, 16654 LP – 16661. doi:10.1073/pnas.1418778111.

Fitzsimmons, J. N., Carrasco, G. G., Wu, J., Roshan, S., Hatta, M., Conway, T. J., et al. (2015). Partitioning of dissolved iron and iron isotopes into soluble and colloidal phases along the GA03 GEOTRACES North Atlantic Transect. *Deep Sea Res. Part II Top. Stud. Oceanogr.* 116, 130–151.

Fitzsimmons, J. N., John, S. G., Marsay, C. M., Hoffman, C. L., Nicholas, S. L., Toner, B. M., et al. (2017). Iron persistence in a distal hydrothermal plume supported by dissolved-particulate exchange. *Nat. Geosci.* 10, 195–201. doi:10.1038/ngeo2900.

Fouquet, Y. (1997). Discovery and first submersible investigations on the Rainbow Hydrothermal Field on the MAR (36 14'N). *Eos Trans. Am. Geophys. Union* 78, 832.

Fouquet, Y., Barriga, F., Charlou, J.-L., Elderfield, H., German, C. R., Ondreas, H., et al. (1998). FLORES diving cruise with Nautile near the Azores-First dives on the Rainbow field: hydrothermal seawater/mantle interaction. *InterRidge News* 7, 24–28.

Fouquet, Y., Cambon, P., Etoubleau, J., Charlou, J. L., Ondréas, H., Barriga, F. J. A. S., et al. (2013a). Geodiversity of hydrothermal processes along the mid-atlantic ridge and ultramafic-hosted mineralization: A new type of oceanic Cu-Zn-Co-Au volcanogenic massive sulfide deposit. *Geophys. Monogr. Ser.* 188, 321–367. doi:10.1029/2008GM000746.

Fouquet, Y., Cambon, P., Etoubleau, J., Charlou, J. L., OndréAs, H., Barriga, F. J. A. S., et al. (2013b). "Geodiversity of hydrothermal processes along the Mid-Atlantic Ridge and ultramafic-hosted mineralization: A new type of oceanic Cu-Zn-Co-Au volcanogenic massive sulfide deposit," in *Diversity Of Hydrothermal Systems On Slow Spreading Ocean Ridges Diversity Of Hydrothermal Systems On Slow Spreading Ocean Ridges* (Wiley-Blackwell), 321–367. doi:10.1029/2008GM000746.

Fouquet, Y., Charlou, J.-L., Donval, J.-P., Radford-Knoery, J., Pelle, P., Ondreas, H., et al. (1994). A detailed study of the Lucky-Strike hydrothermal site and discovery of a new hydrothermal site:«Menez-Gwen». Preliminary results of DIVA 1 cruise (5-29 May, 1994). *Inter-Ridge News* 3, 14–17.

Fouquet, Y., Stackelberg, U. Von, Charlou, J. L., Donval, J. P., Erzinger, J., Foucher, J. P., et al. (1991). Hydrothermal activity and metallogenesis in the Lau back-arc basin. *Nature* 349, 778–781. doi:10.1038/349778a0.

Frierdich, A. J., Helgeson, M., Liu, C., Wang, C., Rosso, K. M., and Scherer, M. M. (2015).

Iron Atom Exchange between Hematite and Aqueous Fe(II). *Environ. Sci. Technol.* 49, 8479–8486. doi:10.1021/acs.est.5b01276.

Gamo, T., Chiba, H., Masuda, H., Edmonds, H. N., Fujioka, K., Kodama, Y., et al. (1996). Chemical characteristics of hydrothermal fluids from the TAG Mound of the Mid-Atlantic Ridge in August 1994: Implications for spatial and temporal variability of hydrothermal activity. *Geophys. Res. Lett.* 23, 3483–3486.

Gartman, A., and Findlay, A. J. (2020). Impacts of hydrothermal plume processes on oceanic metal cycles and transport. *Nat. Geosci.* 13, 396–402. doi:10.1038/s41561-020-0579-0.

Gartman, A., Findlay, A. J., and Luther III, G. W. (2014). Nanoparticulate pyrite and other nanoparticles are a widespread component of hydrothermal vent black smoker emissions. *Chem. Geol.* 366, 32–41.

Gartman, A., and Luther, G. W. (2014). Oxidation of synthesized sub-micron pyrite (FeS2) in seawater. *Geochim. Cosmochim. Acta* 144, 96–108.

German, C. R., Campbell, A. C., and Edmond, J. M. (1991a). Hydrothermal scavenging at the Mid-Atlantic Ridge: Modification of trace element dissolved fluxes. *Earth Planet. Sci. Lett.* 107, 101–114. doi:10.1016/0012-821X(91)90047-L.

German, C. R., Casciotti, K. A., Dutay, J.-C., Heimbürger, L. E., Jenkins, W. J., Measures, C. I., et al. (2016). Hydrothermal impacts on trace element and isotope ocean biogeochemistry. *Philos. Trans. R. Soc. A Math. Phys. Eng. Sci.* 374. doi:10.1098/rsta.2016.0035.

German, C. R., Fleer, A. P., Bacon, M. P., and Edmond, J. M. (1991b). Hydrothermal scavenging at the Mid-Atlantic Ridge: radionuclide distributions. *Earth Planet. Sci. Lett.* doi:10.1016/0012-821X(91)90128-5.

German, C. R., Klinkhammer, G. P., and Rudnicki, M. D. (1996). The Rainbow hydrothermal plume, 36°15′N, MAR. *Geophys. Res. Lett.* doi:10.1029/96GL02883.

German, C. R., Legendre, L. L., Sander, S. G., Niquil, N., Luther Iii, G. W., Bharati, L., et al. (2015). Hydrothermal Fe cycling and deep ocean organic carbon scavenging: Model-based evidence for significant POC supply to seafloor sediments. *Earth Planet. Sci. Lett.* 419, 143–153. doi:10.1016/j.epsl.2015.03.012.

German, C. R., and Sparks, R. S. J. (1993). Particle recycling in the TAG hydrothermal plume. *Earth Planet. Sci. Lett.* 116, 129–134. doi:10.1016/0012-821X(93)90049-F.

German, C. R., and Von Damm, K. L. (2004). "Hydrothermal processes," in *The Oceans and Marine Geochemistry*, eds. H. D. Holland, K. K. Turekian, and H. Elderfield (Elsevier-Pergamon), 181–222.

Gledhill, M., and Buck, K. (2012). The Organic Complexation of Iron in the Marine Environment: A Review. *Front. Microbiol.* 3, 69.

Goldberg, E. D. (1954). Marine geochemistry 1. Chemical scavengers of the sea. *J. Geol.* 62, 249–265.

González-Davila, M., Santana-Casiano, J. M., and Millero, F. J. (2005). Oxidation of iron (II) nanomolar with H_2O_2 in seawater. *Geochim. Cosmochim. Acta* 69, 83–93.

González-Dávila, M., Santana-Casiano, J. M., and Millero, F. J. (2006). Competition between

O_2 and H_2O_2 in the oxidation of Fe (II) in natural waters. *J. Solution Chem.* 35, 95–111.

González-Santana, D., González-Dávila, M., Lohan, M. C., Artigue, L., Planquette, H., Sarthou, G., et al. Variability in iron (II) oxidation kinetics across diverse hydrothermal sites on the northern Mid Atlantic Ridge. *Geochim. Cosmochim. Acta*.

Gordon, R. M., Martin, J. H., and Knauer, G. A. (1982). Iron in north-east Pacific waters. *Nature* 299, 611–612.

Goto, S., Gamo, T., Chiba, H., Fujioka, K., and Mitsuzawa, K. (2007). Contribution of heat outputs from high- and low-temperature hydrothermal sources to the neutrally buoyant plume at the TAG hydrothermal mound, Mid-Atlantic Ridge. *Earth, Planets Sp.* 59, 1141–1146. doi:10.1186/BF03352057.

Grand, M. M., Laes-Huon, A., Fietz, S., Resing, J. A., Obata, H., Luther, G. W., et al. (2019). Developing Autonomous Observing Systems for Micronutrient Trace Metals. *Front. Mar. Sci.* 6, 35. doi:10.3389/fmars.2019.00035.

Gray, S. E. C., DeGrandpre, M. D., Moore, T. S., Martz, T. R., Friederich, G. E., and Johnson, K. S. (2011). Applications of in situ pH measurements for inorganic carbon calculations. *Mar. Chem.* 125, 82–90. doi:10.1016/j.marchem.2011.02.005.

Guieu, C., Bonnet, S., Petrenko, A., Menkes, C., Chavagnac, V., Desboeufs, K., et al. (2018). Iron from a submarine source impacts the productive layer of the Western Tropical South Pacific (WTSP). *Sci. Rep.* 8, 9075. doi:10.1038/s41598-018-27407-z.

Gurvich, E. G. ed. (2006). "Recent Metalliferous Sediments in the Oceans BT - Metalliferous Sediments of the World Ocean: Fundamental Theory of Deep-Sea Hydrothermal Sedimentation," in (Berlin, Heidelberg: Springer Berlin Heidelberg), 7–126. doi:10.1007/3-540-30969-1_2.

Hansard, S. P., Landing, W. M., Measures, C. I., and Voelker, B. M. (2009). Dissolved iron(II) in the Pacific Ocean: Measurements from the PO2 and P16N CLIVAR/CO2 repeat hydrography expeditions. *Deep Sea Res. Part I Oceanogr. Res. Pap.* 56, 1117–1129. doi:10.1016/J.DSR.2009.03.006.

Hatta, M., Measures, C. I., Wu, J., Roshan, S., Fitzsimmons, J. N., Sedwick, P. N., et al. (2015). An overview of dissolved Fe and Mn distributions during the 2010–2011 U.S. GEOTRACES north Atlantic cruises: GEOTRACES GA03. *Deep Sea Res. Part II Top. Stud. Oceanogr.* 116, 117–129. doi:10.1016/j.dsr2.2014.07.005.

Hawkes, J. A., Connelly, D. P., Gledhill, M., and Achterberg, E. P. (2013). The stabilisation and transportation of dissolved iron from high temperature hydrothermal vent systems. *Earth Planet. Sci. Lett.* 375, 280–290.

Hawkes, J. A., Connelly, D. P., Rijkenberg, M. J. A., and Achterberg, E. P. (2014). The importance of shallow hydrothermal island arc systems in ocean biogeochemistry. *Geophys. Res. Lett.* 41, 942–947.

Hawkes, J. A., Hansen, C. T., Goldhammer, T., Bach, W., and Dittmar, T. (2016). Molecular alteration of marine dissolved organic matter under experimental hydrothermal conditions. *Geochim. Cosmochim. Acta* 175, 68–85. doi:10.1016/j.gca.2015.11.025.

Herzig, P. M., Petersen, S., and Hannington, M. D. (2002). Polymetallic massive sulphide deposits at the modern seafloor and their resource potential. ISA Technical Study 2. *Int. Seabed Authority, Kingst. Jamaica (116 pp.)*.

Ho, T., Quigg, A., Finkel, Z. V, Milligan, A. J., Wyman, K., Falkowski, P. G., et al. (2003). The elemental composition of some marine phytoplankton 1. *J. Phycol.* 39, 1145–1159.

Holmes, T. M., Wuttig, K., Chase, Z., Schallenberg, C., van der Merwe, P., Townsend, A. T., et al. (2020). Glacial and Hydrothermal Sources of Dissolved Iron (II) in Southern Ocean Waters Surrounding Heard and McDonald Islands. *J. Geophys. Res. Ocean.* 125. doi:10.1029/2020JC016286.

Hong, H., and Kester, D. R. (1986). Redox state of iron in the offshore waters of Peru[1]. *Limnol. Oceanogr.* 31, 512–524.

Horner, T. J., Williams, H. M., Hein, J. R., Saito, M. A., Burton, K. W., Halliday, A. N., et al. (2015). Persistence of deeply sourced iron in the Pacific Ocean. *Proc. Natl. Acad. Sci. U. S. A.* 112, 1292–1297. doi:10.1073/pnas.1420188112.

Hutchins, D. A., and Bruland, K. W. (1998). Iron-limited diatom growth and Si:N uptake ratios in a coastal upwelling regime. *Nature* 393, 561–564. doi:10.1038/31203.

Hutchins, D. A., DiTullio, G. R., Zhang, Y., and Bruland, K. W. (1998). An iron limitation mosaic in the California upwelling regime. *Limnol. Oceanogr.* 43, 1037–1054.

Hutchins, D. A., Hare, C. E., Weaver, R. S., Zhang, Y., Firme, G. F., DiTullio, G. R., et al. (2002). Phytoplankton iron limitation in the Humboldt Current and Peru Upwelling. *Limnol. Oceanogr.* 47, 997–1011.

Hutchins, D. A., Witter, A. E., Butler, A., and Luther, G. W. (1999). Competition among marine phytoplankton for different chelated iron species. *Nature* 400, 858–861.

James, R. H., Elderfield, H., and Palmer, M. R. (1995). The chemistry of hydrothermal fluids from the Broken Spur site, 29 N Mid-Atlantic Ridge. *Geochim. Cosmochim. Acta* 59, 651–659.

Johnson, K. S., Michael Gordon, R., and Coale, K. H. (1997). What controls dissolved iron concentrations in the world ocean? *Mar. Chem.* 57, 137–161. doi:10.1016/S0304-4203(97)00043-1.

Kadko, D. (1993). An assessment of the effect of chemical scavenging within submarine hydrothermal plumes upon ocean geochemistry. *Earth Planet. Sci. Lett.* 120, 361–374.

Kelley, D. S., Karson, J. A., Blackman, D. K., Früh-Green, G. L., Butterfield, D. A., Lilley, M. D., et al. (2001). An off-axis hydrothermal vent field near the Mid-Atlantic Ridge at 30 N. *Nature* 412, 145–149.

Kelley, D. S., Karson, J. A., Früh-Green, G. L., Yoerger, D. R., Shank, T. M., Butterfield, D. A., et al. (2005). A Serpentinite-Hosted Ecosystem: The Lost City Hydrothermal Field. *Science (80-.).* 307, 1428 LP – 1434. doi:10.1126/science.1102556.

Kester, D. R., Byrne Jr, R. H., and Liang, Y.-J. (1975). "Redox reactions and solution complexes of iron in marine systems," in (ACS Publications).

King, D. W. (1998). Role of carbonate speciation on the oxidation rate of Fe (II) in aquatic systems. *Environ. Sci. Technol.* 32, 2997–3003.

King, D. W., Lounsbury, H. A., and Millero, F. J. (1995). Rates and Mechanism of Fe(II) Oxidation at Nanomolar Total Iron Concentrations. *Environ. Sci. Technol.* 29, 818–824. doi:10.1021/es00003a033.

Kinoshita, M., Kawada, Y., Tanaka, A., and Urabe, T. (2006). Recharge/discharge interface of a secondary hydrothermal circulation in the Suiyo Seamount of the Izu-Bonin arc, identified by submersible-operated heat flow measurements. *Earth Planet. Sci. Lett.* 245, 498–508. doi:10.1016/j.epsl.2006.02.006.

Klar, J. K., Homoky, W. B., Statham, P. J., Birchill, A. J., Harris, E. L., Woodward, E. M. S., et al. (2017). Stability of dissolved and soluble Fe(II) in shelf sediment pore waters and release to an oxic water column. *Biogeochemistry* 135, 49–67. doi:10.1007/s10533-017-0309-x.

Kleint, C., Hawkes, J. A., Sander, S. G., and Koschinsky, A. (2016). Voltammetric investigation of hydrothermal iron speciation. *Front. Mar. Sci.* 3, 75. doi:10.3389/fmars.2016.00075.

Klinkhammer, G., Elderfield, H., Greaves, M., Rona, P. A., and Nelsen, T. A. (1986). Manganese geochemistry near high-temperature vents in the Mid-Atlantic Ridge rift valley. *Earth Planet. Sci. Lett.* 80, 230–240. doi:10.1016/0012-821X(86)90107-X.

Klinkhammer, G., Rona, P. A., Greaves, M., and Elderfield, H. (1985). Hydrothermal manganese plumes in the Mid-Atlantic Ridge rift valley. *Nature* 314, 727. doi:10.1038/314727a0.

Klunder, M. B., Bauch, D., Laan, P., de Baar, H. J. W., Heuven, S. V, and Ober, S. (2012). Dissolved iron in the Arctic shelf seas and surface waters of the central Arctic Ocean: Impact of Arctic river water and ice-melt. *J. Geophys. Res. Ocean.* 117. doi:10.1029/2011JC007133.

Klunder, M. B., Laan, P., Middag, R., de Baar, H. J. W., and Van Ooijen, J. C. (2011). Dissolved iron in the Southern Ocean (Atlantic sector). *Deep Sea Res. Part II Top. Stud. Oceanogr.* 58, 2678–2694.

Koch, B. P., Witt, M., Engbrodt, R., Dittmar, T., and Kattner, G. (2005). Molecular formulae of marine and terrigenous dissolved organic matter detected by electrospray ionization Fourier transform ion cyclotron resonance mass spectrometry. *Geochim. Cosmochim. Acta* 69, 3299–3308.

Lagerström, M. E., Field, M. P., Séguret, M., Fischer, L., Hann, S., and Sherrell, R. M. (2013). Automated on-line flow-injection ICP-MS determination of trace metals (Mn, Fe, Co, Ni, Cu and Zn) in open ocean seawater: Application to the GEOTRACES program. *Mar. Chem.* 155, 71–80. doi:10.1016/j.marchem.2013.06.001.

Laglera, L. M., and Van den Berg, C. M. G. (2007). Wavelength dependence of the photochemical reduction of iron in Arctic seawater. *Environ. Sci. Technol.* 41, 2296–2302.

Lalou, C., Reyss, J., Brichet, E., Rona, P. A., and Thompson, G. (1995). Hydrothermal activity on a 10^5-year scale at a slow-spreading ridge, TAG hydrothermal field, Mid-Atlantic Ridge 26° N. *J. Geophys. Res. Solid Earth* 100, 17855–17862. doi:10.1029/95JB01858.

Landing, W. M., and Bruland, K. W. (1987). The contrasting biogeochemistry of iron and manganese in the Pacific Ocean. *Geochim. Cosmochim. Acta* 51, 29–43.

Langmuir, C., Humphris, S., Fornari, D., Van Dover, C., Von Damm, K., Tivey, M. K., et al. (1997). Hydrothermal vents near a mantle hot spot: the Lucky Strike vent field at 37N

on the Mid-Atlantic Ridge. *Earth Planet. Sci. Lett.* 148, 69–91.

Lannuzel, D., Schoemann, V., De Jong, J., Chou, L., Delille, B., Becquevort, S., et al. (2008). Iron study during a time series in the western Weddell pack ice. *Mar. Chem.* 108, 85–95.

Liu, M., and Tanhua, T. (2019). Characteristics of water masses in the Atlantic Ocean based on GLODAPv2 data. *Ocean Sci. Discuss.*, 1–43.

Liu, X., and Millero, F. J. (2002). The solubility of iron in seawater. *Mar. Chem.* 77, 43–54. doi:10.1016/S0304-4203(01)00074-3.

Lohan, M. C., Aguilar-Islas, A. M., and Bruland, K. W. (2006). Direct determination of iron in acidified (pH 1.7) seawater samples by flow injection analysis with catalytic spectrophotometric detection: Application and intercomparison. *Limnol. Oceanogr. Methods* 4, 164–171. doi:10.4319/lom.2006.4.164.

Lough, A. J. M., Connelly, D. P., Homoky, W. B., Hawkes, J. A., Chavagnac, V., Castillo, A., et al. (2019a). Diffuse Hydrothermal Venting: A Hidden Source of Iron to the Oceans. *Front. Mar. Sci.* 6, 329. doi:10.3389/fmars.2019.00329.

Lough, A. J. M., Homoky, W. B., Connelly, D. P., Comer-Warner, S. A., Nakamura, K., Abyaneh, M. K., et al. (2019b). Soluble iron conservation and colloidal iron dynamics in a hydrothermal plume. *Chem. Geol.* 511, 225–237.

Lough, A. J. M., Klar, J. K., Homoky, W. B., Comer-Warner, S. A., Milton, J. A., Connelly, D. P., et al. (2017). Opposing authigenic controls on the isotopic signature of dissolved iron in hydrothermal plumes. *Geochim. Cosmochim. Acta* 202, 1–20. doi:10.1016/j.gca.2016.12.022.

Ludwig, K. A., Kelley, D. S., Butterfield, D. A., Nelson, B. K., and Früh-Green, G. L. (2006). Formation and evolution of carbonate chimneys at the Lost City Hydrothermal Field. *Geochim. Cosmochim. Acta* 70, 3625–3645.

Lueker, T. J., Dickson, A. G., and Keeling, C. D. (2000). Ocean pCO_2 calculated from dissolved inorganic carbon, alkalinity, and equations for K_1 and K_2: validation based on laboratory measurements of CO_2 in gas and seawater at equilibrium. *Mar. Chem.* 70, 105–119.

Luther, G. W., Kostka, J. E., Church, T. M., Sulzberger, B., and Stumm, W. (1992). Seasonal iron cycling in the salt-marsh sedimentary environment: the importance of ligand complexes with Fe (II) and Fe (III) in the dissolution of Fe (III) minerals and pyrite, respectively. *Mar. Chem.* 40, 81–103.

Lyons, T. W., Reinhard, C. T., and Planavsky, N. J. (2014). The rise of oxygen in Earth's early ocean and atmosphere. *Nature* 506, 307–315. doi:10.1038/nature13068.

Macdonald, K. C. (1983). "A geophysical comparison between fast and slow spreading centers: constraints on magma chamber formation and hydrothermal activity," in *Hydrothermal Processes at seafloor spreading centers* (Springer), 27–51.

Machado-Infante, J., Ramírez-Caballero, G., and Barajas-Meneses, M. (2016). Study of the adsorption capacity of Fe(II) dissolved in water by using a mineral rich in Manganese Dioxide (MnO2) from Colombia . *DYNA* 83, 223–228.

Mahowald, N. M., Baker, A. R., Bergametti, G., Brooks, N., Duce, R. A., Jickells, T. D., et al. (2005). Atmospheric global dust cycle and iron inputs to the ocean. *Global*

Biogeochem. Cycles 19. doi:10.1029/2004GB002402.

Maldonado, M. T., and Price, N. M. (1999). Utilization of iron bound to strong organic ligands by plankton communities in the subarctic Pacific Ocean. *Deep Sea Res. Part II Top. Stud. Oceanogr.* 46, 2447–2473.

Maldonado, M. T., and Price, N. M. (2001). Reduction and transport of organically bound iron by Thalassiosira oceanica (Bacillariophyceae). *J. Phycol.* 37, 298–310.

Mandernack, K. W., and Tebo, B. M. (1993). Manganese scavenging and oxidation at hydrothermal vents and in vent plumes. *Geochim. Cosmochim. Acta* 57, 3907–3923. doi:10.1016/0016-7037(93)90343-U.

Martin, J. H. (1990). Glacial-interglacial CO2 change: The Iron Hypothesis. *Paleoceanography* 5, 1–13. doi:10.1029/PA005i001p00001.

Martin, J. H., and Fitzwater, S. E. (1988). Iron deficiency limits phytoplankton growth in the north-east Pacific subarctic. *Nature* 331, 341–343. doi:10.1038/331341a0.

Martin, J. H., Gordon, R. M., and Fitzwater, S. E. (1990). Iron in Antarctic waters. *Nature* 345, 156–158.

Massoth, G., Baker, E., Worthington, T., Lupton, J., de Ronde, C., Arculus, R., et al. (2007). Multiple hydrothermal sources along the south Tonga arc and Valu Fa Ridge. *Geochemistry, Geophys. Geosystems* 8. doi:10.1029/2007GC001675.

Massoth, G. J., Baker, E. T., Feely, R. A., Lupton, J. E., Collier, R. W., Gendron, J. F., et al. (1998). Manganese and iron in hydrothermal plumes resulting from the 1996 Gorda Ridge Event. *Deep Sea Res. Part II Top. Stud. Oceanogr.* 45, 2683–2712.

Massoth, G. J., Baker, E. T., Lupton, J. E., Feely, R. A., Butterfield, D. A., Von Damm, K. L., et al. (1994). Temporal and spatial variability of hydrothermal manganese and iron at Cleft segment, Juan de Fuca Ridge. *J. Geophys. Res. Solid Earth* 99, 4905–4923.

Measures, C., Hatta, M., Fitzsimmons, J., and Morton, P. (2015). Dissolved Al in the zonal N Atlantic section of the US GEOTRACES 2010/2011 cruises and the importance of hydrothermal inputs. *Deep Sea Res. Part II Top. Stud. Oceanogr.* 116, 176–186.

Middag, R., De Baar, H. J. W., Laan, P., and Bakker, K. (2009). Dissolved aluminium and the silicon cycle in the Arctic Ocean. *Mar. Chem.* 115, 176–195.

Middag, R., Van Slooten, C., De Baar, H. J. W., and Laan, P. (2011). Dissolved aluminium in the Southern Ocean. *Deep Sea Res. Part II Top. Stud. Oceanogr.* 58, 2647–2660.

Miller, W. L., King, D. W., Lin, J., and Kester, D. R. (1995). Photochemical redox cycling of iron in coastal seawater. *Mar. Chem.* 50, 63–77.

Millero, F. J. (1985). The effect of ionic interactions on the oxidation of metals in natural waters. *Geochim. Cosmochim. Acta* 49, 547–553.

Millero, F. J. (1986). The pH of estuarine waters. *Limnol. Oceanogr.* 31, 839–847. doi:10.4319/lo.1986.31.4.0839.

Millero, F. J., and Sotolongo, S. (1989). The oxidation of Fe (II) with H_2O_2 in seawater. *Geochim. Cosmochim. Acta* 53, 1867–1873.

Millero, F. J., Sotolongo, S., and Izaguirre, M. (1987). The oxidation kinetics of Fe(II) in

seawater. *Geochim. Cosmochim. Acta* 51, 793–801. doi:10.1016/0016-7037(87)90093-7.

Millero, F. J., Yao, W., and Aicher, J. (1995). The speciation of Fe (II) and Fe (III) in natural waters. *Mar. Chem.* 50, 21–39.

Mills, R. A., Wells, D. M., and Roberts, S. (2001). Genesis of ferromanganese crusts from the TAG hydrothermal field. *Chem. Geol.* 176, 283–293. doi:10.1016/S0009-2541(00)00404-6.

Moore, C. M., Mills, M. M., Arrigo, K. R., Berman-Frank, I., Bopp, L., Boyd, P. W., et al. (2013). Processes and patterns of oceanic nutrient limitation. *Nat. Geosci.* 6, 701–710. doi:10.1038/ngeo1765.

Moore, C. M., Mills, M. M., Milne, A., Langlois, R., Achterberg, E. P., Lochte, K., et al. (2006). Iron limits primary productivity during spring bloom development in the central North Atlantic. *Glob. Chang. Biol.* 12, 626–634.

Morel, F. M. M., Kustka, A. B., and Shaked, Y. (2008). The role of unchelated Fe in the iron nutrition of phytoplankton. *Limnol. Oceanogr.* 53, 400–404.

Moriceau, B., Goutx, M., Guigue, C., Lee, C., Armstrong, R., Duflos, M., et al. (2009). Si–C interactions during degradation of the diatom Skeletonema marinoi. *Deep Sea Res. Part II Top. Stud. Oceanogr.* 56, 1381–1395. doi:10.1016/j.dsr2.2008.11.026.

Mottl, M. J., Holland, H. D., and Corr, R. F. (1979). Chemical exchange during hydrothermal alteration of basalt by seawater-II. Experimental results for Fe, Mn, and sulfur species. *Geochim. Cosmochim. Acta* 43, 869–884. doi:10.1016/0016-7037(79)90225-4.

Mottl, M. J., and McConachy, T. F. (1990). Chemical processes in buoyant hydrothermal plumes on the East Pacific Rise near 21 N. *Geochim. Cosmochim. Acta* 54, 1911–1927.

Murton, B. J., and Van Dover, C. L. (1993). ALVIN dives on the Broken Spur hydrothermal vent field at 29 10′ N on the Mid-Atlantic Ridge. *Bridg. Newsl.* 5, 11–14.

Nelsen, T. A., Klinkhammer, G. P., Trefry, J. H., and Trocine, R. P. (1987). Real-time observation of dispersed hydrothermal plumes using nephelometry: examples from the Mid-Atlantic Ridge. *Earth Planet. Sci. Lett.* doi:10.1016/0012-821X(87)90160-9.

Nishioka, J., Obata, H., and Tsumune, D. (2013). Evidence of an extensive spread of hydrothermal dissolved iron in the Indian Ocean. *Earth Planet. Sci. Lett.* 361, 26–33.

Noble, A. E., Lamborg, C. H., Ohnemus, D. C., Lam, P. J., Goepfert, T. J., Measures, C. I., et al. (2012). Basin-scale inputs of cobalt, iron, and manganese from the Benguela-Angola front to the South Atlantic Ocean. *Limnol. Oceanogr.* 57, 989–1010.

O'Sullivan, D. W., Hanson, A. K., Miller, W. L., and Kester, D. R. (1991). Measurement of Fe (II) in surface water of the equatorial Pacific. *Limnol. Oceanogr.* 36, 1727–1741.

O'Sullivan, D. W., Neale, P. J., Coffin, R. B., Boyd, T. J., and Osburn, C. L. (2005). Photochemical production of hydrogen peroxide and methylhydroperoxide in coastal waters. *Mar. Chem.* 97, 14–33.

Obata, H., Karatani, H., and Nakayama, E. (1993). Automated Determination of Iron in Seawater by Chelating Resin Concentration and Chemiluminescence Detection. *Anal. Chem.* 65, 1524–1528. doi:10.1021/ac00059a007.

Pérez-Almeida, N., González, A. G., Santana-Casiano, J. M., and González-Dávila, M.

(2019). Iron and copper redox interactions in UV-seawater: A kinetic model approach. *Chem. Geol.* 506, 149–161.

Pernet-Coudrier, B., Waeles, M., Filella, M., Quentel, F., and Riso, R. D. (2013). Simple and simultaneous determination of glutathione, thioacetamide and refractory organic matter in natural waters by DP-CSV. *Sci. Total Environ.* 463–464, 997–1005. doi:10.1016/j.scitotenv.2013.06.053.

Pichler, T., and Veizer, J. (1999). Precipitation of Fe(III) oxyhydroxide deposits from shallow-water hydrothermal fluids in Tutum Bay, Ambitle Island, Papua New Guinea. *Chem. Geol.* 162, 15–31. doi:10.1016/S0009-2541(99)00068-6.

Planquette, H., and Sherrell, R. M. (2012). Sampling for particulate trace element determination using water sampling bottles: methodology and comparison to in situ pumps. *Limnol. Oceanogr. Methods* 10, 367–388. doi:10.4319/lom.2012.10.367.

Planquette, H., Statham, P. J., Fones, G. R., Charette, M. A., Moore, C. M., Salter, I., et al. (2007). Dissolved iron in the vicinity of the Crozet Islands, Southern Ocean. *Deep. Res. Part II Top. Stud. Oceanogr.* 54, 1999–2019. doi:10.1016/j.dsr2.2007.06.019.

Pollard, R., Sanders, R., Lucas, M., and Statham, P. J. (2007). The Crozet Natural Iron Bloom and Export Experiment (CROZEX). *Deep. Res. Part II Top. Stud. Oceanogr.* 54, 1905–1914. doi:10.1016/j.dsr2.2007.07.023.

Raven, J. A. (1990). Predictions of Mn and Fe use efficiencies of phototrophic growth as a function of light availability for growth and of C assimilation pathway. *New Phytol.* 116, 1–18.

Raven, J. A., Evans, M. C. W., and Korb, R. E. (1999). The role of trace metals in photosynthetic electron transport in O-2-evolving organisms. *Photosynth. Res.* 60, 111–149. doi:10.1023/a:1006282714942.

Resing, J. A., Baker, E. T., Lupton, J. E., Walker, S. L., Butterfield, D. A., Massoth, G. J., et al. (2009). Chemistry of hydrothermal plumes above submarine volcanoes of the Mariana Arc. *Geochemistry, Geophys. Geosystems* 10.

Resing, J. A., Sedwick, P. N., German, C. R., Jenkins, W. J., Moffett, J. W., Sohst, B. M., et al. (2015). Basin-scale transport of hydrothermal dissolved metals across the South Pacific Ocean. *Nature* 523, 200–203. doi:10.1038/nature14577.

Rona, P. A. (1980). TAG Hydrothermal Field: Mid-Atlantic Ridge crest at latitude 26°N. *J. Geol. Soc. London.* 137, 385–402. doi:10.1144/gsjgs.137.4.0385.

Rona, P. A. (2005). TAG hydrothermal field: A key to modern and ancient seafloor hydrothermal VMS ore-forming systems BT. in *Mineral Deposit Research: Meeting the Global Challenge*, eds. J. Mao and F. P. Bierlein (Berlin, Heidelberg: Springer Berlin Heidelberg), 687–690.

Rona, P. A., Klinkhammer, G., Nelsen, T. A., Trefry, J. H., and Elderfield, H. (1986). Black smokers, massive sulphides and vent biota at the Mid-Atlantic Ridge. *Nature* 321, 33–37. doi:10.1038/321033a0.

Rona, P. A., and Speer, K. G. (1989). An Atlantic hydrothermal plume: Trans-Atlantic geotraverse (TAG) area, Mid-Atlantic Ridge crest near 26°N. *J. Geophys. Res. Solid Earth* 94, 13879–13893. doi:10.1029/JB094iB10p13879.

Rose, A. L., and Waite, T. D. (2002). Kinetic model for Fe (II) oxidation in seawater in the absence and presence of natural organic matter. *Environ. Sci. Technol.* 36, 433–444.

Rose, A. L., and Waite, T. D. (2003a). Effect of dissolved natural organic matter on the kinetics of ferrous iron oxygenation in seawater. *Environ. Sci. Technol.* 37, 4877–4886.

Rose, A. L., and Waite, T. D. (2003b). Kinetics of iron complexation by dissolved natural organic matter in coastal waters. *Mar. Chem.* 84, 85–103.

Rouxel, O., Toner, B., Germain, Y., and Glazer, B. (2018). Geochemical and iron isotopic insights into hydrothermal iron oxyhydroxide deposit formation at Loihi Seamount. *Geochim. Cosmochim. Acta* 220, 449–482.

Roy, E. G., and Wells, M. L. (2011). Evidence for regulation of Fe (II) oxidation by organic complexing ligands in the Eastern Subarctic Pacific. *Mar. Chem.* 127, 115–122.

Roy, E. G., Wells, M. L., and King, D. W. (2008). Persistence of iron (II) in surface waters of the western subarctic Pacific. *Limnol. Oceanogr.* 53, 89–98.

Rudnicki, M. D., and Elderfield, H. (1992). Theory applied to the Mid-Atlantic ridge hydrothermal plumes: the finite-difference approach. *J. Volcanol. Geotherm. Res.* 50, 161–172. doi:10.1016/0377-0273(92)90043-D.

Rudnicki, M. D., and Elderfield, H. (1993). A chemical model of the buoyant and neutrally buoyant plume above the TAG vent field, 26 degrees N, Mid-Atlantic Ridge. *Geochim. Cosmochim. Acta* 57, 2939–2957. doi:10.1016/0016-7037(93)90285-5.

Rue, E. L., and Bruland, K. W. (1995). Complexation of iron(III) by natural organic ligands in the Central North Pacific as determined by a new competitive ligand equilibration/adsorptive cathodic stripping voltammetric method. *Mar. Chem.* 50, 117–138. doi:10.1016/0304-4203(95)00031-L.

Rue, E. L., and Bruland, K. W. (1997). The role of organic complexation on ambient iron chemistry in the equatorial Pacific Ocean and the response of a mesoscale iron addition experiment. *Limnol. Oceanogr.* 42, 901–910.

Saito, M. A., Noble, A. E., Tagliabue, A., Goepfert, T. J., Lamborg, C. H., and Jenkins, W. J. (2013). Slow-spreading submarine ridges in the South Atlantic as a significant oceanic iron source. *Nat. Geosci.* 6, 775–779. doi:10.1038/ngeo1893.

Saito, M. A., Sigman, D. M., and Morel, F. M. M. (2003). The bioinorganic chemistry of the ancient ocean: the co-evolution of cyanobacterial metal requirements and biogeochemical cycles at the Archean–Proterozoic boundary? *Inorganica Chim. Acta* 356, 308–318. doi:10.1016/S0020-1693(03)00442-0.

Samperio-Ramos, G., Casiano, J. M. S., and Dávila, M. G. (2016). Effect of ocean warming and acidification on the Fe (II) oxidation rate in oligotrophic and eutrophic natural waters. *Biogeochemistry* 128, 19–34.

Sander, S. G., and Koschinsky, A. (2011). Metal flux from hydrothermal vents increased by organic complexation. *Nat. Geosci.* 4, 145–150. doi:10.1038/ngeo1088.

Sands, C. M., Connelly, D. P., Statham, P. J., and German, C. R. (2012). Size fractionation of trace metals in the Edmond hydrothermal plume, Central Indian Ocean. *Earth Planet. Sci. Lett.* 319, 15–22.

Santana-Casiano, J. M., González-Dávila, M., González, A. G., and Millero, F. J. (2010). Fe (III) reduction in the presence of catechol in seawater. *Aquat. geochemistry* 16, 467–482.

Santana-Casiano, J. M., González-Dávila, M., González, A. G., Rico, M., López, A., and Martel, A. (2014). Characterization of phenolic exudates from Phaeodactylum tricornutum and their effects on the chemistry of Fe (II)–Fe (III). *Mar. Chem.* 158, 10–16.

Santana-Casiano, J. M., González-Dávila, M., and Millero, F. J. (2004). The oxidation of Fe (II) in $NaCl^-$ HCO_3^- and seawater solutions in the presence of phthalate and salicylate ions: a kinetic model. *Mar. Chem.* 85, 27–40.

Santana-Casiano, J. M., González-Dávila, M., and Millero, F. J. (2005). Oxidation of nanomolar level of Fe(II) with oxygen in natural waters. *Environ. Sci. Technol.* 39, 2073–2079. doi:10.1021/es049748y.

Santana-Casiano, J. M., González-Dávila, M., and Millero, F. J. (2006). The role of Fe(II) species on the oxidation of Fe(II) in natural waters in the presence of O_2 and H_2O_2. *Mar. Chem.* 99, 70–82. doi:10.1016/j.marchem.2005.03.010.

Santana-Casiano, J. M., González-Dávila, M., Rodríguez, M. J., and Millero, F. J. (2000). The effect of organic compounds in the oxidation kinetics of Fe(II). *Mar. Chem.* 70, 211–222. doi:10.1016/S0304-4203(00)00027-X.

Santana-González, C., González-Dávila, M., Santana-Casiano, J. M., Gladyshev, S., and Sokov, A. (2019). Organic matter effect on Fe (II) oxidation kinetics in the Labrador Sea. *Chem. Geol.* 511, 238–255.

Santana-González, C., Santana-Casiano, J. M., González-Dávila, M., and Fraile-Nuez, E. (2017). Emissions of Fe(II) and its kinetic of oxidation at Tagoro submarine volcano, El Hierro. *Mar. Chem.* 195, 129–137. doi:10.1016/j.marchem.2017.02.001.

Santana-González, C., Santana-Casiano, J. M., González-Dávila, M., Santana-del Pino, A., Gladyshev, S., and Sokov, A. (2018). Fe (II) oxidation kinetics in the North Atlantic along the 59.5° N during 2016. *Mar. Chem.* 203, 64–77.

Sarradin, P.-M., Le Bris, N., Le Gall, C., and Rodier, P. (2005). Fe analysis by the ferrozine method: Adaptation to FIA towards in situ analysis in hydrothermal environment. *Talanta* 66, 1131–1138. doi:10.1016/j.talanta.2005.01.012.

Sarthou, G., Bucciarelli, E., Chever, F., Hansard, S. P., González-Dávila, M., Santana-Casiano, J. M., et al. (2011). Labile Fe(II) concentrations in the Atlantic sector of the Southern Ocean along a transect from the subtropical domain to the Weddell Sea Gyre. *Biogeosciences* 8, 2461–2479. doi:10.5194/bg-8-2461-2011.

Schallenberg, C., Davidson, A. B., Simpson, K. G., Miller, L. A., and Cullen, J. T. (2015). Iron (II) variability in the northeast subarctic Pacific Ocean. *Mar. Chem.* 177, 33–44.

Schlosser, C., and Croot, P. L. (2008). Application of cross-flow filtration for determining the solubility of iron species in open ocean seawater. *Limnol. Oceanogr. Methods* 6, 630–642.

Schlosser, C., Streu, P., and Croot, P. L. (2013). Vivaspin ultrafiltration: A new approach for high resolution measurements of colloidal and soluble iron species. *Limnol. Oceanogr. Methods* 11, 187–201.

Schrope, M. (2010). Trace that metal. *Nature* 463, 145. doi:10.1038/463145a.

Searle, R. (2013). *Mid-ocean ridges*. Cambridge University Press.

Sedwick, P. N., Sohst, B. M., Ussher, S. J., and Bowie, A. R. (2015). A zonal picture of the water column distribution of dissolved iron(II) during the U.S. GEOTRACES North Atlantic transect cruise (GEOTRACES GA03). *Deep. Res. Part II Top. Stud. Oceanogr.* 116, 166–175. doi:10.1016/j.dsr2.2014.11.004.

Seyfried, W. E., and Ding, K. (1993). The effect of redox on the relative solubilities of copper and iron in Cl-bearing aqueous fluids at elevated temperatures and pressures: An experimental study with application to subseafloor hydrothermal systems. *Geochim. Cosmochim. Acta* 57, 1905–1917. doi:10.1016/0016-7037(93)90083-9.

Shaked, Y., Kustka, A. B., and Morel, F. M. M. (2005). A general kinetic model for iron acquisition by eukaryotic phytoplankton. *Limnol. Oceanogr.* 50, 872–882.

Sharqawy, M. H., Lienhard, V. J. H., and Zubair, S. M. (2010). The thermophysical properties of seawater: a review of existing correlations and data. *Desalin. Water Treat.* 16, 354–380. doi:10.5004/dwt.2010.1079.

Smith, P. A., and Cronan, D. S. (1983). The geochemistry of metalliferous sediments and waters associated with shallow submarine hydrothermal activity (Santorini, Aegean Sea). *Chem. Geol.* 39, 241–262. doi:10.1016/0009-2541(83)90017-7.

Socolofsky, S., and Adams, E. (2002). Multi-phase plumes in uniform and stratified crossflow. *J. Hydraul. Res.* 40, 661–672. doi:10.1080/00221680209499913.

Speer, K. G., and Marshall, J. (1995). The growth of convective plumes at seafloor hot springs. *J. Mar. Res.* 53, 1025–1057. doi:10.1357/0022240953212972.

Speer, K. G., and Rona, P. A. (1989). A model of an Atlantic and Pacific hydrothermal plume. *J. Geophys. Res.* 94, 6213–6220. doi:10.1029/jc094ic05p06213.

Spiess, F. N., Macdonald, K. C., Atwater, T., Ballard, R., Carranza, A., Cordoba, D., et al. (1980). East Pacific Rise: hot springs and geophysical experiments. *Science (80-.).* 207, 1421–1433.

Statham, P. J., German, C. R., and Connelly, D. P. (2005). Iron (II) distribution and oxidation kinetics in hydrothermal plumes at the Kairei and Edmond vent sites, Indian Ocean. *Earth Planet. Sci. Lett.* 236, 588–596. doi:10.1016/J.EPSL.2005.03.008.

Statham, P. J., Yeats, P. A., and Landing, W. M. (1998). Manganese in the eastern Atlantic Ocean: Processes influencing deep and surface water distributions. *Mar. Chem.* 61, 55–68. doi:10.1016/S0304-4203(98)00007-3.

Straub, K. L., Benz, M., and Schink, B. (2001). Iron metabolism in anoxic environments at near neutral pH. *FEMS Microbiol. Ecol.* 34, 181–186.

Straub, K. L., Schönhuber, W. A., Buchholz-Cleven, B. E. E., and Schink, B. (2004). Diversity of ferrous iron-oxidizing, nitrate-reducing bacteria and their involvement in oxygen-independent iron cycling. *Geomicrobiol. J.* 21, 371–378.

Stumm, W., and Lee, G. F. (1961). Oxygenation of ferrous iron. *Ind. Eng. Chem.* 53, 143–146.

Sunda, W. G. (2001). “Bioavailability and bioaccumulation of iron in the sea,” in *The*

Biogeochemistry of iron in seawater, eds. D. R. Turner and K. A. Hunter (Wiley Chichester, UK), 396.

Swift, R. S. (1996). Organic Matter Characterization. *Methods Soil Anal.*, 1011–1069. doi:doi:10.2136/sssabookser5.3.c35.

Tagliabue, A., Aumont, O., and Bopp, L. (2014). The impact of different external sources of iron on the global carbon cycle. *Geophys. Res. Lett.* 41, 920–926.

Tagliabue, A., Bopp, L., Dutay, J. C., Bowie, A. R., Chever, F., Jean-Baptiste, P., et al. (2010). Hydrothermal contribution to the oceanic dissolved iron inventory. *Nat. Geosci.* 3, 252–256. doi:10.1038/ngeo818.

Tagliabue, A., Bowie, A. R., Boyd, P. W., Buck, K. N., Johnson, K. S., and Saito, M. A. (2017). The integral role of iron in ocean biogeochemistry. *Nature* 543, 51–59. doi:10.1038/nature21058.

Tagliabue, A., and Resing, J. (2016). Impact of hydrothermalism on the ocean iron cycle. *Philos. Trans. R. Soc. A Math. Phys. Eng. Sci.* 374. doi:10.1098/rsta.2015.0291.

Tagliabue, A., and Völker, C. (2011). Towards accounting for dissolved iron speciation in global ocean models. *Biogeosciences* 8, 3025–3039.

Tamura, H., Goto, K., Yotsuyanagi, T., and Nagayama, M. (1974). Spectrophotometric determination of iron (II) with 1, 10-phenanthroline in the presence of large amounts of iron (III). *Talanta* 21, 314–318.

Taylor, S. R. (1964). Abundance of chemical elements in the continental crust: a new table. *Geochim. Cosmochim. Acta* 28, 1273–1285.

Theis, T. L., and Singer, P. C. (1974). Complexation of iron (II) by organic matter and its effect on iron (II) oxygenation. *Environ. Sci. Technol.* 8, 569–573.

Thibon, F., Blichert-Toft, J., Tsikos, H., Foden, J., Albalat, E., and Albarède, F. (2019). Dynamics of oceanic iron prior to the Great Oxygenation Event. *Earth Planet. Sci. Lett.* 506, 360–370. doi:10.1016/j.epsl.2018.11.016.

Timmermans, K. R., Gerringa, L. J. A., de Baar, H. J. W., van der Wagt, B., Veldhuis, M. J. W., de Jong, J. T. M., et al. (2001). Growth rates of large and small Southern Ocean diatoms in relation to availability o iron in natural seawater. *Limnol. Oceanogr.* 46, 260–266. doi:10.4319/lo.2001.46.2.0260.

Toner, B. M., Fakra, S. C., Manganini, S. J., Santelli, C. M., Marcus, M. A., Moffett, J. W., et al. (2009). Preservation of iron(II) by carbon-rich matrices in a hydrothermal plume. *Nat. Geosci.* 2, 197. doi:10.1038/ngeo433.

Trivett, D. A., and Williams III, A. J. (1994). Effluent from diffuse hydrothermal venting: 2. Measurement of plumes from diffuse hydrothermal vents at the southern Juan de Fuca Ridge. *J. Geophys. Res. Ocean.* 99, 18417–18432.

Turekian, K. K. (1977). The fate of metals in the oceans.

Twining, B. S., Baines, S. B., and Fisher, N. S. (2004). Element stoichiometries of individual plankton cells collected during the Southern Ocean Iron Experiment (SOFeX). *Limnol. Oceanogr.* 49, 2115–2128.

Ussher, S. J., Achterberg, E. P., and Worsfold, P. J. (2004). Marine biogeochemistry of iron.

Environ. Chem. 1, 67–80.

van Haren, H., Duineveld, G., and de Stigter, H. (2017). Prefrontal bore mixing. *Geophys. Res. Lett.* 44, 9408–9415.

van Hulten, M., Dutay, J.-C., Middag, R., de Baar, H., Roy-Barman, M., Gehlen, M., et al. (2016). Manganese in the world ocean: a first global model. *Biogeosciences Discuss.* doi:10.5194/bg-2016-282.

Van Schooneveld, H. G., Litchy, M. R., and Grant, D. C. (2011). A Novel Method for Measuring the Sizes and Concentrations of 5-500 nm Particles in Colloidal Suspensions. in *Technical Proceedings of the 2011 Nanotechnology conference*.

Vedamati, J., Goepfert, T., and Moffett, J. W. (2014). Iron speciation in the eastern tropical South Pacific oxygen minimum zone off Peru. *Limnol. Oceanogr.* 59, 1945–1957.

Voelker, B. M., Morel, F. M. M., and Sulzberger, B. (1997). Iron redox cycling in surface waters: effects of humic substances and light. *Environ. Sci. Technol.* 31, 1004–1011.

Voelker, B. M., and Sedlak, D. L. (1995). Iron reduction by photoproduced superoxide in seawater. *Mar. Chem.* 50, 93–102.

Voelker, B. M., and Sulzberger, B. (1996). Effects of fulvic acid on Fe (II) oxidation by hydrogen peroxide. *Environ. Sci. Technol.* 30, 1106–1114.

Von Damm, K. L. (1995). Controls on the chemistry and temporal variability of seafloor hydrothermal fluids. *Seafloor hydrothermal Syst. Phys. Chem. Biol. Geol. Interact.* 91, 222–247. doi:10.1029/GM091p0222.

Waeles, M., Cotte, L., Pernet-Coudrier, B., Chavagnac, V., Cathalot, C., Leleu, T., et al. (2017). On the early fate of hydrothermal iron at deep-sea vents: A reassessment after in situ filtration. *Geophys. Res. Lett.* 44, 4233–4240. doi:10.1002/2017GL073315.

Waite, T. D., and Morel, F. M. M. (1984). Photoreductive dissolution of colloidal iron oxides in natural waters. *Environ. Sci. Technol.* 18, 860–868.

Wang, H., Yang, Q., Ji, F., Lilley, M. D., and Zhou, H. (2012). The geochemical characteristics and Fe (II) oxidation kinetics of hydrothermal plumes at the Southwest Indian Ridge. *Mar. Chem.* 134, 29–35.

Wichers, S. (2005). Verification of numerical models for hydrothermal plume water through field measurements at TAG. doi:10.1575/1912/1640.

Worsfold, P. J., Lohan, M. C., Ussher, S. J., and Bowie, A. R. (2014). Determination of dissolved iron in seawater: A historical review. *Mar. Chem.* 166, 25–35. doi:10.1016/j.marchem.2014.08.009.

Wu, J., Wells, M. L., and Rember, R. (2011). Dissolved iron anomaly in the deep tropical–subtropical Pacific: Evidence for long-range transport of hydrothermal iron. *Geochim. Cosmochim. Acta* 75, 460–468.

Wuttig, K., Townsend, A. T., van der Merwe, P., Gault-Ringold, M., Holmes, T., Schallenberg, C., et al. (2019). Critical evaluation of a seaFAST system for the analysis of trace metals in marine samples. *Talanta* 197, 653–668. doi:10.1016/j.talanta.2019.01.047.

Xiong, J., Fischer, W. M., Inoue, K., Nakahara, M., and Bauer, C. E. (2000). Molecular

evidence for the early evolution of photosynthesis. *Science (80-.).* 289, 1724–1730.

Yoon, J.-E., Yoo, K.-C., Macdonald, A. M., Yoon, H.-I., Park, K.-T., Yang, E. J., et al. (2018). Reviews and syntheses: Ocean iron fertilization experiments – past, present, and future looking to a future Korean Iron Fertilization Experiment in the Southern Ocean (KIFES) project. *Biogeosciences* 15, 5847–5889. doi:10.5194/bg-15-5847-2018.

Yuan, J., and Shiller, A. M. (2001). The distribution of hydrogen peroxide in the southern and central Atlantic ocean. *Deep Sea Res. Part II Top. Stud. Oceanogr.* 48, 2947–2970.

Yücel, M., Gartman, A., Chan, C. S., and Luther, G. W. (2011). Hydrothermal vents as a kinetically stable source of iron-sulphide-bearing nanoparticles to the ocean. Nature Publishing Group doi:10.1038/ngeo1148.

Appendix A – SeaFAST compiler

```
% Created by David Gonzalez Santana
%
% This script gets all the files from a folder named ExportYYYYMMDD. From the files
it extracts
% the counts over time for the different elements and integrates to give
% you a single result. It does this for everyfile and compiles them into a
% matrix which is then exported into an excel file.
%
% Date of creation: 12-04-2018
% Last modification: 15-06-2019
%
% E-mail for enquiries: david.gonzalezsantana@univ-brest.fr
%                       davidglez1994@gmail.com (personal, always active)
clear
clc
disp('Started, please wait')
```

Data location

```
%%%%%%%%%%%%%%%%%%%%%%%%%%%%%%%%%%%%%%%%%%%%%%%%%%%%%%%%%%%%%%%%%%%%%%%%%%%%%%%
% Insert directory of the folder with the files
directory = 'C:\Users\gonzalezs\Dropbox\PhD\ICP\2020\Export20200717'; % file
location
%%%%%%%%%%%%%%%%%%%%%%%%%%%%%%%%%%%%%%%%%%%%%%%%%%%%%%%%%%%%%%%%%%%%%%%%%%%%%%%
datalist = dir(directory);

quant_files = length(datalist); %calculate the number of files + 2 extra
datalist = datalist(3:quant_files); % Get the data files - the 2 extra
quant_files = quant_files-2; % we do not count the extra files
```

Files

```
name_file = datalist(1).name; % name of the file
loc_file = strcat(directory,'\',name_file); % location of the file
delimiterIn = '\t';
headerlinesIn = 12;
data = importdata(loc_file,delimiterIn,headerlinesIn); % Import file
[datacolumn,datarow]=size(data.data); % number of rows and columns in a data file
results = zeros(quant_files,datarow-1); %output matrix
headers1 = importdata(loc_file ,'\t',1); % get all headers
headers2 = headers1(1,2:end); % get real headers
Indium = find(contains(headers2,'In115(MR)')); % finds location in the results that
has In115
```

Choose and open datafiles

```
for file=1:quant_files
    name_file = datalist(file).name; % name of the file
    loc_file = strcat(directory,'\',name_file); % location of the file
    delimiterIn = '\t';
    headerlinesIn = 12;
    data = importdata(loc_file,delimiterIn,headerlinesIn); % Import file
```

Work in the file

```
    for element = 2:datarow
        if element == Indium+1
            areacal = 0;
            areacal = median(data.data(datacolumn-3:datacolumn,element));
        else
            cur_elem = data.data(:,element); % data form the current element
            median_a3 = median(cur_elem(1:3)); % mean of the first three values
            median_z7 = median(cur_elem(datacolumn- 6:datacolumn)); %mean of the
last seven values
            slope = (median_z7-median_a3)/(datacolumn-5); %calculate the slope as
Dy/Dx
            areacal =0; % Tare the area calculated
            for position = 4:datacolumn-7
                height = cur_elem(position)- slope*(position-3); % height between
the curve and the baseline
                if height < 0 % do not get negative heights
                    height = 0;
                end
                areacal = areacal + height; %Like a Riemann integral
            end
        end
        results(file,element-1) = areacal; % write the result
    end
end
disp('Done with ICPMS001.m');
```

```
Done with ICPMS001.m
```

Data preparation

```
disp('Started, please wait')
```

```
Started, please wait
```

Read the elements

```
Pb208 = find(contains(headers2,'Pb208(MR)'));
Mn55 = find(contains(headers2,'Mn55(MR)'));
Fe56 = find(contains(headers2,'Fe56(MR)'));
Co59 = find(contains(headers2,'Co59(MR)'));
Cu63 = find(contains(headers2,'Cu63(MR)'));
Zn66 = find(contains(headers2,'Zn66(MR)'));
Fe57 = find(contains(headers2,'Fe57(MR)'));
Ni60 = find(contains(headers2,'Ni60(MR)'));
Cu65 = find(contains(headers2,'Cu65(MR)'));
In115 = Indium;
```

Sort the data

```
sorted = zeros(quant_files,datarow-

1);

sorted(:,1) = results(:,Pb208);

sorted(:,2) = results(:,Mn55);

sorted(:,3) = results(:,Fe56);

sorted(:,4) = results(:,Co59);

sorted(:,5) = results(:,Cu63);

sorted(:,6) = results(:,Zn66);

sorted(:,7) = results(:,Fe57);

sorted(:,8) = results(:,Ni60);

sorted(:,9) = results(:,Cu65);

sorted(:,10) = results(:,In115);
```

Create the headers

```
xheader =
[{'Sample'},{'Pb208'},{'Mn55'},{'Fe56'},{'Co59'},{'Cu63'},{'Zn66'},{'Fe57'},{'Ni60'
},{'Cu65'},{'In115'}];
yheader = {datalist(1,1).name(1:end-4)};
for filename=2:quant_files
    yheader = [yheader;{datalist(filename,1).name(1:end-4)}];
end
```

Combine

```
combination = [yheader,num2cell(sorted)]; %yheader+results
```

Export

```
T=cell2table(combination,'VariableNames',xheader);
filename = 'Datafrom201800606Step1.xlsx';
writetable(T,filename,'Sheet',1,'Range','A1')
T=cell2table(combination,'VariableNames',xheader);
fnamepos = strfind(directory,'Exp');
fnameini = directory(fnamepos:end);
filename = strcat(fnameini,'_noindium.xlsx');
writetable(T,filename);

clc;
disp('Done with ICPMS001.m');
disp('Done with ICPMS002.m');
disp(strcat('File saved as', {' '},filename));
```

```
Done with ICPMS001.m

Done with ICPMS002.m

    'File saved as Export20200717_noindium.xlsx'
```

Indium correct

```
disp('Started, please wait')
In_corrected = zeros(quant_files,datarow);

for yaxis=1:quant_files
    for xaxis=1:datarow-1-1
        if yaxis==1
            In_corrected(yaxis,xaxis) = sorted(yaxis,xaxis);
            In_ratio = 1;
        else
            In_ratio = sorted(yaxis,datarow-1)/sorted(1,datarow-1);
            In_corrected(yaxis,xaxis) = sorted(yaxis,xaxis)/In_ratio;
        end
    end
    In_corrected(yaxis,datarow) = In_ratio;
end
In_corrected(:,datarow-1) = sorted(1,datarow-1);
```

```
Started, please wait
```

Export

```
combination = [yheader,num2cell(In_corrected)]; %yheader+results
xheader =
[{'Sample'},{'Pb208'},{'Mn55'},{'Fe56'},{'Co59'},{'Cu63'},{'Zn66'},{'Fe57'},{'Ni60'
},{'Cu65'},{'In115'},{'Inratio'}];

T=cell2table(combination,'VariableNames',xheader);
%fnameini = directory(end-13:end);
%fname = strcat(fnameini,'.dat');
fnamepos = strfind(directory,'Exp');
fnameini = directory(fnamepos:end);
fname = strcat(fnameini,'.xlsx');
writetable(T,fname);
clc;
disp('Done with ICPMS001.m');
disp('Done with ICPMS002.m');
disp(strcat('File saved as', {' '},filename)); % no In correction
disp('Done with ICPMS003.m');
disp(strcat('File saved as', {' '},fname)); % In corrected
```

```
Done with ICPMS001.m

Done with ICPMS002.m

    'File saved as Export20200717_noindium.xlsx'

Done with ICPMS003.m

    'File saved as Export20200717.xlsx'
```

Appendix B – Research collaborations

B.1. Published manuscripts

B.1.1. Birchill et al. (2019)

The eastern extent of seasonal iron limitation in the high latitude North Atlantic Ocean

Birchill, A. J., Hartner, N. T., Kunde, K., Siemering, B., Daniels, C., Gonzalez-Santana, D., Milne, A., Ussher, S. J., Worsfold, P. J., Leopold, K., Painter, S. C., & Lohan, M. C. (2019). The eastern extent of seasonal iron limitation in the high latitude North Atlantic Ocean. *Scientific reports*, 9(1), 1-12.

Abstract

The availability of iron (Fe) can seasonally limit phytoplankton growth in the High Latitude North Atlantic (HLNA), greatly reducing the efficiency of the biological carbon pump. However, the spatial extent of seasonal iron limitation is not yet known. We present autumn nutrient and dissolved Fe measurements, combined with microphytoplankton distribution, of waters overlying the Hebridean (Scottish) shelf break. A distinct biogeochemical divide was observed, with Fe deficient surface waters present beyond the shelf break, much further eastwards than previously recognised. Due to along and on-shelf circulation, the Hebridean shelf represents a much-localised source of Fe, which does not fertilise the wider HLNA. Shelf sediments are generally thought to supply large quantities of Fe to overlying waters. However, for this Fe to influence upper-ocean biogeochemical cycling, efficient off-shelf transport mechanisms are required. This work challenges the view that the oceanic surface waters in close proximity to continental margins are iron replete with respect to marine primary production demands.

B.1.2. Long et al. (2019)

Effects of copper on the dinoflagellate *Alexandrium minutum* and its allelochemical potency

Long, M., Holland, A., Planquette, H., González-Santana, D., Whitby, H., Soudant, P., Sarthou, G., Hégaret, H., & Jolley, D. F. (2019). Effects of copper on the dinoflagellate Alexandrium minutum and its allelochemical potency. *Aquatic Toxicology*, 210, 251-261.

Abstract

The dinoflagellate Alexandrium minutum produces toxic compounds, including paralytic shellfish toxins, but also some unknown extracellular toxins. Although copper (Cu) is an essential element, it can impair microalgal physiology and increase their toxic potency. This study investigated the effect of different concentrations of dissolved Cu (7, 79 and 164 nmol L^{-1}) on A. minutum allelochemical potency, here defined as negative effects of a protist on competing protists through the release of chemicals. This was studied in relation to its physiology. The effects of Cu were assessed on A. minutum growth, reactive oxygen species level, photosynthesis proxies, lipid metabolism, exudation of dissolved organic compounds, allelochemical potency and on the associate free bacterial community of A. minutum. Only the highest Cu exposure (164 nmol L^{-1}) inhibited and delayed the growth of A. minutum, and only in this treatment did the allelochemical potency significantly increase, when the dissolved Cu concentration was still toxic. Within the first 7 days of the high Cu treatment, the physiology of A. minutum was severely impaired with decreased growth and photosynthesis, and increased stress responses and free bacterial density per algal cell. After 15 days, A. minutum partially recovered from Cu stress as highlighted by the growth rate, reactive oxygen species level and photosystem II yields. This recovery could be attributed to the apparent decrease in background dissolved Cu concentration to a non-toxic level, suggesting that the release of exudates may have partially decreased the bioavailable Cu fraction. Overall, A. minutum appeared quite tolerant to Cu, and this work suggests that the modifications in the physiology and in the exudates help the algae to cope with Cu exposure. Moreover, this study shows the complex interplay between abiotic and biotic factors that can influence the dynamic of A. minutum blooms. Modulation in allelochemical potency of A. minutum by Cu may have ecological implications with an increased competitiveness of this species in environments contaminated with Cu.

B.1.3. Kunde et al. (2019)

Iron Distribution in the Subtropical North Atlantic: The Pivotal Role of Colloidal Iron

Kunde, K., Wyatt, N. J., González-Santana, D., Tagliabue, A., Mahaffey, C., & Lohan, M. C. (2019). Iron Distribution in the Subtropical North Atlantic: The Pivotal Role of Colloidal Iron. *Global Biogeochemical Cycles*, 33(12), 1532-1547.

Abstract

The low availability of the essential micronutrient iron (Fe) in the ocean impacts the efficiency of the biological carbon pump, and hence, it is vital to elucidate its sources, sinks, and internal cycling. We present size-fractionated dissolved Fe (dFe, <0.2 μm) measurements from 130 surface samples and 7 full-depth profiles from the subtropical North Atlantic during summer 2017 and demonstrate the pivotal role of colloidal (cFe, 0.02 to 0.2 μm) over soluble (sFe, <0.02 μm) Fe in controlling the dFe distribution. In the surface (<5 m), a strong west-to-east decrease in dFe (1.53 to 0.26 nmol L^{-1}) was driven by a dust gradient, which retained dFe predominantly as cFe (61% to 85% of dFe), while sFe remained largely constant at 0.19 ± 0.05 nmol L^{-1}. In the euphotic zone, the attenuation of dFe resulted from the depletion of cFe (0% to 30% of dFe), with scavenging as an important driver. In the mesopelagic, cFe was released from sinking biogenic and lithogenic particles, creating a zone of elevated dFe (0.7 to 1.0 nmol L^{-1}) between 400 to 1100 m depth. While the ocean interior, below the mesopelagic and above the seafloor boundary, exhibited a narrow range of cFe (40% to 60% of dFe), the abyssal cFe fraction varied in range from 26% to 76% due to interactions with seafloor sediments and a hydrothermal source with almost 100% cFe. Overall, our results produced an hourglass shape for the vertical cFe-to-dFe fraction and highlight the primary control of cFe on the dFe distribution.

B.2. Manuscripts under review

B.2.1. González-Delgado et al.

Chemical characterization of Punta de Fuencaliente CO_2 seeps system (La Palma Island, NE Atlantic Ocean): a new natural laboratory for ocean acidification studies

González-Delgado, S., González-Santana, D., Santana-Casiano, M., González-Dávila, M., Hernández, C. A., Sangil, C., & Hernández, J. C. (2020). Chemical characterization of Punta de Fuencaliente CO_2 seeps system (La Palma Island, NE Atlantic Ocean): a new natural laboratory for ocean acidification studies. *Biogeosciences Discussions*, 1-16.

Abstract

We present a new natural carbon dioxide (CO_2) system located off the southern coast of La Palma Island (Canary Islands, Spain). Like others CO_2 seeps, these seeps can be used as an analogue to study the effects of ocean acidification (OA) on the marine realm. With this aim, we present an accurate chemical characterization of the seeps system carbon emissions, describing the carbon system dynamics, by measuring pH, A_T and C_T, as well as, Ω aragonite and calcite. Our explorations on the area have found several emission points with similar chemical features. Here, the CO_2 emission flux varies between 2.8 kg CO_2 d^{-1} to 28 kg CO_2 d^{-1}, becoming a significant source of carbon. CO_2 seeps are of volcanic origin and the alteration of local ocean chemistry is due to acid brackish water discharges. Although this kind of acidified system is not a perfect image of future oceans, this area of La Palma island is an exceptional spot to perform studies aimed to understand the effect of different levels of OA on the functioning of marine ecosystems. These studies can then be used to comprehend how life has persisted through past Eras, with higher atmospheric CO_2, or to predict the consequences of present fossil fuel usage on the marine ecosystem of the future oceans.

Appendix C – Published article

Processes Driving Iron and Manganese Dispersal From the TAG Hydrothermal Plume (Mid-Atlantic Ridge): Results From a GEOTRACES Process Study

González-Santana, D., Planquette, H., Cheize, M., Whitby, H., Gourain, A., Holmes, T., Guyader, V., Cathalot, C., Pelleter, E., Fouquet, T., & Sarthou, G. (2020). Processes Driving Iron and Manganese Dispersal From the TAG Hydrothermal Plume (Mid-Atlantic Ridge): Results From a GEOTRACES Process Study. *Frontiers in Marine Science*, *7*, 568.

Abstract

Hydrothermal vents are a recognized source of trace elements to the ocean inventory. Nevertheless, the contribution of slow-spreading ridges remains poorly resolved. To address this, high-resolution dissolved (<0.45 μm) iron (dFe) and manganese (dMn) samples were collected during the GEOTRACES HERMINE GApr07 process study at the Mid Atlantic Ridge. Samples were collected at nine stations, from the TAG vent site to 75 km south-southwest following the neutrally buoyant plume. Concentrations of dMn and dFe ranged from 71 ± 6 and 51 ± 2 nmol kg^{-1} right above the vent site to 0.43 ± 0.01 and 1.56 ± 0.02 nmol kg^{-1} at the most distal station, respectively. Using a 5-box model coupled with our data, we show that as the plume traveled away from the vent, aggregation processes controlled dFe concentrations in the first 2 km, with an aggregation rate averaging between 8.0 ± 0.6 and 0.11 ± 0.04 nmol L^{-1} d^{-1}, respectively in the first and second kilometer. Aggregation, likely of small colloidal particles, led to partitioning of the size fractionated Fe pool, as 6% of the dFe was moved into the particulate size fraction. Further away, disaggregation processes became more prevalent, with rates ranging from 0.27 ± 0.02 to 0.008 ± 0.001 nmol L^{-1} d^{-1}, enriching the dFe pool by 10%. The computed decrease of hydrothermal Fe within the neutrally buoyant plume was likely caused by flocculation of small Fe oxyhydroxide particles. This process resulted in Fe aggregate formation with radii estimated to range between 14 and 20 μm in the first km from TAG. Between 2 and 30 km from the vent site, the radii ranged between 2 and 4 μm.

DOCTORAT SCIENCES BRETAGNE DE LA MER LOIRE ET DU LITTORAL

UBO Université de Bretagne Occidentale

Titre : Processus contrôlant la dispersion et la spéciation redox du fer dissous d'origine hydrothermale (dorsale médio-atlantique)

Mots clés : Cycle biogéochimique du fer, spéciation redox, sources hydrothermales, GEOTRACES

Résumé : Jusqu'à récemment, le rôle de l'activité hydrothermale dans le cycle des éléments traces et ses effets sur les cycles biogéochimiques ont été largement sous-estimés. En particulier, la contribution des dorsales à propagation lente reste mal résolue. Au cours de cette thèse, j'ai utilisé deux approches afin d'approfondir nos connaissances sur le cycle du fer (Fe) dans ces environnements. Tout d'abord, j'ai déterminé les concentrations et les constantes de taux d'oxydation du fer(II) (Fe (II)) autour de six sites hydrothermaux le long de la dorsale médio-atlantique (GA13). J'ai élargi la gamme de température de l'équation préexistante de taux d'oxydation du Fe (II) (kFe) afin de mieux contraindre ces taux dans l'océan profond où la température de l'eau de mer n'est que de 2 °C. Mes résultats montrent que même si la matière organique et les particules contribuent généralement à diminuer les k_{Fe} en produisant un temps de demi-vie de Fe (II) plus longs, les environnements hydrothermaux ont tendance à présenter des k_{Fe} plus élevées. Ainsi, les concentrations mesurées de Fe (II) pourraient ne représenter que 10 à 65% des concentrations initiales. Contrairement aux eaux océaniques profondes qui sont caractérisées par de faibles concentrations (<0,1 nmol L^{-1}) en Fe (II), les sites hydrothermaux acides agissent comme des sources avec des concentrations atteignant 70 nmol L^{-1}. Par ailleurs, j'ai étudié les processus qui affectent le Fe oxydé dans le panache à flottabilité neutre provenant du site hydrothermal TAG grâce à des échantillons collectés à haute résolution spatiale (GApr07). Mes résultats montrent que l'agrégation des particules prédomine dans les deux premiers kilomètres et que leur désagrégation prévaut entre 2 et 30 km de distance de TAG.

Title : Processes driving the dispersion and redox speciation of hydrothermally sourced dissolved iron (Mid-Atlantic Ridge)

Keywords : Biogeochemichal iron cycle, redox speciation, hydrothermal vents, GEOTRACES

Abstract : Hydrothermal vents are now recognized sources of trace elements to the ocean inventory. However, the contribution of slow-spreading ridges remains poorly resolved. In this Thesis I used two approaches to further advance our knowledge on the iron (Fe) cycle knowledge in hydrothermal environments. First, I determined the reduced iron (Fe(II)) oxidation rate constants (kFe) and Fe(II) concentrations in deep ocean waters and six different hydrothermal vent sites along the Mid-Atlantic Ridge during a transect study (GEOTRACES GA13). I expanded the temperature range of the existing Fe(II) oxidation rate equation to better constrain kFe in the deep ocean where seawater temperature reaches values lower than 2 °C. My results show that even though organic matter and particles generally contribute to decrease kFe (producing longer Fe(II) half-life times), hydrothermal environments tend to present higher kFe. Consequently, measured Fe(II) concentrations could potentially only account for 10 to 65 % of the original Fe(II) concentrations. While deep ocean waters were characterised by low (<0.1 nmol L-1) Fe(II) concentrations, acidic hydrothermal vent sites acted as Fe(II) sources with measured dFe(II) concentrations reaching values as high as 70 nmol L-1. Secondly, I developed a box model where I studied the processes which affect the oxidised Fe within the neutrally buoyant plume (aggregation, disaggregation, precipitation, and dilution) from the TAG hydrothermal vent site using high spatial resolution samples collected in a GEOTRACES process study (GApr07) and a box model. I show that particle aggregation predominated within the first two kilometres, and that disaggregation prevailed between 2 and 30 km from the vent site maintaining the suspended dissolved Fe.